HIGH RESOLUTION LASER SPECTROSCOPY OF THE $\tilde{A}^2\Pi$ - $\tilde{X}^2\Sigma^+$ SYSTEM OF CaOH AND CaOD RADICALS: ANALYSIS OF RENNER-TELLER, SPIN-ORBIT, K-TYPE RESONANCE AND FERMI RESONANCE INTERACTIONS

by

MINGGUANG LI

Submitted in partial fulfillment of
the requirements for the degree of
DOCTOR OF PHILOSOPHY
at
Dalhousie University
Halifax, Nova Scotia, Canada
July 1995

DALHOUSIE UNIVERSITY

FACULTY OF GRADUATE STUDIES

The undersigned hereby certify that they have read and recommend to the Faculty of Graduate Studies for acceptance a thesis entitled "High Resolution Laser Spectroscopy of the $\tilde{A}^2\Pi$ - $\tilde{X}^2\Sigma^+$ System of CaOH and CaOD Radicals: Analysis of Renner-Teller, Spin-Orbit, K-Type Resonance and Fermi Resonance Interactions"

by Mingguang Li

in partial fulfillment of the requirements for the degree of Doctor of Philosophy.

Dated August 24, 1995

External Examiner

Research Supervisor

Examining Committee

DALHOUSIE UNIVERSITY

DATE: August 25, 1995

AUTHOR: Mingguang Li

TITLE: "High Resolution Laser Spectroscopy of the $\tilde{A}^2\Pi - \tilde{X}^2\Sigma^+$ System of CaOH and CaOD Radicals: Analysis of Renner-Teller, Spin-Orbit, K-Type Resonance and Fermi Resonance Interactions"

DEPARTMENT OR SCHOOL: Department of Chemistry, Dalhousie University

DEGREE: Ph.D. CONVOCATION: Fall YEAR: 1995

Permission is herewith granted to Dalhousie University to circulate and to have copied for non-commercial purposes, at its discretion, the above title upon the request of individuals or institutions.

Signature of Author

TABLE OF CONTENTS

	PAGE
TABLE OF CONTENTS	iv
LIST OF FIGURES	vii
LIST OF TABLES	ix
ABSTRACT	x
LIST OF ABBREVIATIONS AND SYMBOLS	xi
ACKNOWLEDGEMENTS	xv
CHAPTER 1 Introduction	1
1.1 Brief History	2
1.2 Electronic Structure	5
1.3 Objectives of the Present Spectroscopic Studies of CaOH and CaOD	7
CHAPTER 2 Theoretical Background	13
2.1 Normal Vibrations	13
2.2 Vibronic and Spin-orbit Interactions	13
CHAPTER 3 Experimental Arrangement and Techniques	22
3.1 Broida Oven	22
3.2 Laser Excitation Spectroscopy	24
3.3 Resolved Fluorescence Spectroscopy	27
3.4 Intermodulated Fluorescence Spectroscopy	29
CHAPTER 4 Analysis of the $\tilde{A}^2\Pi(000)$ - $\tilde{X}^2\Sigma^+(000)$ Band of CaOD	32
4.1 Introduction	32
4.2 Laser Excitation Spectra	33
4.3 Least Squares Fit and Results	35
4.4 Isotope Relations of the Molecular Constants	40

CHAPTER 5 Excited Vibrational Levels in the $\tilde{X}^2\Sigma^+$ State of CaOH/CaOD 42

5.1 Introduction 42

5.2 Experimental Method 42

5.3 Resolved LIF Spectra 43

5.4 Results 47

5.5 Concluding Remarks 50

CHAPTER 6 Analysis of the $\tilde{A}$(010) - $\tilde{X}$(010)/(000) Bands of CaOH/CaOD 52

6.1 Introduction 52

6.2 Experimental Method; Excitation Spectra 53

6.3 Level Crossing and Quantum Mechanical Interference 62

6.4 Effective Hamiltonian Matrix 70

6.5 Least Squares Fit 77

6.6 Results and Discussion 77

6.7 Concluding Remarks 85

CHAPTER 7 Analysis of the $\tilde{A}$(100)/(020) - $\tilde{X}$(020)/(000) Bands of CaOH/CaOD 86

7.1 Introduction 86

7.2 Fermi Resonance 87

7.3 Laser Excitation Spectra 91

7.4 Resolved Fluorescence Spectra 99

7.5 Effective Hamiltonian Matrix 103

7.6 Least Squares Fit and Results 108

7.7 Discussion and Further Results 111

7.8 Concluding Remarks 128

CHAPTER 8 Equilibrium Geometry and Force Field in the $\tilde{A}$ and $\tilde{X}$ States of CaOH/CaOD 130

8.1 Introduction 130

8.2 Summary of the Molecular Constants 131

8.3 Equilibrium Geometry 133

8.4 Harmonic Force Field and Coriolis Coupling Constants 134

8.5 Vibration-rotation Interactions and Anharmonic Force Constants 139

8.6 Concluding Remarks 142

CONCLUSION 144

APPENDIX Tables of Rotational Transitions in the $\tilde{A}^2\Pi$ - $\tilde{X}^2\Sigma^+$ System of CaOH and CaOD 146

BIBLIOGRAPHY 194

LIST OF FIGURES

FIGURE NUMBER	TITLE	PAGE
2.1	Potential functions for the bending vibration in Σ, Π and Δ electronic states of linear molecules	15
2.2	Vector diagram of Hund's case (a) coupling of a linear triatomic molecule	16
2.3	Vibronic energy level diagram in the $\tilde{A}^2\Pi$ and $\tilde{X}^2\Sigma^+$ states of CaOH and CaOD; Selective detection scheme	21
3.1	Broida oven	23
3.2	Experimental set up for laser excitation spectroscopy	25
3.3	Experimental set up for resolved fluorescence spectroscopy	28
3.4	Schematic diagram for intermodulated fluorescence spectroscopy	30
4.1	A Portion of the Doppler-limited excitation spectrum of the CaOD $\tilde{A}(000)$ - $\tilde{X}(000)$ band	34
5.1	Fluorescence spectrum of CaOD $\tilde{A}(100)$ - $\tilde{X}(100)$ obtained by excitation of the $\tilde{A}(100)$ - $\tilde{X}(000)$ $R_2(18½)$ rotational transition	45
5.2	Energy level diagram for the case (a) $^2\Pi$ - case (b) $^2\Delta$ transition	46
6.1	The $\tilde{A}(010)$ - $\tilde{X}(010)/(000)$ vibronic transitions observed via laser excitation for both CaOH and CaOD	54
6.2	A portion of the excitation spectrum of the CaOH $\tilde{A}(010)\kappa^2\Sigma^{(-)}$ - $\tilde{X}(000)^2\Sigma^+$ subband	56
6.3	Energy level diagram for the $\tilde{A}(010)\kappa,\mu^2\Sigma$ - $\tilde{X}(000)^2\Sigma^+$ subbands	57
6.4	A portion of the excitation spectrum of the CaOD $\tilde{A}(010)^2\Delta$ - $\tilde{X}(010)^2\Pi$ R_1 branch (J''=29½ - 36½)	60
6.5	Reduced rotational term values of the $\tilde{A}(010)$ vibronic components of CaOH, obtained by subtraction of $BJ(J+1)$ with B=0.34024 cm^{-1}	63

6.6 Reduced rotational term values of the $\tilde{A}(010)$ vibronic components of CaOD, obtained by subtraction of $\bar{B}J(J+1)$ with $\bar{B}$=0.30904 cm^{-1} 65

6.7 Resolved LIF spectra of CaOH 68

6.8 The vibronic interactions between the (030) and (010) levels in the $\tilde{A}^2\Pi$ state 83

7.1 The $\tilde{A}(100)/(020)$ - $\tilde{X}(020)/(000)$ vibronic subbands observed via laser excitation for CaOH 88

7.2 The $\tilde{A}(100)/(020)$ - $\tilde{X}(020)/(000)$ vibronic subbands observed via laser excitation for CaOD 89

7.3 Energy level diagram of the $\tilde{A}^2\Pi$ (100) and (020) vibronic levels illustrating the effects of Renner-Teller, spin-orbit and Fermi resonance interactions 92

7.4 A portion of the excitation spectrum of the CaOH $\tilde{A}(020)\mu^2\Pi$ - $\tilde{X}(000)^2\Sigma^+$ subbands 96

7.5 A portion of the excitation spectrum of CaOD 98

7.6 Resolved LIF spectrum from excitation of the $\tilde{A}(020)\mu^2\Pi_{3/2}$ - $\tilde{X}(000)^2\Sigma^+$ $Q_2(8½)$ + $Q_2(32½)$ transitions of CaOH 100

7.7 Resolved LIF spectrum from excitation of the $\tilde{A}(020)\mu^2\Pi_{1/2}$ - $\tilde{X}(000)^2\Sigma^+$ $Q_1(13½)$ transition of CaOH 101

7.8 Resolved LIF spectrum from excitation of the $\tilde{A}(020)\mu^2\Pi_{1/2}$ - $\tilde{X}(000)^2\Sigma^+$ $Q_1(27½)$ transition of CaOH 102

7.9 K-type doublings, $\Delta\bar{\nu} = \bar{\nu}_e - \bar{\nu}_f$, in the $\tilde{A}^2\Pi$ (020) and (100) vibronic states of CaOH 121

7.10 K-type doublings, $\Delta\bar{\nu} = \bar{\nu}_e - \bar{\nu}_f$, in the $\tilde{A}^2\Pi$ (020) and (100) vibronic states of CaOD 122

LIST OF TABLES

TABLE NUMBER	TITLE	PAGE
4.1	Matrix representation of a Hund's case (a) $^2\Pi$ state	37
4.2	Molecular constants for the (000) levels of CaOD and CaOH	39
5.1	Molecular constants for excited vibrational levels in the $\tilde{X}^2\Sigma^+$ state of CaOH and CaOD	49
6.1	Effective Hamiltonian matrix for the $\tilde{A}^2\Pi(010)$ vibronic states of CaOH and CaOD	72
6.2	Molecular constants of the (000) and (010) levels in the $\tilde{A}^2\Pi$ and $\tilde{X}^2\Sigma^+$ states of CaOH and CaOD	78
7.1	Effective Hamiltonian matrix for the (100) and (020) $^2\Pi$ vibronic states of CaOH/CaOD	104
7.2	Matrix representation for $v_2=2$ in a $^2\Sigma^+$ electronic state	107
7.3	Molecular constants of the (100) and (020) levels in the $\tilde{A}^2\Pi$ and $\tilde{X}^2\Sigma^+$ states of CaOH and CaOD	110
7.4	Molecular parameters for CaOH/CaOD in the $\tilde{A}^2\Pi$ and $\tilde{X}^2\Sigma^+$ states	116
7.5	Mixing percentages of the $^2\Pi$ vibronic states of CaOH and CaOD	123
8.1	Molecular parameters for CaOH and CaOD in the $\tilde{A}^2\Pi$ state	132
8.2	Molecular parameters for CaOH and CaOD in the $\tilde{X}^2\Sigma^+$ state	132
8.3(a)	Calculated and experimental values of q^v	138
8.3(b)	Calculated and experimental values of D	138

ABSTRACT

A systematic spectroscopic investigation of the $\tilde{A}^2\Pi$ - $\tilde{X}^2\Sigma^+$ band system of CaOH and CaOD radicals has been carried out. The gas phase radicals were produced in a Broida oven. A Coherent 699-29 ring dye laser was operated in single mode. Extensive and highly precise data have been recorded using laser excitation spectroscopy and resolved fluorescence spectroscopy.

The $\tilde{A}(000)$ - $\tilde{X}(000)$ band of CaOD has been studied, yielding accurate molecular constants that are essential for further studies of excited vibrational levels. The excited vibrational levels, $v_1 \leq 4$ and $v_2 = 2$, in the $\tilde{X}^2\Sigma^+$ state of CaOH/CaOD have been rotationally analyzed via dispersion of the laser induced fluorescence.

High resolution analysis of the $\tilde{A}(010)$ - $\tilde{X}(010)/(000)$ and $\tilde{A}(100)/(020)$ - $\tilde{X}(020)/(000)$ bands of CaOH/CaOD has been performed. For each isotopomer, the measured line positions were fitted to a global deperturbation model that simultaneously takes account of the Renner-Teller, spin-orbit and K-type resonance or Fermi resonance interactions occurring in the $\tilde{A}^2\Pi$ state. The present work has obtained the largest data base with high precision for a linear molecule exhibiting these interactions, and has accomplished the most comprehensive and rigorous matrix deperturbations.

Employing the equilibrium rotational constants determined for the two isotopic molecules, the molecular equilibrium bond lengths in both the $\tilde{A}$ and $\tilde{X}$ states have been calculated.

In the present work, the Renner-Teller parameters, Fermi resonance parameters, Coriolis coupling constants and the molecular force field have been determined, for the first time, for an alkaline earth monohydroxide molecule.

LIST OF ABBREVIATIONS AND SYMBOLS

α_i	Vibration-rotation interaction constant
A	Spin-orbit coupling constant
A_D	Centrifugal distortion correction to the spin-orbit coupling constant
A_{eff}	Effective spin-orbit coupling constant
Å	Ångström unit (1×10^{-10} m)
B_v	Rotational constant for the vibrational level v
B_e	Equilibrium rotational constant
$\beta_{B,ij}$	Correction to rotational constants of vibronic states from third-order perturbation theory
c	Speed of light (2.99792458×10^8 ms^{-1})
D	Debye unit
D_v	Centrifugal distortion constant for the vibrational level v
d_i	Degeneracy of the vibrational mode ν_i
ϵ	Renner-Teller parameter
$\epsilon\omega_2$	Renner-Teller parameter
$\epsilon_D\omega_2$	Centrifugal distortion correction to the Renner-Teller parameter
e	Rotation-independent parity label
f	Rotation-independent parity label
f_{ij}	Harmonic force constants in curvilinear internal coordinates
f_{ijj}	Cubic anharmonic force constants in curvilinear internal coordinates
ϕ_{ijj}	Cubic anharmonic force constants in dimensionless normal coordinates
ϕ	Angle between the plane of the bent molecule and a reference plane
$F_{1,2}$	Spin components
γ_v	Spin-rotation constant for the vibrational level v
γ_D	Centrifugal distortion correction to γ_v

γ_{22}	Vibration-rotation interaction constant; coefficient of $(v_2+1)^2$
γ_{ll}	Vibration-rotation interaction constant; coefficient of ℓ^2
G_v	Vibrational energy (cm^{-1})
G	Vibrational angular momentum operator
$G_\pm$	Ladder operator of vibrational angular momentum
G_0	Vibrational energy with respect to the zero-point level
g_{22}	Vibrational anharmonicity constant; coefficient of ℓ^2
g_k	Non-adiabatic correction to the vibronic energy
$\hat{g}_4$	Anharmonic parameter accounting for the vibrational dependence of $\epsilon\omega_2$
H_v	Centrifugal distortion constant; coefficient of $[J(J+1)]^3$
H	Hamiltonian operator
h	Planck constant ($6.626\ 075\ 5(40) \times 10^{-34}$ Js)
$\hbar$	$\hbar = h/2\pi$
I_e	Moment of inertia at equilibrium
J	Total angular momentum quantum number (exclusive of nuclear spin)
J	Total angular momentum operator
$J_\pm$	Ladder operator of total angular momentum
κ	Vibronic state label for higher energy component
K	Vibronic angular momentum quantum number
k_{ijj}	Cubic anharmonic force constant in normal coordinates
Λ	Quantum number of the electron orbital angular momentum about the internuclear axis
L	Electron orbital angular momentum operator
L	Electron orbital angular momentum quantum number
ℓ	Vibrational angular momentum quantum number
λ_d	Drum wavelength of the monochromator
LIF	Laser induced fluorescence

μ	Vibronic state label for lower energy component
MOH	Metal monohydroxide
θ	Azimuthal angle describing the orientation of electron with respect to an arbitrary reference plane
ν_i	Vibrational mode; also for fundamental vibrational frequency (cm^{-1})
$\tilde{\nu}$	Frequency in unit of cm^{-1}
N	Total angular momentum operator (excluding electron spin and nuclear spin)
N	Total angular momentum quantum number (excluding electron spin and nuclear spin)
ω_i	Harmonic vibrational frequency of i^{th} vibrational mode in unit of cm^{-1}
p^e	Λ-type doubling constant
P	Vibronic angular momentum quantum number ($P = K + \Sigma$)
PMT	Photomultiplier tube
q^v	ℓ-type doubling constant
q^e	Λ-type doubling constant
q_i	Dimensionless normal coordinate
Q_i	Normal coordinate
r_e	Equilibrium bond length
Δr_{ij}	Displacements from equilibrium nuclear separations
R	Nuclear rotational angular momentum operator
S/N	Signal-to-noise ratio
S	Total electron spin angular momentum operator
$S_{\pm}$	Ladder operator of electron spin angular momentum
S	Total electron spin angular momentum quantum number
$\hat{\sigma}^2$	Variance of non-linear least squares fit
σ_z	Pauli matrix

T_{ev}	electronic-vibrational term value (cm^{-1})
v_i	Vibrational quantum number of the vibrational mode ν_i
$V^{\pm}$	Potential energy function for the bending vibration
V_F	Fermi resonance operator
W_1	Fermi resonance parameter
W_2	Fermi resonance parameter
x_{ik}	Vibrational anharmonicity constant
ζ_{ij}	Coriolis coupling constant

ACKNOWLEDGEMENTS

I wish to express my deep appreciation to Professor John Coxon for his encouragement and friendship. His liberal direction and constant support made this thesis work something of which I shall always be proud.

I am greatly indebted to the Graduate Studies Committee of the Department of Chemistry and the Supervisory Committee for their support.

The collaboration with my fellow graduate student Paul Presunka was very fruitful and enjoyable. The camaraderie of my fellow Canadian and Chinese students made this whole experience worthwhile.

The support system of this department has been very helpful. The assistance I received ensured that this research program was fulfilled as effectively as possible, and is gratefully acknowledged.

I would also like to thank Professor John Brown (Oxford University) for valuable discussions on the Hamiltonian and Professor Robert Field (M. I. T.) for his enthusiastic interest and encouragement in the process of this research.

Most of all, I would like to thank my wife, Lingxia, and my daughters, Tao and Zhi, whose love, understanding and support during the entire thesis work has been more important to me than I can ever say.

CHAPTER 1

Introduction

Gas phase alkaline earth monohydroxides, M-OH (M=Be, Mg, Ca, Sr, and Ba), have attracted much attention from both experimental and theoretical groups during the last 15 years. This interesting class of free radicals provides a number of ideal systems for optical studies since they are readily produced in the laboratory and their low-lying electronic states are located in a convenient region for dye laser excitation.

The present research program has attempted a systematic investigation of the $\tilde{A}^2\Pi$ - $\tilde{X}^2\Sigma^+$ system of two isotopic molecules, CaOH and CaOD. Extensive data with high precision have been recorded. Several types of interactions encountered in the $\tilde{A}^2\Pi$ state, namely, Renner-Teller, spin-orbit, K-type resonance and Fermi resonance, have been analyzed and treated using a *global matrix deperturbation* approach. The molecular equilibrium geometry and force field have been evaluated from the deperturbed molecular constants and perturbation parameters of the two isotopomers.

This first chapter provides background information about the molecules under consideration. The two objectives of the present research program are described in detail.

Chapter 2 gives a brief description of the theory on the normal vibrations and the angular momentum couplings in a linear triatomic molecule. Some empirical expressions for the vibronic levels are also presented.

A large part of the effort has been devoted to the experimental work. The experimental arrangement is described in Chapter 3. The technique, *selective detection* of the laser induced fluorescence, has been crucial for obtaining high quality spectra in the present work, and will be emphasized.

Chapters 4, 5, 6 and 7 form the main body of this thesis. The individual bands observed in this work are described respectively in the four chapters. An effective Hamiltonian taking account of the rotational structure, K-type doubling, Renner-Teller and spin-orbit couplings, and centrifugal distortion effects is presented in Chapter 6. This Hamiltonian is the basis for the success of the global matrix deperturbation of the $\tilde{A}(010)$ and the $\tilde{A}(100)/(020)$ vibronic manifolds. The treatment of the K-type resonance and the Fermi resonance is given in Chapters 6 and 7, respectively.

An important outcome of the present work is the molecular equilibrium geometry and force field, which are described in Chapter 8. Coriolis coupling constants have been derived from the harmonic force field, and yield calculated ℓ-type doubling constants that are in excellent agreement with experimental values.

Finally, the appendix contains 25 tables that list all the rotational transitions in the $\tilde{A}^2\Pi$ - $\tilde{X}^2\Sigma^+$ system of CaOH and CaOD recorded in this work. The importance of these tables is considered equal to that of the text.

1.1 Brief History

The reddish and greenish emission of CaOH was first observed by Herschel in 1823[1] when calcium-containing salts were added to an alcohol flame. However, the actual identity of the emitting molecular species remained uncertain for many years. By analogy with the emissions of the isoelectronic CaF and other alkaline earth halide diatomic molecules, James and Sugden[2] in 1955 suggested CaOH as the emitter and assumed the assignment of the red and green bands as the $\tilde{A}^2\Pi$ - $\tilde{X}^2\Sigma^+$ and $\tilde{B}^2\Sigma^+$ - $\tilde{X}^2\Sigma^+$ transitions, respectively. It was suggested that the similar bands observed in strontium and barium flames arise from the corresponding monohydroxides. Since then, numerous flame

investigations of these radicals have been undertaken because of the wide applications in analytical chemistry of flame emission and absorption for testing the presence of the alkaline earth metals. Substitution of D_2O for H_2O in the flames showed a clear isotope effect for the strontium bands[3], which gave some degree of confirmation to the assignment of SrOH. However, no isotope effect was detected in the spectra of the Ca flames[4].

The low-lying electronic states of the alkaline earth monohydroxides have very similar potentials. The Franck-Condon principle heavily favors the $\Delta v_i = 0$ sequences in which the bands are extensively overlapped. In the high temperature flames, where a large number of excited vibrational levels in the ground electronic state are populated, the band structures are so dense that even laser induced spectra appear almost featureless. In spite of ~150 years of spectroscopic effort since Herschel's first observation, it was only recently, 1983, that the identification of MOH as the dominant emitters in flame sources was unequivocally established.

In 1983, Wormsbecher *et al.*[5] found that substantial amounts of metal-containing polyatomic molecules could be produced in a low-temperature, low-pressure flow system, known as a Broida oven[6], which had been used previously for producing diatomic molecules. This system generated molecules in a much lower state of thermal excitation ($T \approx 700$ K) than the earlier flame sources ($T \approx 2400$ K) so that the spectral density was greatly reduced. Harris and co-workers soon performed high resolution laser spectroscopy of CaOH/CaOD[7] and SrOH/SrOD[8] produced in this new molecular source. In Ref. 7, a vibrational analysis of the $\tilde{X}^2\Sigma^+$ and $\tilde{A}^2\Pi$ states of CaOH/CaOD, a rotational analysis of the $\tilde{A}(000)$ - $\tilde{X}(000)$ band of CaOH and partial analysis of the $\tilde{A}(000)$ - $\tilde{X}(000)$ band of CaOD were all reported for the first time. Harris *et al.* were thus able to confirm the identification of CaOH as the dominant emitter observed previously

in flames, and to establish the linear geometry of the molecule.

This key development sparked a large number of further spectroscopic studies[9-18] of the alkaline earth monohydroxides; many other monovalent derivatives of the alkaline earth metals were also explored. Using the laser induced fluorescence technique combined with the Broida oven as the molecular source, rotational structure of the (000) - (000) and (100) - (100) bands of the $\tilde{B}$ - $\tilde{X}$ system of CaOH/CaOD were investigated by Bernath *et al.*[9,14] and by Li *et al.*[10]. Li and co-workers[11] also analyzed the rotational structure of the CaOH $\tilde{A}^2\Pi_{1/2}(100)$ - $\tilde{X}^2\Sigma^+(000)$ subband, but were unable, at that time, to perform an analysis of the $\tilde{A}^2\Pi_{3/2}(100)$ - $\tilde{X}^2\Sigma^+(000)$ subband owing to a severe perturbation from the $\tilde{A}^2\Pi(020)$ level. During the last five years, this molecule has been studied experimentally by at least four groups. Jarman and Bernath[17] investigated the $\tilde{C}^2\Delta$ - $\tilde{X}^2\Sigma^+$ transition of CaOH and CaOD with cw ring dye lasers. Steimle and co-workers[18] measured the permanent electric dipole moments of CaOH in the $\tilde{X}^2\Sigma^+$, $\tilde{A}^2\Pi$ and $\tilde{B}^2\Sigma^+$ states, using a recently developed laser ablation technique[19,20] for molecular production combined with their supersonic molecular beam Stark spectrometer. This new technique produces the CaOH sample with a rotational temperature as low as 50 K, which dramatically simplifies the laser excitation spectrum. These authors also observed the hyperfine structure[21] of CaOH in the $\tilde{X}^2\Sigma^+(000)$ state via microwave-optical double resonance with the same laser ablation - supersonic molecular beam apparatus. Ziurys *et al.*[16] obtained the pure rotational spectrum of CaOH and determined accurate molecular constants for the $\tilde{X}^2\Sigma^+(000)$ state using millimeter-wave absorption spectroscopy. The study of CaOH and CaOD in the present work has been focused on the $\tilde{A}^2\Pi$ - $\tilde{X}^2\Sigma^+$ system and the results will be reported in detail in Chapters 4 - 8. A parallel study of SrOH by Coxon and Presunka in this laboratory has recently provided extensive complementary

information for this molecule[22-24].

Theoretical interest in CaOH and other alkaline earth monohydroxides has been stimulated by the recent progress in spectroscopy. Bauschlicher *et al.*[25] performed a detailed *ab initio* study of the bending potentials of alkaline earth monohydroxides which revealed the different admixtures of covalent character in these molecules. Except for BeOH, the alkaline earth monohydroxides have only a very small degree of covalent character and were confirmed to possess linear geometry. These authors also calculated dissociation energies[25,26] for the alkali and alkaline earth monohydroxides and permanent electric dipole moments[27] for the $\tilde{X}$, $\tilde{A}$ and $\tilde{B}$ states of CaOH. Ortiz[28] performed electron propagator calculations and predicted the energies of several excited electronic states for $CaCH_3$, $CaNH_2$, CaOH and CaF. A semiempirical electrostatic polarization model was employed by Mestdagh and Visticot[29] to calculate the binding energies and dipole moments for the low-lying electronic states of alkali and alkaline earth monohydroxides. Recently, an alternative semiempirical approach by Allouche and Aubert-Frecon[30], based on ligand field theory, was applied to the Ca, Sr and Ba monohydroxides and resulted in the energies, molecular wavefunctions and dipole moments for the three lowest excited states. Employing the ligand field model, Jakubek and Field[31] performed a calculation of the molecular spin-orbit parameter in the CaOH $\tilde{C}^2\Delta$ state using atomic spin-orbit parameters. They demonstrated the non-negligible contributions to the molecular spin-orbit parameter from the orbitals that have only few percentage mixing coefficients.

1.2 Electronic Structure

It is well accepted that the OH group behaves very much like a fluorine ligand when bonded to an alkaline earth metal atom M. The electronic

structure of the M-OH molecules may be characterized as closed shell M^{2+} and OH^- ions with the addition of an unpaired electron in a molecular orbital localized on the metal center. The low-lying electronic transitions involve promotion of the electron in the non-bonding ns_σ orbital ($\tilde{X}$ state), localized on the metal, to a metal $np_\pi(n\text{-}1)d_\pi$ ($\tilde{A}$ state) or a metal $np_\sigma(n\text{-}1)d_\sigma$ ($\tilde{B}$ state) hybrid orbital. Since the transitions are localized on the metal and involve only the non-bonding electron, the potential surfaces of the excited electronic states are quite similar to that of the ground state. As a consequence, $\Delta v_i = 0$ sequences are dominant in the spectra and exhibit severely overlapped bands. The relatively low frequency bending vibrations and the $\tilde{A}$ state angular momentum couplings (vibronic, spin-orbit, *etc.*) further contribute to the congestion and complexity of the spectra.

The permanent electric dipole moment is a sensitive function of the properties of the valence electrons. Steimle *et al.*[18] have measured this important quantity for CaOH and SrOH in the $\tilde{X}^2\Sigma^+$, $\tilde{A}^2\Pi_{1/2,3/2}$ and $\tilde{B}^2\Sigma^+$ states. The values are obtained as 1.465, 0.836, 0.766 and 0.744 D, respectively, for CaOH, and 1.900, 0.590, 0.424 and 0.396 D for SrOH. The two molecules are expected to be highly ionic, which would predict much larger dipole moments. The small experimental values have been explained[18] as a consequence of the large polarization of the Ca^+ open-shell orbital away from OH^-.

For ionic molecules, like most of the alkaline earth monohydroxides, the chemical bonding is dominated by electrostatic forces. The minimum energy structures of these molecules are linear. BeOH was predicted[25] to be bent owing to the increased ionization potential of the metal and, accordingly, a diminished ionic contribution to the bonding. MgOH was proved to be linear by experimental observations[15]. However, *ab initio* calculations[25] have shown that the bending potential is quite flat, and only a small amount of energy is

needed to bend the MgOH molecule. For CaOH, SrOH and BaOH, ionic bonding is by far the dominant factor, and a linear structure is confirmed by both theory and experiment.

1.3 Objectives of the Present Spectroscopic Studies of CaOH and CaOD

Metal monohydroxide molecules are of considerable astrophysical interest[32]. The theoretical studies of Tsuji[33] predicted that monohydroxides and monochlorides form the major alkali, alkaline earth and aluminum species in cool stars. A tentative assignment of a CaOH absorption band in late-type M dwarf stars was reported by Pesch[34]; however, a radiotelescope search[35] failed to detect CaOH in circumstellar envelopes where CaOH was predicted to be an abundant compound. A very small permanent electric dipole moment obtained from theoretical calculations was assumed to be the reason of the failure. However, pure rotational transitions in the CaOH ground state have been observed recently in laboratories using millimeter-wave absorption[16] and microwave-optical double resonance[21]. These new observations will certainly encourage new searches in the space.

Spectroscopic results have been used frequently by quantum chemists to judge the quality of their theoretical calculations. Several groups have performed such calculations on CaOH and other alkaline earth monohydroxides as summarized in Section 1.1. Many of the results are yet to be confirmed by further spectroscopic experiments.

The spectroscopic method has been one of the premier methods for measuring concentrations and internal energy distributions of reactant and product species in reaction dynamics and kinetics studies. This method is powerful, of course, only if the relevant rovibronic levels have been well characterized. The previous spectral information on the monohydroxides of Ca,

Sr and Ba was used by Parson and co-workers[36,37] in studying chemiluminescent reactions of the metals with hydrogen peroxide. It was found that the ground state metal atoms produce both the metal oxides and metal monohydroxides in excited electronic states, while the metastable atoms produce solely metal monohydroxides. However, more spectroscopic information, especially for the excited vibrational levels of the MOH $\tilde{A}$ - $\tilde{X}$ system, are needed for further investigations.

The theoretical study of linear triatomic molecules in the spectroscopic regard has advanced far ahead of experiments. Renner's classical paper[38] "*On the theory of the interaction between electronic and nuclear motion in linear triatomic molecules*" appeared in 1934, while the first example[39] in the spectrum of NH_2 was reported 23-years later. Numerous quantum mechanical as well as empirical studies have been carried out since then. Nielsen[40] derived expressions for the vibration-rotation energies of linear X-Y-Z type molecules in non-degenerate electronic states. Pople[41] extended Renner's theory to take account of spin-orbit coupling, and derived vibronic energies of the non-rotating molecule in a $^2\Pi$ electronic state. Hougen[42] then established detailed expressions for rotational energy levels in a $^2\Pi$ electronic state by means of perturbation theory, but without including Λ-type and ℓ-type doublings. He also studied the effects of Fermi resonance[43] and anharmonicity[44] on the vibronic energy levels in Π electronic states. These early studies have been summarized by Herzberg[45]. Brown and Jorgensen[46] later derived more detailed anharmonic corrections for linear triatomic molecules in non-degenerate and degenerate electronic states. Jungen and Merer[47], and Brown and Jorgensen[48] carried out thorough quantum mechanical studies of the Renner-Teller effect, based on Renner's original study, with modern formulation which is convenient for practical use. Johns[49,50] and Brown[51]

studied the K-type doubling, which is a combination of electronic (Λ-type) and vibrational (ℓ-type) contributions in Π electronic states. These doubling effects are significant in today's high resolution spectroscopy and cause much complexity in the spectra. In the last three decades, a great deal of experimental work has been done on linear triatomic radicals. Most effort has been directed to 15-electron species, in particular BO_2[52,53], NCO[54,55,56], NCS[57,58] and CO_2^+ [59,60], all of which have a $^2\Pi$ ground electronic state. Interactions such as Renner-Teller, spin-orbit, K-type resonance or Fermi resonance have been observed in these radicals by high resolution spectroscopy. Some detailed analysis and modeling of these interactions was conducted for the NCO $\tilde{X}^2\Pi$ (010), (100)/(020) and (040)/(120)/(200) levels[55,56,61] and for the BO_2 $\tilde{A}^2\Pi_u(010)$ level[52,53]. Another class of linear triatomic radicals which exhibits these interactions and has been studied to some extent is the alkaline earth monohydroxides. However, previous work on MgOH[15], CaOH[7,9,10,11,14,16], SrOH[8,12] and BaOH[13] has not provided much information on excited vibrational levels, nor for the Renner-Teller effect and resonance interactions.

The present research program has been initiated with two objectives. The first is to conduct a systematic investigation on the excited vibrational levels of CaOH and CaOD; this would encompass the three normal modes in the $\tilde{X}^2\Sigma^+$ and $\tilde{A}^2\Pi$ states, and hence provide adequate information for accurate evaluation of the equilibrium geometry and the force field. The Ca-O stretching mode and the bending mode in the $\tilde{X}$ and $\tilde{A}$ states have now been characterized quite satisfactorily by the present work. Unfortunately, investigation of the excited O-H stretch vibrations has not been successful, despite a substantial effort. In fact, no excited O-H stretch vibrational level has ever been observed for any metal monohydroxide. Nevertheless, the

information for the CaOH/CaOD $\tilde{A}$ - $\tilde{X}$ system collected by this work has formed the largest data base for an alkaline earth monohydroxide molecule. By making reasonable assumptions for the O-H stretch mode, the molecular equilibrium geometry and force field have been evaluated with an appreciable accuracy.

The second objective of the present research is to investigate various interactions such as the Renner-Teller, spin-orbit, K-type resonance and Fermi resonance encountered in the $\tilde{A}^2\Pi$ state and to treat them in a global matrix deperturbation approach. The significance of such investigation may be justified in four aspects. First, although these interactions have been studied by many theoretical researchers[38,41-51], the resulting theories have only been applied to and tested in a few molecular systems[53,55,56,61] for which the data sets are either limited or have only moderate precision. The present work has obtained probably the largest data base with high precision for a linear triatomic molecule exhibiting these interactions, and has given the most comprehensive and rigorous test of the relevant theories so far. Second, a set of molecular constants that are appropriate for comparison with *ab initio* results and for evaluation of the geometrical structure and force field can only be obtained from a thorough deperturbation analysis of these interactions. The empirical effective "molecular constants" obtained directly from perturbed spectra often lack physical meaning and, hence, give misleading information. Third, some of the interaction parameters extracted from deperturbation analysis provide valuable additional information. For example, the Fermi resonance parameter W provides a direct measure of some of the cubic anharmonic force constants, and the vibration-rotation interaction parameters, α, determine linear combinations of the cubic force constants. Fourth, these interactions exist quite commonly in linear molecules and have precluded acquisition of spectroscopic information of many molecular systems. A

systematic investigation and deperturbation of these interactions would lead to a better understanding and improved practical means for dealing with these problems.

The $\tilde{A}^2\Pi$ electronic state is of particular interest in the present research because it contains more information than any other low-lying electronic state of this molecule. The coupling between the electron orbital angular momentum and the nuclear vibrational angular momentum has the first order effect only in a Π electronic state. The interaction between the electron orbital motion and the nuclear rotation, known as Λ-type doubling, has by far the largest effect in a Π electronic state.

The fact that $\omega_1 \approx 2\omega_2$ in CaOH and CaOD is unique among alkaline earth monohydroxides. Fermi resonance interactions arising from the associated degeneracies cause additional complexity in the spectra of CaOH/CaOD. However, they also provide an opportunity for understanding such interaction in a degenerate electronic state and for gaining valuable information on the cubic force field which can not be directly obtained in the absence of a resonance.

The simultaneous investigation of two isotopic molecules, CaOH and CaOD, is an important feature of the present work. The acquisition of spectroscopic data for both isotopomers has proved very valuable in providing crucial clues for analysis of the generally complex spectra. Isotope relations are an excellent diagnostic for the quality assessment of the molecular parameters determined by usually difficult and complicated deperturbations involving various interactions, such as Renner-Teller, spin-orbit and K-type resonance or Fermi resonance. The present research represents a rare example of a study of such interactions, based on highly precise and extensive data, that is conducted simultaneously for two isotopomers.

Since isotopic molecules have the same electronic structure the potential function, under the influence of which the nuclei are moving, is the same to a very high order of approximation. However, owing to the difference in the masses, the vibrational frequencies as well as the rotational constants are different. Spectroscopic information from molecules isotopic with the one considered gives additional equations for the force constants and for the bond lengths. As is well known, the number of force constants is larger than the number of vibrational frequencies; similarly, the geometrical structure can not be found from data for a single isotopomer. Therefore, in order to determine the force field and the equilibrium geometrical structure for a polyatomic molecule, it is necessary to have spectroscopic information from more than one isotopic molecule.

An isotopic change from H to D gives the largest relative mass change and, therefore, the largest isotope effect on the spectra and molecular constants. This is a tremendous advantage for the present research. It makes the use of isotopic information, as described above, particularly effective.

CHAPTER 2

Theoretical Background

2.1 Normal Vibrations

CaOH is a linear molecule, for which there are three normal modes of vibration[62]. v_1 and v_3 denote the quantum numbers for the Ca–O and O–H stretching vibrations, respectively; v_2 is the quantum number for the bending vibration, which has two degrees of freedom and is doubly degenerate. The vibrational energy levels are expressed[62] in cm^{-1} as

$$G(v_1\ v_2\ v_3) = \sum_i \omega_i (v_i + \tfrac{1}{2}d_i) + \sum_i \sum_{k \geq i} x_{ik} (v_i + \tfrac{1}{2}d_i)(v_k + \tfrac{1}{2}d_k) + g_{22}\, \ell^2 + \ldots \quad (2.1)$$

Here $d_i = 1$ for non-degenerate vibrations and $d_i = 2$ for the doubly degenerate vibration. ω_i is the harmonic frequency (cm^{-1}) of the corresponding normal vibration, x_{ik} and g_{22} are anharmonicity constants, and ℓ is a quantum number for the angular momentum about the internuclear axis created by the bending vibration. ℓ can take the values: v_2, v_2-2, . . . 1 or 0. The magnitude of the vibrational angular momentum is $\ell\hbar$.

2.2 Vibronic and Spin-orbit Interactions

In a degenerate electronic state ($\Lambda \geq 1$), the cylindrical symmetry of an exactly linear molecule makes it possible for the two orthogonal electronic components to lie at the same energy. However, as the nuclei move off the linear axis, their charges develop an electric dipole moment that disturbs the motion of the electrons and leads to coupling of the electron motion with the instantaneous configuration of the nuclei. This *vibronic* coupling is a breakdown of the Born-Oppenheimer approximation. The doubly degenerate electronic state is now split into two components which can be described by

distinct electronic wave functions, one symmetric and one antisymmetric with respect to reflection in the plane of the bent molecule. The energies of the two components diverge from one another as the amplitude of the bending motion increases. This phenomenon was first recognized by Teller and Herzberg[63] and was considered in detail by Renner[38]. The vibronic interaction has since become known as the Renner-Teller effect. Fig. 2.1 depicts the potential functions[45] for the bending vibration in Σ, Π and Δ electronic states of linear molecules. The abscissa is the bending coordinate r. The zero-order potential function can be written[45]

$$V^0 = a\, r^2 + b\, r^4 + \ldots \tag{2.2}$$

and the splitting of the potential function in Π, Δ, ... states has the form

$$V^+ - V^- = \alpha\, r^2 + \beta\, r^4 + \ldots \tag{2.3}$$

which manifests the magnitude of the vibronic interaction. For a (non-degenerate) Σ electronic state, there is no splitting. For a state with $\Lambda \geq 2$, such as a Δ state, the coefficient α is zero, and the splitting becomes noticeable only at very large r values. The vibronic splitting is significant only in Π electronic states.

Fig. 2.2 shows a vector diagram of Hund's case (a) coupling[64] for a linear triatomic molecule. The interaction of the electronic and vibrational angular momenta results in a vibronic angular momentum with a magnitude of $K\hbar$, where

$$K = \Lambda + \ell \tag{2.4}$$

Here Λ is the quantum number of the electron orbital angular momentum about the internuclear axis. Electronic states are labeled as Σ, Π, Δ, ... according to the values of $\Lambda = 0, 1, 2, \ldots$ The vibronic states are also labeled as Σ, Π, Δ, ... but correspond to $K = 0, 1, 2, \ldots$ With the coupling of electronic and vibrational momenta, K is a good quantum number,

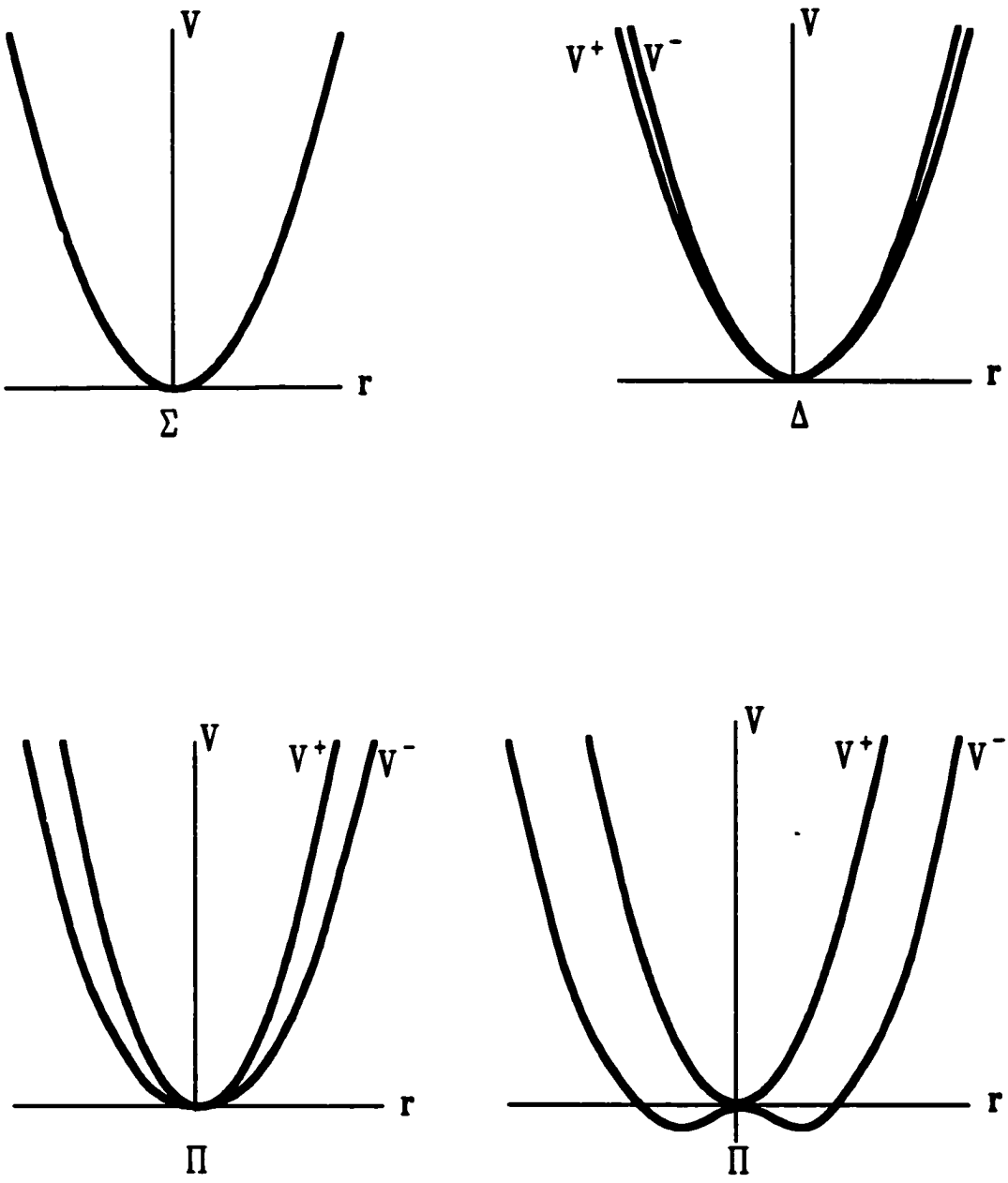

Fig. 2.1: Potential functions for the bending vibration in Σ, Π and Δ electronic states of linear molecules

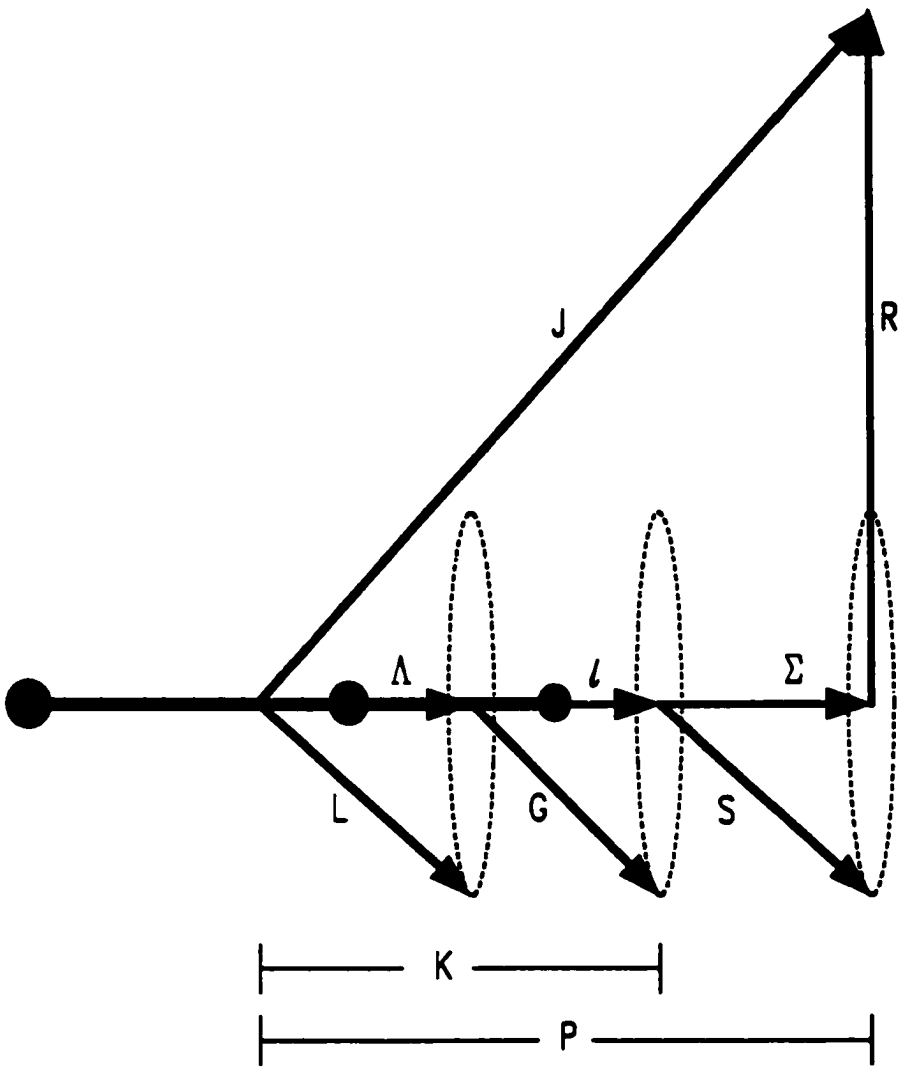

Fig. 2.2: Vector diagram of Hund's case (a) coupling of a linear triatomic molecule

L - electron orbital angular momentum

S - electron spin angular momentum

G - bending vibrational angular momentum

R - nuclear rotational angular momentum

while Λ and ℓ are no longer good quantum numbers.

When the electron spin is considered and is coupled with the internuclear axis, the resultant vibronic angular momentum has the magnitude $P\hbar$, and the quantum number P is defined as

$$P = \Lambda + \ell + \Sigma \tag{2.5}$$

where Σ is the quantum number of the electron spin angular momentum about the internuclear axis.

In quantum mechanical calculations, it is convenient to let the above symbols Λ, ℓ, Σ, K and P represent signed quantities; positive and negative values correspond to projections of the angular momenta along the linear axis in opposite directions. When used for labeling electronic or vibronic states, however, Λ, K and P are only given positive values.

For a Π electronic state, the interaction between the electron orbital angular momentum and the nuclear vibrational angular momentum can be represented[65-67] by two operators in a multipole expansion of the vibronic Hamiltonian. A dipolar operator couples electronic states with the selection rules $\Delta\Lambda = -\Delta\ell = \pm 1$, which is sometimes called Herzberg-Teller coupling. The vibronic wavefunction for a Π electronic state is perturbed to first order by Σ and Δ electronic states and the energy levels are affected in the second (and higher) order of perturbation theory. A quadrupolar operator couples the two components of the Π state with the selection rules $\Delta\Lambda = -\Delta\ell = \pm 2$. This coupling gives a contribution to the vibronic energies primarily in first order. The combined effect of the two operators is commonly regarded as the Renner-Teller effect.

The vibronic structure of a $^2\Pi$ electronic state has been theoretically studied, after Renner and Teller, by many authors. Among them Pople[41], Hougen[42], Merer[47], Brown[48] and Herzberg[45] have given results that are most

frequently used in spectroscopy.

For a vibronic level with $K = v_2 + 1$, which is called a "unique" level, the vibronic interaction has no first order effect. Its electron orbital angular momentum L_z is not "quenched" and, thus, the spin-orbit coupling attains the maximum value with a small second order correction from the vibronic interaction. It behaves much like a diatomic state and the vibronic energies, in unit of cm^{-1}, are expressed as

$$E(v_2\, K\, \Sigma) = \omega_2(v_2+1) \pm \tfrac{1}{2} A\, [\, 1 - \tfrac{1}{8}\epsilon^2 K(K+1)\,] - \tfrac{1}{8}\epsilon^2 \omega_2 K(K+1) \qquad (2.6)$$

where the last term is a small correction stemming from a second order vibronic effect ($\Delta v_2 \neq 0$) within the same electronic state.

A non-adiabatic correction term, introduced by Brown[66], is not included at present and will be considered in the Hamiltonian described later in Chapter 6.

The vibronic levels characterized by a quantum number of $K < v_2+1$ occur in pairs. This is a result of the splitting of the potential illustrated in Fig. 2.1. For $K \neq 0$, the vibronic energies are given by

$$E^{\kappa}(v_2\, K\, \Sigma) = \omega_2\, (1 - \tfrac{1}{8}\epsilon^2)\, (v_2+1) + r \mp \tfrac{1}{2} A_{eff} \qquad (2.7)$$

$$E^{\mu}(v_2\, K\, \Sigma) = \omega_2\, (1 - \tfrac{1}{8}\epsilon^2)\, (v_2+1) - r \pm \tfrac{1}{2} A_{eff} \qquad (2.8)$$

where

$$r = \tfrac{1}{2} \sqrt{A^2 + \epsilon^2\omega_2^2\, [(v_2+1)^2 - K^2]} \qquad (2.9)$$

and

$$A_{eff} = \frac{1}{8r} \epsilon^2\, \omega_2\, K\, (v_2+1)\, A \qquad (2.10)$$

Here, κ and μ label the higher and lower vibronic components, respectively, with the same K. A is the "true" spin-orbit coupling constant and ϵ is the Renner-Teller parameter. $\epsilon\omega_2$ is also known as the Renner-Teller parameter and is commonly used as a variable parameter in fitting vibronic expressions to spectroscopic data. The spacing between the κ and μ vibronic components is

2r, depending on both spin-orbit and vibronic couplings. In each vibronic component the effective spin-orbit splitting A_{eff} as expressed by Eq. 2.10, is much smaller than that in the "unique" level, indicating that the orbital angular momentum L_z is largely "quenched" by the first order vibronic interaction. As a consequence the rotational levels of these vibronic components conform closely to Hund's case (b). In addition, the effective spin-orbit splittings for the κ and μ components have opposite signs, as shown by the last terms in Eqs. 2.7 and 2.8. These important features must be considered in analysis of high-resolution spectra.

For $K = 0$, the Σ^+ and Σ^- vibronic components are dependent only on V^+ (or V^-) and V^- (or V^+), respectively. Their term values can also be expressed by Eqs. 2.7 and 2.8, but with $A_{eff} = 0$. Which of the two Σ components lies higher in energy can be inferred from the correlation diagram between the orbitals of bent and linear molecules, given by Walsh[68]. However, in practice, it is often more convenient to determine the symmetry species by analyzing the rotational structure using Hougen's expressions[42] and/or comparing relative intensities of relevant sub-bands, as will be described in detail later in Chapter 6. The wavefunctions of the two Σ vibronic components are often mixed owing to spin-orbit interactions and, hence, partially lose their character as levels with Σ^+ and Σ^- symmetries. Nevertheless, their symmetries are still distinguishable from the spectra; and the sign of the Renner-Teller parameter ϵ can be determined accordingly using the simplified expression

$$E^{\pm}_{K=0} = \omega_2 (v_2+1) (1 \pm \epsilon)^{1/2} \qquad (2.11)$$

where $\pm$ refer to Σ^+ and Σ^-, respectively. When ϵ is positive, the Σ^+ vibronic component lies at higher energy than Σ^-.

According to common practice, the full label of a vibronic level consists

of three parts. The first part represents the electronic state, the second encloses the vibrational quantum numbers in the order of v_1, v_2 and v_3 with brackets (the quantum number ℓ appears as a superscript above v_2 when appropriate), and the third denotes the vibronic symmetry. For example, $\tilde{A}^2\Pi(020)\mu^2\Pi_{3/2}$ denotes the vibronic level $\mu^2\Pi_{3/2}$ of the v_2=2 level in the $\tilde{A}^2\Pi$ electronic state.

Fig. 2.3 shows a schematic diagram of the vibronic levels in the $\tilde{A}^2\Pi$ and $\tilde{X}^2\Sigma^+$ states of CaOH and CaOD.

Term values of the vibronic levels in a $^2\Pi$ electronic state can, in principle, be calculated using Eqs. 2.6 - 2.10. Expressions for rotational structures of the vibronic levels have been derived by Hougen[42]. However, in practice, it is often difficult to represent and interpret observed spectra that are subject to the Renner-Teller interaction, especially when high precision data are available. This situation is largely attributed to the fact that various other interactions such as spin-orbit and Coriolis interactions and Fermi resonance are often present along with the vibronic interaction so that the resulting spectra are very complex. The vibronic and rotational levels can be accurately reproduced only by a detailed matrix deperturbation approach that simultaneously takes account of the various interactions and performs a global fit to the observed quantities. This approach is in fact the main feature of the work presented in this thesis. Nevertheless, the vibronic formulas described above and Hougen's rotational expressions normally give good approximations and are convenient guidance for spectrum analysis, particularly at the early stage.

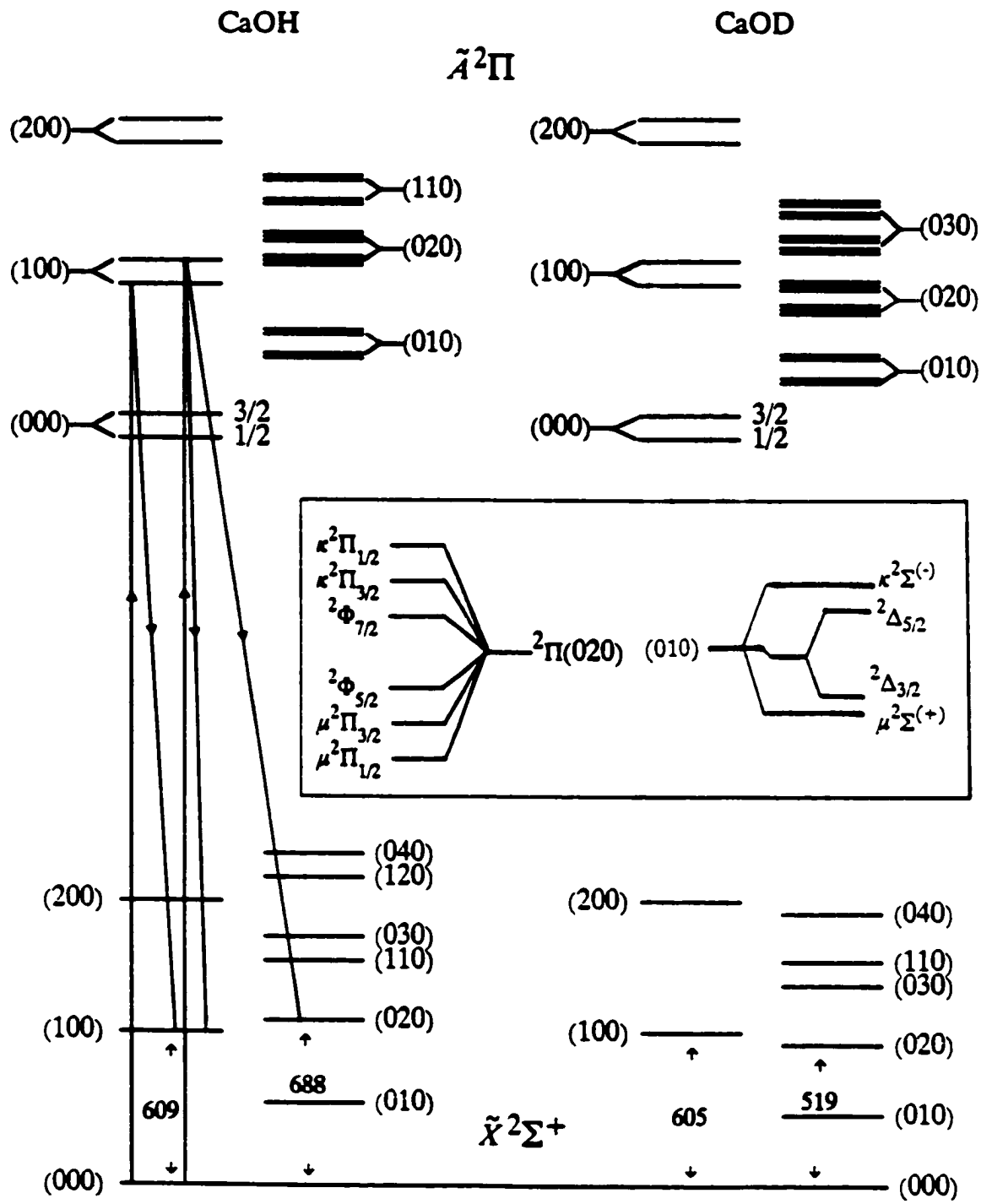

Fig. 2.3: Vibronic energy level diagram in the $\tilde{A}^2\Pi$ and $\tilde{X}^2\Sigma^+$ states of CaOH and CaOD; Selective detection scheme

CHAPTER 3

Experimental Arrangement and Techniques

3.1 Broida Oven

Gas phase CaOH/CaOD radicals were produced in a home-made Broida oven[6]. The design of the oven structure was based on a modified version used by Prof. Field's group at MIT, and is shown schematically in Fig. 3.1. Calcium metal contained in a small alumina crucible is resistively heated by a tungsten wire basket. The temperature is maintained slightly higher than the melting point (~839°C) of the calcium metal to achieve high metal vapor pressure and stable operation. A flow of Ar gas entrains the metal atoms and carries them a few centimeters up to a reaction region in the fluorescence chamber where oxidant vapor is present. The total pressure is typically 3-7 Torr and the oxidant vapor partial pressure is ~10 mTorr.

In the experiments on CaOH, an exothermic reaction of $Ca + H_2O_2$ produced a sufficient amount of CaOH radicals, characterized by strong orange color chemiluminescence. For production of CaOD, however, D_2O_2 is not commercially available. The reaction of $Ca + D_2O$ is endothermic and the resulting chemiluminescence was extremely weak. A microwave discharge (2450 MHz) through the D_2O flow prior to reaction with Ca vapor was then employed and resulted in orange color chemiluminescence almost as strong as that of CaOH. The mechanism for such signal enhancement has not been completely clear. It is most likely that the microwave discharge created a large population of the D_2O molecules at excited vibrational levels, which promoted endothermic reactions very effectively[69,70]. When the microwave discharge was initiated using a Tesla coil, problems from damage to the electronics of the dye laser system were encountered. Fortunately, it was found that the microwave

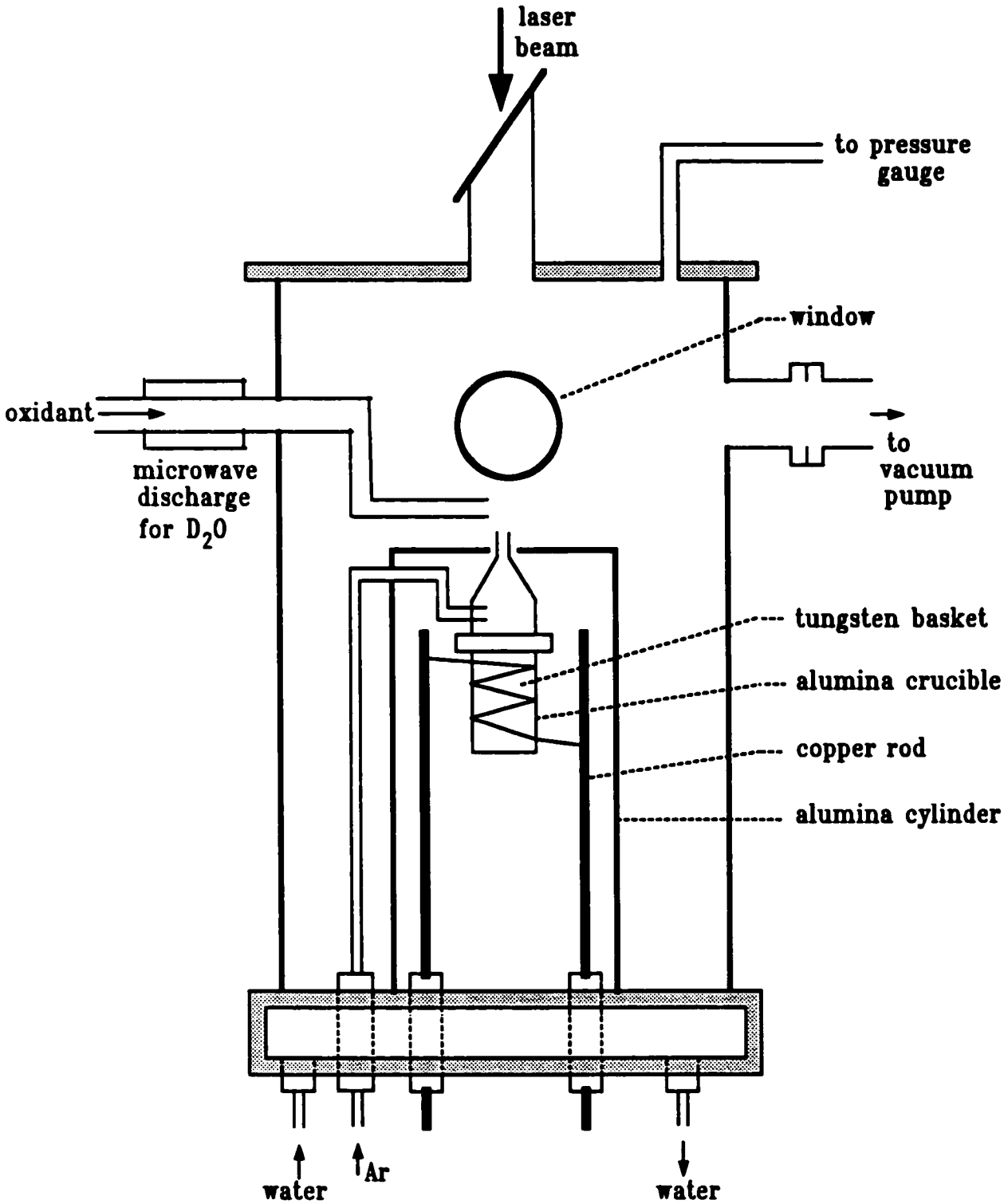

Figure 3.1: Broida Oven

discharge could be induced without the use of the Tesla coil by carefully adjusting the total pressure in the chamber to about 2 Torr.

3.2 Laser Excitation Spectroscopy

Fig. 3.2 shows a schematic diagram of the experimental set up for the laser excitation spectroscopy. A computer-controlled ring dye laser (Coherent Radiation 699-29) was operated in single mode with an effective line width of 1 MHz. It was pumped by an argon ion laser (CR-18) with 6.0 W output power at 514.5 nm single line. The output power of the dye laser varied from 100 to 600 mW depending on the output frequency and the type of the dye being used. The selection of the laser dye depends on the spectral region to be scanned. The output laser beam was modulated by a mechanical chopper (540 Hz frequency) and directed vertically through the fluorescence chamber, parallel to the flow direction of the CaOH/CaOD radicals. The laser-induced fluorescence (LIF) was imaged onto the entrance slit of a 1.26m Spex monochromator fitted with an RF-shielded GaAs photomultiplier tube (RCA C31034A-02) cooled at -20^{o}C. The output signal of the PMT was fed to a lock-in amplifier for phase sensitive detection to suppress the unwanted chemiluminescence. The spectrum obtained from the lock-in amplifier was then stored in the Apple computer of the Coherent 699-29 laser system.

The spectral line width was dominated by Doppler broadening, which was typically 1.2 GHz in the present molecular source. Line positions of the excitation spectrum were measured using the internal wavemeter of the 699-29 laser. An I_2 fluorescence excitation spectrum was recorded simultaneously by splitting a small fraction (~ 5%) of the output laser beam and directing it through an I_2 cell. The I_2 spectrum was compared to the standard I_2 atlas[71] to calibrate the frequency measurement of the wavemeter. The average

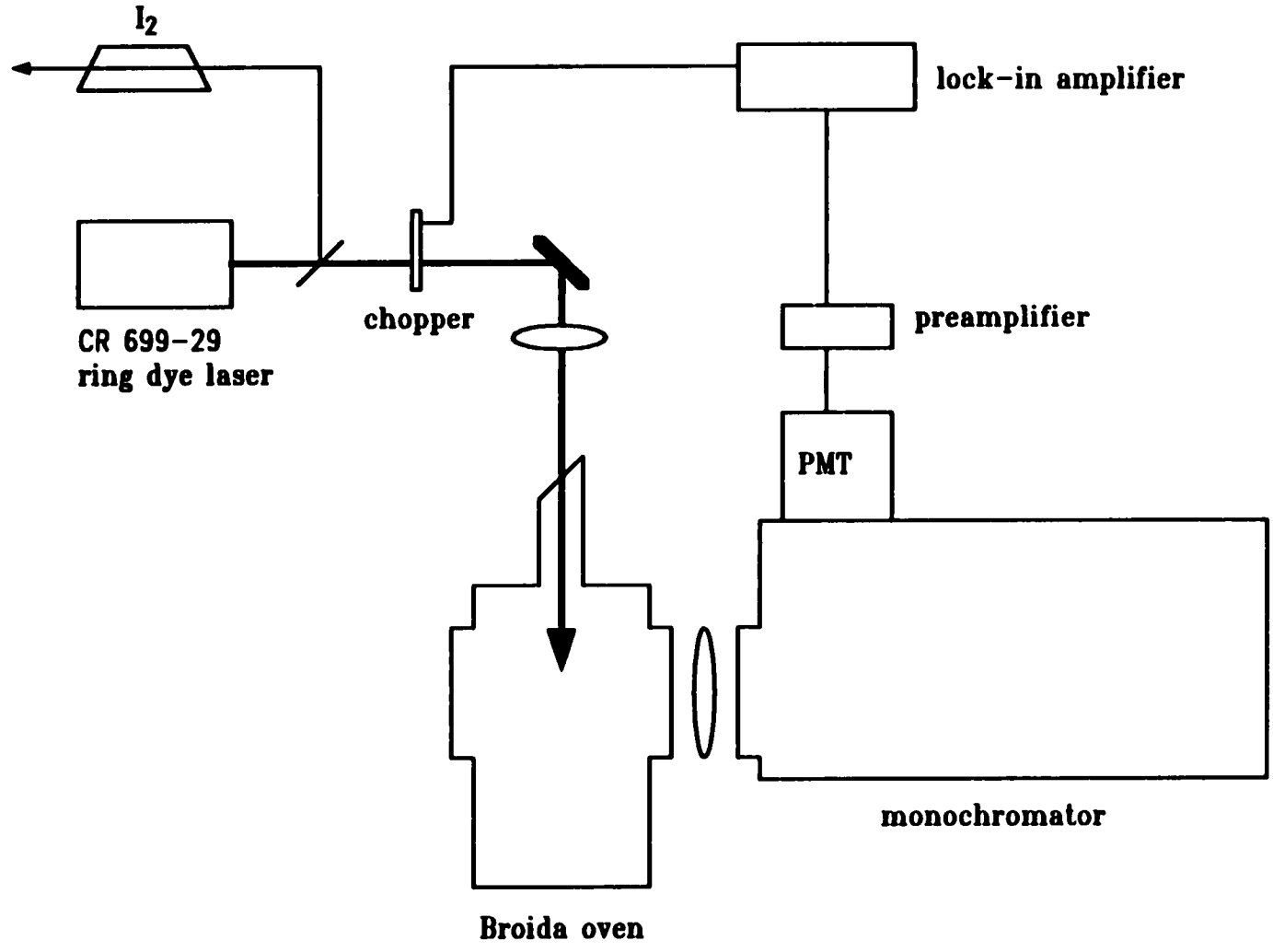

Fig. 3.2: Experimental set up for laser excitation spectroscopy

measurement accuracy for a well resolved rotational line was estimated to be 0.003 cm^{-1}.

When recording excitation spectra, the monochromator was used as a tunable narrow band-pass filter to selectively detect the LIF. The slit width of the monochromator was set typically at 1 mm, corresponding to a spectral width of ~3.5 Å. The primary advantage of such selective detection lies in the ability of this technique to simplify a highly congested spectrum and to completely suppress the scattered laser light. As described in Chapter 1, the excitation spectra of the alkaline earth monohydroxides are very congested due to the similar potentials involved. Although the use of the Broida oven has greatly reduced the spectral density, a majority of the excitation spectra were still too congested to analyze. The Renner-Teller, spin-orbit and Coriolis interactions and Fermi resonances further contribute to the spectral complexity. Selective detection has been an essential and powerful technique for the investigation of the CaOH and CaOD radicals. Fig. 2.3 depicts the experimental scheme. When $\Delta v_1 = +1$ or $\Delta v_2 = +2$ transitions are exited, $\Delta v_i = 0$ emissions are the dominant (> 90%) component of the LIF. By maintaining the monochromator at a frequency that is lower than the scanning laser frequency by an amount corresponding to the vibrational interval, the $\Delta v_i = 0$ component of the LIF is selectively detected. The use of this technique completely blocked the scattered laser light and largely suppressed other coincident bands which have different lower state vibrational spacings.

A second type of selective detection scheme has also been frequently employed; namely, scanning the laser frequency over the *R*-branch and detecting the LIF from the corresponding *P*-branch, or *vice-versa*. The use of this scheme almost completely suppressed any other bands and left only the desired lines in the spectrum. This technique requires some preliminary knowledge of

the rotational structure, and is particularly suitable for the final scan to extract a clean spectrum from the otherwise highly congested area.

In all the present work on CaOH and CaOD, not only has the selective detection resulted in much simplified spectra and enhanced signal/noise ratio, it has also proved to be a valuable diagnostic tool for analyzing overlapped and perturbed bands, as will be described in detail in Chapters 6 and 7.

3.3 Resolved Fluorescence Spectroscopy

Dispersion of laser induced fluorescence has been conducted for three basic purposes: (I) to identify the vibronic species of the upper state from spectral patterns and relative intensities; (II) to establish assignments of the quantum number J and e/f parity for rotational lines by means of the P-R separation method; (III) to investigate the vibration-rotation structures of the ground electronic state.

The experimental set up is illustrated in Fig. 3.3. As for the excitation spectroscopy, the dye laser was operated in single mode, the laser beam was traveling vertically through the fluorescence chamber and the LIF was imaged onto the entrance slit of the monochromator. However, the slit width was much narrower in this case, and the laser frequency was fixed at a particular rotational transition. The LIF was dispersed and recorded in the first order of the 1.26 m Spex monochromator which was fitted with a 2400 grooves/mm grating. The signal was detected using a GaAs photomultiplier tube (RCA C31034A-02) cooled at -20°C in a RF-shielded housing. The output of the PMT was fed into a PAR 1120 amplifier/discriminator and then a PAR 1105 photon counter. The dark current was normally less than 10 counts s^{-1}. Depending on the intensity of the LIF signal, the slit width was varied in a range of 40 - 60 μm, corresponding to a resolution range of 0.2 - 0.35 cm^{-1}.

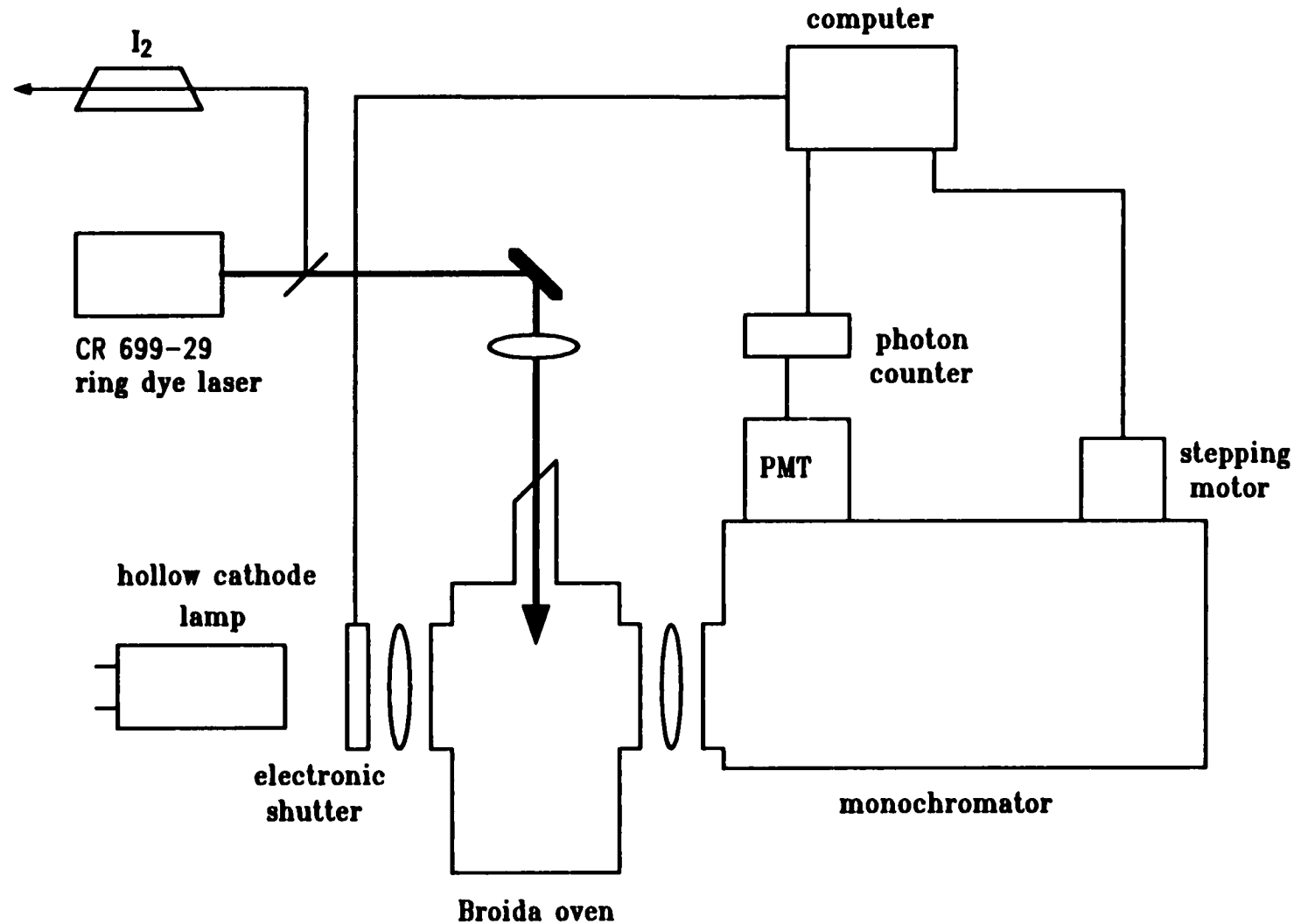

Fig. 3.3: Experimental set up for resolved fluorescence spectroscopy

Calibration of the monochromator was accomplished using a uranium hollow cathode lamp operated continuously. A TTL-controlled electric shutter is positioned between the uranium lamp and the Broida oven to control the detection of the calibration signals. The monochromator, photon counting system and electric shutter were controlled by a MINC PDP-11 computer via a highly versatile lab-built computer interface[72]. There are three primary advantages to this experimental system: (1) direct computer control of the experiment; (2) experimental and calibration spectra were recorded simultaneously, thereby eliminating time dependent errors associated with the drum wavelengths; and (3) electronic data acquisition. The differences between the measured drum wavelengths λ_d and the atlas wavelengths[73] of the uranium lines were fitted to a function[72]

$$\Delta\lambda = a + b\lambda_d + c\lambda_d^2 + \alpha \sin [2\pi(\lambda_d - \beta)/5] \qquad (3.1)$$

where the sine function takes into account the periodic error of the grating rotation lead screw. The fitted function was then used to obtain calibrated wavelengths for the experimental transitions. For each resolved LIF spectrum a set of 10 - 15 uranium lines spanning the wavelength region (10 - 30 Å) of interest were recorded and a least squares fit performed. The average measurement accuracy was estimated to be about 0.03 cm^{-1}.

3.4 Intermodulated Fluorescence Spectroscopy

This technique[74] was used to eliminate Doppler broadening which is the dominant factor affecting the line width in the excitation spectra, and is typically 1.2 GHz in the present system. The experimental scheme is shown in Fig. 3.4. The laser beam was split into two beams with equal intensities, which were modulated at different frequencies f_1 and f_2. The two beams passed through the flow of CaOH/CaOD molecules in opposite directions. When the

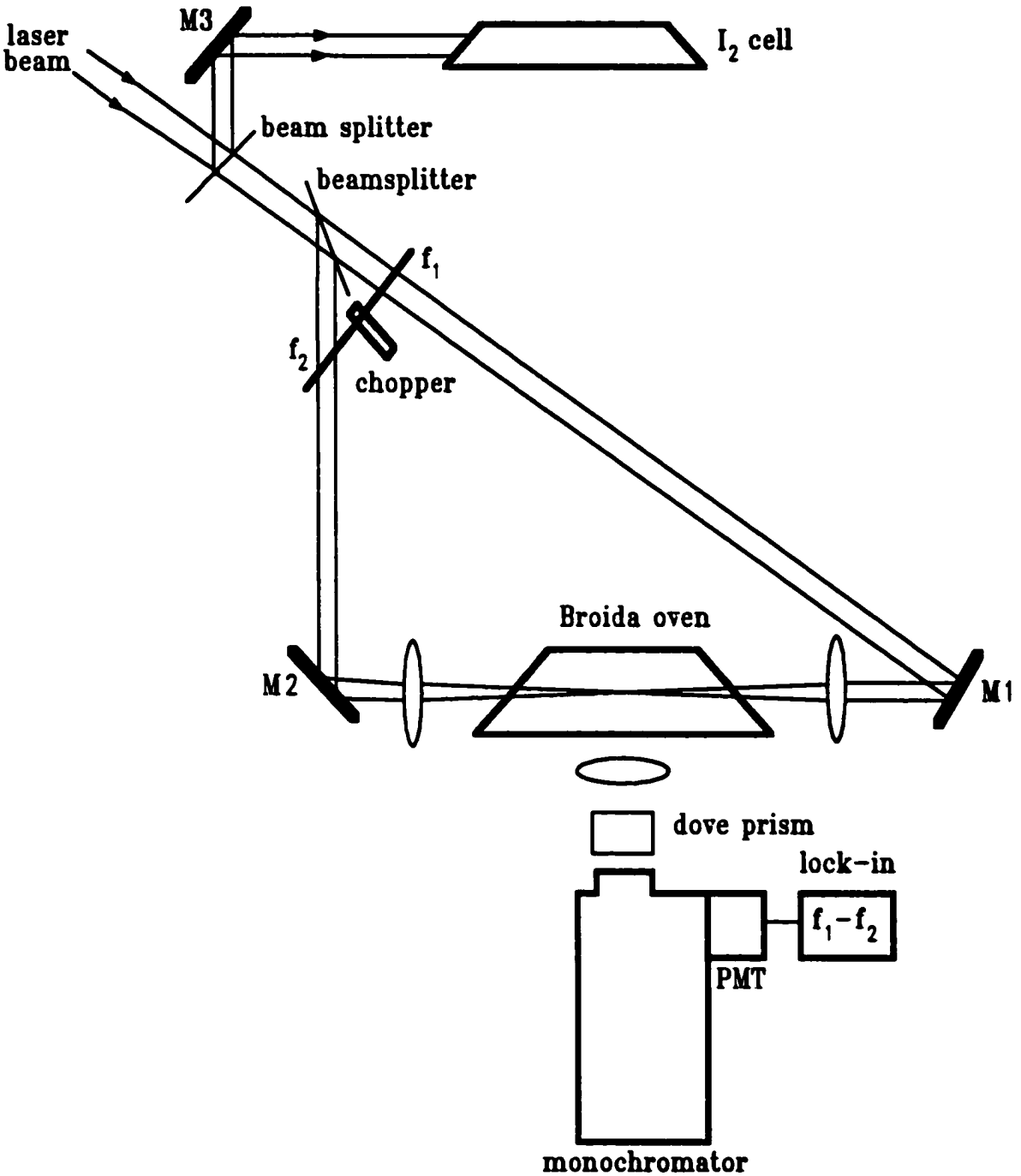

Fig. 3.4: Schematic diagram for intermodulated fluorescence spectroscopy

laser frequency was on-resonance with a rotational transition, the two beams interacted with the same group of molecules that have zero velocity component along the axis of the laser beam. A narrow signal based on the saturation effect was then obtained by detecting the laser induced fluorescence with the lock-in amplifier tuned to the frequency $(f_1 + f_2)$ or $(f_1 - f_2)$. The line width was then mainly dependent on the pressure broadening which was typically 100 - 150 MHz in our Broida oven. This technique is more sensitive than found with ordinary saturation spectroscopy, which detects the intensity change of the transmitted beam.

CHAPTER 4

Analysis of the $\tilde{A}^2\Pi(000)$ - $\tilde{X}^2\Sigma^+(000)$ Band of CaOD

4.1 Introduction

A detailed rotational analysis of the (000)-(000) band is an essential prerequisite to any further study of the $\tilde{A}$ - $\tilde{X}$ system involving excited vibrational levels. This band has the same fine structure as that of a Hund's case (a) $^2\Pi$ - case (b) $^2\Sigma^+$ band of a diatomic molecule[64]. It consists of two subbands with six branches for each subband. Owing to very small spin-rotation splittings in the lower state, each Q-line is coincident with a P- or an R-line. Hence, a total of eight branches are observable under Doppler limited resolution. A rotational analysis of this band for CaOH was first performed by Hilborn *et al.*[7], and a complementary study was described later by Bernath *et al.*[75]. Hilborn *et al.*[7] also attempted to observe this band for CaOD. However, it was possible for them to record only two branches, Q_1 and P_1, with relatively low precision (0.011 cm^{-1}), probably owing to the severe overlap of the hot bands and the poorer signal strengths for CaOD. As a consequence, only two effective parameters, B_v and D_v, for the $\tilde{A}^2\Pi_{1/2}$ spin component, along with B_v and D_v for the $\tilde{X}^2\Sigma^+(000)$ state, were determined with low accuracy. Later, Bernath and co-workers[14,17] obtained more accurate constants B_v, D_v and γ_v for the $\tilde{X}^2\Sigma^+(000)$ state of CaOD via observation of the $\tilde{B}^2\Sigma^+$ - $\tilde{X}^2\Sigma^+$ and $\tilde{C}^2\Delta$ - $\tilde{X}^2\Sigma^+$ systems. However, the molecular constants for the $\tilde{A}^2\Pi(000)$ state remained virtually unknown. In order to obtain these constants, which are crucial for further study of CaOD, the $\tilde{A}(000)$ - $\tilde{X}(000)$ band has been reinvestigated in the present work.

4.2 Laser Excitation Spectra

Gas phase CaOD radicals were produced in a Broida oven. A Coherent 699-29 ring dye laser was operated in single mode with Kitan red dye. The laser-induced fluorescence was imaged onto the entrance slit of the Spex monochromator. Instead of detecting the LIF back to the $\tilde{X}^2\Sigma^+(000)$ state, as was the case in the work of Hilborn *et al.*[7], the monochromator was set to selectively detect the LIF down to the $\tilde{X}^2\Sigma^+(100)$ state. This was an advantageous approach even though a large part of the fluorescence was lost; (about 90% of the LIF from the $\tilde{A}(000)$ level occurs to the $\tilde{X}^2\Sigma^+(000)$ level). By this means, it was possible to greatly simplify the spectrum and effectively suppress the scattered laser light, which is too intense to eliminate completely by any spatial filter. A portion of the excitation spectrum of the $(Q_2 + P_{21})$ branch obtained in this manner is illustrated in Fig. 4.1.

The second type of selective detection scheme was also employed; namely, scanning the laser frequency over the *R*-branch and detecting fluorescence from the corresponding *P*-branch, or *vice-versa.* This technique was used for the final scan, in which a spectrum with excellent signal/noise ratio was obtained.

In order to obtain reliable molecular constants, an important strategy, which has been overlooked by some authors, is worth pointing out. As mentioned before, there are a total of four $(Q + P)$ and $(Q + R)$ composite branches. The spin-rotation splitting within each composite line increases with rotational quantum number J. For values of J greater than 15½, these composite lines become noticeably broadened. However, the splittings cannot be resolved for $J \leq 50½$ in the Doppler-limited spectrum. Each measured line frequency is somewhere between the two lines, depending on their relative

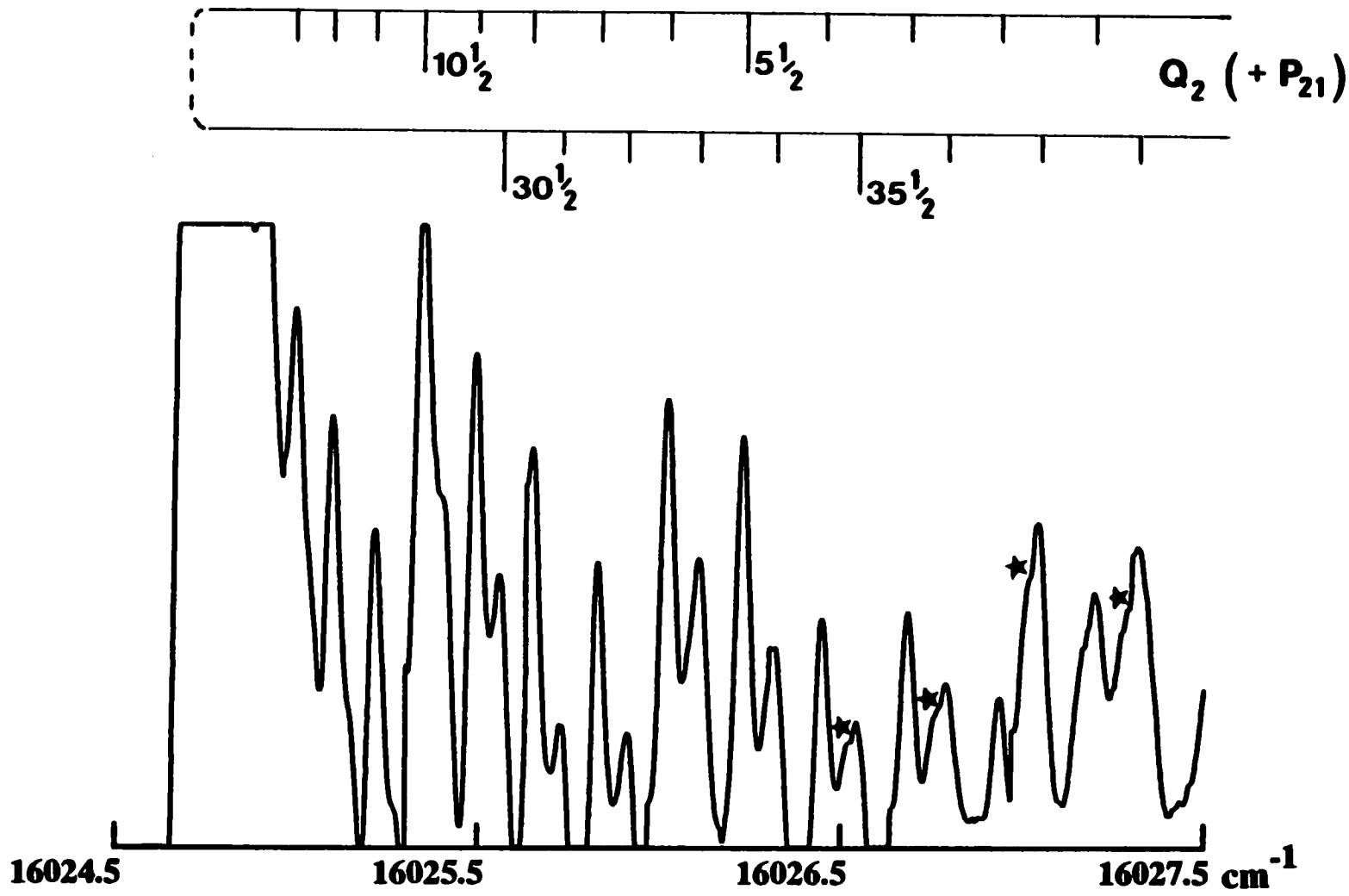

Fig. 4.1: A portion of the Doppler-limited excitation spectrum of the CaOD $\tilde{A}(000)$ - $\tilde{X}(000)$ band; The shoulders marked with an asterisk are the unresolved P_{21} lines.

intensities. Errors introduced in this way will certainly degrade the quality of the derived molecular constants, especially the higher-order constants such as D, p, q, A_D and γ. Accordingly, for those composite branches recorded with Doppler-limited resolution, only the line positions for $J \leq 15½$ were retained in the data set. All single branches were recorded, and as many lines as possible were measured. Such data are highly accurate and adequate for a fit of all of the molecular constants for both upper and lower states, except the spin-rotation constant γ of the lower state. The sub-Doppler technique, intermodulated fluorescence spectroscopy, was then employed to resolve the spin-rotation splittings for a total of 50 composite lines, (Q_2 + P_{21}) and (Q_{21} + R_2). Not all of the composite lines were scanned with the sub-Doppler technique because data acquisition was slower than that of the Doppler limited technique by a factor of 10, and the only purpose is to determine just one constant, γ. The sub-Doppler linewidth is 100 - 150 MHz at ~ 3 Torr total pressure in the fluorescence chamber. The measurement precision for these lines was limited by the precision of the wavemeter (0.003 cm^{-1}), not by the resolution. A computer program for measuring overlapped lines consisting of two or more Gaussian profiles, developed in this laboratory, was used to measure the composite (Q_1 + R_{12}) branch recorded with Doppler limited resolution, and also achieved similar precision.

The average measurement uncertainty was estimated to be 0.003 cm^{-1} for both Doppler-limited and sub-Doppler spectra.

4.3 Least Squares Fit and Results

The assignment of the rotational transitions was performed simply using the combination differences of the lower state, for which the molecular constants had been determined previously[17]. The $\tilde{A}^2\Pi(000)$ state was expressed

in a matrix representation shown in Table 4.1. The rotational levels of the $\tilde{X}^2\Sigma^+(000)$ state were expressed as

$$F_1(N) = B_v N(N+1) - D_v N^2(N+1)^2 + \tfrac{1}{2}\gamma_v N \quad (4.1)$$

$$F_2(N) = B_v N(N+1) - D_v N^2(N+1)^2 - \tfrac{1}{2}\gamma_v (N+1) \quad (4.2)$$

where F_1 and F_2 denote the spin components with $J = N + \frac{1}{2}$ and $J = N - \frac{1}{2}$, respectively.

A weighted, nonlinear least squares fitting procedure was used to fit the data of this band. The computer program for this procedure accepts either transition frequencies or term values as input data, along with initial guesses of the molecular parameters. In the present work only rotational transition frequencies were used as input data. Each measured rotational line is weighted by the square of the reciprocal of its estimated uncertainty, $w_i=(\delta y_i)^{-2}$. The initial values of the parameters are used to evaluate the Hamiltonian matrix, which is numerically diagonalized. The resulting eigenvalues are employed to calculate transition frequencies, which are then compared to the experimentally measured frequencies. Based on the differences between the calculated and measured frequencies, the values of the parameters are adjusted and a set of new eigenvalues are computed. This procedure is repeated until convergence is achieved. One of the advantages of this fitting procedure is that all the data of a band are used to fit all the parameters simultaneously. The statistical quality of the fit is given by the variance

$$\hat{\sigma}^2 = \frac{1}{N-m} \sum_{i=1}^{N} \frac{(y_i^{obs} - y_i^{calc})^2}{\delta y_i^2} \quad (4.3)$$

where $(N - m)$ is the number of degrees of freedom (number of data points minus number of varied parameters), and y_i is the transition frequency. The variance is a dimensionless number with value near 1 if the estimates of δy_i are reasonable and the fitting model is appropriate.

TABLE 4.1: Matrix Representation of a Hund's Case(a) $^2\Pi$ State

$\langle\, ^2\Pi_{3/2};\, J \pm \,\rangle$	$\langle\, ^2\Pi_{1/2};\, J \pm \,\rangle$
$T_v + \frac{1}{2}[A_v + A_{D_v}(z - 2)] + B_v(z - 2) - D_v[(z - 2)^2 + z - 1]$	$-[B_v - 2D_v(z - 1) \mp \frac{1}{2} q_v(J + \frac{1}{2})]\,(z - 1)^{1/2}$
$-[B_v - 2D_v(z - 1) \mp \frac{1}{2} q_v(J + \frac{1}{2})]\,(z - 1)^{1/2}$	$T_v - \frac{1}{2}[A_v + A_{D_v} z] + B_v z - D_v(z^2 + z - 1) \mp \frac{1}{2}(p_v + 2q_v)(J + \frac{1}{2})$

$z = (J + \frac{1}{2})^2$; the upper/lower signs refer to e/f levels.

In the case where severe perturbations occur to the upper or/and lower states and perturbation theory is no longer adequate to treat them, the Hamiltonian matrix needs to be expanded to include the perturbing state(s). The present computer program is very flexible for changing the matrix. It would be most desirable to record experimental data for the perturbing state(s) as well as the perturbed state(s) and to perform a global fit of the complete data set involving all major interacting states to the expanded Hamiltonian. This is often practically possible because the perturbing state(s) will gain transition strengths, if weak originally, through wavefunction mixing with the perturbed state. This approach is termed as a *global matrix deperturbation* approach in the present research work. When the bending vibration is excited by one or two quanta in the $\tilde{A}^2\Pi$ electronic state of CaOH/CaOD, the vibrational level is split into several components owing to the Renner-Teller and spin-orbit couplings. Strong K-type resonance interactions occur among the vibronic components in the $\tilde{A}(010)$ state, and strong Fermi resonance interactions occur between the components of the $\tilde{A}(100)$ and $\tilde{A}(020)$ levels. A global matrix deperturbation approach will be used to treat these systems, which are described in detail in Chapters 6 and 7.

The variance of the present fit was $\hat{\sigma}^2 = (1.022)^2$, in accord with an estimated measurement accuracy of 0.003 cm^{-1}. A total of 427 rotational transitions were included in the fit. These transitions with their quantum number J, measured line positions and residuals (observed - calculated) are listed in Table 1 in the Appendix. The fit has produced a set of well determined molecular constants for both the $\tilde{A}^2\Pi(000)$ and $\tilde{X}^2\Sigma^+(000)$ states, which are listed in Table 4.2.

TABLE 4.2: Molecular Constants[a] (cm^{-1}) for the (000) Levels of CaOD and CaOH

	CaOD		CaOH	
	$\tilde{X}^2\Sigma^+(000)$	$\tilde{A}^2\Pi(000)$	$\tilde{X}^2\Sigma^+(000)$[b]	$\tilde{A}^2\Pi(000)$[c]
T_{e_v}	0.0	15995.0160(3)	0.0	15998.1220(7)
A_v		66.7622(5)		66.8181(12)
B_v	0.3029872(60)	0.3090313(59)	0.33433411(1)	0.3412200(23)
D_v	$0.2943(16) \times 10^{-6}$	$0.2981(15) \times 10^{-6}$	$0.38600(3) \times 10^{-6}$	$0.3891(11) \times 10^{-6}$
γ_v	$0.1030(11) \times 10^{-2}$		$0.115964(23) \times 10^{-2}$	
p_v		-0.03942(2)		-0.04287(9)
q_v		$-0.2810(6) \times 10^{-3}$		$-0.3257(74) \times 10^{-3}$
A_{Dv}[d]		$-0.1349(4) \times 10^{-3}$		$-0.1786(20) \times 10^{-3}$

[a]Values in parentheses are 1σ standard deviations, in units of the last significant digit of the corresponding constant.

[b]From ref. 16.

[c]Redetermined with the matrix of Table 4.1 using the data from refs. 7 and 75.

[d]This A_{D_v} corresponds to the effective parameter $\tilde{A}_{D_v}$ in the text.

4.4 Isotope Relations of the Molecular Constants

It is interesting to examine the isotope relations between the molecular constants for CaOD and CaOH. For diatomic molecules, the ratios of equilibrium values of some molecular constants are isotopically invariant. These ratios are: p_e/B_e, q_e/B_e^2, A_{De}/B_e and γ_e/B_e. The molecular constants of the (000) level of a linear triatomic molecule are expected to obey these isotope relations quite well. Bernath and Brazier[75] fitted the constants for the CaOH $\tilde{A}^2\Pi(000)$ level by combining their data and the data from Ref. 7. However, since no energy level expressions were given in Ref. 75, a new fit has been performed employing the combined data set from Refs. 7 and 75 and the matrix used in the present work so that the best possible comparison could be made. The standard deviation of the fit for CaOH was 0.0065 cm^{-1}, and the refitted constants are also listed in Table 4.2. The isotopic ratios of some of the molecular constants taken from Table 4.2 are as follows:

$\tilde{X}(000)$: $B^D/B^H = 0.90624(2)$; $\gamma^D/\gamma^H = 0.89(1)$

$\tilde{A}(000)$: $B^D/B^H = 0.90567(2)$; $p^D/p^H = 0.920(2)$; $(q^D/q^H)^{1/2} = 0.93(2)$;

$A_D^D/A_D^H = 0.76(1)$

where the labels H and D denote CaOH and CaOD, respectively. Clearly, except for A_D, the isotope relations are satisfied very well. As first pointed out by Veseth[76], the constants A_D and γ in a $^2\Pi$ state are experimentally indistinguishable. The fitted parameter A_D is actually a linear combination of γ and the "true" A_D. For diatomic molecules, Brown and Watson[77] have shown that the contributions of A_{D_e} and γ_e to the rotational energy have different isotope effects. It is possible, therefore, to separate A_{D_e} and γ_e by combining data from two or more isotopomers. The relation given by Ref. 77 is

$$\tilde{A}_{D_e} = A_{D_e} - 2B_e\gamma_e/(A_e - 2B_e) \qquad (4.4)$$

where $\tilde{A}_{D_e}$ is the fitted or apparent parameter while A_{D_e} and γ_e are the

separated or *true* parameters. (A_{D_e}/B_e) and (γ_e/B_e) are isotopically invariant. Assuming Eq. 4.4 is approximately valid for the $\tilde{A}^2\Pi(000)$ level of CaOH/CaOD, and employing the fitted constants for both isotopomers from Table 4.2, the separate parameters A_{D_v} and γ_v can be calculated:

A_{D_v}(CaOH) = 0.000135 cm^{-1} $\quad$ A_{D_v}(CaOD) = 0.000123 cm^{-1}

γ_v(CaOH) = 0.0304 cm^{-1} $\quad$ γ_v(CaOD) = 0.0276 cm^{-1}

The "true" A_D values are now positive while the fitted $\tilde{A}_D$ values are negative. The "true" A_D may be expressed[78,79] for a diatomic state as

$$A_D = -2D_e \alpha_A (\alpha_e + 6B_e^2/\omega_e)^{-1} \qquad (4.5)$$

Considering the values of A_v and B_v in the $\tilde{A}^2\Pi$ (010), (100) and (020) levels of CaOH/CaOD (see Chapters 6 - 8 and Tables 6.2, 7.3 and 8.1), the α_A's are negative and the α_e's are positive; and thus the "true" values of A_D should be positive. This is consistent with the separated results.

In the investigation of the $\tilde{A}^2\Pi$ (010) state described later in Chapter 6, the constants A_D and γ_v were found separable owing to the existence of the Renner-Teller effect. The values of A_D and γ_v obtained from $\tilde{A}^2\Pi$ (000) and $\tilde{A}^2\Pi$ (010) are in good agreement.

It is to be noticed that the above values of γ_v include contributions from the spin-rotation interaction and the second order $H_{SO} \times H_{rot}$ effect, the later being usually dominant.

The constants for the CaOD $\tilde{X}^2\Sigma^+(000)$ state determined by this work are in very good agreement with those determined by Ref. 17, which are B = 0.3029549(66),D = 0.2934(19) × 10^{-6},andγ = 0.0953(25) × 10^{-2} cm^{-1}. The value of γ determined by this work using the sub-Doppler technique has a smaller standard error and obeys the isotope relation better than that from Ref. 17.

CHAPTER 5

Excited Vibrational Levels in the $\tilde{X}^2\Sigma^+$ State of CaOH/CaOD

5.1 Introduction

Several excited levels associated with the ν_1 and ν_2 vibrational modes in the $\tilde{X}^2\Sigma^+$ state of CaOH and CaOD have been rotationally analyzed. This was achieved via dispersion of laser induced fluorescence from selectively populated rotational levels of the $\tilde{A}^2\Pi$ (100) state.

There are two objectives for this part of the work. The first is to obtain the vibration-rotation structure of the ground electronic state with relatively high precision. The second is to facilitate investigations of excited electronic states. As well known, the low-lying excited electronic states have potential surfaces very similar to that of the ground state. The vibration-rotation structures of the excited states to be studied may be well predicted from the knowledge of the ground state. Further, knowing accurate vibrational spacings of the ground state is crucial for effectiveness of selective LIF detection which has been the most powerful technique used in studies of excited electronic states in the present work.

5.2 Experimental Method

The experimental set up is the same as that depicted in Fig. 3.3. Populating individual rotational levels of the $\tilde{A}^2\Pi$ (100) state was achieved with the Coherent 699-29 laser operating in single mode with Rhodamine 6G dye. A computer controlled spectrometer/calibration system was used. The experimental details have been described in Section 3.3. Fluorescence to the (100), (200) and (020) levels of the $\tilde{X}^2\Sigma^+$ state was recorded with a slit width of 40 μm, while for the much weaker fluorescence to the (300) and (400)

levels, either a 50 or 55 μm slit width was used.

The upper state, $\tilde{A}^2\Pi$ (100), had been previously studied to some extent for both CaOH and CaOD in this laboratory[80]. One of its two spin-components was found strongly perturbed by Fermi resonance with the $\tilde{A}^2\Pi$ (020) level. The rotational levels of the two spin-components were then fitted separately using purely empirical expressions. Although Fermi resonance interactions severely distorted and complicated the spectra, they provide a *window* to gain access to the excited bending $\tilde{A}$ (020) level, which is otherwise difficult to reach from the $\tilde{X}$(000) level owing to the small Franck-Condon factor. Since the $\tilde{A}$ (100) level contains significant $\tilde{A}$ (020) character, the $\tilde{X}$(020) level as well as the $\tilde{X}(v_1 00)$ levels can be studied via resolved fluorescence following excitation of the $\tilde{A}$ (100) level. A complete analysis of the Fermi diad, $\tilde{A}$ (100) ~ (020), will be presented in Chapter 7.

5.3 Resolved LIF Spectra

In order to observe the excited Ca-O stretching levels in the $\tilde{X}^2\Sigma^+$ state, the rotational levels of the CaOH $\tilde{A}^2\Pi_{1/2}$(100) or the CaOD $\tilde{A}^2\Pi_{3/2}$(100) state were populated. Since these levels are only weakly perturbed by the (100)-(020) Fermi resonance, they retain strong transition strengths in fluorescence to the $\tilde{X}^2\Sigma^+$ v_1 levels. This was important for observation of the v_1 = 2, 3 and 4 levels in the $\tilde{X}$ state. The transition strength decreases with increasing value of $|\Delta v_1|$; for CaOH, the fluorescence intensities to the $\tilde{X}$(100), (200) and (300) levels are approximately in the ratio of 1 : 0.1 : 0.008. The $\tilde{A}$(100) - $\tilde{X}$(400) fluorescence was extremely weak and only the stronger of the two fluorescence lines was observed in each spectrum. For CaOD, the overall intensity of the spectrum was weaker than that of CaOH, and only the (100), (200) and (300) levels of the $\tilde{X}$ state were observed. The

relative intensities of these bands, however, were similar to those for CaOH.

Fig. 5.1 shows a resolved LIF spectrum belonging to the $\tilde{A}(100)$ - $\tilde{X}(100)$ band recorded by exciting the CaOD $\tilde{A}(100)$ - $\tilde{X}(000)$ $R_2(18\frac{1}{2})$ rotational transition. The $P_2(20\frac{1}{2})$ fluorescence line has approximately half intensity of the $R_2(18\frac{1}{2})$ + $Q_{21}(19\frac{1}{2})$ line, which is expected for a typical $^2\Pi$ (case a) - $^2\Sigma$ (case b) transition. In addition to these two main lines, many extra lines induced by collisional energy transfer appear in the spectrum. In Fig. 5.1, the Q_2 head was formed by parity-changing collisions. These collisional lines provide additional information. A maximum of three collisional lines on each side of the main line could be measured to the same accuracy as the main line, and were included in the data sets. Other lines further away from the main line have poorer and broadened lineshapes and were excluded from the data set unless an average line position could be found from several different spectra. The resolved $\tilde{A}(100)$ - $\tilde{X}(200)$ LIF spectra also contained many collisional lines, albeit with lower intensities, while the $\tilde{A}(100)$ - $\tilde{X}(300)$ spectra exhibited only two main lines and a collisionally induced Q_2 head.

Access to the (02^00) and (02^20) bending levels of the $\tilde{X}^2\Sigma^+$ ground state was achieved by populating selected rotational levels of the $\tilde{A}^2\Pi$ (100) state perturbed strongly by Fermi resonance with the $\tilde{A}^2\Pi$ (020) level. This corresponds to excitation of the CaOH $\tilde{A}^2\Pi_{3/2}(100)$ - $\tilde{X}^2\Sigma^+(000)$ and the CaOD $\tilde{A}^2\Pi_{1/2}(100)$ - $\tilde{X}^2\Sigma^+(000)$ transitions. The $\tilde{X}^2\Sigma^+(020)$ level is split into ℓ=0 ($^2\Sigma^+$) and ℓ=2 ($^2\Delta$) components due to anharmonicity of the bending vibration. The rotational structure of the $\tilde{X}(02^00)^2\Sigma^+$ level is similar to that of the $\tilde{X}(000)^2\Sigma^+$ level. The $\tilde{X}(02^20)^2\Delta$ state also belongs to Hund's case(b), with a very small splitting of each J-level into two ℓ-type doubled components. The resolved LIF pattern of the $\tilde{A}(100)^2\Pi$(a) - $\tilde{X}(020)^2\Delta$(b) transitions can be inferred from the energy level diagram shown in Fig. 5.2. The intensity of

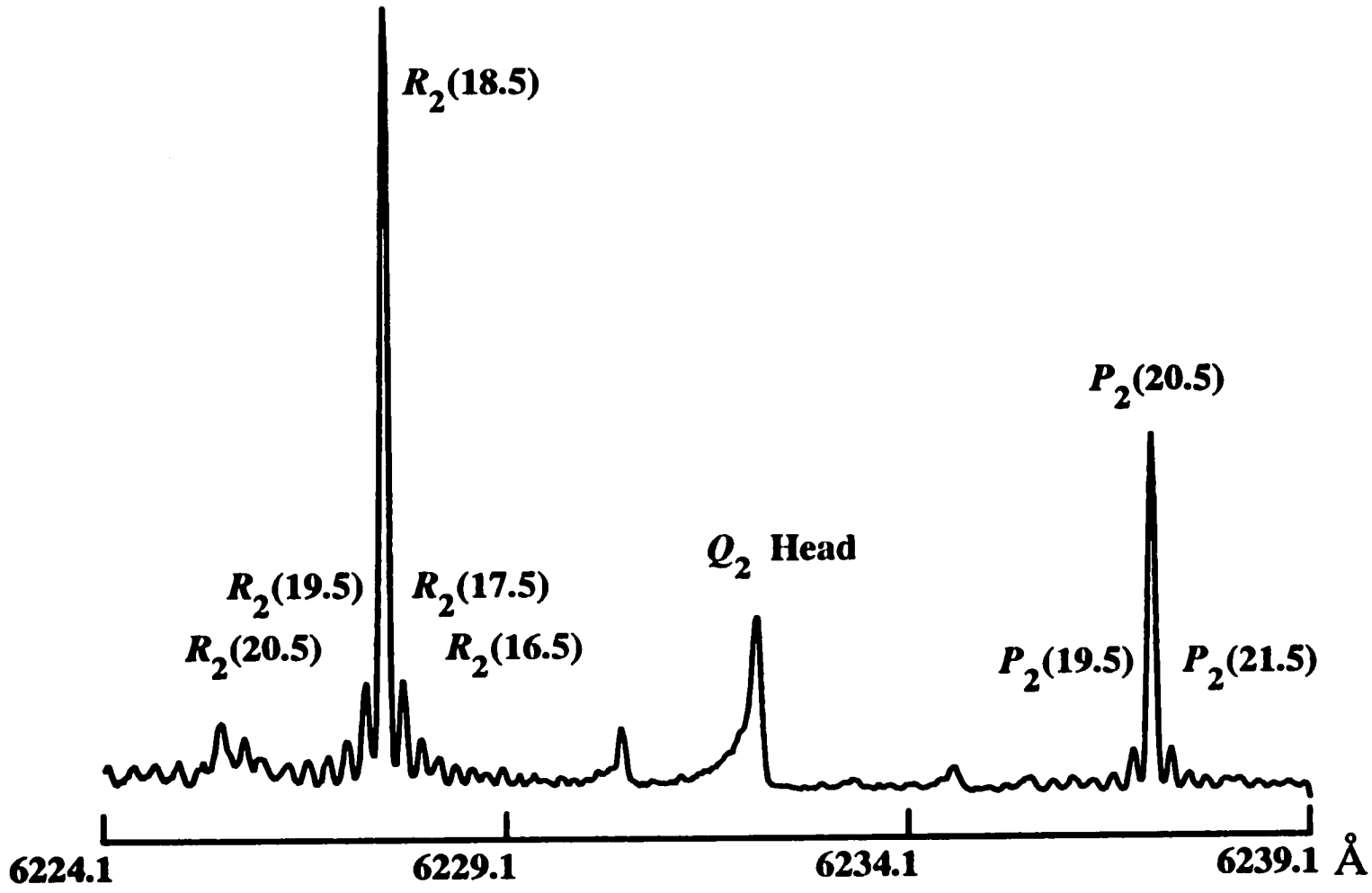

Fig. 5.1: Fluorescence spectrum of CaOD $\tilde{A}(100)$ - $\tilde{X}(100)$ obtained by excitation of the $\tilde{A}(100)$ - $\tilde{X}(000)$ $R_2(18½)$ rotational transition.

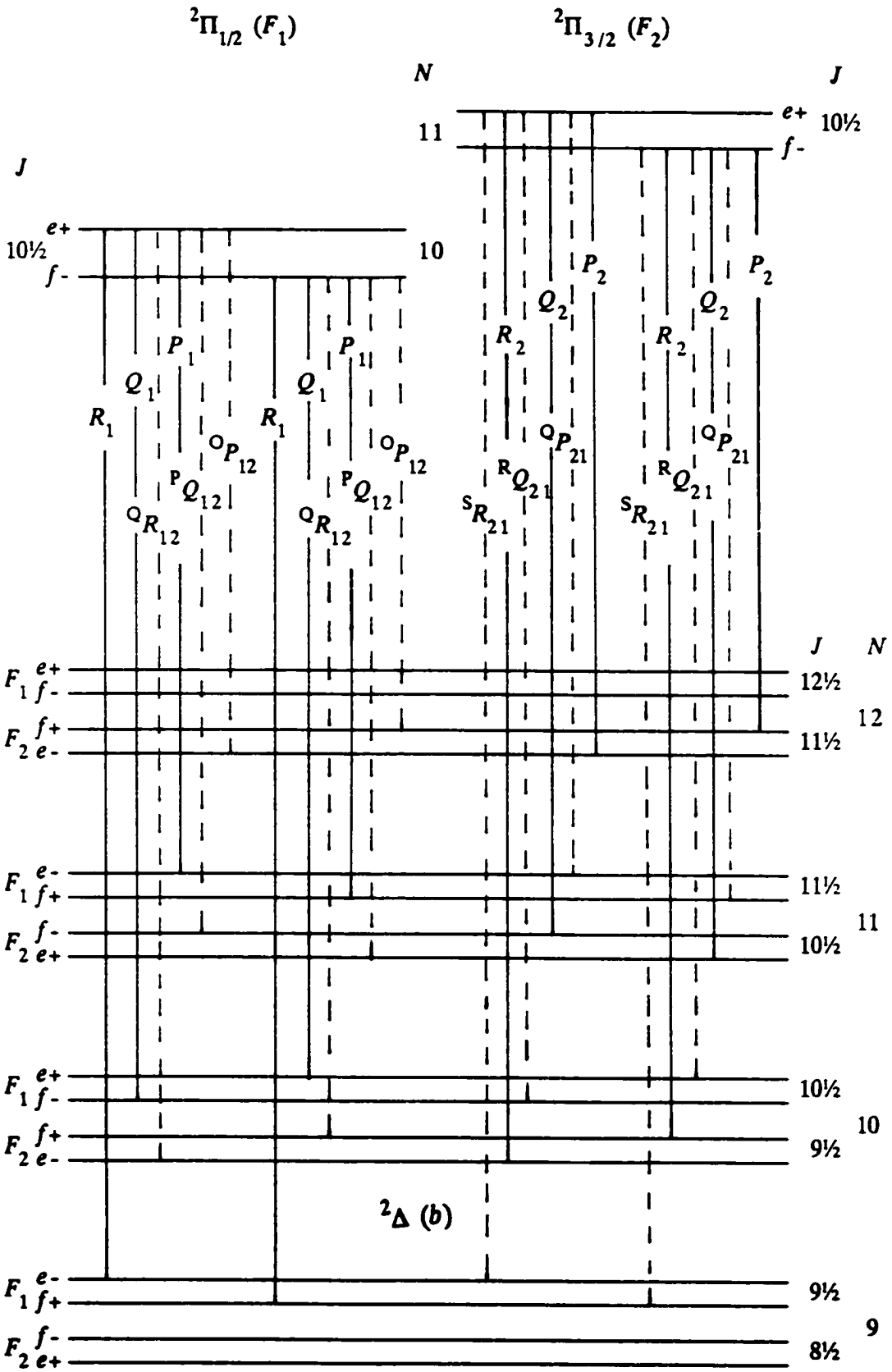

Fig. 5.2: Energy level diagram for the case (a) $^2\Pi$ - case (b) $^2\Delta$ transition

fluorescence to the $\tilde{X}(020)$ bending levels is, in general, only slightly lower than that to the $\tilde{X}(100)$ level, indicating strong (100) ~ (020) mixing in the upper levels. This mixing increases with increasing rotational quantum number J.

5.4 Results

The frequencies and assignments of the observed fluorescence transitions for CaOH and CaOD are listed in Tables 2 and 3, respectively, in the Appendix. Each band was fitted by a weighted, non-linear least squares procedure. The upper state, $\tilde{A}^2\Pi(100)$, shows typical case (a) coupling and was represented by empirical expressions

$$F_1(J,^e_f) = T_{ev}^{(1)} + B_v^{(1)}J(J+1) - D_v^{(1)}J^2(J+1)^2 + H^{(1)}J^3(J+1)^3 \mp \tfrac{1}{2} P_v(J+\tfrac{1}{2}) \mp \tfrac{1}{2} P_{Dv}J(J+1)(J+\tfrac{1}{2}\mp 1) \quad (5.1)$$

and

$$F_2(J,^e_f) = T_{ev}^{(2)} + B_v^{(2)}J(J+1) - D_v^{(2)}J^2(J+1)^2 + H_v^{(2)}J^3(J+1)^3 \mp Q_v(J-\tfrac{1}{2})(J+\tfrac{1}{2})(J+\tfrac{1}{2}+1) \quad (5.2)$$

The values of the effective parameters in Eqs. 5.1 and 5.2 were taken from Ref. 80 and held fixed in the fits. The rotational levels of the $\tilde{X}(02^00)$ level, as well as those of the $\tilde{X}(v_100)$ levels, were expressed by Eqs. 4.1 and 4.2 in Section 4.3. Following Herzberg[45], the expressions for the rotational levels of the $X(02^20)^2\Delta$ state are

$$F_1(N,^e_f) = T_v + B_v\,[N(N+1) - \ell^2] - D_v\,[N(N+1) - \ell^2]^2 + \tfrac{1}{2}\gamma_v N \pm \tfrac{1}{2} q_v N^2(N+1)^2 \quad (5.3)$$

$$F_2(N,^e_f) = T_v + B_v\,[N(N+1) - \ell^2] - D_v\,[N(N+1) - \ell^2]^2 - \tfrac{1}{2}\gamma_v (N+1) \mp \tfrac{1}{2} q_v N^2(N+1)^2 \quad (5.4)$$

where F_1 and F_2 denote spin components with $J = N+\frac{1}{2}$ and $J = N-\frac{1}{2}$, respectively. The effective parameter q_v is used to express the extremely small ℓ-type

splittings in the $^2\Delta$ vibronic state, and is to be distinguished from the normal ℓ-type doubling constant q^v used in $^2\Pi$ vibronic states. Values of q_v were not determined by the present data and were held fixed at zero in the fits. The spin-rotation constants γ_v for the observed vibrational levels in the $\tilde{X}^2\Sigma^+$ state were expected to be close to that for the $\tilde{X}(000)$ level. Accordingly, γ_v was held fixed at the value of 0.00111 cm^{-1} taken from Ref. 7 for all the vibrational levels reported in this part of the work. Since the main interest was in the vibrational term values and rotational constants, only the rotational levels with $J \leq 30½$ were observed for most of the bands. Given the resolution and precision of the spectrometer, the centrifugal distortion constants D_v'' could not be determined, and were fixed at the values found previously for the X(000) level, 0.3869 $\times 10^{-6}$ and 0.273 $\times 10^{-6}$ cm^{-1} for CaOH and CaOD, respectively. In the only exception, the $\tilde{A}(100)$ - $\tilde{X}(100)$ band of CaOD, the rotational levels were observed up to J=48½; in this case, the fitted value of D_v'' for the $\tilde{X}(100)$ level was well determined as 0.283(10) $\times 10^{-6}$ cm^{-1}, which is very close to the value of 0.273 $\times 10^{-6}$ cm^{-1} for the $\tilde{X}(000)$ level.

The vibrational term values and rotational constants determined from the resolved LIF bands in this work are listed in Table 5.1.

Based on the vibrational term values and rotational constants for several excited levels, some additional parameters for the $\tilde{X}^2\Sigma^+$ state may be derived. The parameter α_1, characterizing vibration-rotation interactions in the ν_1 mode, has been evaluated from the $B(v_1\ 0\ 0)$ values according to the expression

$$B_v = B_e - \sum \alpha_i\ (v_i + ½\ d_i) \qquad (5.5)$$

where d_i=1 for non-degenerate and d_i=2 for doubly degenerate vibrations. From Eq. 5.5, $B(v_1\ 0\ 0)$ can be expressed as

$$B(v_1\ 0\ 0) = B(0\ 0\ 0) - \alpha_1\ v_1 \qquad (5.6)$$

TABLE 5.1: Molecular Constants[a] (cm^{-1}) for Excited Vibrational Levels in the $\tilde{X}^2\Sigma^+$ State of CaOH and CaOD

	CaOH	
	T_v	B_v
(000)	0.0	0.33433411[b]
(100)	609.015(10)	0.33219(3)
(200)	1210.150(8)	0.32995(2)
(300)	1803.054(15)	0.32772(4)
(400)	2387.272(77)	0.32579(20)
(020) $^2\Sigma^+$	688.671(15)	0.33303(4)
(020) $^2\Delta$	713.040(9)	0.33252(3)
g_{22}	6.092[c]	
α_1	0.002200(10)	

	CaOD	
	T_v	B_v
(000)	0.0	0.3029872[b]
(100)	604.903(7)	0.30102(2)
(200)	1204.159(7)	0.29905(2)
(300)	1797.605(11)	0.29729(3)
(020) $^2\Sigma^+$	519.151(12)	0.30246(12)
(020) $^2\Delta$	536.334(15)	0.30233(4)
g_{22}	4.296[c]	
α_1	0.001877(22)	

[a]Values in parentheses are one standard error in units of the last digit of the corresponding constant.

[b]from Table 4.2 in Chapter 4.

[c]calculated from the separation between the (02^00) and (02^20) levels, not deperturbed from the Fermi resonance.

A least squares fit using Eq. 5.6 was performed to obtain the α_1-value for each isotopomer. Very little deviation from linear behavior of the B-values was found in the fit so that the α_1-values as listed in Table 5.1 were well determined.

The parameters ω_1 and x_{11} would normally have been estimated from the vibrational term values. However, as in the $\tilde{A}$ state, there are perturbations originating from Fermi resonance between the (v_1 v_2 v_3) and (v_1-1 v_2+2 v_3) levels in the $\tilde{X}$ state. These perturbations have a significant effect on the vibrational term values (shifts of a few wavenumbers), as described later in Chapter 7, so that a deperturbation process is required before further parameters can be derived. Such perturbations are J-independent and, hence, do not affect the B-values.

Hilborn *et al.*[7] reported a low resolution vibrational analysis for both CaOH and CaOD, using laser frequencies fixed at selected band heads and dispersing the LIF. The vibrational spacings in the $\tilde{X}^2\Sigma^+$ state measured by Hilborn *et al.* are generally in reasonably good agreement (to within 1-4 cm^{-1}) with those obtained in the present work through rotational analysis, which have much higher accuracy and no ambiguity. However, for CaOD, there is a significant discrepancy for the level spacings of the bending vibration; the (010)-(000) and (030)-(010) spacings found in Ref. 7 are 240 and 480 cm^{-1}, respectively, while the (020)-(000) spacing from the present measurement is 519.151(12) cm^{-1}. This discrepancy is probably due to misassignments in the low resolution spectrum of Ref. 7.

5.5 Concluding Remarks

The analysis of excited vibrational levels in CaOH and CaOD has been difficult owing to the congested band systems, which are further complicated

by Renner-Teller, spin-orbit and some resonance interactions in the $\tilde{A}$ state. Such analysis will largely rely on dispersion of LIF. Detailed vibrational and rotational information of the ground electronic state is essential for identification and analysis of the dispersed LIF spectra. Such information will also make the selective detection of the LIF more accurate and, therefore, more effective in simplifying and characterizing excitation spectra. The selective LIF detection has been of vital importance to excitation spectroscopy in the present work. As a matter of fact, the results of this work have been used, prior to publication, by Jarman and Bernath[17] to facilitate the analysis of the $\tilde{C}^2\Delta$ - $\tilde{X}^2\Sigma^+$ system of CaOH and CaOD.

CHAPTER 6

Analysis of the $\tilde{A}(010)$ - $\tilde{X}(010)/(000)$ Bands of CaOH/CaOD

6.1 Introduction

This chapter describes high resolution analysis of the fundamental bending vibrations in the $\tilde{A}^2\Pi$ and $\tilde{X}^2\Sigma^+$ states of CaOH/CaOD. The analysis of the (010) level in the $\tilde{A}^2\Pi$ electronic state provides the simplest and most accurate picture for the Renner-Teller interaction because any other vibrational level with $v_2>1$ in the $\tilde{A}$ state is affected by Fermi resonance which severely complicates the vibronic structure. It is one of the main targets in this research program to investigate the interaction between the electron orbital angular momentum and the nuclear vibrational angular momentum.

Most of the previous work concerning the Renner-Teller effect in a linear radical was done on the 15-electron species, BO_2[52,53], NCO[54-56], NCS[57,58] and CO_2^+ [59,60]. The present work represents the first investigation of the Renner-Teller effect for an alkaline earth monohydroxide molecule, and has determined the parameter $\epsilon\omega_2$ for two isotopomers based on an extensive and highly precise data base.

The (010) vibrational level in the $\tilde{A}^2\Pi$ state is split into a $^2\Delta$ and two $^2\Sigma$ vibronic components due to the Renner-Teller interaction, as described in Section 2.2. The parallel bands $\tilde{A}(010)\kappa^2\Sigma,\mu^2\Sigma$ - $\tilde{X}(000)^2\Sigma^+$ are the forbidden components of a dipole allowed electronic transition, $^2\Pi$ - $^2\Sigma^+$, which is characterized by perpendicular bands with $\Delta K = \pm 1$. These parallel bands gain transition strengths through Herzberg-Teller vibronic mixing of the upper state with other electronic states, probably mainly the $\tilde{B}^2\Sigma^+$ state. The $\tilde{A}(010)^2\Delta$ - $\tilde{X}(000)^2\Sigma^+$ transition has $\Delta K = 2$ and is strictly forbidden. The

only path to reach $\tilde{A}(010)^2\Delta$ is to excite the hot band $\tilde{A}(010)$ - $\tilde{X}(010)$. Fig. 6.1 shows schematically the vibronic transitions investigated in the present work for both CaOH and CaOD.

There are K-type resonance interactions between $\mu^2\Sigma$ and $^2\Delta_{3/2}$ and between $\kappa^2\Sigma$ and $^2\Delta_{5/2}$ owing to their closeness in energy. Quantum mechanical interference originating from these interactions leads to anomalous branch intensities. A global matrix deperturbation including all $^2\Sigma$ and $^2\Delta$ components is the key for a satisfactory treatment of the observed bands.

6.2 Experimental Method; Excitation Spectra

The experimental details are the same as described in Sections 3.2 and 3.3. The Coherent 699-29 ring dye laser was operated in single mode with Rhodamin 6G dye for the $\tilde{A}(010)^2\Sigma$ - $\tilde{X}(000)^2\Sigma$ bands and Sulforhodamin B dye for the $\tilde{A}(010)^2\Delta,^2\Sigma$ - $\tilde{X}(010)^2\Pi$ bands. The laser induced fluorescence was imaged onto the entrance slit of the Spex monochromator which functions as a tunable band-pass filter for selective detection of the LIF. Line positions of the excitation spectra were measured using the internal wavemeter of the 699-29 laser and calibrated using the I_2 excitation spectra. The average measurement accuracy was estimated to be 0.0035 cm^{-1}.

The two $^2\Sigma$ vibronic levels are strongly mixed due to the spin-orbit interaction and, hence, partially lose their character as levels with $^2\Sigma^+$ and $^2\Sigma^-$ symmetries. The transitions to these two $^2\Sigma$ levels from the $\tilde{X}(000)^2\Sigma^+$ level are very weak, and only occur through borrowed transition strengths; on the other hand, the transitions from the $\tilde{X}(010)^2\Pi$ vibronic level are allowed and strong. Despite their weakness, however, excitation of the $\tilde{A}(010)^2\Sigma$ - $\tilde{X}(000)^2\Sigma^+$ transitions was chosen because of two distinct advantages. First, the (010) - (000) band is simpler than the (010) - (010) band, and the former

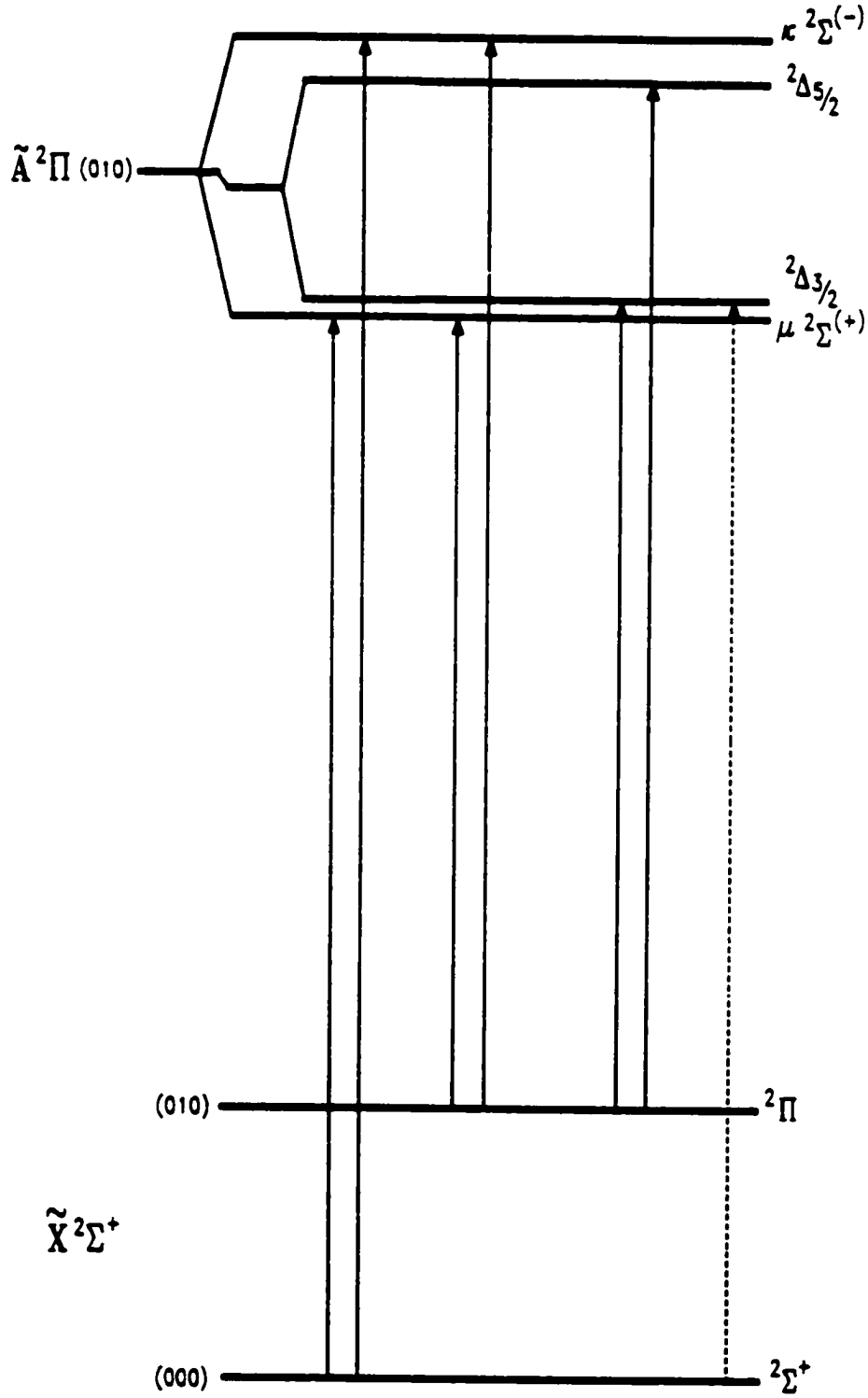

Fig. 6.1: The $\tilde{A}(010)$ - $\tilde{X}(010)/(000)$ vibronic transitions observed via laser excitation for both CaOH and CaOD; the dotted line indicates the observed extra transition induced by the K-type resonance.

is located in a less congested area than the latter. Second, the selective detection technique, detecting the $\tilde{A}(010)^2\Sigma$ - $\tilde{X}(010)^2\Pi$ LIF, could be used most effectively to simplify the spectrum and enhance the signal/noise ratio. Fig. 6.2 illustrates a portion of the excitation spectrum of the CaOH $A(010)\kappa^2\Sigma^{(-)}$ - $X(000)^2\Sigma^+$ subband obtained using selective LIF detection. From photon-counting measurement of the LIF intensities this subband is approximately 100 times weaker than the allowed perpendicular band $\tilde{A}(100)^2\Pi$ - $\tilde{X}(000)^2\Sigma^+$. However, the signal/noise ratio was very satisfactory owing to the advantageous approach.

All eight branches of the $\tilde{A}(010)\kappa^2\Sigma,\mu^2\Sigma$ - $\tilde{X}(000)^2\Sigma^+$ subbands were recorded for each isotopomer. The branch structures of the two subbands are depicted in Fig. 6.3. The rotational quantum number assignments were established using the lower state combination differences $\Delta_2F''(J)$, which had been well defined by Ref. 16 for CaOH and by the work in Chapter 4 of this thesis for CaOD. However, particular care was necessary because the spin-rotation splittings in the $X(000)$ level are so small that the difference between $\Delta_2F''(J)$ for *f*-levels and $\Delta_2F''(J + 1)$ for *e*-levels is very small, ~ 0.002 cm^{-1} at $J = 39½$. Consequently, the *J*-numbering can be changed by one unit depending upon the *e* or *f* parity assignment of the transitions. Fortunately, for CaOH, the first line of the $\kappa^2\Sigma$ - $\tilde{X}^2\Sigma^+$ *P*-branch could be assigned unambiguously as $P(1½)$ with *f* - *f* symmetry. If this line were to originate from an *e*-parity level, it would be assigned as P(2½); however, there is then no line in the expected position for the $P(1½)$ transition. The assignment of this line was the key for establishing the *J*-numbering and *e/f* symmetry for the entire subband. The rotational assignment for the $\mu^2\Sigma$ - $\tilde{X}^2\Sigma^+$ subband was more difficult because of the high density of lines in the origin region, which precluded an unequivocal identification of the first line. The

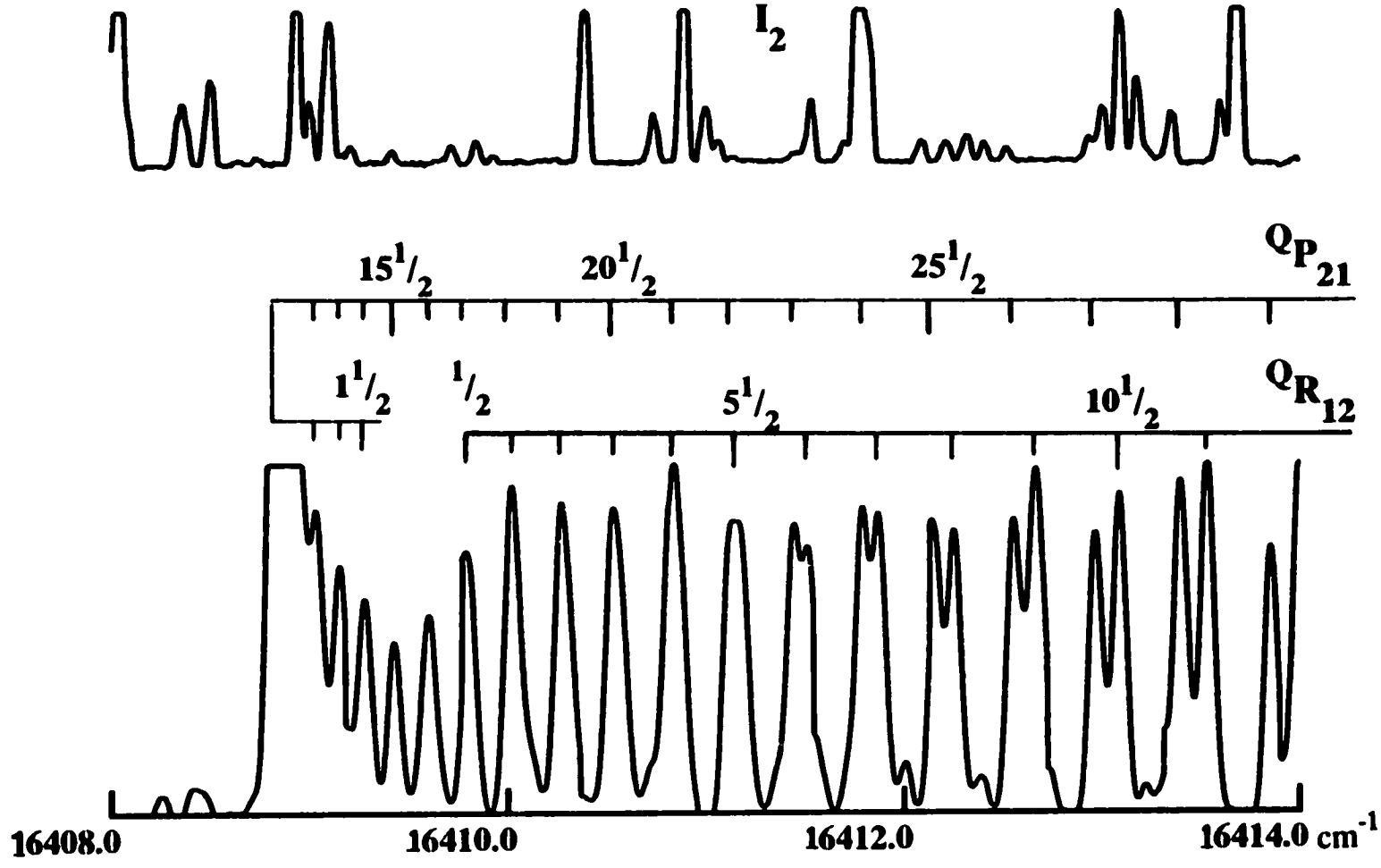

Fig. 6.2: A portion of the excitation spectrum of the CaOH $\tilde{A}(010)\kappa^2\Sigma^{(-)}$ - $\tilde{X}(000)^2\Sigma^+$ subband, recorded using selective detection with a 350 cm^{-1} frequency difference.

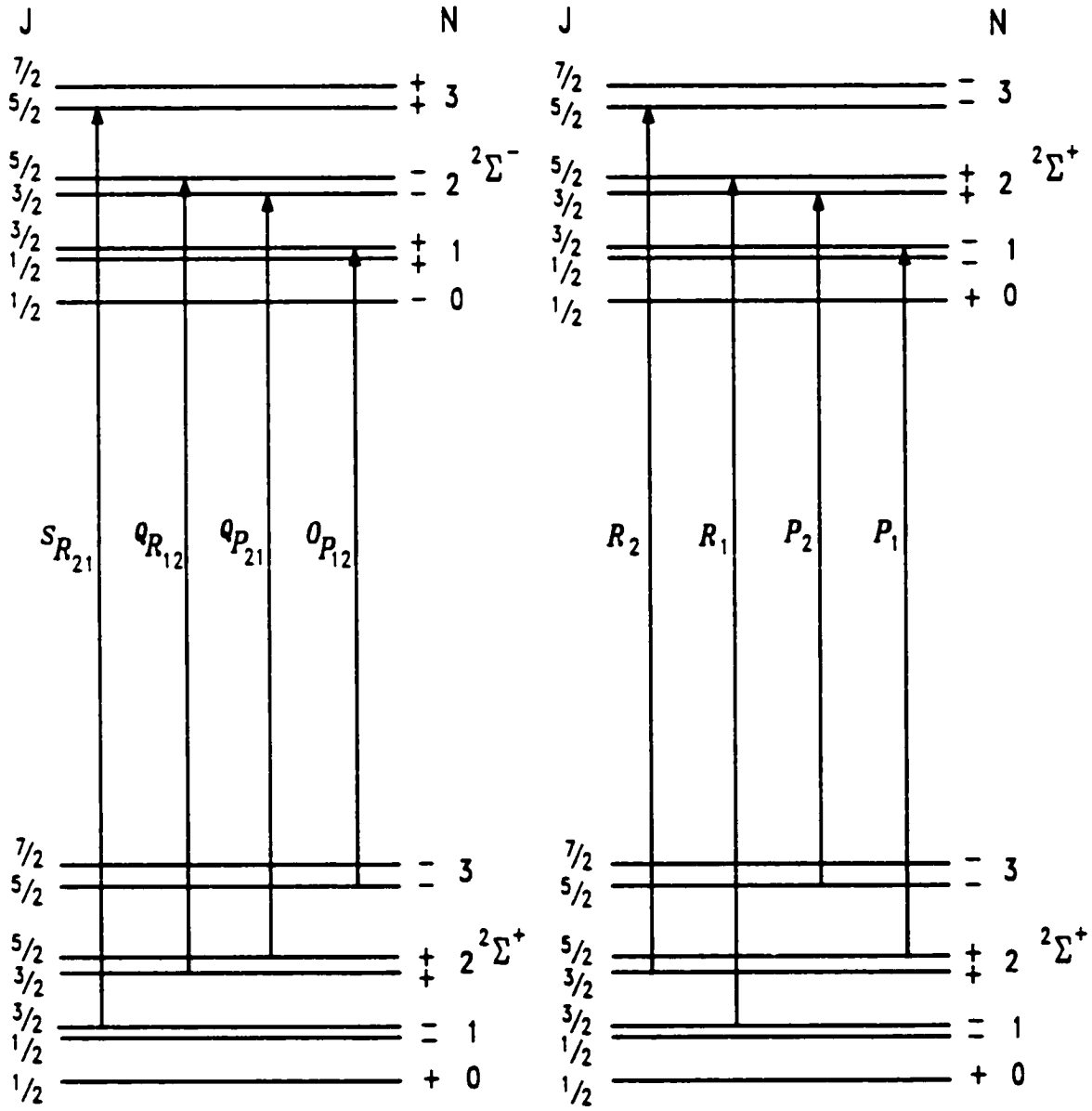

Fig. 6.3: Energy level diagram for the $\tilde{A}(010)\kappa,\mu^2\Sigma$ - $\tilde{X}(000)^2\Sigma^+$ subbands

correctness of the assignments for this subband was assessed by consistency with the $\kappa^2\Sigma$ - $\tilde{X}^2\Sigma^+$ subband in the model fitting and by the resolved LIF spectra. The rotational structures of the $\kappa^2\Sigma$ and $\mu^2\Sigma$ vibronic levels, based on the above assignment, reveal that the $\kappa^2\Sigma$ level behaves more like a $^2\Sigma^-$ state, while $\mu^2\Sigma$ is more like $^2\Sigma^+$. The overall intensity of the $\mu^2\Sigma$ - $\tilde{X}^2\Sigma^+$ subband is approximately three times that of the $\kappa^2\Sigma$ - $\tilde{X}^2\Sigma^+$ subband; this relative intensity information decisively confirmed the symmetry identification of the two $^2\Sigma$ vibronic components The sign of the Renner-Teller parameter in the $\tilde{A}^2\Pi$ state was consequently determined to be negative, according to Eq. 2.11. The two vibronic components have been labeled as $\kappa^2\Sigma^{(-)}$ and $\mu^2\Sigma^{(+)}$, respectively; the branches were thus labelled as $^{O}P_{12}$, $^{Q}P_{21}$, $^{Q}R_{12}$ and $^{S}R_{21}$ for the $\kappa^2\Sigma^{(-)}$ - $\tilde{X}^2\Sigma^+$ subband and P_1, P_2, R_1 and R_2 for the $\mu^2\Sigma^{(+)}$ - $\tilde{X}^2\Sigma^+$ subband. After assigning the CaOH spectra, the CaOD spectra were readily assigned because of the close similarity.

The $\tilde{A}(010)\kappa^2\Sigma, \mu^2\Sigma$ - $\tilde{X}(000)^2\Sigma$ subbands of CaOH/CaOD were first fitted using the expressions (27) in Ref. 42. These fits yielded preliminary estimates of the $\tilde{A}(010)$ vibrational term values, the Renner-Teller parameters $\epsilon\omega_2$, the rotational constants B^{κ} and B^{μ}, and the effective parameters γ^{κ} and γ^{μ}. The assignments of the quantum numbers and parities of the rotational lines were confirmed by the fact that the values of γ^{κ} and γ^{μ} fall in the range between 0 and $2B$. However, these fits were not satisfactory; although the variances of the fits for the $\kappa^2\Sigma$ - $^2\Sigma$ subbands were close to unity, those for the $\tilde{A}(010)\mu^2\Sigma$ - $\tilde{X}(000)^2\Sigma$ subbands were 4.0 and 6.0 for CaOH and CaOD, respectively. In addition, the fitted centrifugal distortion constants D^{μ} and γ_D^{μ} were anomalously large. This problem appeared to be a consequence of a *K*-type resonance between the nearby $^2\Delta$ and $^2\Sigma$ vibronic components. The $\mu^2\Sigma$ components were more seriously perturbed than

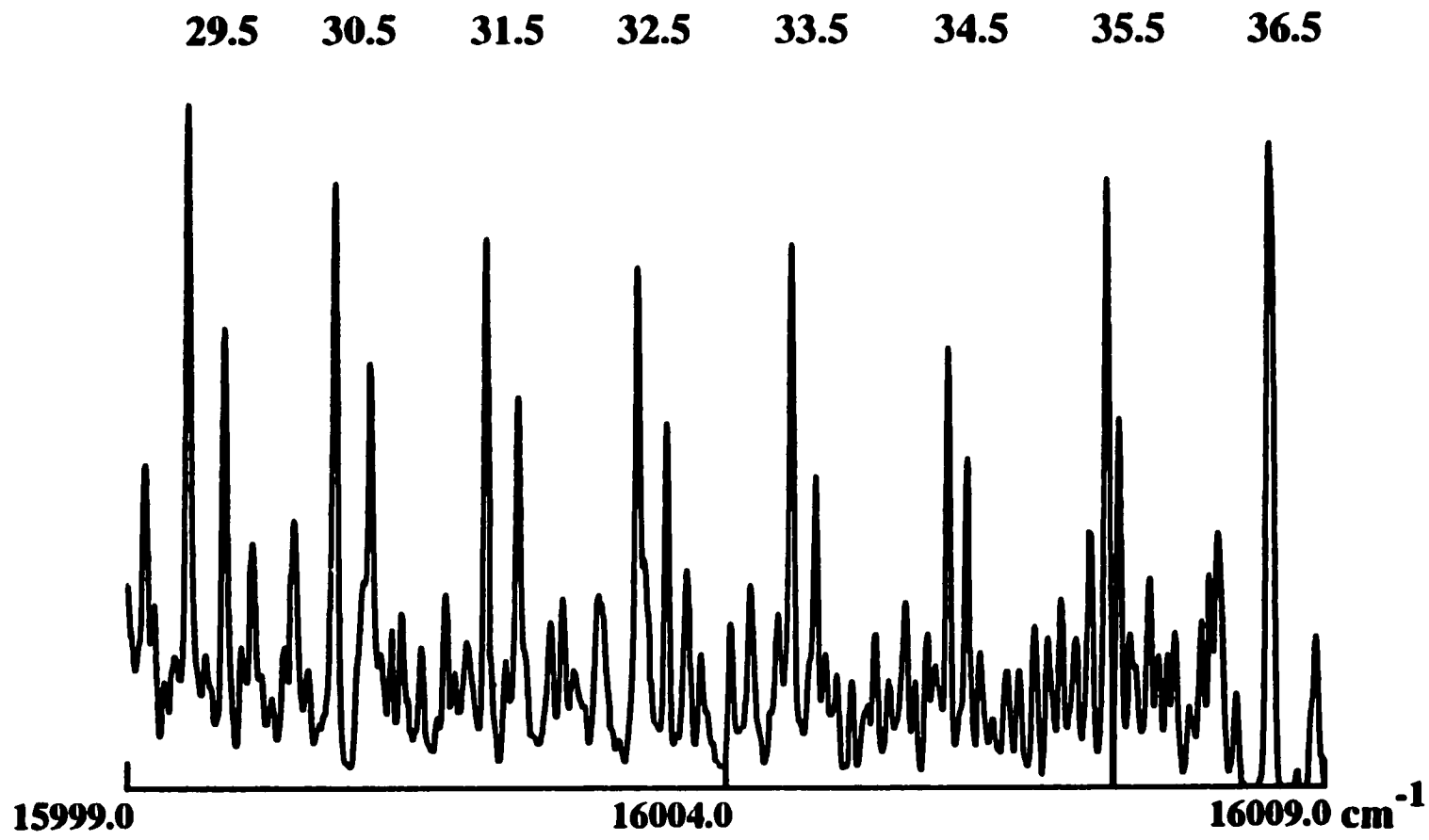

Fig. 6.4: A portion of the excitation spectrum of the CaOD $\tilde{A}(010)^2\Delta$ - $\tilde{X}(010)^2\Pi$ R_1 branch (J'' = 29½ - 36½); the splitting of each line is a combined effect of the $\tilde{X}(010)^2\Pi$ ℓ-type doubling and the $\tilde{A}(010)^2\Delta$ K-type doubling.

smaller in the upper state and larger in the lower state. Under Doppler limited resolution (~ 0.04 cm^{-1}), the ℓ-type splitting was resolved at $J \geq 8½$, while the spin-rotation splitting was not resolved until $J \geq 50½$. The overall appearance of this band of CaOH was quite similar to that of CaOD. However, minor differences were noticeable. Since the magnitude of the Renner-Teller parameter $\epsilon\omega_2$ for the $\tilde{A}^2\Pi$ state of CaOD is significantly smaller than that of CaOH, while the two isotopomers have similar values of the spin-orbit parameter A, the spacings between the corresponding $^2\Delta$ and $^2\Sigma$ vibronic components for CaOD are smaller and the interactions are consequently stronger. This situation results in faster growing K-type splittings in the $^2\Delta$ vibronic levels for CaOD than for CaOH. The K-type splittings of the $^2\Delta_{3/2}$ component tend to cancel the ℓ-type splittings of the $\tilde{X}(010)^2\Pi$ state at high J. As a consequence, for example, the splitting of the R_1 branch of CaOD increases and reaches a maximum at $J = 27½$; it then slowly decreases and becomes unresolvable at $J = 36½$; at still higher values of J, the splittings open again, but with reversed order. A portion of the CaOD R_1 branch is illustrated in Fig. 6.4. For the R_1 branch of CaOH, the mergence of the two split components comes much later and was not observed at the highest observed J-value, $J = 42½$, owing to the smaller K-type splittings for CaOH. The K-type splittings of the $^2\Delta_{5/2}$ component are very small and have little effect on the spectra.

The computer program for measuring overlapped lines consisting of two or more Gaussian profiles was used to measure the unresolved $Q+R$ or $Q+P$ lines. This technique is very accurate when the two lines are partially resolved or have different relative intensities so that a main peak and a shoulder are formed. The accuracy of this technique has been tested against the sub-Doppler technique, intermodulated fluorescence, in the work on the CaOD

$\tilde{A}(000)$ - $\tilde{X}(000)$ band. The measurement accuracy was mainly determined by the 699-29 wavemeter. However, the spectra recorded in the present work were much more complicated and suffered more blending than that of the (000) - (000) band. The overall measurement accuracy was slightly lower and was estimated to be 0.0035 cm^{-1}. In some cases (mostly for CaOD) where more than two lines were coincident, the measured line positions were assigned an estimated error of 0.005 cm^{-1}.

In order to conduct a matrix treatment including all interacting vibronic components, it is necessary to establish accurate relative positions between the $^2\Sigma$ and $^2\Delta$ vibronic components by experiment. A few branches of the $\tilde{A}(010)\,\kappa^2\Sigma, \mu^2\Sigma$ - $\tilde{X}(010)^2\Pi$ hot bands were recorded via LIF excitation for both CaOH and CaOD.

6.3 Level Crossing and Quantum Mechanical Interference

Reduced term values of the $\tilde{A}(010)$ vibronic components are plotted as a function of J in Figs. 6.5 and 6.6 for CaOH and CaOD, respectively. Level crossings between the $^2\Delta$ and $^2\Sigma$ components are clearly revealed when the matrix elements for the K-type resonance are set to zero. When the K-type resonance interactions are "switched on", the level crossing appears to be "avoided"; however, the leading character of the eigenfunction is switched after the crossing point, as indicated by the altered symbols in Figs. 6.5 and 6.6.

It was seen that the interaction between the $\kappa^2\Sigma$ and $^2\Delta_{5/2}$ components is small for both isotopomers. The K-type splittings of the $^2\Delta_{5/2}$ component reach 0.030 cm^{-1} at J = 42½ for CaOH and at J = 34½ for CaOD. On the other hand, striking level shifts and K-type splittings are seen in the $^2\Delta_{3/2}$ and $\mu^2\Sigma$ components. The main reason for this different behavior is that the

Fig. 6.5: Reduced rotational term values of the $\tilde{A}(010)$ vibronic components of CaOH, obtained by subtraction of $BJ(J+1)$ with B=0.34024 cm^{-1}. The filled symbols correspond to the observed levels; the open symbols indicate the deperturbed levels (i.e., with the K-resonance matrix elements set to zero). When the two types of levels cannot be distinguished in the plot, half-filled symbols are used.

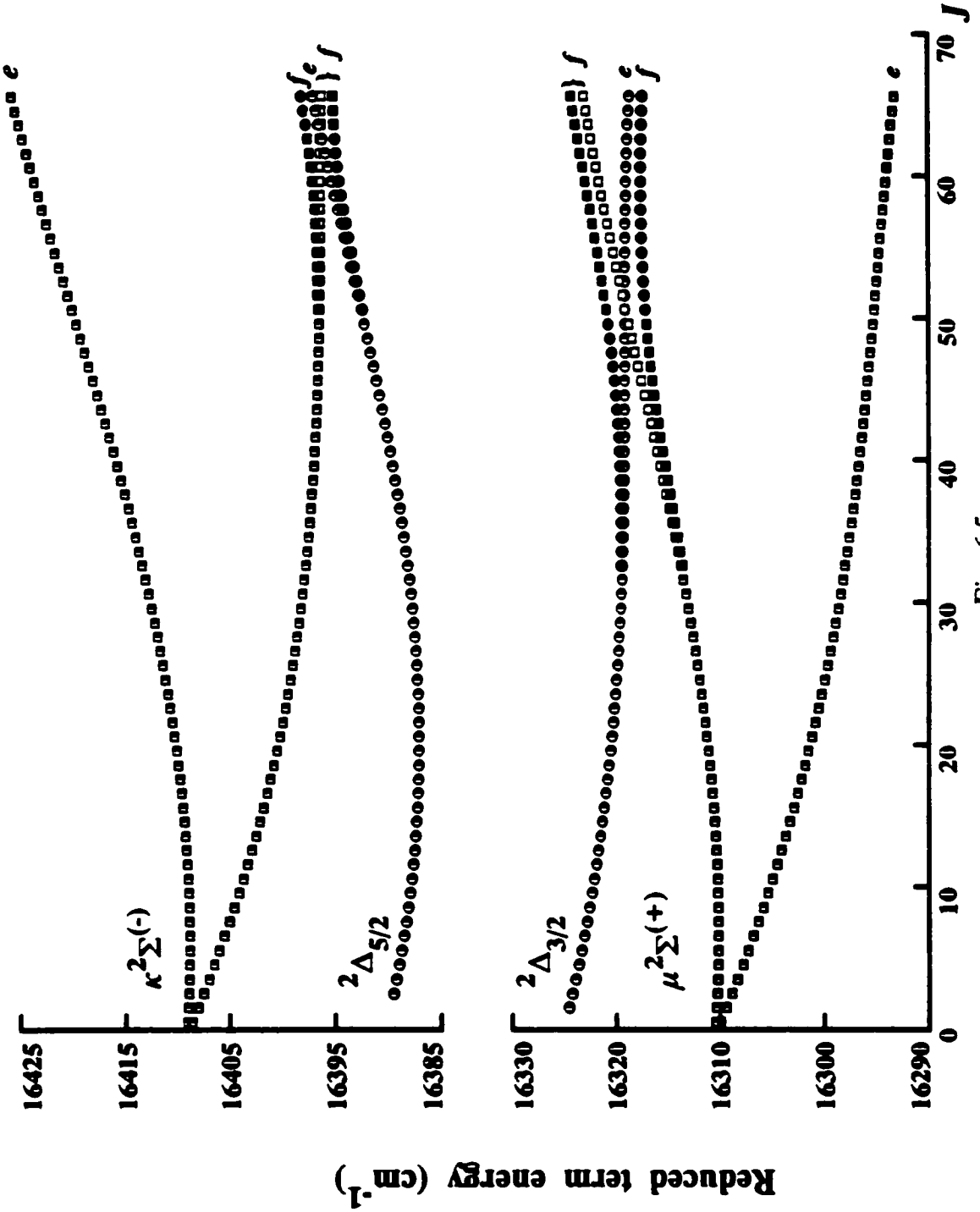
Reduced term energy (cm-1)
16425
16415
16405
16395
16385
16330
16320
16310
16300
16290
0
10
20
30
40
50
60
70
J
e
f
κ 2Σ(-)
2Δ5/2
2Δ3/2
μ 2Σ(+)

Fig. 6.5

Fig. 6.6: Reduced rotational term values of the $\tilde{A}(010)$ vibronic components of CaOD, obtained by subtraction of $\bar{B}J(J+1)$ with $\bar{B}=0.30904$ cm^{-1}. The symbols employed are as given for Fig. 6.5.

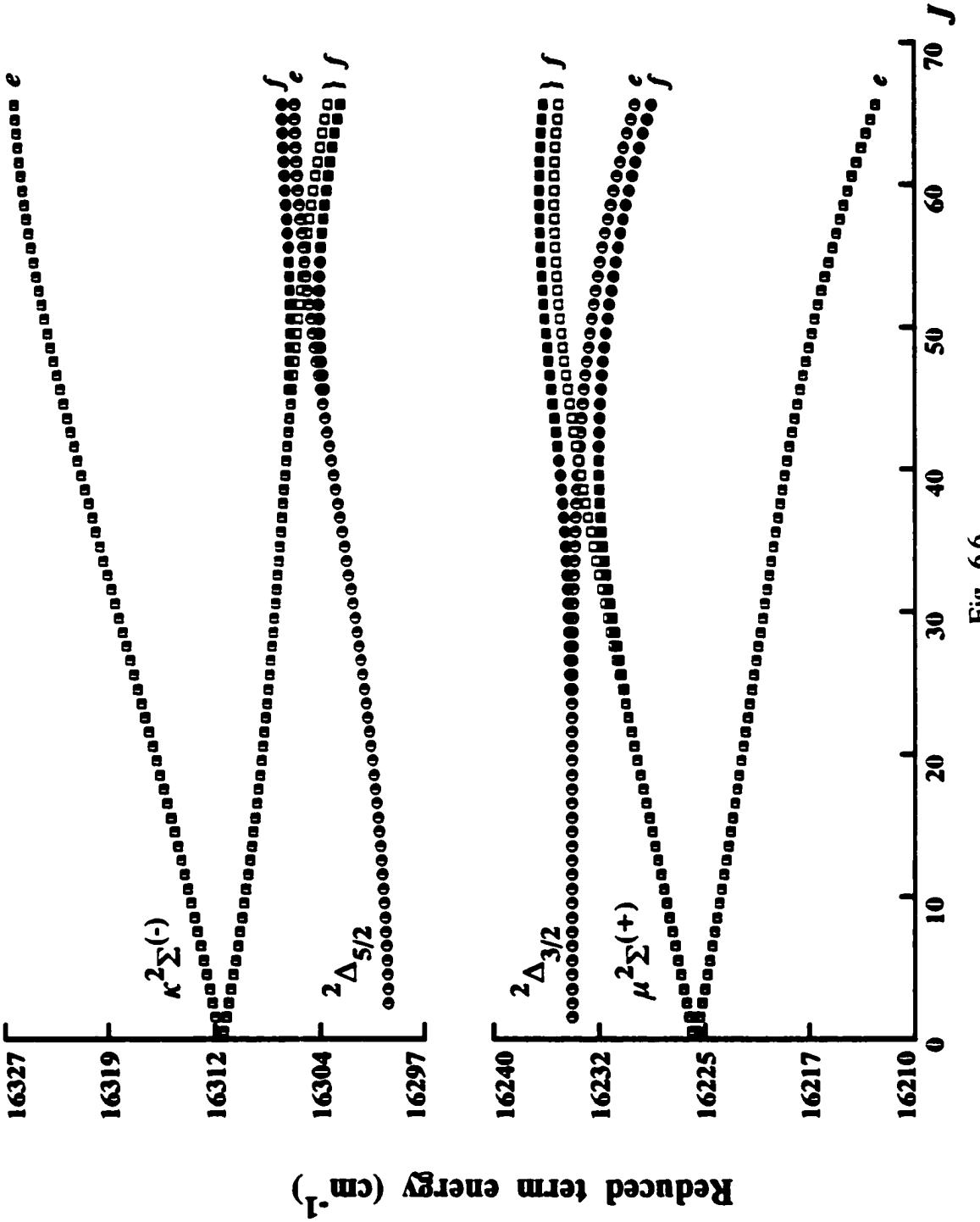
Reduced term energy (cm-1)
16327
16319
16312
16304
16297
16240
16232
16225
16217
16210
0
10
20
30
40
50
60
70
J
e
f
e
f
f
e
f
e
f
κ 2Σ(-)
2Δ5/2
2Δ3/2
μ 2Σ(+)

Fig. 6.6

matrix element between the $^2\Delta_{3/2}$ and $\mu^2\Sigma$ components contains both Λ-type and ℓ-type doubling contributions, while that between the $\kappa^2\Sigma$ and $^2\Delta_{5/2}$ components has an ℓ-type doubling contribution only.

Owing to the strong interaction between the $^2\Delta_{3/2}$ and $\mu^2\Sigma$ components, especially in the neighborhood of the crossing point (J' = 50½ for CaOH and J' = 40½ for CaOD), dramatic quantum mechanical interference has been observed between the $\tilde{A}(010)^2\Delta_{3/2}$ - $\tilde{X}(010)^2\Pi$ and $\tilde{A}(010)\mu^2\Sigma$ - $\tilde{X}(010)^2\Pi$ transitions. Figs. 6.7(a) and 6.7(b) demonstrate anomalous relative intensities caused by such an interference effect in the resolved LIF spectra for CaOH. From the final fit of the present work, the mixing percentages of the two interacting levels at J' = 53½ with f-parity are 57.13% $\mu^2\Sigma$ + 37.43% $^2\Delta_{3/2}$ for the higher energy level, and 38.47% $\mu^2\Sigma$ + 56.65% $^2\Delta_{3/2}$ for the lower energy level. In order to avoid confusion, the labeling of the branches in the spectra shown in Fig. 6.7 is made as if the upper level belongs to the $\tilde{A}(010)\mu^2\Sigma^+$ vibronic component, regardless of the change in leading character. Of course, such labeling does not then represent the complete physical picture owing to the strong mixing. For comparison, a resolved LIF spectrum with J' = 32½ is shown in Fig. 6.7(c), which illustrates a near normal intensity pattern with only a small perturbation. The similar phenomenon has been observed also for CaOD.

Another consequence of the strong interaction is the observation of extra lines in the excitation spectrum of the $\tilde{A}(010)\mu^2\Sigma$ - $\tilde{X}(000)^2\Sigma$ band. Such extra lines were not found, however, in the spectrum observed at the earlier stage of this work; this paradoxical situation was later understood as the combined consequence of the selective detection method and the interference effect. When the R_2 branch of this band was excited, the R_2 + $^RQ_{21}$ branch LIF of the $\tilde{A}(010)\mu^2\Sigma$ - $\tilde{X}(010)^2\Pi$ band was selectively detected; the frequency difference between the laser and the detected LIF was equal to the vibrational spacing.

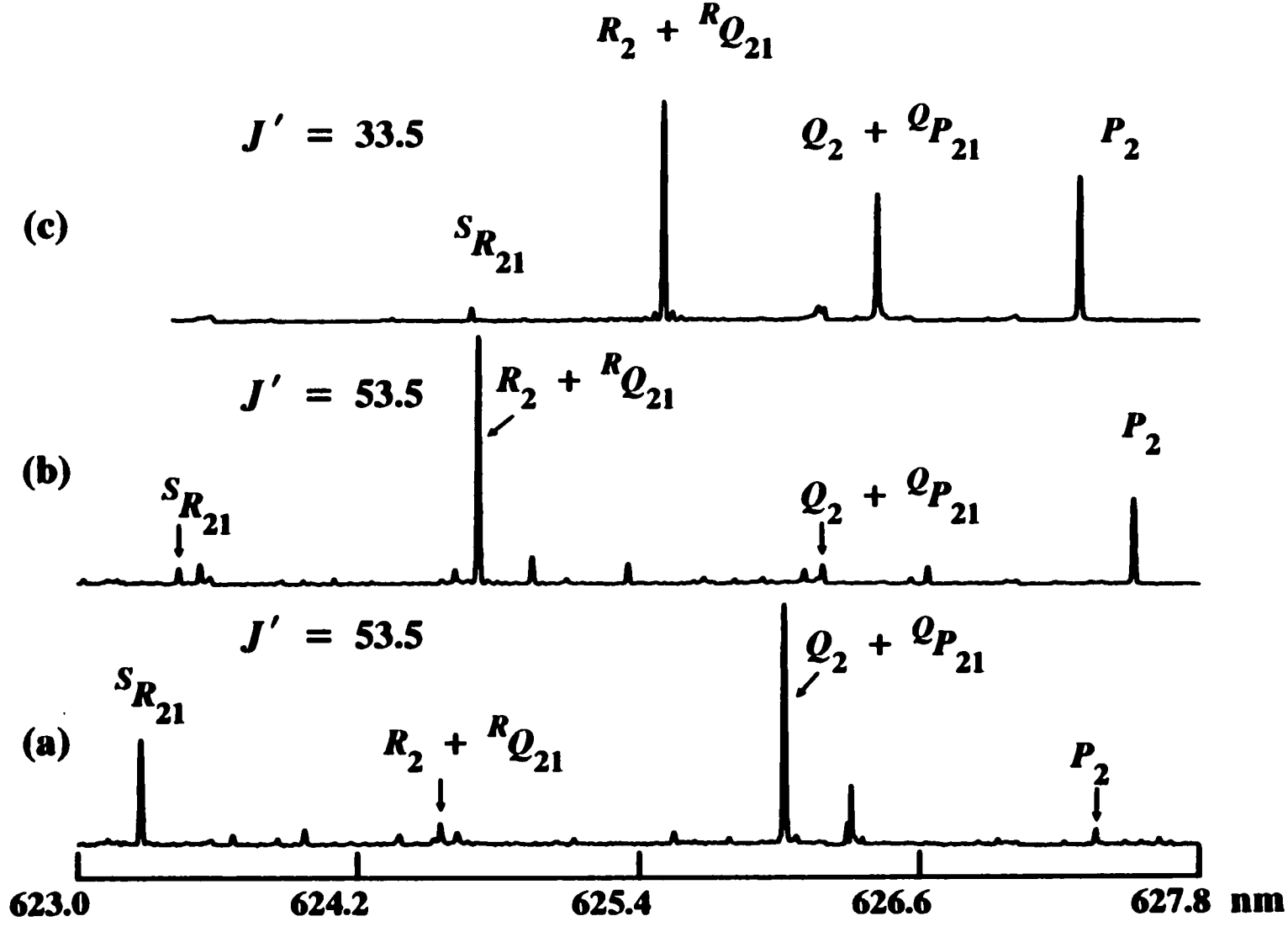
$R_2 + {}^RQ_{21}$
$J' = 33.5$
$Q_2 + {}^QP_{21}$
P_2
(c)
$^SR_{21}$
$J' = 53.5$
$R_2 + {}^RQ_{21}$
P_2
(b)
$^SR_{21}$
$Q_2 + {}^QP_{21}$
$J' = 53.5$
$Q_2 + {}^QP_{21}$
$^SR_{21}$
(a)
$R_2 + {}^RQ_{21}$
P_2
623.0
624.2
625.4
626.6
627.8 nm

Fig. 6.7

The R_2 + $^RQ_{21}$ branch originating from the level of lower energy of the two interacting levels is always strong, both before and after the crossing point, regardless of the leading character change, as shown in Fig. 6.7(b) and 6.7(c). On the other hand, the same branch is extremely weak when it originates from the level of higher energy of the interacting levels, as shown in Fig. 6.7(a). This accounts for the observation of only a set of smoothly progressing "main" lines in the earlier experiments; these were regarded as transitions of the $\tilde{A}(010)\mu^2\Sigma$ - $\tilde{X}(000)^2\Sigma$ subband, though the levels after the crossing point were later seen to have $^2\Delta_{3/2}$ leading character. After realizing a possible interference effect, and accordingly changing the branch that was detected, the "extra" lines were observed and have been considered to belong to the forbidden $\tilde{A}(010)^2\Delta_{3/2}$ - $\tilde{X}(000)^2\Sigma$ subband, though the levels after the crossing point have $\mu^2\Sigma$ leading character. The extra lines corresponding to the $\tilde{A}(010)^2\Delta_{5/2}$ - $\tilde{X}(000)^2\Sigma$ transitions are very weak, and no attempt has been made to observe them.

6.4 Effective Hamiltonian Matrix

As discussed in Section 6.2, it is necessary to conduct a global matrix deperturbation including all four vibronic components, $\kappa^2\Sigma$, $\mu^2\Sigma$, $^2\Delta_{5/2}$ and $^2\Delta_{3/2}$, in order to satisfactorily reproduce the observed bands. A similar approach has previously been followed for NCO[55] and BO_2[53]. Bolman *et al.*[55] developed a simple matrix to take account of the $^2\Sigma \sim {}^2\Delta$ K-type resonance found in the NCO $\tilde{X}^2\Pi(010)$ state. Adam *et al.*[53] later extended the matrix of Ref. 55 to fit their more precise data for the BO_2 $\tilde{A}^2\Pi(010)$ state. In the present work, the matrix of Ref. 53 was adopted, but significant modifications were required.

The Hamiltonian matrix used in this work for the global deperturbation of

TABLE 6.1: Effective Hamiltanian Matrix for the $\tilde{A}^2\Pi(010)$ Vibronic States of CaOH and CaOD

$\lvert {}^2\Delta_{5/2},\pm\rangle$	$\lvert {}^2\Delta_{3/2},\pm\rangle$	$\lvert \kappa^2\Sigma,\pm\rangle$	$\lvert \mu^2\Sigma,\pm\rangle$
$T_{ev} + 2g_K - \frac{3}{4}\epsilon^2\omega_2 + \frac{1}{2}A(1 - \frac{3}{4}\epsilon^2)$ $+ (B_1 + \frac{1}{2}A_{D1})(z - 6)$ $- (D_1 - \frac{1}{2}A_{H1})(z^2 - 11z + 32)$ $- \frac{1}{2}\gamma_1 - \gamma_{D1}(z - 5)$	$-(B_1 - \frac{1}{2}\gamma_1)(z - 4)^{1/2}$ $+2D_1(z - 4)^{3/2}$ $+\frac{1}{2}\gamma_{D1}(z - 3)(z - 4)^{1/2}$	$\frac{1}{2}q^v(z^2 - 5z + 4)^{1/2}$	$\pm\frac{1}{2}q^e(z^2 - 5z + 4)^{1/2}$
	$T_{ev} + 2g_K - \frac{3}{4}\epsilon^2\omega_2 - \frac{1}{2}A(1 - \frac{3}{4}\epsilon^2)$ $+ (B_1 - \frac{1}{2}A_{D1})(z - 2)$ $- (D_1 + \frac{1}{2}A_{H1})z(z - 3)$ $- \frac{1}{2}\gamma_1 - \gamma_{D1}(z - 3)$	$[\pm\frac{1}{2}q^c z^{1/2} - q^v](z - 1)^{1/2}$	$[\mp\frac{1}{2}(p^e + 2q^e) + \frac{1}{2}q^v z^{1/2}]$ $\times (z - 1)^{1/2}$
		$T_{ev} - \frac{1}{4}\epsilon^2\omega_2 + \frac{1}{2}A(1 - \frac{1}{4}\epsilon^2)$ $+(B_2 + \frac{1}{2}A_{D2})z$ $- (D_2 - \frac{1}{2}A_{H2})(z^2 + z)$ $\mp\epsilon_D\omega_2 z^{1/2} - \frac{1}{2}\gamma_2 - \gamma_{D2}z$	$\pm\epsilon\omega_2 - (B_2 - \frac{1}{2}\gamma_2)z^{1/2}$ $+ 2D_2 z^{3/2} \pm \epsilon_D\omega_2 z$ $+ \frac{1}{2}\gamma_{D2}(z + 1)z^{1/2}$
			$T_{ev} - \frac{1}{4}\epsilon^2\omega_2 - \frac{1}{2}A(1 - \frac{1}{4}\epsilon^2)$ $+(B_2 - \frac{1}{2}A_{D2})z$ $- (D_2 + \frac{1}{2}A_{H2})(z^2 + z)$ $\mp\epsilon_D\omega_2 z^{1/2} - \frac{1}{2}\gamma_2 - \gamma_{D2}z$

The basis functions are defined as $|J\ P, \pm\rangle = 2^{-1/2}\{|\Lambda\ \ell\ \Sigma, J\ P\rangle \pm |-\Lambda\ -\ell\ -\Sigma, J\ -P\rangle\}$. The upper and lower signs refer to the *e* and *f* levels, respectively. The subscripts 1 and 2 denote the $^2\Delta$ and $^2\Sigma$ components, respectively. $z = (J + \frac{1}{2})^2$.

The Renner-Teller operator H^{RT} in Eq. 6.5 is defined[48] under the harmonic approximation by

$$H^{RT} = \tfrac{1}{2}\epsilon\omega_2 q^2 \sigma_z , \tag{6.8}$$

where $\epsilon\omega_2$ is the Renner-Teller parameter, q is a dimensionless coordinate associated with the bending vibration, and σ_z is a Pauli matrix $\begin{pmatrix} 1 & 0 \\ 0 & -1 \end{pmatrix}$ representing reflection of the electrons in the molecular plane. The matrix elements of $\tfrac{1}{2} q^2 \sigma_z$ can be given in the general forms,

$$\langle \tfrac{1}{2} q^2 \sigma_z \rangle_{v,v} = \tfrac{1}{2}[(v + 1)^2 - K^2]^{1/2} \tag{6.9}$$

and

$$\langle \tfrac{1}{2} q^2 \sigma_z \rangle_{v\pm2,v} = \tfrac{1}{4}\{[\pm(v + 1) + 2 + K][\pm(v + 1) + K]\}^{1/2} , \tag{6.10}$$

where v is the bending vibrational quantum number. Here H^{RT} has matrix elements that obey selection rules $\Delta\Lambda = \pm2$, $\Delta\ell = \mp2$ and $\Delta\Sigma = 0$, and will, therefore, only have an off-diagonal matrix element between the $\kappa^2\Sigma$ and $\mu^2\Sigma$ basis states for the $\tilde{A}(010)$ level. The effect of the matrix element of Eq. 6.10 is included in the ΔT terms of Eqs. 6.6 and 6.7.

The centrifugal distortion of the Renner-Teller effect may be written as

$$H_D^{RT} = \epsilon_D\omega_2 (\tfrac{1}{2} q^2 \sigma_z) \mathbf{R}^2 \tag{6.11}$$

which has matrix elements that obey the selection rules: $\Delta\Lambda = \pm2$, $\Delta\ell = \mp2$, $\Delta\Sigma = 0,\pm1$ and $\Delta P = 0,\pm1$.

The $g_K(G_z + L_z)L_z$ operator is a nonadiabatic correction to the vibronic energies, which was first recognized by Brown[66]; its eigenvalue is $g_K K\Lambda$. The magnitude of g_K gives a measure of the vibronic perturbations of Σ and Δ electronic states on the Π electronic state.

$B\mathbf{R}^2$ is the operator for the end-over-end rotation of the molecule. $\mathbf{R}$ is defined as $\mathbf{R} = \mathbf{J} - \mathbf{L} - \mathbf{G} - \mathbf{S}$, and $\mathbf{R}^2$ is restricted to

$$\mathbf{R}^2 = (\mathbf{J}^2 - J_z^2 + \mathbf{S}^2 - S_z^2) - (J_+S_- + J_-S_+) \tag{6.12}$$

since the terms off-diagonal in Λ and v have been removed after the contact

transformations and the eigenvalues of $(\mathbf{L}^2 - L_z^2 + \mathbf{G}^2 - G_z^2)$ are the same for all vibronic components and can be included with the electronic-vibrational energy term. The eigenvalue of J_z is $P = \Lambda + \ell + \Sigma$, and the ladder operators $J_\pm$ and $S_\pm$ are defined by

$$J_\pm \, |J\, P\rangle = [J(J+1) - P(P \mp 1)]^{1/2} \, |J\, P \mp 1\rangle \tag{6.13}$$

$$S_\pm \, |S\, \Sigma\rangle = [S(S+1) - \Sigma(\Sigma \pm 1)]^{1/2} \, |S\, \Sigma \pm 1\rangle \, . \tag{6.14}$$

The constant B has been given separate values for the $^2\Delta$ and $^2\Sigma$ components, as denoted in Table 6.1 by B_1 and B_2, respectively. However, the $\kappa^2\Sigma$ and $\mu^2\Sigma$ components share the same B, instead of two different B constants as in Ref. 53. It is likely that the two $^2\Sigma$ components have slightly different B-values owing to some high order perturbations[81] that are not considered in the present matrix, and the fitted B-value is approximately the mean of the two B-values. It is preferred to obtain such a mean value because it is probably the one closest to the "true" single B-value and is also convenient to use. The same argument is also applied to the centrifugal distortion constant D.

Treatment of spin-rotation coupling follows a different approach in this work over that in Ref. 53 in which a "spin-rotation" term $\frac{1}{2}\gamma^{\mu,\kappa}(J + \frac{1}{2})$ was introduced into the diagonal matrix elements corresponding to the $\mu^2\Sigma$ and $\kappa^2\Sigma$ basis states with opposite sign, $\pm$ and $\mp$, respectively. When such an approach was used for the $\tilde{A}(010)$ levels of CaOH/CaOD, it was found that γ^μ and γ^κ had quite different values and the isotopic ratio $\bar{\gamma}_v$(CaOD)/$\bar{\gamma}_v$(CaOH) of the average γ-values ($\bar{\gamma}_v = \frac{1}{2}(\gamma^\mu + \gamma^\kappa)$) was 0.689, much smaller than the ratio B_v(CaOD)/B_v(CaOH) = 0.908. In the Hamiltonian matrix described in the present work the spin-rotation terms were derived directly from the $\gamma\mathbf{R}\cdot\mathbf{S}$ operator. The isotopic ratio of the fitted γ-values is 0.946 which is in good agreement with B_v(CaOD)/B_v(CaOH)=0.908. By analyzing the present matrix, it was seen

that the parameters $\gamma^{\mu,\kappa}$ used in Ref. 53 were actually equal to $2\gamma\epsilon\omega_2/\Delta E$, where ΔE is the spacing between the $\kappa^2\Sigma$ and $\mu^2\Sigma$ basis states and is approximately equal to A_v.

As first described by Veseth[76], in a $^2\Pi$ state of a diatomic molecule, the spin-rotation constant γ and the centrifugal distortion constant A_D of the spin-orbit coupling make indistinguishable contributions to the energy levels even though they originate from distinct physical mechanisms and have different matrix elements. In an analogous fashion for a linear triatomic $^2\Pi$ state, the parameters γ and A_D are heavily correlated in the unique $^2\Delta$ vibronic components of the $\tilde{A}(010)$ level. However, the situation in the two $^2\Sigma$ components is quite different. Owing to the addition of the Renner-Teller term, $\pm\epsilon\omega_2$, and its centrifugal distortion term, $\pm\epsilon_D\omega_2(J + \frac{1}{2})^2$, into the off-diagonal matrix elements between the two $^2\Sigma$ basis states, the correlation between γ and A_D is eliminated. It is possible, therefore, to fit separate values for γ and A_D. In the practical fit, a single γ was used for both $^2\Delta$ and $^2\Sigma$ components so that separated A_D-values could be determined for both $^2\Delta$ and $^2\Sigma$ components, though the γ-value is essentially determined by the $^2\Sigma$ components and it could have slightly different values for $^2\Delta$ and $^2\Sigma$.

H_K is the Hamiltonian responsible for the K-type resonance and includes contributions from both Λ-type and ℓ-type doublings, $H_K = H_\Lambda + H_\ell$. The effective operator for the Λ-type doubling may be expressed[82] as

$$H_\Lambda = \tfrac{1}{2} q^e (\Lambda_+^2 J_-^2 + \Lambda_-^2 J_+^2) - \tfrac{1}{2} (p^e + 2q^e) (\Lambda_+^2 J_- S_- + \Lambda_-^2 J_+ S_+) \qquad (6.15)$$

which has the selection rules $\Delta\ell = 0$, $\Delta\Lambda = \pm 2$, $\Delta\Sigma = 0, \mp 1$ and $\Delta P = \pm 2, \pm 1$. p^e and q^e are the conventional Λ-type doubling constants. The ladder operators $\Lambda_\pm^2$ and $J_\pm^2$ are defined by

$$\Lambda_\pm^2 \, |n\ \Lambda = \mp 1\rangle = + \, |n\ \Lambda = \pm 1\rangle \qquad (6.16)$$

$$J_{\pm}^2 \; |J\,P\rangle = [J(J+1) - P(P \mp 1)]^{1/2}\,[J(J+1) - (P \mp 1)(P \mp 2)]^{1/2} \; |J\,P\mp 2\rangle \tag{6.17}$$

The effective operator for the ℓ-type doubling may be expressed[83] as,

$$H_\ell = \tfrac{1}{2}\, q^v\, [\,\tfrac{1}{2}(G_+^2 J_-^2 + G_-^2 J_+^2) - (G_+^2 J_- S_- + G_-^2 J_+ S_+)] \tag{6.18}$$

with the selection rules $\Delta\Lambda = 0$, $\Delta\ell = \pm 2$, $\Delta\Sigma = 0, \mp 1$ and $\Delta P = \pm 2, \pm 1$. The ladder operator $G_{\mp}^2$ is defined by

$$G_{\mp}^2 \; |v_2\; \ell \pm 2\rangle = [(v_2 \mp \ell)(v_2 \pm \ell + 2)]^{1/2} \; |v_2\; \ell\rangle\,. \tag{6.19}$$

The definition of this operator has the advantage of removing v_2 dependence from the ℓ-type doubling constant q^v. The phase choice used here for the ℓ-type doubling is consistent with that for the Λ-type doubling. However, it should be emphasized that this choice is the reverse of that normally used in infrared spectroscopy. As a consequence, q^v is defined by

$$q^v = -\frac{2B^2}{\omega_2}\left\{1 + 4\sum_{n=1,3}\frac{\zeta_{2n}^2\omega_2^2}{\omega_n^2 - \omega_2^2}\right\}, \tag{6.20}$$

where ζ_{2n} is the Coriolis coupling constant. Except for the negative sign, this expression is essentially the same as that given by Nielsen[84].

For the $v_2 = 1$ ($^2\Pi$ vibronic) level of the $\tilde{X}^2\Sigma^+$ state, the rotational structure is best described by Hund's case (b) coupling, and was expressed[55] as

$$F_1(N) = T_v + B_v[N(N+1) - \ell^2] - D_v[N(N+1) - \ell^2]^2 + \tfrac{1}{2}\gamma_v N \pm \tfrac{1}{2}q^v N(N+1) \tag{6.21}$$

$$F_2(N) = T_v + B_v[N(N+1) - \ell^2] - D_v[N(N+1) - \ell^2]^2 - \tfrac{1}{2}\gamma_v(N+1) \mp \tfrac{1}{2}q^v N(N+1) \tag{6.22}$$

where F_1 and F_2 denote the spin components with $J = N + \tfrac{1}{2}$ and $J = N - \tfrac{1}{2}$, respectively. The upper and lower signs refer to the e and f levels, respectively. Again, the phase convention here is chosen as described above and q^v is defined by Eq. 6.20. The rotational levels of the $\tilde{X}(000)^2\Sigma^+$ state

were represented using the same expressions of Eqs. 6.21 and 6.22, but with $T_v = \ell = q^v = 0$.

6.5 Least Squares Fit

A weighted, non-linear least squares fit was carried out employing the matrix of Table 6.1 and the expressions of Eqs. 6.21 and 6.22. For each isotopomer, the fit included all the observed bands: $(010)\kappa^2\Sigma^{(-)}$, $\mu^2\Sigma^{(+)}$ - $(000)^2\Sigma^+$, $(010)^2\Delta$ - $(010)^2\Pi$, $(010)\kappa^2\Sigma^{(-)}, \mu^2\Sigma^{(+)}$ - $(010)^2\Pi$, and the K-resonance induced $(010)^2\Delta_{3/2}$ - $(000)^2\Sigma^+$ band of the $\tilde{A}$ - $\tilde{X}$ system. A total of 939 and 878 rotational lines of these bands have been measured and fitted with variances of $\hat{\sigma}^2 = 1.041^2$ and 1.080^2 for CaOH and CaOD, respectively. Since the estimates of $\hat{\sigma}^2$ are close to unity, the measurements are reproduced on average to within the measurement accuracy of 0.0035 cm^{-1}. The measured line positions along with their quantum numbers J and residuals $(\bar{\nu}_{obs.} - \bar{\nu}_{calc.})$ obtained from the least squares fits are listed in tables 4 - 13 in the Appendix. The molecular parameters of the $\tilde{X}(000)$ state were held fixed at the values determined in Ref. 16 for CaOH and in the work of Chapter 4 for CaOD, respectively, while the parameters for the $\tilde{X}(010)$ and $\tilde{A}(010)$ states were allowed to vary simultaneously; the fitted values are listed in Table 6.2. For comparison, the constants for the $\tilde{A}(000)$ and $\tilde{X}(000)$ levels are also listed in Table 6.2.

6.6 Results and Discussion

The least squares estimates of the parameter g_K are 0.5937(5) and 0.4462(5) cm^{-1} for CaOH and CaOD, respectively. As described in Ref. 66, this parameter contains contributions from vibronic perturbations by Σ and Δ electronic states; the Σ contribution is positive while the Δ contribution is

TABLE 6.2: Molecular Constants[a] of the (000) and (010) Levels in the $\tilde{A}^2\Pi$ and $\tilde{X}^2\Sigma^+$ States of CaOH and CaOD

	CaOH		CaOD	
	$\tilde{A}(000)$	$\tilde{A}(010)$	$\tilde{A}(000)$	$\tilde{A}(010)$
T_{ev}	15998.1220(7)	16360.3890(4)	15995.0160(3)	16269.0030(4)
A_v	66.8181(12)	67.0951(7)	66.7622(5)	66.9474(8)
A_{Dv}	0.135×10^{-3}	$0.1232(7) \times 10^{-3}(^2\Delta)$	0.123×10^{-3}	$0.1166(9) \times 10^{-3}(^2\Delta)$
		$0.140(2) \times 10^{-2}(^2\Sigma)$		$0.095(1) \times 10^{-2}(^2\Sigma)$
A_H		$-0.140(3) \times 10^{-6}$		$-0.133(2) \times 10^{-6}$
$\epsilon\omega_2$		-36.2634(6)		-26.9601(8)
$\epsilon_D\omega_2$		$0.741(8) \times 10^{-3}$		$0.705(8) \times 10^{-3}$
g_K		0.5937(5)		0.4462(5)
B_v	0.3412200(23)	$0.3402609(16)\ (^2\Delta)$	0.3090313(59)	$0.3090759(17)\ (^2\Delta)$
		$0.3402123(9)\ (^2\Sigma)$		$0.3090115(8)\ (^2\Sigma)$
D_v	$0.3891(11) \times 10^{-6}$	$0.3976(5) \times 10^{-6}(^2\Delta)$	$0.2981(15) \times 10^{-6}$	$0.3058(6) \times 10^{-6}(^2\Delta)$
		$0.3990(5) \times 10^{-6}(^2\Sigma)$		$0.3049(3) \times 10^{-6}(^2\Sigma)$
γ_v	0.0304	0.02617(5)	0.0276	0.02475(6)
γ_D		$-0.119(2) \times 10^{-4}$		$-0.134(2) \times 10^{-4}$
p^e	-0.04287(9)	-0.04472(8)	-0.03942(2)	-0.04009(6)
q^e	$-0.3257(74) \times 10^{-3}$	$-0.3072(84) \times 10^{-3}$	$-0.2810(6) \times 10^{-3}$	$-0.2632(91) \times 10^{-3}$
q^v		$-0.6978(17) \times 10^{-3}$		$-0.7576(14) \times 10^{-3}$
	$\tilde{X}(000)$[b]	$\tilde{X}(010)$	$\tilde{X}(000)$	$\tilde{X}(010)$
T_{ev}		352.9259(9)		266.8398(10)
B_v	0.33433411(1)	0.3334580(16)	0.3029872(60)	0.3030726(16)
D_v	$0.38600(3) \times 10^{-6}$	$0.3930(5) \times 10^{-6}$	$0.2943(16) \times 10^{-6}$	$0.3054(5) \times 10^{-6}$
γ_v	0.00115964(23)	0.001184(11)	0.001030(11)	0.001124(12)
q^v		$-0.7181(2) \times 10^{-3}$		$-0.7621(4) \times 10^{-3}$

[a]All values are in cm^{-1}; values in parentheses are 1σ standard deviations in units of the last significant digit of the corresponding constant. The values of A_H and γ_D were determined only for the $(010)^2\Sigma$ components; those for $^2\Delta$ were fixed at zero.

[b]From Ref. 16.

negative. The closest states, $\tilde{B}^2\Sigma^+$ and $\tilde{C}^2\Delta$, have been located by Bernath and co-workers[9,17] at ~2000 and ~5000 cm^{-1} above the $\tilde{A}^2\Pi$ state, respectively. The positive values of g_K thus seem quite reasonable. Since the considerable transition strength of the forbidden $\tilde{A}(010)^2\Sigma$ - $\tilde{X}(000)^2\Sigma$ bands is a manifestation of the sizable $\tilde{A}^2\Pi$ ~ $\tilde{B}^2\Sigma^+$ vibronic interaction, the small magnitudes of g_K are probably due to significant cancellation by the $\tilde{C}^2\Delta$ perturbation.

The fundamental frequency of the bending vibration in the $\tilde{X}^2\Sigma^+$ state is simply equal to the term value of the (010) level, which has been determined as 352.9259(9) and 266.8398(10) cm^{-1} by the least squares fit for CaOH and CaOD, respectively. The fundamental bending frequency of the $\tilde{A}^2\Pi$ state can be calculated using the (000) term value determined in Chapter 4 of this thesis, which should be corrected by $-\frac{1}{4}\epsilon^2\omega_2 + g_K$, and the (010) term value in this work. The ν_2-values for the $\tilde{A}^2\Pi$ state are thus determined as 361.9541(8) and 273.7727(5) cm^{-1} for CaOH and CaOD, respectively. Owing to the large mass of Ca compared to H or D, the bending vibration of the molecule can be viewed as essentially the motion of the H or D atom relative to the Ca–O bond axis. As a consequence, the bending frequency of CaOD is significantly smaller than that of CaOH.

Both parameters ϵ and $\epsilon\omega_2$ describing the Renner-Teller effect appear in the matrix. $\epsilon\omega_2$ is one of the key parameters defining the vibronic structure and has been accurately determined from the experimental data for both isotopomers. On the other hand, the parameter ϵ is not sensitive to the least squares fit. It is certainly not appropriate to fit both ϵ and $\epsilon\omega_2$ while they are related by a definite factor of ω_2. The parameter ϵ was, hence, held fixed at the estimated values, ϵ=-0.10 for CaOH and ϵ=-0.098 for CaOD, in the two fits. In the next chapter, the values of ω_2 are estimated based on the

information from the $\tilde{A}(020)$ level combined with the information from the $\tilde{A}(000)$ and $\tilde{A}(010)$ levels. When ϵ is calculated employing the ω_2-values from next chapter and the $\epsilon\omega_2$-values from this chapter, the results are ϵ=-0.099 for CaOH and ϵ=-0.097 for CaOD, in excellent agreement with the estimated values used in the fits.

A comparison between the molecular parameters of the (010) and the (000) levels is particularly instructive in gauging the quality of the model fitting. The list of parameters in Table 6.2 for the (000) and (010) levels of the $\tilde{A}$ and $\tilde{X}$ states of CaOH/CaOD shows that for almost every major parameter, such as A_v, B_v, D_v, γ_v, p^e and q^e, the value for the (010) level is very consistent with that of the (000) level. Also, the fitted q^v-values of the $\tilde{A}(010)$ level are very close to those of the $\tilde{X}(010)$ level, indicating that the deperturbation in the $\tilde{A}^2\Pi$ state has successfully separated the electronic and vibrational contributions to the K-type doubling, even though the two contributions are experimentally indistinguishable and normally difficult to separate by spectroscopic analysis It should be noticed that the Λ-type and ℓ-type doubling constants appear only in the off-diagonal matrix elements of the $\tilde{A}(010)$ Hamiltonian and are hence very sensitive to the overall accuracy of the data set and to the validity of the Hamiltonian matrix. Such consistency lends strong confidence to the data set and the model employed in the present work.

As previously noticed[9], the spin-rotation constant γ of the $\tilde{B}^2\Sigma^+$ state has a value very close to that of the $\tilde{A}^2\Pi$ state Λ-doubling constant p^e, as expected if these two electronic states form a unique perturber pair. However, the q^e-values are approximately 1.4 times larger than (p^eB/A). This is an indication that these two states do not completely satisfy the "pure precession" hypothesis. This situation is consistent with the somewhat

different electronic configurations of the two states indicated by theoretical studies[27,30]. Brown[51] pointed out that there is a vibrational contribution (q^{vib}) to the electronic parameter q^e, defined by

$$q^{vib} = \frac{B^2\epsilon}{\omega_2} \sum_{n=1,3} \zeta_{2n}^2 \left\{ 1 - \frac{4\omega_2^2}{(\omega_n + \omega_2)^2} \right\} . \qquad (6.23)$$

However, the values of q^{vib} for both CaOH and CaOD, estimated using the constants derived later in this paper, are only about 10% of q^e, so that this contribution is only a minor factor in the present case.

As mentioned in Section 6.4, the parameters γ and A_D in the $\tilde{A}(010)$ level are separable due to the Renner-Teller effect. In the work on the $\tilde{A}^2\Pi(000)$ level described in Chapter 4, the parameters γ and A_D were separated using isotope effects. Good agreement in terms of the γ-values has been found between the $\tilde{A}(000)$ and $\tilde{A}(010)$ levels for both CaOH and CaOD. It should be noted, however, that the present fits required separate A_D parameters for the $^2\Delta$ and $^2\Sigma$ components. For both isotopomers, the fitted A_D-value for the $^2\Delta$ component is consistent with that derived from the $\tilde{A}(000)$ level while that for the $^2\Sigma$ components is an order of magnitude larger. It is probable that the anomalously large A_D values for the $^2\Sigma$ components arise principally from perturbations that have not been included or have not been represented adequately by the present Hamiltonian. This explanation is supported by the fact that two other high order parameters, A_H and γ_D, were needed for the $^2\Sigma$ components, but not for the $^2\Delta$ components; these are therefore also to be regarded as effective parameters for handling such perturbations.

The Renner-Teller perturbation from the $\tilde{A}(030)$ level is an immediate candidate for those perturbations. The effect of this perturbation is generally taken as a constant correction to the vibronic energies, $-\frac{1}{4}\epsilon^2\omega_2$ for

$^2\Sigma$ and $-\frac{3}{4}\epsilon^2\omega_2$ for $^2\Delta$. However, given the highly precise data in the present work, the J- and parity-dependence of the energy separations between the (010) and (030) rotational levels is no longer negligible. Fig. 6.8 clearly illustrates such a situation. For example, the smallest energy separation occurs between the e-levels of the (030)$\mu^2\Sigma$ and the (010)$\kappa^2\Sigma$ components, which are connected by the Renner-Teller matrix element, $2^{-1/2}\,\epsilon\omega_2$, and the separation decreases as J increases. A correction term, using second order perturbation theory, explicitly taking account of the J- and parity-dependence of the energy separations, was added to respective diagonal matrix elements of the $^2\Sigma$ and $^2\Delta$ components. Of course, such perturbation has a negligible effect in terms of the J-dependence on the $^2\Delta$ components. A fit including these corrections (with no extra adjustable parameters added into the fit) resulted in 5% improvement of the variance and a general ~40% reduction of the magnitudes of $A_D(^2\Sigma)$, A_H and γ_D for each isotopomer. However, all the primary parameters, T_{ev}, A_v, B_v, D_v, $\epsilon\omega_2$, p^e, q^e and q^v, changed only slightly (with the largest change of about one standard deviation); such small changes are physically insignificant since virtually every parameter has been overdetermined by the extensive and precise data body. This is a clear indication that the present model has given a physically satisfactory representation for the observed quantities. It has been decided, therefore, to present only the results obtained without these corrections. Nevertheless, the test using such corrections is important not only in providing a quantitative measure of the effect of the perturbations from the (030) level, but also in lending more confidence to the results of the present work.

Owing to the high density of the vibronic levels in the $\tilde{A}^2\Pi$ electronic state, the various interactions between these levels pose a significant challenge to the deperturbation approach. The success of a deperturbation

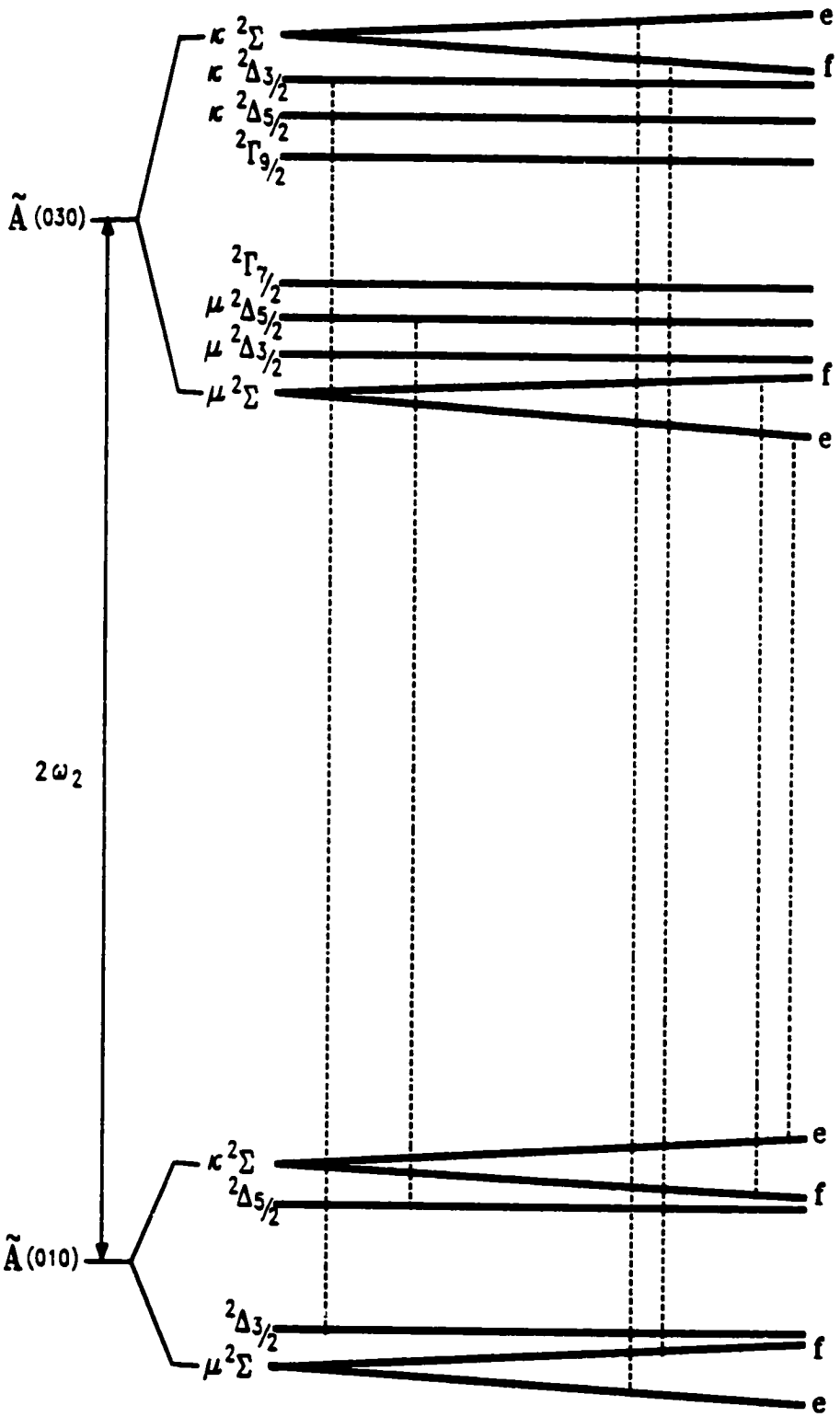

Fig. 6.8: The vibronic interactions between the (030) and (010) levels in the $\tilde{A}^2\Pi$ state. The broken lines connect the vibronic levels that can interact with each other through the Renner-Teller operator.

model can be assessed in various ways; the parameters determined in this chapter have been compared with those for the zero-point levels obtained in Chapter 4. Another valuable indicator is the examination of isotope relations. In a strict sense, the isotope relations are obeyed only for parameters describing the molecular equilibrium configuration; in general, such relations still hold approximately for low-lying excited vibrational levels. However, owing to the small mass of the hydrogen, anharmonicity becomes a very significant effect as the bending vibration is excited. The molecular parameters are the expectation values of the corresponding radial Hamiltonian operators integrated over the anharmonic wavefunctions. It has been noticed that the B_v-values for CaOH and CaOD change in opposite directions when v_2 increases from zero to one. As a result, the isotopic ratio of the B_v-values for the (010) level, shown below, is slightly larger than that for the (000) level (Section 4.4) in both the $\tilde{A}$ and $\tilde{X}$ states. A brief summary about the isotopic behavior of the parameters for the (010) levels is presented as follows.

$$\tilde{X}(010):\ B_v^D/B_v^H = 0.908878(6) \qquad \gamma_v^D/\gamma_v^H = 0.9493(2)$$

$$\tilde{A}(010):\ B_v^D/B_v^H = 0.908320(4) \qquad \gamma_v^D/\gamma_v^H = 0.946(2) \qquad A_D^D/A_D^H = 0.946(10)$$

$$p^{eD}/p^{eH} = 0.896(2) \qquad [q^{eD}/q^{eH}]^{1/2} = 0.926(40)$$

where the superscripts H and D denote CaOH and CaOD, respectively. The B_v-value for the $\tilde{A}(010)$ level is the average value for the $^2\Delta$ and $^2\Sigma$ components. The Λ-type doubling constants p^e and q^e obey the isotope relations quite well. The relatively large deviation from the isotope relation in the parameters γ_v and A_D could occur for two reasons. First, it was found that γ_v and A_D are quite sensitive to the high order perturbations mentioned in the last paragraph; the physical significance of the estimates of these parameters given by the present fits is certainly poorer than is implied

by their 1σ standard deviations. Second, the anharmonicity becomes significant in the $v_2 = 1$ level and its effect on various parameters may not be the same. Nevertheless, examination of the isotopic behavior of the fitted molecular parameters has provided a valuable diagnostic for the deperturbation model and the data set.

6.7 Concluding Remarks

The $\tilde{A}(010)$ - $\tilde{X}(010)/(000)$ bands of CaOH and CaOD have been rotationally analyzed with high precision in this work. The *K*-type resonance occurring in the $\tilde{A}(010)$ vibronic manifold has been successfully modeled using a global matrix deperturbation approach. The strong interactions between the $\tilde{A}(010)$ $^2\Delta_{3/2}$ and $\mu^2\Sigma$ components caused not only large level shifts but also anomalous branch intensities; the latter provided a typical example of the quantum mechanical interference.

The Renner-Teller parameter $\epsilon\omega_2$ has been evaluated for the first time for an alkaline earth monohydroxide radical. The molecular constants obtained from the least squares fits have been examined using several approaches including isotope relations, and have been proved, except a few high order parameters, to be physically meaningful and self- and isotopically-consistent. In particular, the fitted Λ-type doubling constants, p^e and q^e, have been proved to be truly electronic while the ℓ-type doubling constant, q^v, has preserved its vibrational character. The values of q^v calculated in Chapter 8 using Coriolis coupling constants are in excellent agreement with the experimental values obtained in this chapter for both isotopomers.

CHAPTER 7

Analysis of the $\tilde{A}(100)/(020)$ - $\tilde{X}(020)/(000)$ Bands of CaOH/CaOD

7.1 Introduction

The $\tilde{A}^2\Pi(100)/(020)$ vibronic manifold of CaOH and CaOD exhibits strong Fermi resonance, as well as Renner-Teller and spin-orbit interactions. The present work represents the first investigation of Fermi resonance in the studies of alkaline earth monohydroxide molecules.

In the past, most of the spectroscopic studies involving Fermi resonance have been concerned with non-degenerate electronic states. Hougen[43] expanded Fermi's theory[85] to describe such an interaction in degenerate Π electronic states. Owing to the existence of vibronic and spin-orbit interactions along with the Fermi resonance, the spectral analysis and modeling becomes very difficult. There are very few examples of analyzed systems that exhibit these interactions. In the last two decades, most of the significant progress has been associated with 15-electron species, in particular BO_2[86], NCO[56,61], NCS[58] and CO_2^+[59,60], which all have $^2\Pi$ ground electronic states. In the present work, the molecule under consideration has quite different electronic structure, and exhibits strong Fermi resonance in its lowest excited electronic state with $^2\Pi$ symmetry. The present work has produced a much larger and more precise data base than any of the previous studies mentioned above, and has involved two isotopomers.

In the $\tilde{A}^2\Pi$ electronic state of CaOH, the (100) vibrational level is split into two components, $^2\Pi_{1/2}$ and $^2\Pi_{3/2}$, and (020) into six components, $\mu^2\Pi_{1/2}$, $\mu^2\Pi_{3/2}$, $\kappa^2\Pi_{1/2}$, $\kappa^2\Pi_{3/2}$, $^2\Phi_{5/2}$ and $^2\Phi_{7/2}$ by spin-orbit and vibronic interactions. The $(100)^2\Pi$ manifold and the $(020)^2\Pi$ manifold belong to the same symmetry species, and some of the components lie very close in energy,

leading to strong Fermi resonance. It is advantageous and, in fact, necessary to study the two manifolds simultaneously. A global matrix deperturbation including both (100) and (020) $^2\Pi$ vibronic manifolds has been performed in the present work. The $^2\Phi$ components do not interact significantly with any $^2\Pi$ components, and were not considered. Fig. 7.1 and 7.2 show schematically the subbands observed via laser excitation in this work for CaOH and CaOD, respectively. Each number attached to a vertical line indicates the number of rotational transitions observed for the corresponding subband.

7.2 Fermi Resonance

When two vibrational or two vibronic levels of the same symmetry type in a polyatomic molecule lie close in energy, a Fermi resonance interaction takes place. Such an interaction leads to level shifts and wavefunction mixing. This phenomenon is attributable to the cubic anharmonic terms in the potential energy expression. It was first recognized by Fermi[85] in the case of CO_2, which involved the (100) and (020) vibrational levels of a non-degenerate electronic state, the Σ ground state. Some three decades later, Hougen[43] described a quantum mechanical treatment of Fermi resonance for linear triatomic Π electronic states, which are subject simultaneously to the Renner-Teller effect. He defined an anharmonic perturbation operator responsible for the $(v_1+1\ v_2\ v_3) \sim (v_1\ v_2+2\ v_3)$ type Fermi resonance in the form

$$V_F = \tfrac{1}{2}\,(k'_{122} + k''_{122})\,Q_1 r^2 + \tfrac{1}{2}\,(k'_{122} - k''_{122})\,Q_1 r^2\,2\cos 2(\theta-\phi) \qquad (7.1)$$

Here Q_1 is the coordinate (mass-adjusted) corresponding to the ν_1 stretching mode and r is the polar coordinate (mass-adjusted) corresponding to the amplitude of the bending vibration. k'_{122} and k''_{122} are the anharmonic force constants associated with the two component potential energy functions, V' and

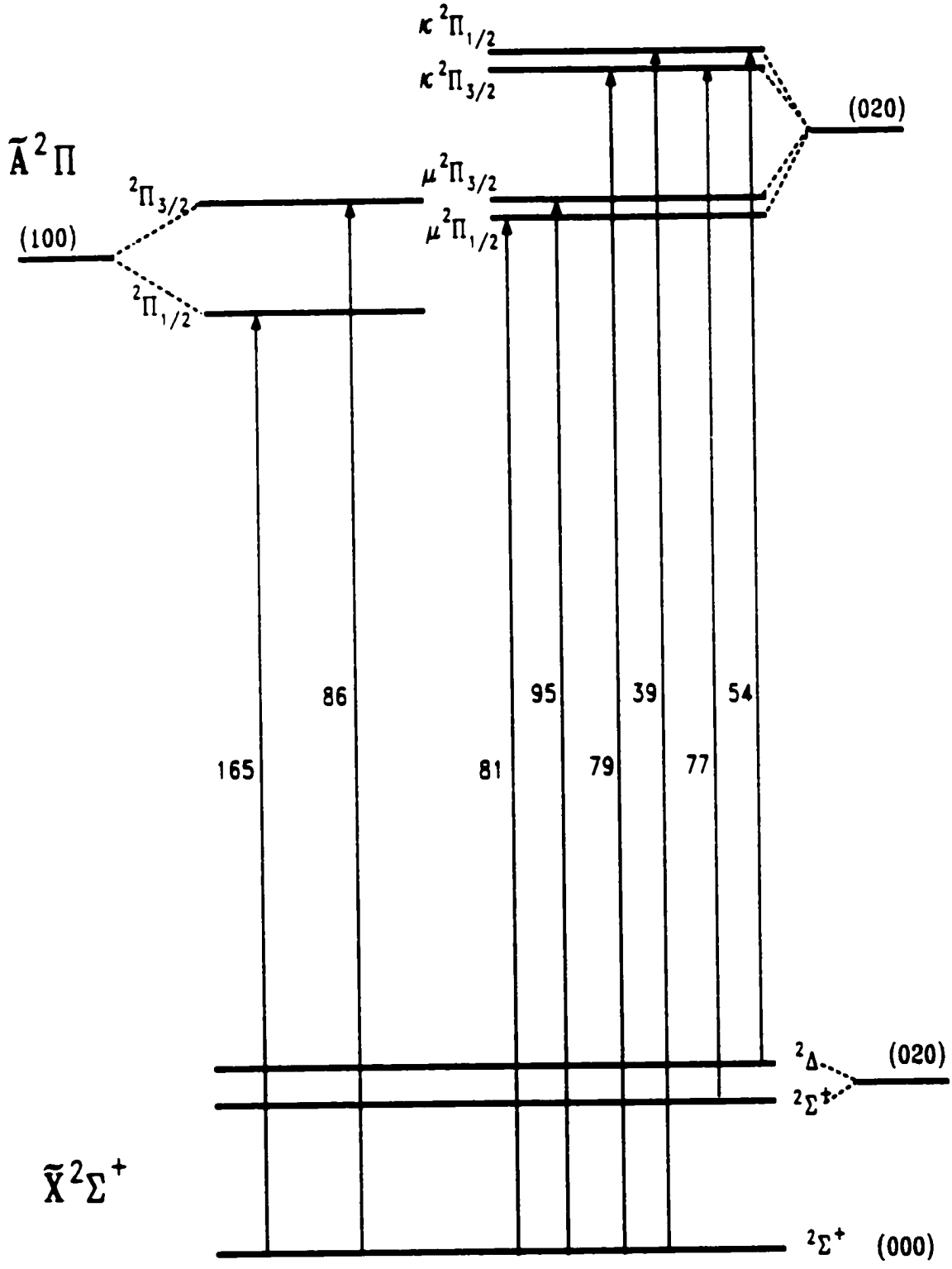

Fig. 7.1: The $\tilde{A}$(100)/(020) - $\tilde{X}$(020)/(000) vibronic subbands observed via laser excitation for CaOH

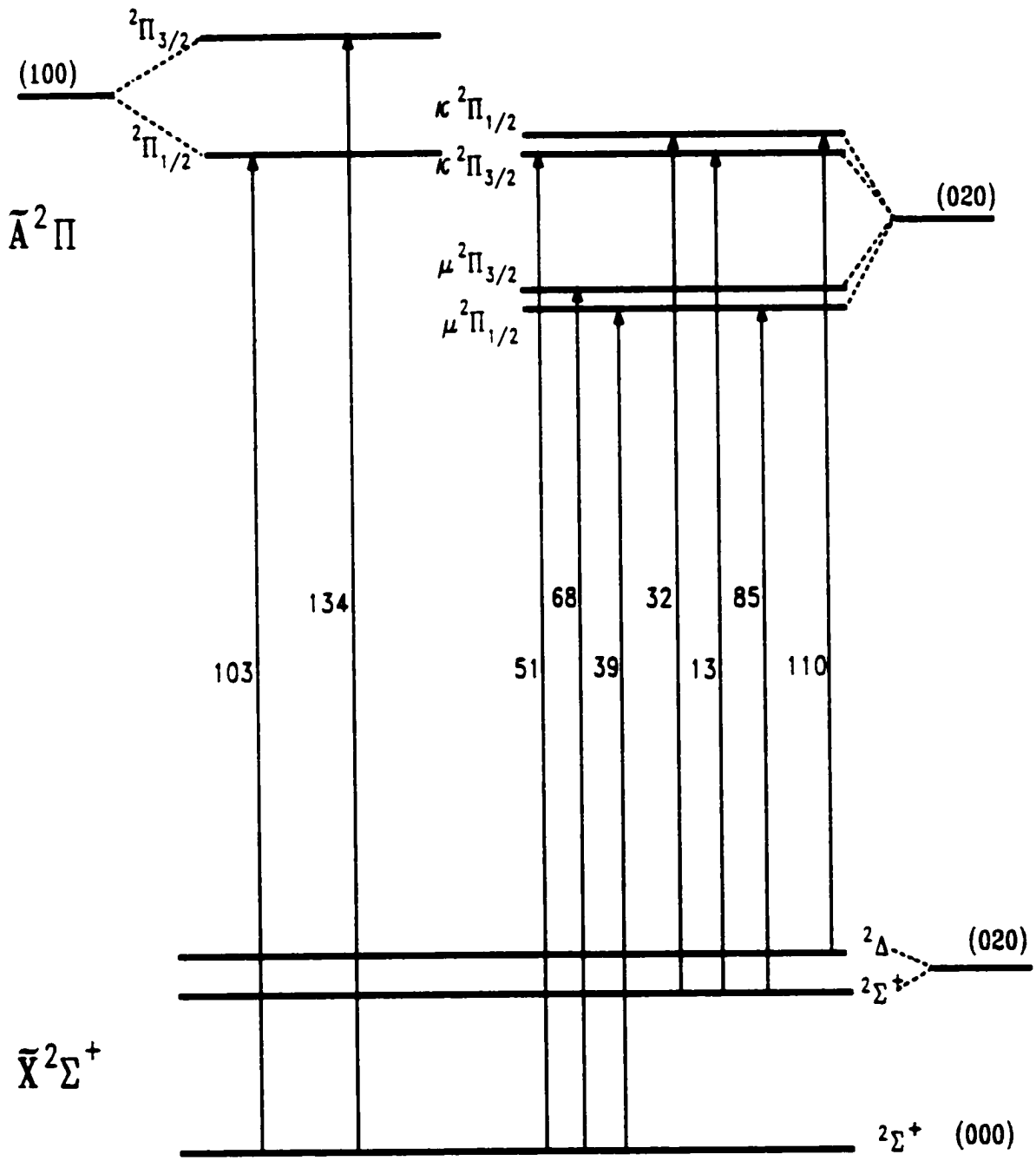

Fig. 7.2: The $\tilde{A}$(100)/(020) - $\tilde{X}$(020)/(000) vibronic subbands observed via laser excitation for CaOD

V'', caused by Renner-Teller splitting. ϕ is the angle between the plane of the bent molecule and an arbitrary reference plane. θ is the azimuthal angle of the electron (a one-electron model is being discussed here) with respect to the reference plane. This operator acts on the functions of the basis set $|v_1\ v_2\ v_3,\ \Lambda\ \ell\ \Sigma\rangle$, which can be combined to form wave functions that are symmetric or antisymmetric with respect to a reflection of the electronic coordinates in the plane of the bent molecule. The matrix elements of the Fermi interaction can be evaluated according to the formulas[43]

$$\langle v_1+1\ v_2\ v_3,\ \Lambda\ell\Sigma|V_F|v_1\ v_2+2\ v_3,\ \Lambda\ell\Sigma\rangle = W_1\ [(v_1+1)\ (v_2+2-\ell)\ (v_2+2+\ell)]^{1/2} \tag{7.2}$$

$$\langle v_1+1\ v_2\ v_3,\ \Lambda\ell\Sigma|V_F|v_1\ v_2+2\ v_3,\ \Lambda\mp2\ \ell\pm2\ \Sigma\rangle = W_2\ [(v_1+1)\ (v_2+2\pm\ell)\ (v_2+4\pm\ell)]^{1/2}. \tag{7.3}$$

Here two Fermi resonance parameters, W_1 and W_2, were introduced for a Π electronic state, replacing the single parameter W for a non-degenerate electronic state. They are defined by

$$W_1 = \tfrac{1}{2}\ (k'_{122}+k''_{122})\ (\hbar/4\pi c\omega_2)\ (\hbar/4\pi c\omega_1)^{1/2} \tag{7.4}$$

$$W_2 = \tfrac{1}{2}\ (k'_{122}-k''_{122})\ (\hbar/4\pi c\omega_2)\ (\hbar/4\pi c\omega_1)^{1/2} \tag{7.5}$$

where ω_1 and ω_2 are harmonic vibrational frequencies. As implied by Eq. 7.5, the magnitude of W_2 is dependent on the magnitude of the vibronic interaction which leads to the splitting of the potential. From Eqs. 7.2 and 7.3, the selection rules for Fermi resonance can be inferred as $\Delta v_2 = \pm2$, Δv_1 (or Δv_3) $= \mp1$ and $\Delta P = 0$. For a $^2\Pi$ electronic state, Hougen[43] has derived the Fermi resonance matrix elements using equations 7.2 and 7.3 and the vibronic wave functions obtained from a first-order perturbation treatment of the Renner-Teller and spin-orbit effects, which are both assumed to be small compared to the bending frequency. These matrix elements have been employed in Refs. 52, 56 and 61, and in the present work.

CaOH and CaOD have similar Ca-O stretch frequencies (ω_1) but quite different bending frequencies (ω_2). As a consequence, the Fermi resonance in the $\tilde{A}^2\Pi$ electronic state has quite different patterns for CaOH and CaOD. As illustrated in Fig. 7.1 for CaOH, the two vibronic levels, $\tilde{A}(100)^2\Pi_{3/2}$ and $\tilde{A}(020)\mu^2\Pi_{3/2}$, are almost degenerate. These two levels are directly connected by a Fermi resonance matrix element, as seen later from Table 7.1 in Section 7.5. The resulting interaction is extremely strong, but is *J*-independent. The nearby $\tilde{A}(020)\mu^2\Pi_{1/2}$ interacts with these two levels through *J*-dependent matrix elements, including spin-uncoupling and ℓ-type doubling. As shown in Fig. 7.2 for CaOD, the near degeneracy of the $\tilde{A}(100)^2\Pi_{1/2}$ and $\tilde{A}(020)\kappa^2\Pi_{3/2}$ creates even more problems to spectrum analysis and model fitting, since the interaction between the two levels is *J*-dependent, caused by the operators H(spin-uncoupling) × H(Fermi resonance). In order to demonstrate the effects of various interactions, Fig. 7.3 shows a schematic diagram for the example of the six $^2\Pi$ vibronic levels of CaOH involved in this work. The broken lines represent the observed levels at J = 1½. The solid lines represent the levels when the Fermi resonance parameters are set to zero. This diagram was drawn using the molecular constants and perturbation parameters determined in the final fit. As seen in Fig. 7.3, the $\tilde{A}(100)^2\Pi_{3/2}$ and $\tilde{A}(020)\mu^2\Pi_{3/2}$ vibronic components experience the largest energy shifts. Their wavefunctions are thus nearly equally mixed.

7.3 Laser Excitation Spectra

The experimental set up has been described in Section 3.2. A Coherent 699-29 ring dye laser was operated in single mode with Rhodamin 6G dye for the $\tilde{A}(100)/(020)$ - $\tilde{X}(000)$ bands and Sulforhodamin B dye for the $\tilde{A}(020)$ - $\tilde{X}(020)$ band. The average measurement uncertainty for rotational transitions was

Fig. 7.3: Energy level diagram (in cm^{-1} units) of the $\tilde{A}^2\Pi$ (100) and (020) vibronic levels illustrating the effect of Renner-Teller, spin-orbit and Fermi resonance interactions. The broken lines represent the observed levels at $J=1\frac{1}{2}$; the solid lines represent the levels when the Fermi resonance parameters are set to zero. The diagram is drawn using the parameters determined in the final fit. The unobserved $\tilde{A}(020)^2\Phi$ vibronic level, expected to lie midway between $\kappa^2\Pi$ and $\mu^2\Pi$, is not shown.

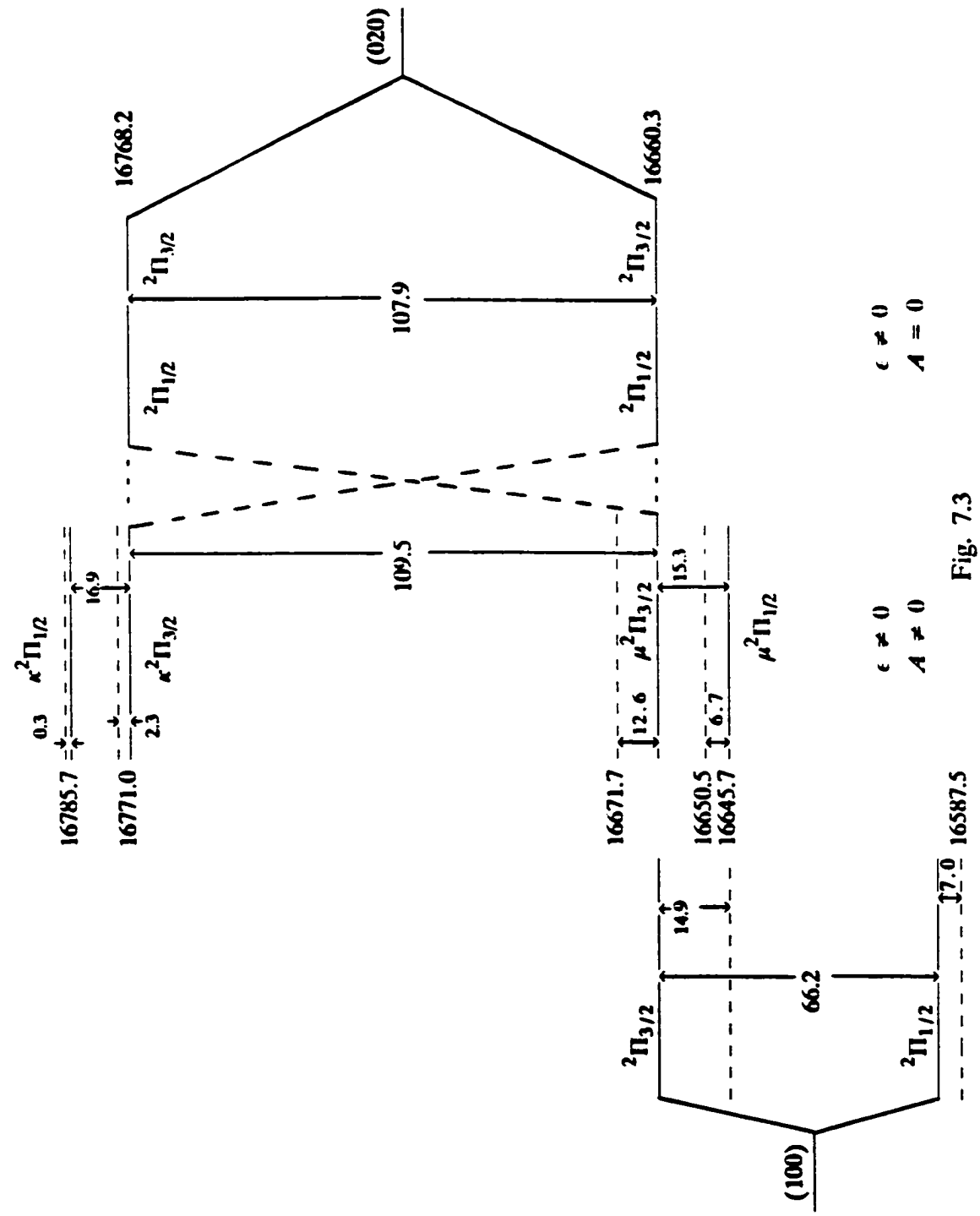
(020)
16768.2
16660.3
$^2\Pi_{3/2}$
$^2\Pi_{1/2}$
107.9
109.5
$\kappa^2\Pi_{1/2}$
$\kappa^2\Pi_{3/2}$
$\mu^2\Pi_{3/2}$
$\mu^2\Pi_{1/2}$
0.3
16.9
2.3
12.6
15.3
6.7
16785.7
16771.0
16671.7
16650.5
16645.7
14.9
66.2
7.0
16587.5
(100)
$\epsilon \neq 0$
$A = 0$
$\epsilon \neq 0$
$A \neq 0$

Fig. 7.3

estimated to be 0.0035 cm^{-1}.

Both $\tilde{A}(100)-\tilde{X}(000)$ and $\tilde{A}(020)-\tilde{X}(000)$ transitions are allowed by dipole selection rules. However, owing to the unfavorable Franck-Condon factors, the (100) - (000) band is approximately ten times weaker than the (000) - (000) band, while the (020) - (000) band is again ~10 times weaker than the (100) - (000) band. Strong Fermi resonance between (100) and (020) tends to mix the two vibrational levels and even the transition strengths between the two bands. However, access to the $(020)\kappa^2\Pi_{1/2}$ vibronic level from $\tilde{X}(000)$ are very weak for both CaOH and CaOD, and mainly rely on hot band excitations from $\tilde{X}(020)$. This can be partially attributed to the small Fermi interaction matrix element between $(020)\kappa^2\Pi_{1/2}$ and $(100)^2\Pi_{1/2}$, as seen later in Table 7.1 ($W_2 \approx 0$).

Although $\Delta v_i = 0$ hot band excitation to the $\tilde{A}(100)/(020)$ levels would have the largest Franck-Condon factors, a majority of the excitation spectra were taken from the $\tilde{X}(000)$ level for both CaOH and CaOD. This approach has a few advantages. First, the $\tilde{X}(000)$ level has much larger population than the excited (100) or (020) level in the Broida oven. Second, it is more convenient for the use of the selective LIF detection, which not only improved the signal/noise ratio and simplified the spectra, but also demonstrated its diagnostic power.

For CaOH, the $\tilde{A}(100)/(020)$ - $\tilde{X}(000)$ bands span a range of 16550 - 16800 cm^{-1}. The excitation spectra were recorded twice in the entire region using selective detection with frequency differences of 609 $cm^{-1}(\approx\omega_1)$ and 688 $cm^{-1}(\approx 2\omega_2)$, respectively. In the lower-frequency region, 16550 - 16630 cm^{-1}, the spectrum was very intense and clean when the frequency difference $\Delta\tilde{\nu}$ was 609 cm^{-1}, while the spectrum with $\Delta\tilde{\nu}$ = 688 cm^{-1} was absent. The spectrum in this region was quickly identified as the $\tilde{A}(100)^2\Pi_{1/2}$ - $\tilde{X}(000)^2\Sigma^+$ subband,

which is not significantly perturbed and showed the expected structure for a $^2\Pi$(a) - $^2\Sigma^+$ transition. In a narrow region, 16640 - 16680 cm^{-1}, the spectrum was extremely congested and complex. The subbands associated with the $\tilde{A}(100)^2\Pi_{3/2}$, $\tilde{A}(020)\mu^2\Pi_{3/2}$ and $\mu^2\Pi_{1/2}$ vibronic components were expected to appear in this region based on the spin-orbit and Renner-Teller parameters determined earlier (Chapter 6). Some parts of the spectra in this region showed different relative intensities between the two scans with $\Delta\bar{\nu}$ = 609 and 688 cm^{-1}, while others showed essentially no change. Although the intensity information provided some clues for spectral analysis, it was necessary to record a large number of resolved fluorescence spectra to identify unequivocally the corresponding vibronic species as well as to assign the *J*-values and *e/f* parities. Fig. 7.4 shows a portion of the excitation spectrum belonging to the $\tilde{A}(020)\mu^2\Pi$ - $\tilde{X}(000)^2\Sigma^+$ band recorded using selective detection with 688 cm^{-1} frequency difference. In this spectrum the Q_2 branch had the same signal intensity when recorded with $\Delta\bar{\nu}$ = 609 cm^{-1}; however, the R_1 and Q_1 lines became weaker with such detection. In the higher-frequency region, 16750 - 16800 cm^{-1}, only the spectrum recorded with $\Delta\bar{\nu}$ = 688 cm^{-1} has appreciable intensity. The $\tilde{A}(020)\kappa^2\Pi_{3/2}$ - $\tilde{X}(000)$ subband was readily picked out with fairly strong P_1 and Q_1 branches. The rotational lines of the two branches did not become noticeably broader even at J' = 40½, indicating that the satellite lines (Q_{12} and R_{12}) are very weak and the upper state conforms to Hund's case (b). The R_1 branch was extremely weak, probably caused by a quantum mechanical interference effect. The $\kappa^2\Pi_{3/2}$ vibronic state was assigned as the F_1 component owing to the negative effective spin-orbit coupling. The $\kappa^2\Pi_{1/2}$ - $\tilde{X}(000)$ subband was very weak. The investigation of the $\kappa^2\Pi_{1/2}$ component mainly relied on the hot band excitation as mentioned before. Since the rotational constants of the $\tilde{X}(02^00)$ and $\tilde{X}(02^20)$ levels were

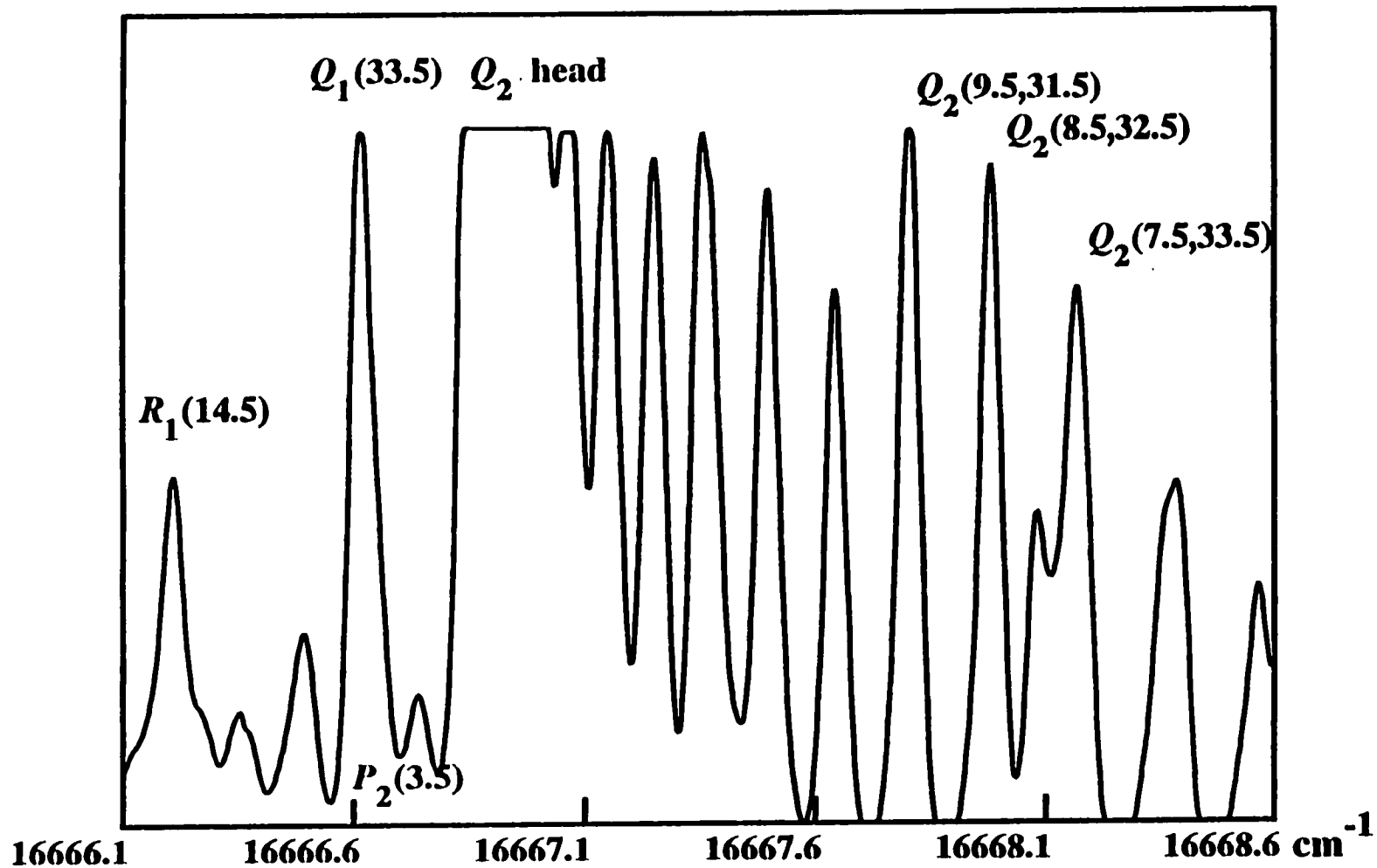

Fig. 7.4: A portion of the excitation spectrum of the CaOH $\tilde{A}(020)\mu^2\Pi$ - $\tilde{X}(000)^2\Sigma^+$ subbands, recorded using selective detection of LIF with a 688 cm^{-1} frequency difference.

determined previously through resolved fluorescence, as described in Chapter 5, the hot band excitation spectra were taken using the second type of selective detection, namely, scanning the *R* branch and detecting the corresponding *P* branch.

In the case of CaOD, the relative positions of the $\tilde{A}(020)$ and $\tilde{A}(100)$ levels are different from those in CaOH, as predicted from the knowledge of the vibrational structures in the $\tilde{X}$ state. The excitation spectra from the $\tilde{X}(000)$ level range from 16470 cm^{-1} to 16700 cm^{-1}. Again, two distinct scans were taken in the whole region, with the frequency differences 605 $cm^{-1}(\approx\omega_1)$ and 519 $cm^{-1}(\approx 2\omega_2)$, respectively, for selective detection. The $\Delta\tilde{\nu}$ = 519 cm^{-1} spectrum exhibits structure with good signal/noise ratio in the lower-frequency region, which was assigned as the $\tilde{A}(020)\mu^2\Pi$ - $\tilde{X}(000)$ subbands. In the higher-frequency region, the $\Delta\tilde{\nu}$ = 605 cm^{-1} spectrum has the highest intensity and was readily identified as the $\tilde{A}(100)^2\Pi_{3/2}$ - $\tilde{X}(000)$ subband. In these two regions only a few resolved fluorescence spectra were required for *J* and *e/f* assignment. In the middle region, 16560 - 16600 cm^{-1}, two subbands involving the $\tilde{A}(100)^2\Pi_{1/2}$ and $\tilde{A}(020)\kappa^2\Pi_{3/2}$ components appear simultaneously. Close degeneracy and strong *J*-dependent mixing between the two components make analysis very difficult. It was necessary to record many resolved fluorescence spectra for vibronic and rotational assignment. Fig. 7.5 shows two nearby band heads in the excitation spectrum, taken with $\Delta\tilde{\nu}$ = 519 cm^{-1}. The band head at the lower frequency side was given a nominal assignment as the $\tilde{A}(020)\kappa^2\Pi_{3/2}$ - $\tilde{X}(000)^2\Sigma^+$ P_1 branch ($\kappa^2\Pi_{3/2}$ is the F_1 component); the other head was assigned as the $\tilde{A}(100)^2\Pi_{1/2}$ - $\tilde{X}(000)^2\Sigma^+$ P_1 branch. When the frequency difference was set at 605 cm^{-1}, the excitation spectrum in the same region appeared essentially the same as the one in Fig. 7.5. This observation is in accord with the heavy mixing of the two upper states; they actually

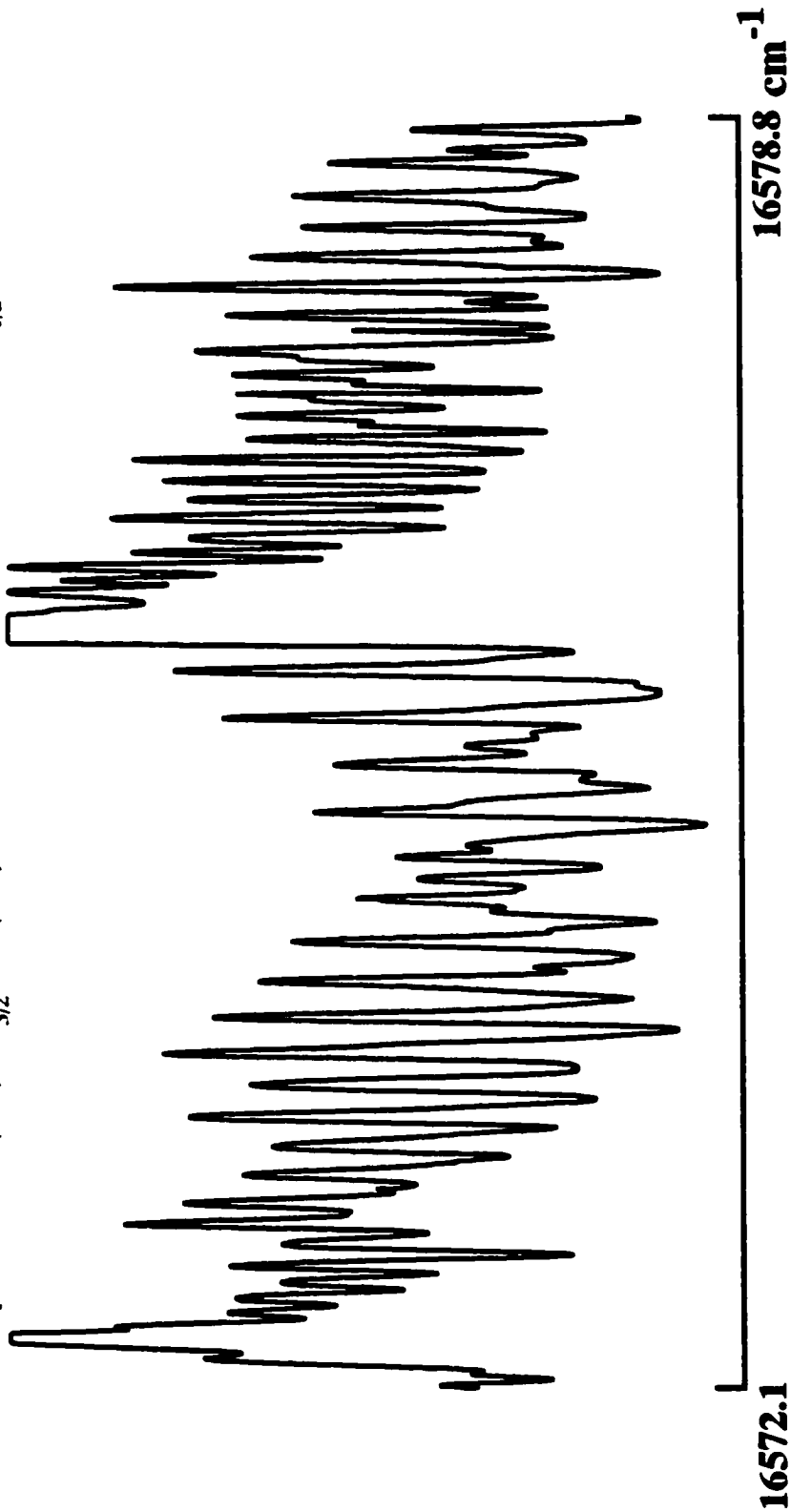

Fig. 7.5: A portion of the excitation spectrum of CaOD, recorded using selective LIF detection with a 519 cm^{-1} frequency difference.

exchange leading characters at $J' \geq 41\frac{1}{2}$. A hot band was excited to probe the $\tilde{A}(020)\kappa^2\Pi_{1/2}$ component as in the case of CaOH. The hot band excitation also served for high resolution analysis of the $\tilde{X}(020)$ level for both CaOD and CaOH.

7.4 Resolved Fluorescence Spectra

Although selective detection provided much diagnostic information, the massive spectral overlap and intensity anomalies required numerous resolved LIF spectra to be recorded to establish definitive assignment of the vibronic species as well as the rotational quantum numbers and *e/f* parities. The experimental set up has been described in Section 3.3. The computer-controlled spectrometer/calibration system provided sufficient resolution ($\leq$ 0.13 A) and high accuracy ($\leq$ 0.035 cm^{-1}). This was crucial for revealing the true fluorescence structures and intensity patterns which were otherwise severely blended or distorted. As an example, Fig. 7.6 shows the resolved LIF spectrum obtained upon excitation of the coincident $Q_2(8\frac{1}{2})$ + $Q_2(32\frac{1}{2})$ transitions in the CaOH $\tilde{A}(020)\mu^2\Pi_{3/2}$ - $\tilde{X}(000)^2\Sigma^+$ subband. The LIF features related to the $\tilde{X}(100)$ level are nearly as strong as those to the $\tilde{X}(020)$ level, indicating a nearly equal mixing of the (100) and (020) characters in the upper level. Figures 7.7 and 7.8 show spectra following excitation of two rotational transitions, $Q_1(13\frac{1}{2})$ and $Q_1(27\frac{1}{2})$, of the CaOH $\tilde{A}(020)\mu^2\Pi_{1/2}$ - $\tilde{X}(000)^2\Sigma^+$ subband, respectively. The relative intensities of the LIF features related to the $\tilde{X}(100)$ level increases from Fig. 7.7 to Fig. 7.8, indicating that mixing of the (100) character in the nominal $(020)\mu^2\Pi_{1/2}$ level increases with increasing *J*. This is the expected consequence of increasing rotation, since the $(020)\mu^2\Pi_{1/2}$ level interacts with the nearby $(100)^2\Pi_{3/2}$ level through *J*-dependent matrix elements such as $\langle(020)\mu^2\Pi_{1/2}|H_{Fermi}|(100)^2\Pi_{1/2}\rangle$ ×

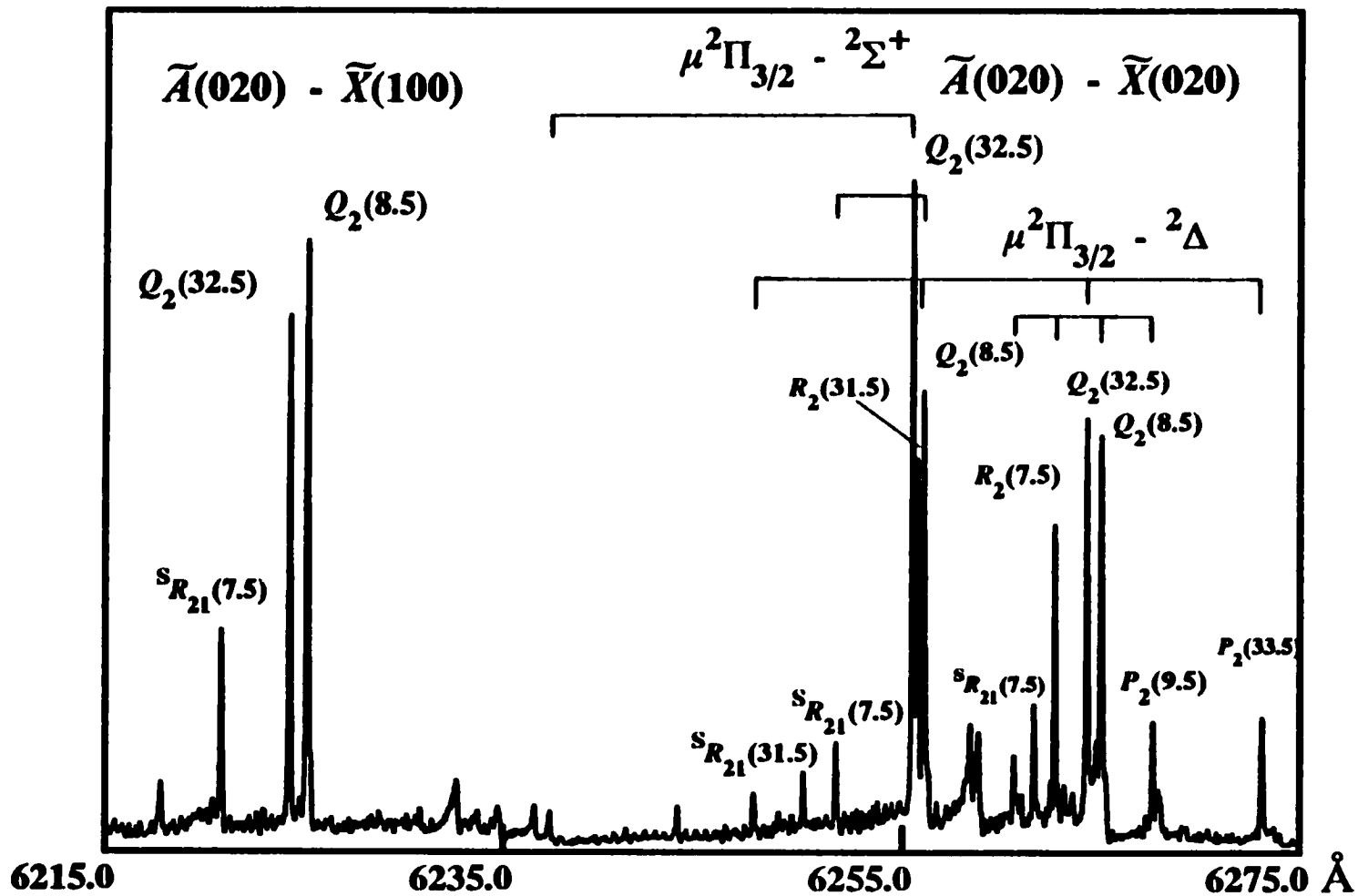

Fig. 7.6: Resolved LIF spectrum from excitation of the $\tilde{A}(020)\mu^2\Pi_{3/2}$ - $\tilde{X}(000)^2\Sigma^+$ $Q_2(8½)$ + $Q_2(32½)$ transitions of CaOH

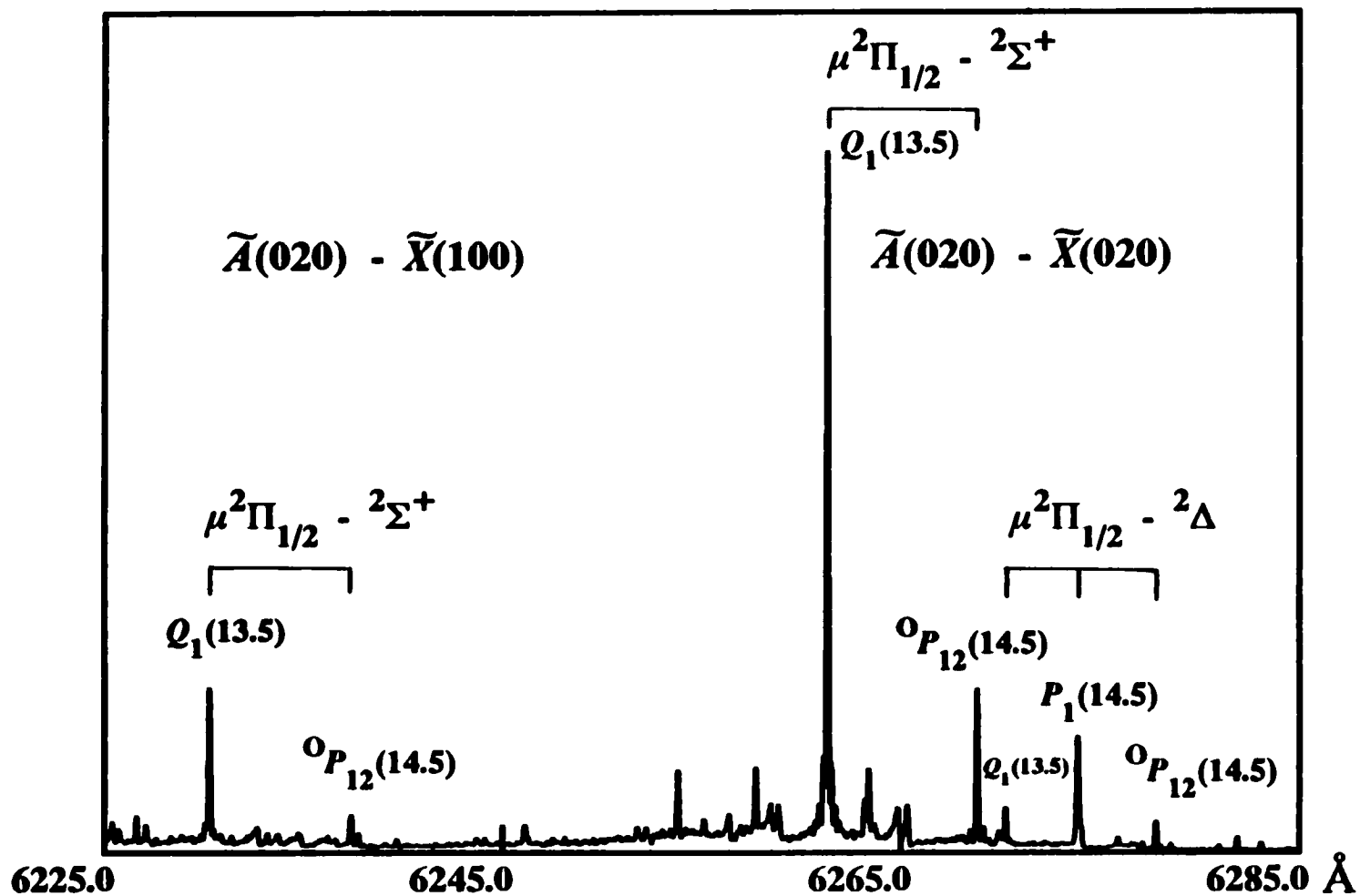

Fig. 7.7: Resolved LIF spectrum from excitation of the $\tilde{A}(020)\mu^2\Pi_{1/2}$ - $\tilde{X}(000)^2\Sigma^+$ $Q_1(13½)$ transition of CaOH

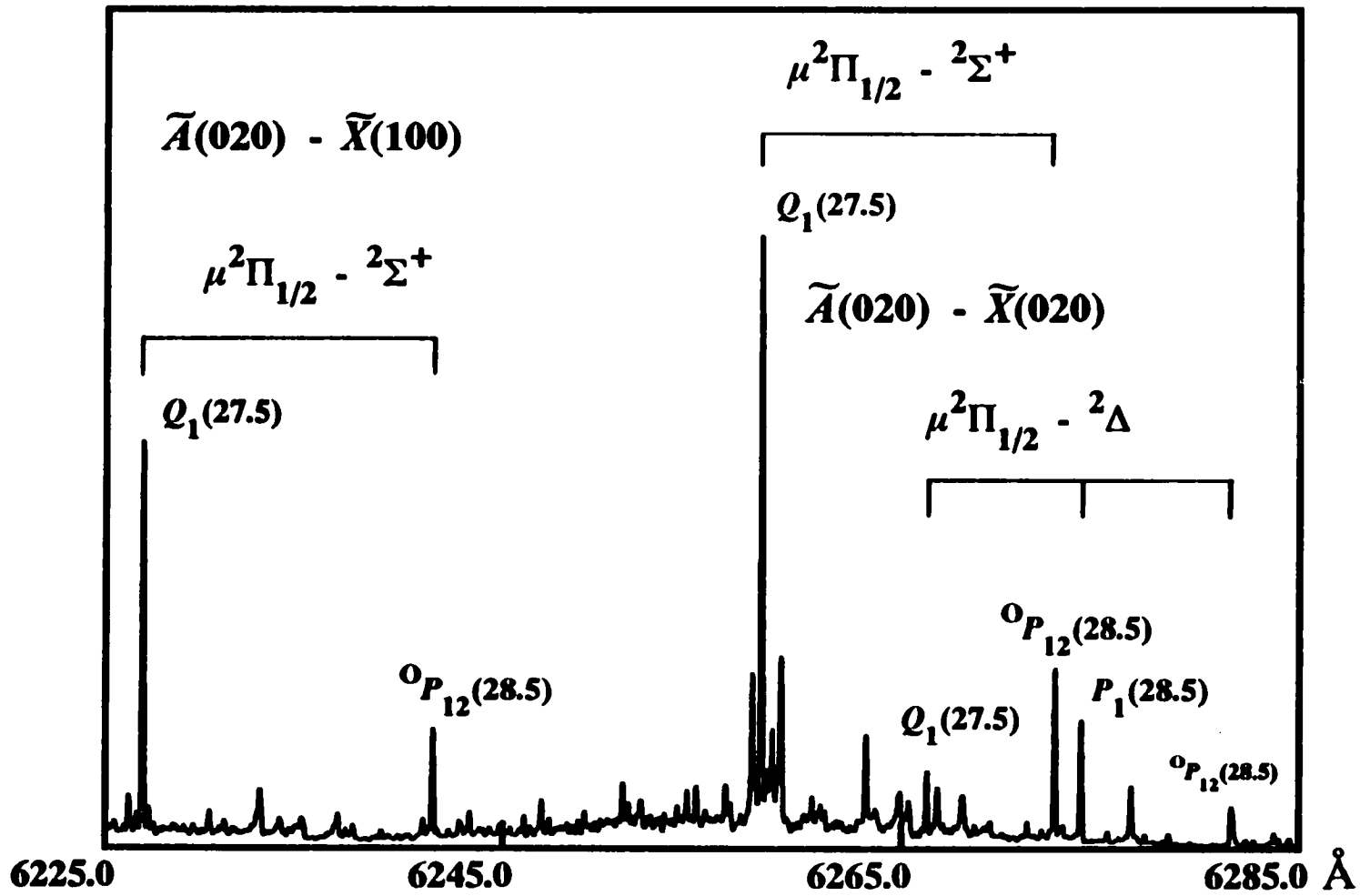

Fig. 7.8: Resolved LIF spectrum from excitation of the $\widetilde{A}(020)\mu^2\Pi_{1/2}$ - $\widetilde{X}(000)^2\Sigma^+$ $Q_1(27½)$ transition of CaOH

$\langle(100)^2\Pi_{1/2}|H_{rot}|(100)^2\Pi_{3/2}\rangle$. Anomalous relative intensities were observed in every resolved LIF spectrum. In Fig. 7.6 the intensity of the R_2 lines is ~3 times higher than that of the P_2 lines. In Figs. 7.7 and 7.8, the R_1 lines are too weak to observe while the P_1 lines are the strongest. These anomalous intensity patterns are the consequence of quantum mechanical interference which was also seen in the $\tilde{A}^2\Pi(010)$ - $\tilde{X}^2\Sigma^+(010)/(000)$ bands.

7.5 Effective Hamiltonian Matrix

It has proved impossible to fit the bands corresponding to the $\tilde{A}(100)$ and the $\tilde{A}(020)$ levels separately since they are linked by such a strong Fermi resonance interaction. It was desirable to carry out a global deperturbation employing a matrix which includes all six vibronic components and simultaneously takes account of the Renner-Teller, spin-orbit and Fermi resonance interactions. Woodward *et al.*[56] performed a matrix deperturbation of the interacting (100) and (020) $^2\Pi$ vibronic states involved in an electronic transition; this was based on a relatively complete and accurate data set for NCO molecule. An effective Hamiltonian matrix has been constructed in the present work for the CaOH/CaOD molecules, and is given in Table 7.1. The matrix of Ref. 56 was employed as a valuable reference. A brief description of the present matrix is given as follows.

A convenient case (a) basis set $|\Lambda\ \ell\ \Sigma,\ P\ J\ \pm\rangle$ has been chosen with the symmetrized form

$$|(100)^2\Pi_{3/2},\ J\ \pm\rangle = 2^{-1/2}\ \{|1\ 0\ \tfrac{1}{2},\ \tfrac{3}{2}\ J\rangle \pm |-1\ 0\ -\tfrac{1}{2},\ -\tfrac{3}{2}\ J\rangle\} \qquad (7.6)$$

$$|(100)^2\Pi_{1/2},\ J\ \pm\rangle = 2^{-1/2}\ \{|1\ 0\ -\tfrac{1}{2},\ \tfrac{1}{2}\ J\rangle \pm |-1\ 0\ \tfrac{1}{2},\ -\tfrac{1}{2}\ J\rangle\} \qquad (7.7)$$

$$|(020)\kappa^2\Pi_{3/2},\ J\ \pm\rangle = 2^{-1/2}\ \{|1\ 0\ \tfrac{1}{2},\ \tfrac{3}{2}\ J\rangle \pm |-1\ 0\ -\tfrac{1}{2},\ -\tfrac{3}{2}\ J\rangle\} \qquad (7.8)$$

$$|(020)\mu^2\Pi_{1/2},\ J\ \pm\rangle = 2^{-1/2}\ \{|1\ 0\ -\tfrac{1}{2},\ \tfrac{1}{2}\ J\rangle \pm |-1\ 0\ \tfrac{1}{2},\ -\tfrac{1}{2}\ J\rangle\} \qquad (7.9)$$

$$|(020)\mu^2\Pi_{3/2},\ J\ \pm\rangle = 2^{-1/2}\ \{|-1\ 2\ \tfrac{1}{2},\ \tfrac{3}{2}\ J\rangle \pm |1\ -2\ -\tfrac{1}{2},\ -\tfrac{3}{2}\ J\rangle\} \qquad (7.10)$$

TABLE 7.1: Effective Hamiltonian Matrix for the (100) and (020) $^2\Pi$ Vibronic States of CaOH/CaOD with $x = J + \frac{1}{2}$ and $z = x^2$

(100)		(020)			
$\|1\ 0\ \frac{1}{2}\rangle$	$\|1\ 0\ -\frac{1}{2}\rangle$	$\|1\ 0\ \frac{1}{2}\rangle$	$\|1\ 0\ -\frac{1}{2}\rangle$	$\|-1\ 2\ \frac{1}{2}\rangle$	$\|-1\ 2\ -\frac{1}{2}\rangle$
$T_1 - \frac{1}{4}\epsilon^2\omega_2 + g_K - \frac{1}{2}\gamma_1$ $+ \frac{1}{2}A_1(1 - \frac{1}{4}\epsilon^2)$ $+(B_1 + \frac{1}{2}A_{D1})(z-2)$ $-D_1(z^2-3z+3) - \frac{1}{2}\gamma_{D1}(2z-3)$	$-(z-1)^{\frac{1}{2}}\|B_1 - \frac{1}{2}\gamma_1$ $- 2D_1(z-1) - \frac{1}{2}\gamma_{D1}z$ $\mp \frac{1}{2}q_1 x\|$	$2W_1 - 2\epsilon W_2$	0	$2\sqrt{2}W_2 - \sqrt{2}\epsilon W_1$	0
	$T_1 - \frac{1}{4}\epsilon^2\omega_2 + g_K - \frac{1}{2}\gamma_1$ $- \frac{1}{2}A_1(1 - \frac{1}{4}\epsilon^2)$ $+(B_1 - \frac{1}{2}A_{D1})x - D_1(z^2+z-1)$ $\mp \frac{1}{2}(p_1+2q_1)x - \gamma_{D1}(z-\frac{1}{2})$	0	$2W_1 - 2\epsilon W_2$	0	$2\sqrt{2}W_2 - \sqrt{2}\epsilon W_1$
		$T_2 - \frac{1}{4}\epsilon^2\omega_2 + g_K - \frac{1}{2}\gamma_2$ $+ \frac{1}{2}A_2(1 - \frac{1}{4}\epsilon^2)$ $+(B_2^0 + \frac{1}{2}A_{D2})(z-2)$ $-D_2(z^2-3z+3) - \frac{1}{2}\gamma_{D2}(2z-3)$	$-(z-1)^{\frac{1}{2}}\|B_2^0 - \frac{1}{2}\gamma_2$ $- 2D_2(z-1) - \frac{1}{2}\gamma_{D2}z$ $\mp \frac{1}{2}q_2 x\|$	$\sqrt{2}\epsilon\omega_2 + \sqrt{2}\epsilon_D\omega_2(z-2)$	$\pm \frac{1}{2}q^v x(2z-2)^{\frac{1}{2}}$ $- \epsilon_D\omega_2(2z-2)^{\frac{1}{2}}$
			$T_2 - \frac{1}{4}\epsilon^2\omega_2 + g_K - \frac{1}{2}\gamma_2$ $- \frac{1}{2}A_2(1 - \frac{1}{4}\epsilon^2)$ $+(B_2^0 - \frac{1}{2}A_{D2})x - D_2(z^2+z-1)$ $\mp \frac{1}{2}(p_2+2q_2)x - \gamma_{D2}(z-\frac{1}{2})$	$\pm \frac{1}{2}q^v x(2z-2)^{\frac{1}{2}}$ $- \epsilon_D\omega_2(2z-2)^{\frac{1}{2}}$	$\sqrt{2}\,\epsilon\omega_2 + \sqrt{2}\,z\,\epsilon_D\omega_2$ $\mp \sqrt{2}\,x\,q^v$
				$T_2 - g_K + 4g_{22} - \frac{1}{2}\gamma_2$ $- \frac{1}{2}A_2(1 - \frac{1}{4}\epsilon^2)$ $+(B_2^2 - \frac{1}{2}A_{D2})(z-2)$ $-D_2(z^2-3z+3) - \frac{1}{2}\gamma_{D2}(2z-3)$	$-(z-1)^{\frac{1}{2}}\|B_2^2 - \frac{1}{2}\gamma_2$ $- 2D_2(z-1) - \frac{1}{2}\gamma_{D2}z\|$
					$T_2 - g_K + 4g_{22} - \frac{1}{2}\gamma_2$ $+ \frac{1}{2}A_2(1 - \frac{1}{4}\epsilon^2)$ $+(B_2^2 + \frac{1}{2}A_{D2})x - D_2(z^2+z-1)$ $- \gamma_{D2}(z - \frac{1}{2})$

The basis functions are defined as $|J\ P\ \pm\rangle = 2^{-\frac{1}{2}}\{|\Lambda\ \ell\ \Sigma, J\ P\rangle \pm |-\Lambda\ -\ell\ -\Sigma, J\ -P\rangle\}$. The upper and lower signs refer to *e* and *f* levels, respectively. The subscripts 1 and 2 denote the (100) and (020) vibrational levels, respectively.

$$|(020)\kappa^2\Pi_{1/2}, J \pm\rangle = 2^{-1/2}\{|-1\ 2\ -\tfrac{1}{2}, \tfrac{1}{2}\ J\rangle \pm |1\ -2\ \tfrac{1}{2}, -\tfrac{1}{2}\ J\rangle\} \qquad (7.11)$$

where the upper and lower signs refer to *e* and *f* levels, respectively. The matrix is thus factorized into two 6 × 6 blocks. The subscripts 1 and 2 refer to the (100) and (020) vibrational levels, respectively. T_1 and T_2 are electronic-vibrational term values, and A_1, A_2, B_1, B_2 ... are conventional molecular constants.

In Ref. 56, the matrix was constructed in a case (a) basis, but a rotational operator N (=J-S-G) was used for evaluation of the relevant matrix elements. In order to obtain results that are consistent with our preceding results for the $\tilde{A}$ (000) and (010) vibrational levels, the rotational operator R (= J-L-S-G), instead of N, has been used in the present work. Section 6.4 of this thesis has given a quite comprehensive effective Hamiltonian for a linear triatomic $^2\Pi$ electronic state. All the matrix elements in Table 7.1, except those for the Fermi resonance and g_{22} terms, have been derived using this Hamiltonian.

An ℓ-type doubling matrix element, $\mp 2^{1/2} q^v x$, between the $(020)\kappa^2\Pi_{1/2}$ and $\mu^2\Pi_{1/2}$ vibronic components has been derived according to Eq. 6.18 in Section 6.4 and added into the matrix of the present work. This element was missing in the matrix of Ref. 56.

The $g_{22}\ell^2$ terms have been chosen in this work to replace the g_4 terms used in Ref. 56 to take into account the anharmonic effect on the vibrational energies. This approach was based on a description of the anharmonic corrections by Hougen and Jesson[44], which was considered to be suitable for the present situation. The advantage of using the g_{22} terms for the $\tilde{A}(020)$ state is that the fitted value of g_{22} can be compared with the corresponding value for the $\tilde{X}$ (020) state and can be used directly to estimate the harmonic bending frequency.

The matrix elements for the Fermi resonance are the same as those used in Ref. 56. They were derived according to Hougen's paper[43].

In comparison with the data of Ref. 56, the present data set for CaOH or CaOD contains more than twice as many lines, and the measurement accuracy of 0.0035 cm^{-1} is approximately 50 times better. Consequently, a few high order parameters, A_D, γ_D and $\epsilon_D\omega_2$, that were not needed in Ref. 56, have been introduced into the present matrix.

The rotational energies in excited bending vibrational levels of electronic $^2\Sigma$ and $^3\Sigma$ states have been studied in detail by Merer and Allegretti[83]. The matrix for $v_2=2$ in a $^2\Sigma$ electronic state in the case (b) representation given in Table 3 of Ref. 83 was used for the CaOH/CaOD $\tilde{X}(020)$ state. A typographic error in the matrix for the $(02^00)^2\Sigma$ level of Ref. 83 has been corrected. For clarification, the matrix used in this work is given in Table 7.2. The expressions for the $\tilde{X}(000)^2\Sigma^+$ level are the same as Eqs. 6.21 and 6.22 in Section 6.4.

The dependence of the rotational constant B_v on bending vibrational quantum numbers v_2 and ℓ in a non-degenerate electronic state can be expressed, according to Lide and Matsumura[87], by

$$B_v = \bar{B}_e - \alpha_2(v_2+1) + \gamma_{22}(v_2+1)^2 + \gamma_{ll}\ell^2 \qquad (7.12)$$

where $\bar{B}_e = B_e - \alpha_1(v_1+½) - \alpha_3(v_3+½)$. It was indeed found in the least squares fits for both isotopomers that different B_v's must be used for the two components with $\ell=0$ and 2 of the $\tilde{X}(020)$ level. They were then labeled as B_Σ and B_Δ, respectively, in the matrix of Table 7.2. In the $\tilde{A}^2\Pi(020)$ level, the basis states with $\ell=0$ and 2 would accordingly have different B_v's which are labeled as B_2^0 and B_2^2 in the matrix of Table 7.1. In the $^2\Pi$ electronic state, a new vibration-rotation correction to B-values, for vibronic components of different ΛK and the same v_2 values, has been introduced by Brown[88]. The

TABLE 7.2: Matrix Representation for $v_2=2$ in a $^2\Sigma^+$ Electronic State

$\|^2\Delta\ (F_2)\rangle$	$\|^2\Delta\ (F_1)\rangle$	$\|^2\Sigma^+\rangle$
$T_v + 4\ g_{22}$		
$+ [B_\Delta - \frac{1}{2}\gamma\frac{1}{x}][x\ (J+\frac{3}{2}) - 4]$	$\gamma\ [(J-\frac{3}{2})\ (J+\frac{5}{2})]^{1/2}\ \frac{1}{x}$	$- q^v\ [x\ (J-\frac{1}{2})(J+\frac{3}{2})(J+\frac{5}{2})]^{1/2}$ [a]
$- D_\Delta\ [x\ (J+\frac{3}{2}) - 4]^2$		
	$T_v + 4\ g_{22}$	
	$+ [B_\Delta + \frac{1}{2}\gamma\frac{1}{x}][x\ (J-\frac{1}{2}) - 4]$	$q^v\ [x\ (J-\frac{3}{2})(J-\frac{1}{2})(J+\frac{3}{2})]^{1/2}$ [b]
	$- D_\Delta\ [x\ (J-\frac{1}{2}) - 4]^2$	
		$T_v + B_\Sigma\ x\ (J + \frac{1}{2} \mp 1)$
		$\pm \frac{1}{2}\gamma\ (J + \frac{1}{2} \mp 1)$
		$- D_\Sigma\ x^2\ (J + \frac{1}{2} \mp 1)^2$

$x = J + \frac{1}{2}$; the upper/lower signs refer to e/f levels.

[a] only for *f*-levels.

[b] only for *e*-levels.

dominant origin of this correction arises in third order perturbation theory, involving Renner-Teller, Fermi resonance and rotational operators. Brown has given the form for this correction

$$\beta_{B,12}\,(v_1+\tfrac{1}{2})(v_2+1)(\Lambda K+1) + \beta_{B,32}\,(v_3+\tfrac{1}{2})(v_2+1)(\Lambda K+1) \qquad (7.13)$$

where $\beta_{B,12}$ and $\beta_{B,32}$ are perturbation parameters. Referring to the basis functions defined in Eqs. 7.6 - 7.11, the ΛK-values are: $\Lambda K=1$ for $\ell=0$ and $\Lambda K=-1$ for $\ell=\pm 2$. The values of B_2^0 and B_2^2 will thus depend on the combined effects expressed in Eqs. 7.12 and 7.3.

7.6 Least Squares Fit and Results

A weighted, non-linear least squares fitting procedure employing the Hamiltonian matrix of Table 7.1 was used to fit a complete data set including all the observed subbands for each isotopomer. The molecular constants and perturbation parameters for the $\tilde{A}(100)/(020)$ and $\tilde{X}(020)$ levels were allowed to vary simultaneously. The constants for the $\tilde{X}(000)$ level had been determined accurately by Ziurys *et al.*[16] for CaOH and by the present work (Chapter 4) for CaOD, and were held fixed in the fits. The numbers of the fitted rotational lines in respective subbands are given in Figs. 7.1 and 7.2. The total numbers of the rotational lines included in the fits are 676 for CaOH and 635 for CaOD. The variances of the fits are $\hat{\sigma}^2=(1.199)^2$ and $\hat{\sigma}^2=(1.228)^2$ for CaOH and CaOD, respectively. The average measurement uncertainty for most rotational lines was estimated to be 0.0035 cm^{-1}, which was used for assigning the weight ($w = 0.0035^{-2}$) to rotational lines in the fit. It appears that the model used here has reproduced the observed quantities quite satisfactorily. Tables 14 through 25 in the Appendix list the wavenumbers and assignments of all rotational lines investigated in this work for the two isotopomers; the residuals between the observed and calculated values are also given in the

tables. It is to be noticed that the two upper (020) vibronic components form an inverted $^2\Pi$ state and, therefore, the F_1/F_2 assignment is the opposite to that for the lower components. The molecular constants and perturbation parameters determined in the fits for both CaOH and CaOD are summarized in Table 7.3.

Investigation of the $\tilde{A}(020)\kappa^2\Pi_{1/2}$ vibronic component relied mainly on the hot band excitation from the $\tilde{X}(020)^2\Delta$ level for both isotopomers, as mentioned before. The branch structure of this subband is referred to the schematic diagram in Fig. 5.2. The $\kappa^2\Pi_{1/2}$ level was assigned as the F_2 component since the effective spin-orbit parameter is negative, and its rotational structure conforms closely to Hund's case (b). This subband was difficult to measure and analyze owing to its weakness (low population in the lower state) and the unresolved spin-rotation splittings in the lower state combined with the *K*-type splittings in the upper state. Although this is a case (b) - case (b) transition, relative intensities between the main and satellite branches change in a complicated fashion due to the quantum mechanical interference. Consequently, the data for this subband were deweighted in the fits ($w = 0.01^{-2}$). For CaOD, there was an additional difficulty in the fit caused by the near degeneracy of $\tilde{A}(100)^2\Pi_{1/2}$ and $\tilde{A}(020)\kappa^2\Pi_{3/2}$. The strong *J*-dependent interaction between the two components has not been satisfactorily modeled by the present effective Hamiltonian. As a consequence, the data for the nominal $\tilde{A}(020)\kappa^2\Pi_{3/2}$ - $\tilde{X}(000)^2\Sigma^+$ subband included in the fit has been restricted to $J' \leq 34½$ to avoid large residuals and contamination of molecular constants.

The parameters γ and q^v in the $\tilde{X}(020)$ state could not be reliably determined and were, hence, restricted at the values for the $\tilde{X}(010)$ level. This is because the spin-rotation splittings in the $\tilde{X}(020)^2\Delta$ and $^2\Sigma^+$ levels

TABLE 7.3: Molecular Constants[a] of the (100) and (020) Levels in the $\tilde{A}^2\Pi$ and $\tilde{X}^2\Sigma^+$ States of CaOH and CaOD

	CaOH		CaOD	
	$\tilde{A}(100)$	$\tilde{A}(020)$	$\tilde{A}(100)$	$\tilde{A}(020)$
T_{ev}	16626.917(1)	16700.172(2)	16614.006(2)	16528.909(3)
A_v	67.159(3)	[67.0951]	67.044(4)	[66.9474]
W_1	10.3250(5)		5.2679(22)	
$\epsilon\omega_2$		-36.5624(7)		-27.1599(13)
g_K		[0.5937]		[0.4462]
g_{22}		7.1939(10)		4.0620(6)
B_v	0.3389047(41)	0.3395830(48) B_2^0	0.3070604(28)	0.3093921(79) B_2^0
		0.3392718(68) B_2^2		0.3089058(113) B_2^2
D_v	0.3780(17) $\times 10^{-6}$	0.4186(17) $\times 10^{-6}$	0.2529(34) $\times 10^{-6}$	0.3175(23) $\times 10^{-6}$
p^e	-0.04405(7)	-0.04547(9)	-0.03926(10)	-0.04155(9)
q^e	-0.4178(58)$\times 10^{-3}$	-0.5423(38) $\times 10^{-3}$	-0.3226(26)$\times 10^{-3}$	-0.6066(74) $\times 10^{-3}$
q^v		-0.7356(9) $\times 10^{-3}$		-0.7593(24) $\times 10^{-3}$
γ_v	[0.0304]	[0.02617]	[0.0276]	[0.02475]
A_{Dv}	0.368(7) $\times 10^{-3}$	-1.38(2) $\times 10^{-3}$	0.193(8) $\times 10^{-3}$	0.477(55) $\times 10^{-3}$
γ_D	-0.513(40) $\times 10^{-5}$	1.098(15) $\times 10^{-5}$	1.197(92) $\times 10^{-5}$	-0.200(38) $\times 10^{-5}$
$\epsilon_D\omega_2$		-0.172(4) $\times 10^{-3}$		0.267(17) $\times 10^{-3}$
	$\tilde{X}(100)$	$\tilde{X}(020)$	$\tilde{X}(100)$	$\tilde{X}(020)$
T_{ev}	609.015(10)	688.670(1)	604.903(7)	519.192(1)
g_{22}		6.0869(12)		4.3027(10)
B_v	0.33219(3)	0.333047(4) ($^2\Sigma$)	0.30102(2)	0.303397(4) ($^2\Sigma$)
		0.332562(11) ($^2\Delta$)		0.303116(15) ($^2\Delta$)
D_v	[0.3869 $\times 10^{-6}$]	0.415(2)$\times 10^{-6}$($^2\Sigma$)	0.283(10) $\times 10^{-6}$	0.333(3) $\times 10^{-6}$($^2\Sigma$)
		0.466(6)$\times 10^{-6}$($^2\Delta$)		0.267(13)$\times 10^{-6}$($^2\Delta$)
γ_v	[0.00111]	[0.001184]	[0.00111]	[0.001124]
q^v		[-0.7181 $\times 10^{-3}$]		[-0.7621 $\times 10^{-3}$]

[a]All values are in cm^{-1}; values in parentheses are 1σ standard deviations in units of the last significant digit of the corresponding constant. W_2=0 was fixed.

are very small and the ℓ-type doubling in the $\tilde{X}(020)^2\Delta$ state is negligible; unfortunately, the corresponding subbands are also too weak to permit a sub-Doppler investigation. Nevertheless, the main parameters for the $\tilde{X}(020)$ state, T_{ev}, B_v, D_v and g_{22}, have been well determined for both isotopomers. The estimations of γ and q^v should be quite reasonable, with any errors having negligible effect on the fits.

7.7 Discussion and Further Results

As seen from the matrix in Table 7.1, the parameter g_K is highly correlated with g_{22}. Since g_K had been accurately determined for both CaOH and CaOD from investigations of the $\tilde{A}(010)$ state, its value was held fixed while g_{22} was allowed to vary. The fitted values of g_{22} for both CaOH and CaOD in the $\tilde{A}$ state are consistent with those in the $\tilde{X}$ state, as shown in Table 7.3. However, small differences have been noticed. The g_{22}-value for the CaOH $\tilde{A}$ state is larger by 15% than that in the $\tilde{X}$ state while, for CaOD, the $\tilde{A}$ state g_{22}-value is slightly smaller than the $\tilde{X}$ state g_{22}. This situation merits further discussion. In the $\tilde{X}$ state, the Fermi interaction between the (100) and (020) levels was not taken into account in the matrix deperturbation of the observed bands. For CaOH, the (100) level is lower than the (02^00) level by ~80 cm^{-1} while the (02^20) level is higher than (02^00) by 24.3 cm^{-1}. The Fermi resonance operator only connects the (100) and (02^00) levels (selection rule $\Delta\ell=0$). The effect of this interaction on vibrational energies is certainly not negligible. However, since the unperturbed energies of the $\tilde{X}(100)$ and (020) levels could not be predicted accurately owing to lack of zero-order vibrational information, it was impossible to treat this interaction rigorously in a matrix approach. Nevertheless, if the Fermi resonance parameter W is assumed to have the same value as that in the $\tilde{A}$

state, this could be a good approximation since the two electronic states have quite similar potentials, the interaction can be treated by solving a simple secular equation

$$\begin{vmatrix} G^0(100) - G & 2W \\ 2W & G^0(02^00) - G \end{vmatrix} = 0 . \qquad (7.14)$$

Here $G^0(100)$ and $G^0(02^00)$ are the unperturbed energies and G is the perturbed energy which has two known values; $2W$ is the perturbation matrix element originating from the Fermi resonance. Employing the unperturbed energies obtained from the above calculation, the unperturbed g_{22}-value is determined as g_{22}=7.53 cm^{-1}, which is now closer to the $\tilde{A}$ state g_{22}-value. In the CaOD $\tilde{X}$ state, the (100) level is higher than the (02^00) level by ~86 cm^{-1}. Using the same approach, the unperturbed g_{22}-value is determined as g_{22}=3.97 cm^{-1}, which is, again, closer to the $\tilde{A}$ state g_{22}-value.

More important results obtained from the above treatment of the Fermi interactions in the $\tilde{X}$ state are, of course, the unperturbed vibrational term values: $G^0(100)$=614.79, $G^0(02^00)$=682.90 cm^{-1} for CaOH, and $G^0(100)$=603.59, $G^0(02^00)$=520.51 cm^{-1} for CaOD. These deperturbed vibrational term values and g_{22}-values of the $\tilde{X}$ state are believed to be more reliable than the perturbed values listed in Table 7.3 and will be used for further calculations in this work. Of course, the above corrections do not imply any change in the quality of the matrix deperturbation of the observed bands described earlier because the $\tilde{X}(100)$~(020) Fermi resonance is an isolated interaction. Besides, this interaction is J- and parity-independent and, hence, will not affect the values of B_v, D_v and γ_v.

As for the treatment of the $\tilde{A}(010)$ state, the Renner-Teller parameter ϵ was held fixed, ϵ(CaOH)=-0.1 and ϵ(CaOD)=-0.098, and $\epsilon\omega_2$ was allowed to vary here for the $\tilde{A}(020)$ state. The spin-orbit constant A_2 is closely correlated

with $\epsilon\omega_2$, and was constrained at the values for the $\tilde{A}(010)$ state listed in Table 6.2. The values of $\epsilon\omega_2$ were determined for both isotopomers by the least squares fits. There is a small increase in magnitude for $\epsilon\omega_2$ as v_2 increases from v_2=1 to v_2=2; Δ = -0.2990(9) and -0.1998(15) cm^{-1} for CaOH and CaOD, respectively. These small increases may be understood as a vibrational dependence of the Renner-Teller effect. Brown and Jorgensen[46,48] introduced a $\hat{g}_4$ term to account for such dependence. This term originates from the anharmonic quartic potential and has the form of $\hat{g}_4 q_2^4 \sigma_z$, in which q_2 and σ_z have been described in Section 6.4. Its matrix elements can be evaluated, according to Ref. 48, using

$$\langle q_2^4 \sigma_z \rangle_{v_2,v_2} = \frac{3}{2} (v_2+1) [(v_2+1)^2 - K^2]^{1/2} . \qquad (7.15)$$

Considering this vibrational dependence, the Renner-Teller parameter $\epsilon\omega_2$ used in the matrices of Table 6.1 and Table 7.1 may be written as $\epsilon\omega_2+6\hat{g}_4$ for $\tilde{A}(010)$ and $\epsilon\omega_2+9\hat{g}_4$ for $\tilde{A}(020)$. Thus, the parameter $\hat{g}_4$ can be directly calculated from the difference between the fitted $\epsilon\omega_2$-values for $\tilde{A}(010)$ and $\tilde{A}(020)$, and its calculated value is $\hat{g}_4$ = -0.0997(3) and -0.0666(5) cm^{-1} for CaOH and CaOD, respectively. These $\hat{g}_4$-values appear quite sensible in that the anharmonicity of the bending vibration in CaOH is markedly larger than that in CaOD. Jarman and Bernath[17] obtained $\hat{g}_4$ = -0.03862(9) cm^{-1} for the CaOD $\tilde{C}^2\Delta$ electronic state, which is comparable with the present result. With $\hat{g}_4$ now known from the preceding discussion, it is possible to obtain the "harmonic" Renner-Teller parameter $\epsilon\omega_2$, excluding the anharmonic $\hat{g}_4$-contributions; estimates of $\epsilon\omega_2$ = -35.6652(19) cm^{-1} for CaOH and $\epsilon\omega_2$ = -26.5605(31) cm^{-1} for CaOD are obtained. Of course, the fitted $\epsilon\omega_2$-value is affected by the assumed value of the spin-orbit constant A_2. Test fits have shown that when the A_2-value was changed by an amount extrapolated from the A-values of $\tilde{A}(000)$ and (010) levels the change of the

fitted $\epsilon\omega_2$-value for $\tilde{A}(020)$ was smaller than Δ=-0.2990 cm^{-1} by a factor of ~20 in the case of CaOH. For CaOD, such change was even smaller. Hence, it can be concluded that the above calculated values for the $\hat{g}_4$ and the "harmonic" $\epsilon\omega_2$ are quite reliable.

The fundamental frequency of the Ca-O stretching vibration in the $\tilde{A}^2\Pi$ state can now be calculated from the (000) and (100) term values: ν_1 = 628.4821(15) cm^{-1} for CaOH and ν_1 = 618.7757(23) cm^{-1} for CaOD. Here, the $\tilde{A}(000)$ term value has been corrected by $-\frac{1}{4}\epsilon^2\omega_2 + g_K$.

Based on the term values of the v_2=0, 1 and 2 levels, and the expression for the vibrational term values referred to the (000) level[62]

$$G_0(v_1\ v_2\ v_3) = \sum_i \omega_i^0 v_i + \sum_i \sum_{k\geq i} x_{ik}^0 v_i v_k + \sum_i \sum_{k\geq i} g_{ik}\ell_i\ell_k + \ldots \qquad (7.16)$$

and the approximation of

$$\omega_2 \approx \omega_2^0 - 2\,x_{22}^0\,, \qquad (7.17)$$

the harmonic frequency of the $\tilde{A}$ state bending vibration may be estimated as ω_2 = 366.435 cm^{-1} and 278.325 cm^{-1} for CaOH and CaOD, respectively. Using these ω_2-values and the "harmonic" $\epsilon\omega_2$-values, the "harmonic" Renner parameters ϵ may be calculated, yielding ϵ = -0.0973 for CaOH and ϵ = -0.0954 for CaOD.

By means of the same approach as above, the harmonic bending frequency in the $\tilde{X}$ state was estimated as ω_2 = 357.23 cm^{-1} and 270.71 cm^{-1} for CaOH and CaOD, respectively. Here, the corrected $\tilde{X}$ state (020) term values and g_{22}-values, calculated in the preceding paragraph, have been used. The harmonic frequency of the Ca-O stretch vibration in the $\tilde{X}$ state is difficult to estimate although the excited levels up to v_1=4 for CaOH and v_1=3 for CaOD have been observed via dispersed LIF. This is due to the existence of the Fermi resonance. The deperturbed term values of the (100) level have been estimated in the preceding paragraph. However, when the quantum number v_1

increases further, more levels are involved into the Fermi polyads: (200)~(120)~(040), (300)~(220)~(140)~(060), *etc.* These interactions will significantly affect the level positions and can not be estimated easily. Therefore, the term values $G^0(100)$ calculated in the preceding paragraph are considered the best approximation for the harmonic frequency ω_1 for CaOH and CaOD.

The preceding calculations have also yielded the values of ω_2^0 and x_{22}^0 for both the $\tilde{A}$ and $\tilde{X}$ states of the two isotopomers; all the calculated quantities in this section are summarized in Table 7.4.

The magnitude of the Fermi resonance parameter W_1 has been well determined for both CaOH and CaOD, although the sign of W_1 was not determinable. The second parameter, W_2, could not be determined by the fit for either isotopomer, and was given a value of zero. This is understood in terms of the moderate size of the Renner-Teller parameter in the CaOH/CaOD $\tilde{A}^2\Pi$ state; W_2 becomes significant only when the Renner-Teller effect is very strong. Even in the $\tilde{X}^2\Pi$ states of NCO[56] and BO_2[86] where the vibronic couplings are relatively strong, $\epsilon\omega_2$=-75.91 and -85.7 cm^{-1}, respectively, W_2 was still not determined. The essentially zero value of W_2 indicates that $(k'_{122}-k''_{122})$ is close to zero, according to Eq. 7.5. Thus, W_1 may be expressed by

$$W_1 = k_{122}\,(\hbar/4\pi c\omega_2)\,(\hbar/4\pi c\omega_1)^{1/2}\,. \qquad (7.18)$$

Employing the $\tilde{A}$ state ω_2-value obtained above and assuming $\omega_1 \approx \nu_1$, the anharmonic force constant k_{122} may be obtained: $k_{122}=2.027\times10^{75}$ for CaOH and $k_{122}=0.7795\times10^{75}$ for CaOD; these constants are the coefficients in the normal coordinate expansion of the potential energy function, and they have the unit of $(k_g\ k_g^{1/2}\ m^4)^{-1}$. More commonly, the Fermi resonance parameter provides a direct measure of the anharmonic force constant ϕ_{122} in the dimensionless

TABLE 7.4(a): Molecular Parameters[a] for CaOH/CaOD in the $\tilde{A}^2\Pi$ State

	CaOH	CaOD
ν_1	628.4821(15)	618.7757(23)
ω_2^0	358.652(3)	272.582(3)
x_{22}^0	-3.892(3)	-2.871(3)
$\epsilon\omega_2$	-35.6652(19)	-26.5605(31)
ϵ	-0.0973	-0.0954
$\hat{g}_4$	-0.0997(3)	-0.0666(5)
k_{122}	2.027×10^{75}	0.779×10^{75}
ϕ_{122}	29.2035(14)	14.8999(62)
α_2	0.001167(9)	0.000005(13)
γ_{22}	0.000087(5)	0.000046(6)
γ_{ll}	-0.000078(4)	-0.000122(5)

TABLE 7.4(b): Molecular Parameters[a] for CaOH/CaOD in the $\tilde{X}^2\Sigma^+$ State

	CaOH	CaOD
ν_1	614.79	603.59
G_{020}^0	682.90	520.51
ω_2^0	349.34	265.49
x_{22}^0	-3.95	-2.61
g_{22}	7.53	3.97
α_2	0.001089(6)	-0.000008(12)
γ_{22}	0.000111(3)	0.000049(5)
γ_{ll}	-0.000121(3)	-0.000070(4)

[a]All parameters are in unit of cm^{-1} except that ϵ is dimensionless and k_{122} is in unit of $(Kg^{3/2}m^4)^{-1}$. $\epsilon\omega_2$ and ϵ are the "harmonic" Renner-Teller parameters.

normal coordinate space,

$$W_1 = 8^{-1/2}\, \phi_{122} \,. \tag{7.19}$$

Eq. 7.19 yields values of ϕ_{122} as 29.2035(14) and 14.8999(62) cm^{-1} for CaOH and CaOD, respectively.

As well known, the vibration-rotation interaction constant α_2 also contains information on the cubic anharmonic force constants like ϕ_{n22}. The relation has been formulated by Nielsen[84] as

$$\alpha_2 = \frac{B_e^2}{\omega_2}\left\{1 + 4\sum_{n=1,3}\frac{\zeta_{2n}^2\,\omega_2^2}{\omega_n^2 - \omega_2^2}\right\} - (2B_e)^{3/2}\left\{\frac{\zeta_{23}\phi_{122}}{\omega_1^{3/2}} + \frac{\zeta_{21}\phi_{322}}{\omega_3^{3/2}}\right\} \tag{7.20}$$

where ζ_{2n} are the Coriolis coupling constants. A calculation of ϕ_{122} from the experimental α_2-values may carried out as follows. The first term on the right hand side of Eq. 7.20 is exactly equal to half of the absolute value of the ℓ-type doubling constant q^v. The values of q^v in the CaOH/CaOD $\tilde{A}$ state have been determined from investigations of the (010) and (020) levels. The q^v-values obtained from the (010) level will be used here since the (010) vibronic manifold is simpler than the (100)/(020) manifold and was slightly better analyzed. In the second term on the right hand side of Eq. 7.20, $\zeta_{21}/\omega_3^{3/2}$ is smaller than $\zeta_{23}/\omega_1^{3/2}$ by a factor of 89 for CaOH and 44 for CaOD (the values of ω_n, ζ_{2n} and B_e are given in Table 8.1 in the next chapter). Hence, the ϕ_{322} term is expected to be much smaller than the ϕ_{122} term and may be neglected at present. Employing the α_2-values obtained in the next paragraph, the following estimates are obtained: ϕ_{122} = -22.9 cm^{-1} for CaOH and ϕ_{122} = 12.0 cm^{-1} for CaOD. The magnitudes of ϕ_{122} evaluated from α_2 are in reasonably good agreement with those evaluated from W_1. The former are somewhat smaller than the latter. This is most likely caused by neglect of the ϕ_{322} term; the constant ϕ_{322} may be considerably larger than ϕ_{122} and have

an opposite sign. The calculations using α_2-values have also given the signs for ϕ_{122}, which are not available from W_1. In the next chapter the corresponding force constants f_{122} and f_{322} in the curvilinear internal coordinate expansion of the potential function will be calculated from the α_2-values. Since f_{122} and f_{322} are isotopically invariant, both constants can be evaluated employing α_2-values of the two isotopic molecules. A non-linear transformation would produce values for ϕ_{122} and ϕ_{322} from both harmonic constants (f_{11}, f_{22}, f_{33}, f_{13}) and anharmonic constants (f_{122} and f_{322}); the harmonic force field in the curvilinear coordinates gives contributions to the anharmonic force constants in the normal coordinates, as will be described later in next chapter. This would give a better verification of the results obtained from the Fermi resonance and, particularly, give an explanation for the large difference between the W_1-values in CaOH and in CaOD.

The parameters that govern the dependence of the rotational constant B_v on the bending vibrational quantum numbers v_2 and ℓ can now be calculated using the fitted B_v-values for the v_2 = 0, 1 and 2 levels and Eq. 7.12. For the $\tilde{X}^2\Sigma^+$ electronic state the calculations are straightforward, resulting in α_2=0.001089(6), γ_{22}=0.000111(3) and γ_{ll}=-0.000121(3) cm^{-1} for CaOH, and α_2=-0.000008(12), γ_{22}=0.000049(5) and γ_{ll}=-0.000070(4) cm^{-1} for CaOD. It is immediately seen that the parameter α_2 in CaOD is essentially zero while γ_{22} and γ_{ll} for CaOD are relatively large, being about half of those for CaOH. It is obvious that the parameter α_2 is much more sensitive to isotopic substitution than the other two parameters, γ_{22} and γ_{ll}. This behavior is strikingly similar to that occurring in the alkali metal hydroxides[87]. More detailed discussion on these parameters will be given in Chapter 8. For the $\tilde{A}$ state, the situation becomes more complicated owing to the effect of the possible new vibration-rotation correction to the $B(020)$-values described by

Eq. 7.13. However, a careful examination of Eq. 7.13 and the basis functions defined in Eqs. 7.8 - 7.11 revealed that the new vibration-rotation correction only affects the value of B_2^0 and has no effect on B_2^2 because of $\Lambda K+1=0$ for $\ell=\pm 2$. Therefore, B_2^2 can still be expressed solely by Eq. 7.12. The magnitude of B_2^0 relative to B_2^2 in the $\tilde{A}$ state still follows the pattern seen in the $\tilde{X}$ state so that the new correction may only have a minor effect on B_2^0; this effect might have significant impact on γ_{ll} but should have minimal impact on α_2 and γ_{22}. Since only α_2 and γ_{22}, not γ_{ll}, will be involved in the calculations of B_e it was decided to ignore the new correction terms of Eq. 7.13 in the expression for B_2^0. For the $\tilde{A}(010)$ state, the mean of the B-values for $^2\Delta$ and $^2\Sigma$ vibronic components was used. The results for the $\tilde{A}$ state are as follows: α_2=0.001167(9), γ_{22}=0.000087(5) and γ_{ll}=-0.000078(4) cm^{-1} for CaOH; α_2=0.000005(13), γ_{22}=0.000046(6) and γ_{ll}=-0.000122(5) cm^{-1} for CaOD. The uncertainties of γ_{ll} may actually be larger than given in the parentheses. As in the $\tilde{X}$ state, α_2 is essentially zero for CaOD in the $\tilde{A}$ state. These results are summarized in Table 7.4.

The K-type doublings in the $\tilde{A}(100)/(020)$ $^2\Pi$ manifold become more complicated due to the existence of the Fermi resonance. The present model has reproduced them, in general, very satisfactorily for both isotopomers. The fitted values of p^e, q^e and q^v are quite consistent with those in the $\tilde{A}(000)$ and (010) levels, except that the q^e-values for the $\tilde{A}(020)$ level are noticeably larger than might be expected. It is difficult at present to pinpoint the main source for this deviation which occurs in both isotopomers. As pointed out in Section 6.4, the definition of the ℓ-type doubling operator in the present work removes the v_2 dependence from the constant q^v. Indeed, the q^v-value obtained from the $\tilde{A}(020)$ level is in very good agreement with that from the $\tilde{A}(010)$ level for both CaOH and CaOD.

Figs. 7.9 and 7.10 illustrate the K-type doublings, defined as $\Delta\tilde{\nu} = \tilde{\nu}_e - \tilde{\nu}_f$, in the six vibronic components for CaOH and CaOD, respectively. For CaOD, the K-type doublings are not severely affected by the Fermi resonance although the $(100)^2\Pi_{1/2}$ and the $(020)\kappa^2\Pi_{3/2}$ components perturb each other strongly. This is because the two components have similar K-doublings, as shown in Fig. 7.9 for CaOH in which the corresponding components encounter minimal Fermi perturbations. The effect of the Fermi interaction on the K-doublings is manifested most dramatically in the $(100)^2\Pi_{3/2}$ and the $(020)\mu^2\Pi_{1/2}$ components of CaOH. The two components have very different K-splittings and interact with each other very strongly. The $(100)^2\Pi_{3/2}$ component normally has negligible K-doublings, but, now has fairly large negative $\Delta\tilde{\nu}$. The $(020)\mu^2\Pi_{1/2}$ component has steadily increasing positive $\Delta\tilde{\nu}$ with increasing J while the corresponding component of CaOD exhibits a sign change of the $\Delta\tilde{\nu}$ at J = 18½.

It should be emphasized that the labeling of some vibronic states is rather difficult because of heavy mixing. The labels that represent leading characters at J = 1½ have been chosen. Table 7.5 lists mixing percentages for each eigenstate at J = 1½, 20½ and 40½. For CaOH, the $(020)\mu^2\Pi_{3/2}$ and $(100)^2\Pi_{3/2}$ states are completely mixed at all J values. As J increases, the interactions of $(020)\mu^2\Pi_{1/2}$ with both $(020)\mu^2\Pi_{3/2}$ and $(100)^2\Pi_{3/2}$ become rapidly stronger and cause complete mixing at $J \geq 30½$. For CaOD, the mixing between $(100)^2\Pi_{1/2}$ and $(020)\kappa^2\Pi_{3/2}$ increases as J increases and the two vibronic states switch leading characters after J=40½.

It is interesting to examine the isotopic behavior of the parameters for the (100) and (020) levels. In addition, the isotopic ratios of the parameters for the (000) and (010) levels which were given earlier in Chapters 4 and 6, respectively, are also listed here so that the self-consistency of

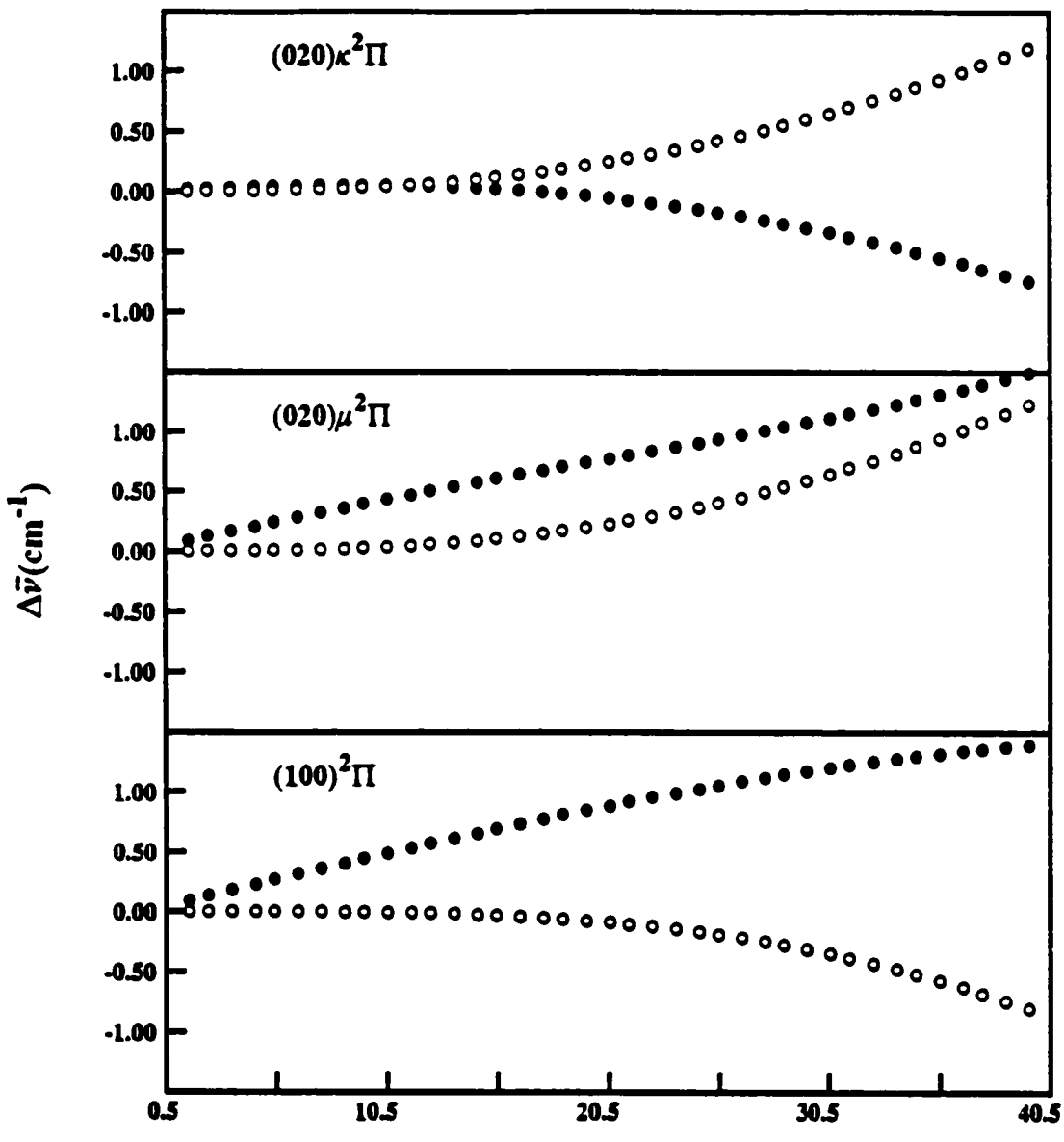

Fig. 7.9: K-type doublings, $\Delta\bar{\nu} = \bar{\nu}_e - \bar{\nu}_f$, in the $\tilde{A}^2\Pi$ (020) and (100) vibronic states of CaOH. • for $^2\Pi_{1/2}$ levels; o for $^2\Pi_{3/2}$ levels.

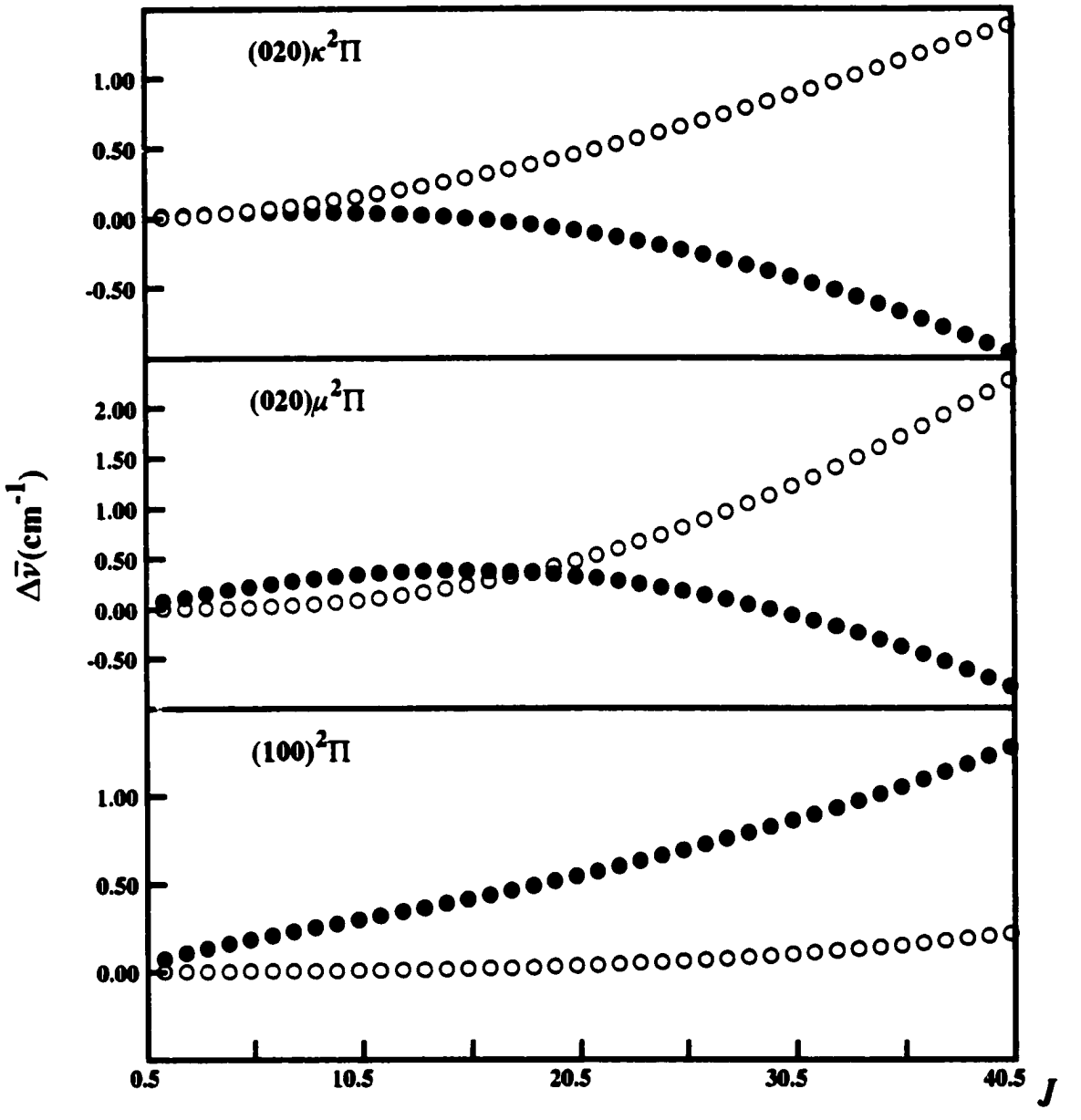

Fig. 7.10: K-type doublings, $\Delta\bar{\nu} = \bar{\nu}_e - \bar{\nu}_f$, in the $\tilde{A}^2\Pi$ (020) and (100) vibronic states of CaOD. • for $^2\Pi_{1/2}$ levels; o for $^2\Pi_{3/2}$ levels.

TABLE 7.5: Mixing percentages of the $^2\Pi$ vibronic states of CaOH and CaOD

e levels of CaOH						
J= 1½	16785.740	16770.962	16671.705	16650.490	16645.701	16587.463
$\kappa^2\Pi_{1/2}$	83.63	.09	.00	15.24	.03	1.00
$\kappa^2\Pi_{3/2}$	.06	66.69	10.23	.02	23.00	.00
$\mu^2\Pi_{3/2}$	.04	31.09	42.08	.01	26.78	.00
$\mu^2\Pi_{1/2}$	16.14	.01	.03	73.85	.13	9.85
$^2\Pi_{3/2}$	.00	2.12	47.65	.22	50.01	.01
$^2\Pi_{1/2}$	.13	.00	.01	10.67	.05	89.14
J=20½	16935.839	16917.470	16821.252	16799.381	16792.880	16735.145
$\kappa^2\Pi_{1/2}$	74.36	9.22	.43	11.27	3.71	1.01
$\kappa^2\Pi_{3/2}$	6.07	60.71	9.70	2.07	21.30	.15
$\mu^2\Pi_{3/2}$	4.05	27.02	41.28	1.64	25.94	.07
$\mu^2\Pi_{1/2}$	15.22	1.06	4.08	55.76	14.23	9.65
$^2\Pi_{3/2}$	.16	1.99	43.25	24.37	29.25	.98
$^2\Pi_{1/2}$	.13	.00	1.26	4.90	5.57	88.14
J=40½	17359.035	17334.039	17244.450	17220.789	17209.557	17152.621
$\kappa^2\Pi_{1/2}$	63.43	19.91	1.16	6.31	8.20	1.01
$\kappa^2\Pi_{3/2}$	12.56	54.27	8.56	4.81	19.27	.53
$\mu^2\Pi_{3/2}$	9.01	21.94	39.90	3.97	24.93	.25
$\mu^2\Pi_{1/2}$	14.55	2.00	11.76	33.58	28.97	9.14
$^2\Pi_{3/2}$	.32	1.88	35.11	51.15	7.98	3.56
$^2\Pi_{1/2}$	.15	.00	3.51	.18	10.66	85.51

TABLE 7.5 (Continued.)

f levels of CaOH						
J= 1½	16785.728	16770.962	16671.704	16650.409	16645.701	16587.374
$\kappa^2\Pi_{1/2}$	83.64	.09	.00	15.22	.03	1.00
$\kappa^2\Pi_{3/2}$	.06	66.69	10.23	.02	23.00	.00
$\mu^2\Pi_{3/2}$	.04	31.09	42.08	.02	26.78	.00
$\mu^2\Pi_{1/2}$	16.12	.01	.03	73.86	.13	9.85
$^2\Pi_{3/2}$	.00	2.12	47.65	.22	50.01	.01
$^2\Pi_{1/2}$	.13	.00	.01	10.66	.05	89.14
J=20½	16935.945	16917.229	16821.019	16798.612	16792.974	16734.266
$\kappa^2\Pi_{1/2}$	73.62	10.13	.30	11.10	3.85	.99
$\kappa^2\Pi_{3/2}$	6.75	60.03	9.72	2.47	20.91	.13
$\mu^2\Pi_{3/2}$	4.42	26.66	41.35	2.21	25.29	.06
$\mu^2\Pi_{1/2}$	14.91	1.21	3.29	55.81	15.16	9.63
$^2\Pi_{3/2}$	.17	1.97	44.23	23.42	29.30	.90
$^2\Pi_{1/2}$	.13	.00	1.10	4.99	5.49	88.29
J=40½	17359.975	17332.794	17243.072	17219.252	17210.442	17151.206
$\kappa^2\Pi_{1/2}$	61.48	22.14	.65	6.43	8.33	.96
$\kappa^2\Pi_{3/2}$	14.26	52.52	8.60	5.87	18.35	.40
$\mu^2\Pi_{3/2}$	9.93	21.10	39.96	5.75	23.10	.16
$\mu^2\Pi_{1/2}$	13.84	2.38	8.44	35.29	31.01	9.04
$^2\Pi_{3/2}$	.35	1.86	39.36	46.25	9.12	3.06
$^2\Pi_{1/2}$	.13	.00	3.00	.41	10.08	86.37

TABLE 7.5 (Continued.)

e levels of CaOD						
J= 1½	16649.218	16594.978	16581.825	16581.004	16490.795	16479.450
$^2\Pi_{3/2}$	98.14	.00	.02	1.71	.13	.00
$\kappa^2\Pi_{1/2}$	.00	80.23	6.51	.44	.01	12.81
$^2\Pi_{1/2}$	.01	5.92	90.97	2.14	.00	.97
$\kappa^2\Pi_{3/2}$	1.75	.04	1.90	73.00	23.26	.04
$\mu^2\Pi_{3/2}$	.10	.02	.60	22.70	76.48	.08
$\mu^2\Pi_{1/2}$	.00	13.78	.00	.00	.11	86.10
J=20½	16783.981	16731.233	16716.794	16713.969	16627.660	16612.828
$^2\Pi_{3/2}$	97.24	.43	.00	2.20	.10	.03
$\kappa^2\Pi_{1/2}$	.01	75.45	.04	11.79	.90	11.81
$^2\Pi_{1/2}$	.84	3.39	67.57	27.21	.16	.83
$\kappa^2\Pi_{3/2}$	1.79	4.84	24.61	45.96	18.52	4.28
$\mu^2\Pi_{3/2}$	.11	2.67	7.46	12.68	67.96	9.13
$\mu^2\Pi_{1/2}$	.02	13.22	.31	.17	12.36	73.92
J=40½	17165.737	17116.296	17097.053	17093.172	17014.069	16991.164
$^2\Pi_{3/2}$	94.96	.97	.12	3.82	.06	.07
$\kappa^2\Pi_{1/2}$	.03	67.65	4.38	15.65	1.33	10.95
$^2\Pi_{1/2}$	2.91	.96	49.85	45.20	.40	.69
$\kappa^2\Pi_{3/2}$	1.90	11.39	36.00	29.30	12.25	9.16
$\mu^2\Pi_{3/2}$	.12	6.61	8.73	6.00	59.97	18.57
$\mu^2\Pi_{1/2}$	.08	12.41	.92	.02	26.01	60.56

TABLE 7.5 (Continued.)

f levels of CaOD						
J= 1½	16649.218	16594.965	16581.752	16581.002	16490.794	16479.373
$^2\Pi_{3/2}$	98.14	.00	.03	1.70	.13	.00
$\kappa^2\Pi_{1/2}$	.00	80.31	6.39	.49	.01	12.80
$^2\Pi_{1/2}$	.01	5.85	90.57	2.60	.00	.97
$\kappa^2\Pi_{3/2}$	1.75	.05	2.28	72.62	23.26	.04
$\mu^2\Pi_{3/2}$	.10	.02	.73	22.58	76.48	.08
$\mu^2\Pi_{1/2}$	.00	13.77	.00	.00	.11	86.12
J=20½	16783.949	16731.323	16716.253	16713.516	16627.185	16612.504
$^2\Pi_{3/2}$	97.29	.45	.02	2.11	.11	.03
$\kappa^2\Pi_{1/2}$	.01	75.05	.11	12.27	.60	11.96
$^2\Pi_{1/2}$	.78	2.92	59.57	35.73	.13	.87
$\kappa^2\Pi_{3/2}$	1.80	5.67	30.69	39.04	19.40	3.40
$\mu^2\Pi_{3/2}$	.11	3.00	9.13	10.70	70.16	6.90
$\mu^2\Pi_{1/2}$	.02	12.92	.47	.15	9.60	76.84
J=40½	17165.522	17117.256	17095.778	17091.794	17011.802	16991.951
$^2\Pi_{3/2}$	95.27	1.06	.08	3.46	.07	.06
$\kappa^2\Pi_{1/2}$	.04	65.33	6.07	16.48	.74	11.34
$^2\Pi_{1/2}$	2.55	.68	49.10	46.60	.28	.79
$\kappa^2\Pi_{3/2}$	1.93	13.73	35.19	27.72	14.32	7.12
$\mu^2\Pi_{3/2}$	.12	7.49	8.28	5.71	65.00	13.40
$\mu^2\Pi_{1/2}$	.07	11.71	1.29	.05	19.59	67.28

the present work can be gauged.

$\tilde{X}^2\Sigma^+$ state:

(000): $B_v^D/B_v^H = 0.90624(2)$ $\gamma_v^D/\gamma_v^H = 0.89(1)$

(100): $B_v^D/B_v^H = 0.90617(10)$

(010): $B_v^D/B_v^H = 0.908878(6)$ $\gamma_v^D/\gamma_v^H = 0.9493(2)$

(020): $B_v^D/B_v^H = 0.91122(6)$

$\tilde{A}^2\Pi$ state:

(000): $B_v^D/B_v^H = 0.90567(2)$ $p^{eD}/p^{eH} = 0.920(2)$ $[q^{eD}/q^{eH}]^{1/2} = 0.93(2)$

(100): $B_v^D/B_v^H = 0.90604(1)$ $p^{eD}/p^{eH} = 0.891(3)$ $[q^{eD}/q^{eH}]^{1/2} = 0.88(1)$

(010): $B_v^D/B_v^H = 0.908320(4)$ $p^{eD}/p^{eH} = 0.896(2)$ $[q^{eD}/q^{eH}]^{1/2} = 0.93(4)$

$\gamma_v^D/\gamma_v^H = 0.946(2)$

(020): $B_v^D/B_v^H = 0.91080(5)$ $p^{eD}/p^{eH} = 0.914(3)$

The above results clearly demonstrate that the isotope relations of the parameters, B_v, p^e, q^e and γ_v, are very well obeyed in the range of $v_1 \leq 1$ and $v_2 \leq 2$ investigated by the present work. The isotopic ratios of the parameters are in excellent agreement between the $\tilde{X}$ and $\tilde{A}$ states. The overall consistency shown in the above ratios lends strong confidence to the data sets and the global matrix deperturbation approach used in the present work. The value of B_v^D/B_v^H increases slowly as v_2 increases in both the $\tilde{X}$ and $\tilde{A}$ states, which is a consequence of the different v_2-dependence of the rotational constants in the two isotopomers. This phenomenon will be discussed in more detail in next chapter.

The correlation between A_D and γ in a $^2\Pi$ state has been discussed in Chapters 4 and 6. In the $\tilde{A}(100)$ and (020) levels, such correlation is maintained. Therefore, in the practical fits, γ_1 and γ_2 were held fixed at the values for the $\tilde{A}(000)$ and (010) levels, respectively, and A_{D1} and A_{D2} were allowed to vary. As seen from Table 7.3, some fitted values of the high-order

parameters (A_D, γ_D and $\epsilon_D\omega_2$) are not reasonable in magnitude or sign. This situation is very difficult to avoid since the interactions, especially at high J, are too strong to give a perfect treatment.

7.8 Concluding Remarks

The $\tilde{A}^2\Pi(100)/(020)$ - $\tilde{X}^2\Sigma^+(020)/(000)$ bands of CaOH and CaOD have been rotationally analyzed with a large and highly precise data base in the present work. The global matrix deperturbation approach has reproduced the observed quantities to nearly within the experimental uncertainty, in spite of the close degeneracy of some vibronic levels and consequent strong Fermi interactions in the upper state. The fitted molecular constants are consistent with those for the (010) and (000) levels and, in particular, still obey isotope relations very well.

The Fermi resonance parameters have been determined for the first time for an alkaline earth monohydroxide molecule. One would normally expect that the Fermi resonance parameters are highly correlated with the vibrational spacing, $\Delta = T^0(100) - T^0(020)$. Indeed, this is the case in the $\tilde{X}^2\Sigma^+$ electronic state. However, in the $\tilde{A}^2\Pi$ electronic state, the (100) and (020) levels are split into several components due to the spin-orbit and vibronic couplings. Since only one of the two (100) spin-components interacts strongly with one or two of the (020) vibronic components, the uneven Fermi interactions within the vibronic manifold break the correlation and lead to the unequivocal determination of W_1, $T^0(100)$ and $T^0(020)$. In addition, the J-independent Fermi resonance matrix elements cause J-dependent interactions because of two factors. The first is the near degeneracy of the interacting vibronic components which have different effective B-values. The second is the cross effect of the Fermi resonance operator with the S-uncoupling and/or

K-type doubling operators. Fitting such *J*-dependent interactions certainly helps in determining the Fermi resonance parameters, as well as other parameters. Finally, the obtained Fermi resonance parameters have given valuable information on the anharmonic force field.

CHAPTER 8

Equilibrium Geometry and Force Field in the $\tilde{A}$ and $\tilde{X}$ States of CaOH/CaOD

8.1 Introduction

One of the ultimate goals of molecular spectroscopy is determination of the molecular equilibrium geometry and force field by making use of the molecular constants derived from experimental data. The zero-point vibrational level and several excited levels of the ν_1 and ν_2 modes in the $\tilde{X}^2\Sigma^+$ and $\tilde{A}^2\Pi$ states have now been well characterized for both CaOH and CaOD. Considerable progress can be made in evaluating equilibrium bond lengths and force constants for the two states.

Much effort to observe excited levels of the ν_3 (O-H stretch) mode has been made by this and some other laboratories. However, no success has been achieved so far. In fact, the excited O-H stretch vibration has not been observed for any metal monohydroxides. It is assumed here that the free anion OH^- could be a good approximation for the OH^- ligand in the $M^+(OH)^-$ molecule. Rosenbaum *et al.*[89] have obtained the harmonic vibration frequency, 3738 cm^{-1}, in the ground state of the free OH^- anion from velocity modulation laser spectroscopy. This value will be used as ω_3 in the following calculations for both the $\tilde{X}^2\Sigma^+$ and $\tilde{A}^2\Pi$ states of CaOH. Although this assumed value could contain appreciable error, it will be shown that the subsequent calculations are insensitive to such error.

Hilborn *et al.*[7] estimated the equilibrium bond lengths for the first time for the CaOH $\tilde{A}$ and $\tilde{X}$ states, based on limited data. In this chapter, the equilibrium bond lengths will be recalculated from a more precise and much larger data base; the force field and the Coriolis coupling constants in the $\tilde{A}$ and $\tilde{X}$ states will also be evaluated.

8.2 Summary of the Molecular Constants

The molecular constants, ω_i , α_i and B_e, for the $\tilde{A}^2\Pi$ and $\tilde{X}^2\Sigma^+$ states of CaOH/CaOD that are used in the following calculations are summarized in Tables 8.1 and 8.2, respectively. The two tables also include all the respective results calculated in this chapter.

For the $\tilde{X}^2\Sigma^+$ state of CaOH/CaOD, the harmonic frequency ω_2 was evaluated in Section 7.7, using the approximation, $\omega_2 \approx \omega_2^0 - 2x_{22}^0$, based on the experimental term values, $G(010)$ and $G(020)$. For the Ca-O stretch mode, the fundamental frequency, $\nu_1=G(100)$, was used as an approximation of the harmonic frequency ω_1. As discussed in Section 7.7, this approximation was considered preferable since the higher excited (v_100) levels experience more and more complicated Fermi resonance interactions, so that the experimentally measured term values, without deperturbation, are not appropriate for derivation of ω_1. Here, both $G(020)$ and $G(100)$ have been corrected from the effect of the Fermi resonance based on an assumption that the $\tilde{X}$ state has the same Fermi resonance constant as the $\tilde{A}$ state. The constant ω_3 for CaOH was assumed to be 3738 cm^{-1}, as mentioned above, while ω_3 for CaOD was found by the subsequent calculation. In order to calculate B_e, three parameters, α_1, α_2 and α_3, need to be evaluated. The parameter α_1 was determined from least squares fits of the $B(v_100)$ values with v_1 = 1 - 4 for CaOH and v_1 = 1 - 3 for CaOD; this was appropriate since the Fermi resonance is J-independent and has no effect on the B-values in the $\tilde{X}$ state. The α_2-values were obtained in Section 7.7. The values of α_3 were taken from the estimates for RbOH and RbOD by Lide and Matsumura[87].

For the $\tilde{A}^2\Pi$ state of CaOH/CaOD, the molecular constants, ω_2 and α_2, were evaluated in Section 7.7. ω_1 was replaced with the fundamental frequency ν_1 obtained in Section 7.7 since only one excited level was observed for this

TABLE 8.1: Molecular Parameters[a] for CaOH and CaOD in the $\tilde{A}^2\Pi$ State

	CaOH	CaOD		CaOH/CaOD
ω_1	628.482	618.776	r_e(Ca—O)	1.9532 Å
ω_2	366.435	278.325	r_e(O—H)	0.9572 Å
ω_3	3738[b]	2709		
B_e	0.3436560	0.3102692	f_{11}	2.849 mdyn/Å
α_1	0.0023153(70)	0.0019709(98)	f_{13}	0.908 mdyn/Å
α_2	0.001167(9)	0.000005(13)	f_{33}	7.894 mdyn/Å
α_3	0.000397[c]	0.000587[c]	f_{22}	0.0640 mdyn•Å
ζ_{21}	0.1603	0.2037	f_{122}	-0.167 mdyn
ζ_{23}	0.9871	0.9790	f_{322}	0.227 mdyn

TABLE 8.2: Molecular Parameters[a] for CaOH and CaOD in the $\tilde{X}^2\Sigma^+$ State

	CaOH	CaOD		CaOH/CaOD
ω_1	614.79	603.59	r_e(Ca—O)	1.9746 Å
ω_2	357.23	270.71	r_e(O—H)	0.9562 Å
ω_3	3738[b]	2717		
B_e	0.3366106	0.3041627	f_{11}	2.669 mdyn/Å
α_1	0.002200(10)	0.001877(22)	f_{13}	0.463 mdyn/Å
α_2	0.001089(6)	-0.000008(12)	f_{33}	7.850 mdyn/Å
α_3	0.000397[c]	0.000587[c]	f_{22}	0.0611 mdyn•Å
ζ_{21}	0.1428	0.1801	f_{122}	-0.165 mdyn
ζ_{23}	0.9898	0.9836	f_{322}	0.136 mdyn

[a] ω_i, α_i, B_e and q^v are in unit of cm^{-1}

[b] estimated based on Ref. 89.

[c] estimated values in Ref. 87.

mode in the $\tilde{A}$ state. α_1 was calculated from $B_v(000)$ and $B_v(100)$. ω_3 and α_3 took the same values as those assumed for the $\tilde{X}^2\Sigma^+$ state.

8.3 Equilibrium Geometry

The linearity of the molecule at equilibrium was first established experimentally by Hilborn *et al.*[7]. This has been further proven by theoretical studies and by the systematic high resolution analysis of the $\tilde{A}$ - $\tilde{X}$ system in the present work.

Evaluation of equilibrium bond lengths of an X-Y-Z type molecule requires values of the equilibrium moments of inertia from two isotopic molecules. The relevant equation is

$$I_e = (m_1 m_2 r_{12}^2 + m_1 m_3 r_{13}^2 + m_2 m_3 r_{23}^2)/M \qquad (8.1)$$

where $M = m_1+m_2+m_3$, and r_{ij} denote the equilibrium internuclear separations with the labels 1, 2 and 3 corresponding to Ca, O and H/D atoms, respectively. The moments of inertia, $I_e = h/(8\pi^2 c B_e)$, can be calculated directly from the equilibrium rotational constants B_e, defined by

$$B_e = B_v(000) + \tfrac{1}{2}\alpha_1 + \tfrac{1}{2}\alpha_3 + \alpha_2 - \gamma_{22} . \qquad (8.2)$$

There is a γ_{22} term in Eq. 8.2; this is different from the normal expressions[62] which only include α_i-terms. Like α_2, the parameter γ_{22} describes the v_2-dependence of the rotational constant B_v, as expressed by Eq. 7.12 in Section 7.5. The contribution of the γ_{22}-term to B_v is important in CaOH and is dominant in CaOD. The values of γ_{22} are listed in Table 7.4.

Hilborn *et al.*[7] obtained the first estimates of the equilibrium bond lengths based on rotational analysis of the CaOH $\tilde{A}(000)$ - $\tilde{X}(000)$ band and partial analysis of the CaOD $\tilde{A}(000)$ - $\tilde{X}(000)$ band. In order to obtain B_e, they employed the values of α_1, α_2 and α_3 from other molecules[7]. In the present work, the values of $B_v(000)$, α_1 and α_2 have been determined from a

more precise and much larger data base, including several excited vibrational levels. The results of the present calculations for the $\tilde{A}$ and $\tilde{X}$ states are listed in Tables 8.1 and 8.2, respectively.

The results show that while the O-H bond length is essentially the same in the two states, the Ca-O bond length in the $\tilde{A}^2\Pi$ state is slightly shorter than that in the $\tilde{X}^2\Sigma^+$ state. This indicates that the "non-bonding" valence electron is actually slightly antibonding in the $\tilde{X}$ state.

8.4 Harmonic Force Field and Coriolis Coupling Constants

Under the Born-Oppenheimer approximation, nuclear degrees of freedom are separated from electronic degrees of freedom, and a potential energy function governs the motion of the nuclei. In principle all the vibration-rotation energy levels and wavefunctions can be calculated based on the potential energy function and atomic masses of the molecule. In a reciprocal fashion, molecular constants extracted from the vibration-rotation spectra can be employed to construct the potential function.

A potential energy function is normally expressed as a power series expansion in nuclear displacement coordinates from the equilibrium configuration. The coefficients in the expansion are the force constants which describe the shape of the potential surface in terms of the coordinates used. The second derivatives of the function near the potential minimum define the harmonic force field. The detailed shape of the potential surface for large displacements from equilibrium defines the anharmonic force field.

In the present work the potential energy function of the CaOH molecule has been expressed in the curvilinear internal coordinate space and has the form,

$$V = \tfrac{1}{2}f_{11}(\Delta r_{12})^2 + f_{13}(\Delta r_{12})(\Delta r_{23}) + \tfrac{1}{2}f_{33}(\Delta r_{23})^2 + \tfrac{1}{2}f_{22}(\Delta\alpha)^2 + f_{122}(\Delta r_{12})(\Delta\alpha)^2 + f_{322}(\Delta r_{23})(\Delta\alpha)^2 + \ldots \quad (8.3)$$

where Δr_{ij} represent the displacements from the equilibrium nuclear separations and $\Delta\alpha$ is the angular displacement associated with the bending vibration. The molecular force field expressed in the curvilinear internal expansion is invariant under an isotopic change of mass; this property makes it possible to determine the force field using spectroscopic information from more than one isotopic species. The second property of the force field in a true bond-stretching and angle-bending (curvilinear) coordinate system is that the quadratic force field gives a good representation of the anharmonicity and, in consequence, the cubic and quartic interaction terms are minimized and the simplest expression for the force field is obtained.

The three harmonic force constants, f_{11}, f_{13} and f_{33}, may be determined from the harmonic frequencies ω_1 and ω_3 for CaOH, combined with ω_1 for CaOD. The harmonic force constant f_{22} can be calculated from the equilibrium bond lengths and ω_2 of either isotopomer. The methods and equations for such evaluations have been discussed by many authors. For clarification, the equations employed in this work are given as follows[90],

$$4\pi^2c^2(\omega_1^2 + \omega_3^2) = (\mu_q f_{33} + \mu_z f_{11} - 2\mu_{qz} f_{13})/(\mu_q\mu_z - \mu_{qz}^2) \quad (8.4)$$

$$16\pi^4c^4(\omega_1^2\omega_3^2) = (f_{11}f_{33} - f_{13}^2)/(\mu_q\mu_z - \mu_{qz}^2) \quad (8.5)$$

where $\mu_q = m_1(m_2 + m_3)/M$, $\mu_z = m_3(m_1 + m_2)/M$ and $\mu_{qz} = m_1m_3/M$, and[91]

$$f_{22} = 4\pi^2c^2\omega_2^2 r_{12}^2 r_{23}^2 \left\{\frac{r_{23}^2}{m_1} + \frac{r_{13}^2}{m_2} + \frac{r_{12}^2}{m_3}\right\}^{-1} \quad (8.6)$$

Once f_{11}, f_{13} and f_{33} were found, the unknown frequency ω_3 for CaOD was calculated from Eqs. 8.4 and 8.5, and used in further calculations.

For each electronic state ($\tilde{A}$ or $\tilde{X}$), two f_{22}-values have been obtained from the two isotopomers and are in excellent agreement, as expected. These

values are as follows: f_{22}(CaOH)=0.0633 and f_{22}(CaOD)=0.0647 mdyn•Å for the $\tilde{A}$ state; f_{22}(CaOH)=0.0605 and f_{22}(CaOD)=0.0617 mdyn•Å for the $\tilde{X}$ state. The f_{22}-value averaged over the two isotopomers for each state will be used.

The harmonic force constants, f_{11}, f_{13}, f_{33} and f_{22}, evaluated here are listed in Tables 8.1 and 8.2 for the $\tilde{A}$ and $\tilde{X}$ states, respectively. As shown in the two tables, the constants f_{11}, f_{33} and f_{22} in the $\tilde{A}$ state have values that are very close to those in the $\tilde{X}$ state. This is expected as the two states have similar potentials described earlier in Chapter 1. However, f_{13} has quite different values between the two states. In the process of the calculations, it was noticed that f_{13} is extremely sensitive to the uncertainties of the ω_1-values. Therefore, the calculated values of f_{13} are expected to have much larger uncertainty than other harmonic force constants.

The Coriolis force plays an important role in the properties of polyatomic molecules. It causes a coupling between rotation and vibration (Coriolis coupling) in a vibrating molecule. The Coriolis coupling directly contributes to the ℓ-type doubling in a degenerate vibrational level. The Coriolis force also leads to an interaction between two vibrational levels in a rotating molecule if the two levels are of different but proper species ($\Delta v_i=\pm 1$, $\Delta v_j=\mp 1$, $\Delta \ell=\pm 1$). This Coriolis interaction is J-dependent and may become strong when the two levels are close in energy (Coriolis resonance). The Coriolis constants contain valuable information on the harmonic force field. In the present case, on the other hand, the Coriolis coupling constants will be calculated from the harmonic force field, using the relation[87]

$$\zeta_{21}^2/\lambda_1 + \zeta_{23}^2/\lambda_3 = (r_{12}^2 f_{11} + 2\, r_{12} r_{23} f_{13} + r_{23}^2 f_{33})/(\lambda_1 \lambda_3 I_e) \qquad (8.7)$$

and the relation[84]

$$\zeta_{21}^2 + \zeta_{23}^2 = 1\,, \qquad (8.8)$$

where $\lambda_i = (2\pi c\omega_i)^2$. The values obtained for ζ_{21} and ζ_{23} in the $\tilde{A}$ and $\tilde{X}$ states for both isotopomers are listed in Table 8.1 and 8.2, respectively.

The ℓ-type doubling constants are dependent on the Coriolis coupling constants and some other constants, ω_1, ω_2, ω_3 and B_e, as expressed in Eq. 6.20. These constants are now available and summarized in Tables 8.1 and 8.2. It will be very interesting to perform calculations of the ℓ-type doubling constants and to provide a comparison between the calculated and the experimentally determined values. It turns out that all the calculated q^v-values are in excellent agreement with the values determined from experimental data. This gives the most eloquent proof of the quality of the data base and the deperturbation models in the present work. The results for the $\tilde{A}$ and $\tilde{X}$ states of both isotopic molecules are given in Table 8.3(a).

The effects of the possible errors of the assumed values of ω_3 and α_3 on the present calculations have been examined for the $\tilde{X}$ state. When the ω_3-value for CaOH was increased by 100 cm^{-1}, the harmonic force constants f_{11}, f_{13} and f_{33} increased by 1%, 5% and 6%, respectively, while the Coriolis constants experienced virtually no change; the ℓ-type doubling constant changed by only 0.2%. When the α_3-values of CsOH and CsOD (0.00038 and 0.00049 cm^{-1} estimated in Ref. 87) were used instead of those for RbOH and RbOD, the only significant change was for the equilibrium O-H bond length from 0.9536 to 0.9552 Å, an increase of only ~0.2%. The changes in other calculated parameters are completely negligible. A similar situation is expected for the $\tilde{A}$ state.

It would be interesting to calculate the centrifugal distortion constants D_e using the calculated Coriolis coupling constants and other molecular constants and, then, compare them with the experimental results. The expression[92] for D_e is

TABLE 8.3(a): Calculated and Experimental Values (cm^{-1}) of q^v

	CaOH		CaOD	
	Exp.[a]	Calc.	Exp.[a]	Calc.
$\tilde{A}$	-0.6978(17) $\times 10^{-3}$	-0.7031 $\times 10^{-3}$	-0.7576(14) $\times 10^{-3}$	-0.7492 $\times 10^{-3}$
$\tilde{X}$	-0.7181(2) $\times 10^{-3}$	-0.6837 $\times 10^{-3}$	-0.7621(4) $\times 10^{-3}$	-0.7324 $\times 10^{-3}$

[a]values for the (010) levels.

TABLE 8.3(b): Calculated and Experimental Values (cm^{-1}) of D

	CaOH		CaOD	
	Exp.[a]	Calc.	Exp.[a]	Calc.
$\tilde{A}$	0.3891(11) $\times 10^{-6}$	0.4008 $\times 10^{-6}$	0.2981(15) $\times 10^{-6}$	0.2997 $\times 10^{-6}$
$\tilde{X}$	0.38600(3) $\times 10^{-6}$	0.3957 $\times 10^{-6}$	0.2943(16) $\times 10^{-6}$	0.2994 $\times 10^{-6}$

[a]values for the (000) levels.

$$D_e = 4\,B_e^3 \left\{ \frac{\zeta_{23}^2}{\omega_1^2} + \frac{\zeta_{21}^2}{\omega_3^2} \right\} \tag{8.9}$$

The results of the calculations for the two isotopomers in the $\tilde{A}$ and $\tilde{X}$ states are in remarkably good agreement with the values obtained from experimental data. This provides further evidence for the quality and self-consistency of the results obtained in the present work. The calculated and experimentally determined values of D_e for the two isotopic molecules are summarized in Table 8.3(b) in which the experimental values of D_v for the (000) levels are used for the experimental D_e.

8.5 Vibration-rotation Interactions and Anharmonic Force Constants

An interesting phenomenon found in the present work is that the rotational constants B_v of the two isotopomers experience opposite changes in both $\tilde{A}$ and $\tilde{X}$ states as the bending mode is excited from $v_2 = 0$ to $v_2 = 1$ and 2. The value of $B(0v_20)$ decreases steadily in CaOH, but increases very slowly in CaOD. As discussed using Eq. 7.12 in Section 7.7, there are three terms (α_2, γ_{22} and γ_{ll}) that contribute to $B(0v_20)$. The α_2-term is by far the dominant term in CaOH for small values of v_2. However, in CaOD, the parameter α_2 is much smaller than γ_{22} and γ_{ll}; it is essentially zero in both the $\tilde{A}$ and $\tilde{X}$ states. This striking isotope effect on the parameter α_2, which characterizes the vibration-rotation interaction, is actually not unusual. Similar situations have been found for the ground states of CsOH/CsOD and RbOH/RbOD[87], which also have a linear structure with low frequency bending vibrations. For example, in the case of CsOD for which the value of α_2 is very small while γ_{22} is march larger, B_v passes through a minimum and eventually becomes larger than B(000).

Lide and Matsumura[87] have carried out a detailed theoretical study of

this phenomenon in alkali metal hydroxide molecules. They have given an expression (Eq. 7.12 in Section 7.7) for the dependence of B_v on v_2 and ℓ. It was found that the α_2 term is generally dominant at low v_2 in the alkali hydroxides, and that the parameter α_2 is considerably more sensitive to isotopic substitution than the other two parameters. In Ref. 87, various mechanisms that contribute to α_2 were analyzed in detail, using an equation which has been given in Section 7.7 (Eq. 7.20). The first part on the right hand side is referred to as a Coriolis contribution and has a magnitude that is exactly half that of the ℓ-type doubling constant q^v. The second part contains the anharmonic force constants ϕ_{122} and ϕ_{322} and, hence, is generally regarded as an anharmonic contribution. However, as first indicated by Pliva[93], the cubic terms in the potential function expressed in normal coordinates actually contain a harmonic component owing to the fact that the transformation from true valence coordinates to normal coordinates is nonlinear. In other words, the purely harmonic force field in the curvilinear coordinates gives rise to quadratic, cubic, and quartic, *etc.*, force constants in the normal coordinates after the transformation. Lide and Matsumura separated the true harmonic component from the anharmonic contribution, which is particularly advantageous for examining isotope effects. Eq. 7.20 for α_2 was reformulated in Ref. 87 as

$$\alpha_2 = (\alpha_2)_{h1} + (\alpha_2)_{h2} + (\alpha_2)_{anh} \tag{8.9}$$

Here $(\alpha_2)_{h1}$ represents the first (Coriolis) part of Eq. 7.20; $(\alpha_2)_{h2}$ is a "pseudoanharmonic" term representing the harmonic contribution, while $(\alpha_2)_{anh}$ is a true anharmonic contribution. The expressions for the last two contributions developed in Ref. 87 are as follows:

$$(\alpha_2)_{h2} = -2B_e^2/\omega_2\,[1 + I_e/(m_2 r_{12} r_{23})] - 4B_e^2/\omega_2\,[\omega_2^4/(\omega_1^2\omega_3^2)]\, r_{12} r_{23} f_{13}/f_{22} + 4B_e^2/\omega_2\,[1 + I_e/(m_2 r_{12} r_{23})]\,[\lambda_2\,\zeta_{21}^2/\lambda_1 + \lambda_2\,\zeta_{23}^2/\lambda_3] \tag{8.10}$$

$$(\alpha_2)_{anh} = -4B_e^2/\omega_2 [\ell_{22}^4 r_{12} r_{23}/(\lambda_1\lambda_3)] [f_{122} (\rho_3 r_{23} f_{33} - \rho_1 r_{12} f_{13}) + f_{322} (\rho_1 r_{12} f_{11} - \rho_3 r_{23} f_{13})] \quad (8.11)$$

where $\lambda_i = (2\pi c\omega_i)^2$, and

$$\ell_{22} = [MI_e/(m_1 m_2 m_3)]^{1/2} (r_{12} r_{23})^{-1} \quad (8.12)$$

$$\rho_1 = [m_3 r_{23}/(MI_e)] [m_1 r_{12} + (m_1 + m_2) r_{23}] \quad (8.13)$$

$$\rho_3 = [m_1 r_{12}/(MI_e)] [m_3 r_{23} + (m_3 + m_2) r_{12}] \quad . \quad (8.14)$$

The first term in Eq. 8.10 is independent of the stretching force field. Since the second and third terms in Eq. 8.10 are very small compared to the first, owing to the small ratios $(\omega_2/\omega_1)^2$ and $(\omega_2/\omega_3)^2$, $(\alpha_2)_{h2}$ is always negative. In most linear triatomic molecules the harmonic contribution is dominant, and the parameter α_2 is hence found to be negative. However, in alkali and alkaline earth monohydroxides, the anharmonic and harmonic parts are comparable in magnitude, but of opposite sign, with the anharmonic part much more sensitive to isotope (H/D) exchange. For the $\tilde{X}^2\Sigma^+$ state, the values of $(\alpha_2)_{h1}$ are, $(\alpha_2)_{h1} = \frac{1}{2} |q^v| = 0.3591 \times 10^{-3}$ cm^{-1} for CaOH and 0.3811×10^{-3} cm^{-1} for CaOD. Using Eq. 8.10, the harmonic terms $(\alpha_2)_{h2}$ were calculated as -1.690×10^{-3} and -1.915×10^{-3} cm^{-1} for CaOH and CaOD, respectively. These results then give $(\alpha_2)_{anh}$ values of 2.420×10^{-3} and 1.526×10^{-3} cm^{-1} for CaOH and CaOD, respectively, indicating that in CaOH the anharmonic contribution to α_2 is a main factor. In contrast, the anharmonic contribution in CaOD is smaller than the harmonic contribution. A similar situation occurs in the $\tilde{A}^2\Pi$ state. The reason for the significant anharmonic contribution to α_2 in MOH molecules has been discussed by Lide and Matsumura[87] and appears to be the combination of the small mass of the H atom and the small force constant of the M-O bond.

After evaluating terms in Eq. 8.11, two equations were obtained for the $\tilde{X}^2\Sigma^+$ state,

$$-0.1199 \times 10^{-5} = 712.68\, f_{122} - 18.71\, f_{322} \qquad (8.15)$$

for CaOH and

$$-0.1125 \times 10^{-5} = 683.61\, f_{122} + 1.071\, f_{322} \qquad (8.16)$$

for CaOD. The anharmonic force constants, f_{122} and f_{322}, in the curvilinear internal coordinates were thus determined from the two isotopic equations, with units of Newton. Their values are listed in Table 8.2. Using the same approach the constants, f_{122} and f_{322}, for the $\tilde{A}^2\Pi$ state were obtained and are listed in Table 8.1. As seen from the two tables, f_{122} has essentially the same values in the $\tilde{A}$ and $\tilde{X}$ states. In the process of the calculations, it appeared that this constant, f_{122}, is not very sensitive to the inaccuracy of any individual parameter that was employed in the calculation and, consequently, it has been well determined. On the other hand, the constant f_{322} is very sensitive to inaccuracies of f_{13}. This is the major reason for the large difference between the values found for the $\tilde{A}$ and $\tilde{X}$ states. Although this constant has not been determined reliably, the f_{322} terms are very small compared with the f_{122} terms; thus f_{322} contributes very little to α_2 and its inaccuracy does not significantly affect the value of f_{122}.

8.6 Concluding Remarks

The subject of determination of the equilibrium configuration and the force field from spectroscopic data for polyatomic molecules has developed considerably in the past two or three decades[94,95]. This may be attributed to the wider understanding of the relevant theory and to the technical advances in spectroscopy. However, there is still a great need for more spectroscopic data with high resolution. Even in the most favorable cases, the experimental data have not been sufficient to determine all the symmetry-allowed force constants characterizing the potential surface without some simplifying

assumptions. The present research has aimed at introducing such study to an alkaline earth monohydroxide molecule. This type of molecules have virtually not been subject to such studies before. The extensive and highly precise data recorded in the present work, combined with the data obtained previously for CaOH and CaOD, have allowed a reasonably reliable determination of the equilibrium bond lengths and force constants, despite the necessary approximate assumptions, mainly on the O-H/D stretching mode. The excellent agreement between the ℓ-type doubling constants that were determined directly from the experimental data and those that were derived from a series of calculations based on other constants and the force field has ultimately verified the integrity of this entire work.

The vibration-rotation interaction parameters, α_i, are the main source of information on the cubic anharmonic force field. The force constants f_{122} and f_{322} have been derived from the α_2-values of the two isotopic species, described in the last section. The Fermi resonance parameters, W, are another valuable source and have given a direct and accurate measure of the cubic force constant, ϕ_{122}, as described in Section 7.7. It would be most desirable if a non-linear transformation of the coordinate system could be made so that the force field (f_{ij} and f_{ijj}) in the curvilinear internal coordinates calculated in this chapter could be converted to the force field in the dimensionless normal coordinates and, then, be compared with the results (ϕ_{122}) obtained directly from the experiments (Fermi resonance) described in the last chapter. Unfortunately, such transformation requires computational techniques which are not immediately available.

CONCLUSION

The present work has been concerned with a systematic investigation of the $\tilde{A}^2\Pi$ - $\tilde{X}^2\Sigma^+$ system of the CaOH and CaOD radicals. The $\tilde{A}^2\Pi$ state is of particular interest because it contains more information than any other low-lying electronic state for this molecule. Specifically, the Renner-Teller effect and the Λ-type doubling only manifest themselves in a Π electronic state (they are very weak or negligible in $\Lambda \neq 1$ electronic states). The spin-orbit splitting of the $\tilde{A}^2\Pi$ state has a magnitude that causes near degeneracy between a spin-component of the (100) state and one or two vibronic components of the (020) state, leading to strong Fermi resonance. These interactions occur simultaneously in a relatively narrow spectral region and pose a great challenge to spectral analysis and model treatment. Once these interactions are thoroughly analyzed and properly modeled, one can obtain valuable information which can not be obtained in a simple system and the relevant theories can be tested most rigorously.

It has been possible, in the present work, to acquire and analyze extensive and highly precise data sets for the $\tilde{A}^2\Pi(010)$ and the $\tilde{A}^2\Pi(100)/(020)$ vibronic manifolds of the two isotopic molecules. Global matrix deperturbations of these two vibronic manifolds have been carried out. Not only most of the observed quantities were reproduced to within their experimental uncertainties, but also a complete set of well deperturbed molecular constants were determined for both isotopomers. Various methods have been used to gauge the quality of the results obtained in this work. It has been shown that the deperturbed molecular constants are self-consistent by comparing the constants between different vibrational levels and between the $\tilde{A}$ and $\tilde{X}$ states. It has also been confirmed that the molecular constants are

isotopically consistent by examining the isotope relations. The present work has indeed given the most comprehensive and rigorous test of the theories dealing with various interactions in linear triatomic molecules. A better understanding of those interactions has been achieved during the process of the spectral analysis and the matrix deperturbations. It may be concluded that one of the two objectives of the present research program, in the aspect described above, has been fulfilled quite satisfactorily.

The equilibrium bond lengths, force field and Coriolis coupling constants for the molecule under consideration have been evaluated. The quality of these results have been assessed by calculating the ℓ-type doubling constants q^v and the centrifugal distortion constants D and, then, comparing them with the corresponding values obtained directly from experimental data. The excellent agreement in these comparisons convincingly demonstrated the high quality of the data sets and deperturbation models and, hence, the results (molecular constants, equilibrium bond lengths and force constants) obtained in the present work. It is unfortunate that the excited O-H stretching vibrations have not been observed despite much effort made in this laboratory and by others. The most probable reason for such difficulty is the extremely small Franck-Condon factors between the $v_3 = 0$ and $v_3 = 1$ levels which have a large energy gap. The lack of information on the O-H stretching mode certainly affects the accuracy of the derived equilibrium bond lengths and force constants, although test calculations have shown that such effects are not very damaging. The objective of the present work in this aspect has not been completely fulfilled. It is hoped that the O-H stretching mode will be observed eventually using more powerful techniques so that complete spectroscopic information can be obtained for accurate determination of the equilibrium geometry and the force field.

APPENDIX

Tables of Rotational Transitions in the $\tilde{A}^2\Pi - \tilde{X}^2\Sigma^+$ System of CaOH and CaOD

For each transition, the tables show the assigned rotational quantum number J, the measured line position in cm^{-1} and the residual between the observed and calculated values.

TABLE 1. Line Positions for the $\tilde{A}^2\Pi$ - $\tilde{X}^2\Sigma^+$ (000) - (000) Band of CaOD

J	R_1		Q_1		R_{12}		P_{12}	
1½			15962.220	0.000				
2½								
3½	15965.786	-0.004	15962.840	-0.001				
4½	15966.767	-0.002	15963.164	-0.002				
5½	15967.755	-0.003	15963.495	-0.005			15956.504	-0.002
6½	15968.751	-0.005	15963.846	0.003			15955.634	0.005
7½	15969.758	-0.005	15964.194	-0.002			15954.757	-0.005
8½	15970.776	-0.003	15964.555	-0.003			15953.906	0.002
9½	15971.802	-0.003	15964.931	0.001			15953.059	0.003
10½	15972.837	-0.003	15965.313	0.002			15952.227	0.009
11½	15973.883	0.000	15965.700	-0.001			15951.397	0.008
12½	15974.939	0.003	15966.101	0.000			15950.574	0.005
13½	15975.999	0.001	15966.512	0.002			15949.767	0.008
14½	15977.070	0.001	15966.927	-0.002				
15½	15978.152	0.002	15967.357	-0.001			15948.176	0.007
16½	15979.236	-0.003					15947.387	-0.001
17½	15980.336	-0.002					15946.614	-0.003
18½	15981.446	0.001					15945.859	0.003
19½	15982.563	0.001					15945.104	-0.001
20½	15983.684	-0.003			15970.150	-0.001	15944.361	-0.002
21½	15984.824	0.002	15970.130	0.001	15970.648	0.000	15943.629	-0.003
22½	15985.957	-0.009	15970.626	0.002	15971.153	-0.001	15942.913	0.003
23½	15987.116	-0.003	15971.133	0.003	15971.670	0.000	15942.195	-0.003
24½	15988.276	-0.004	15971.646	0.002			15941.497	0.000
25½	15989.450	-0.001	15972.170	0.001			15940.800	-0.005
26½	15990.633	0.002			15973.275	0.000	15940.123	0.000
27½	15991.817	-0.003	15973.248	0.001	15973.828	-0.002		
28½	15993.018	0.000	15973.801	0.000	15974.395	0.000	15938.791	0.001
29½	15994.211	-0.014	15974.365	0.001	15974.969	0.000	15938.141	0.002
30½	15995.438	-0.003	15974.938	0.001	15975.552	-0.001	15937.494	-0.004
31½	15996.664	-0.003	15975.520	-0.001	15976.149	0.002	15936.874	0.007
32½	15997.906	0.005	15976.114	0.001	15976.750	-0.001	15936.248	0.001
33½	15999.140	-0.004	15976.716	0.000	15977.365	0.001		
34½	16000.394	-0.002	15977.329	0.000	15977.986	-0.002	15935.035	-0.001
35½	16001.658	0.000	15977.952	0.001	15978.622	0.000	15934.447	0.000
36½	16002.929	0.001	15978.584	0.000	15979.264	-0.001	15933.867	0.000
37½	16004.204	-0.004			15979.920	0.002	15933.305	0.006
38½	16005.495	-0.001	15979.879	0.000	15980.582	0.000	15932.740	0.000
39½	16006.790	-0.004	15980.542	0.001	15981.254	-0.001	15932.194	0.001
40½	16008.102	0.002	15981.213	0.000	15981.939	0.000	15931.652	-0.003
41½	16009.410	-0.006	15981.896	0.000			15931.126	-0.003
42½	16010.744	0.003	15982.584	-0.004	15983.334	-0.001	15930.615	0.002
43½	16012.077	0.002	15983.290	-0.001	15984.048	-0.001	15930.106	-0.001
44½	16013.422	0.004	15984.001	-0.002	15984.775	0.002		
45½	16014.771	0.001	15984.726	0.000	15985.506	-0.001		
46½	16016.135	0.004	15985.458	-0.001	15986.252	0.001		
47½	16017.505	0.004	15986.203	0.001	15987.005	0.000		

TABLE 1. (Continued.)

J	R_1		Q_1		R_{12}		P_{12}	
48½	16018.883	0.002	15986.955	0.000	15987.769	0.000		
49½	16020.271	0.002	15987.718	0.000	15988.546	0.002		
50½	16021.668	0.001	15988.492	0.000	15989.327	-0.002		
51½	16023.075	0.001	15989.275	-0.001	15990.125	0.001		
52½			15990.070	0.000	15990.931	0.002		
53½			15990.874	0.000				
54½			15991.689	0.000				
55½			15992.512	-0.001				
56½			15993.346	-0.003				
57½			15994.189	-0.005				

J	R_2		Q_{21}		Q_2		P_{21}	
½	16028.410	-0.004						
1½	16028.757	0.002			16027.202	-0.001		
2½	16029.111	0.001			16026.939	0.002		
3½	16029.481	0.001			16026.687	0.000		
4½	16029.862	-0.003			16026.451	0.000		
5½	16030.258	-0.007			16026.232	0.001		
6½	16030.676	-0.003			16026.026	0.001		
7½	16031.105	-0.003			16025.834	0.000		
8½	16031.548	-0.004			16025.652	-0.006		
9½	16032.003	-0.007			16025.497	0.000		
10½	16032.479	-0.004			16025.352	0.001		
11½	16032.963	-0.008			16025.220	0.000		
12½					16025.104	0.000		
13½					16025.002	-0.001		
14½	16034.516	-0.006			16024.915	-0.002		
15½								
16½								
17½								
18½								
19½	16037.396	0.000						
20½	16038.011	-0.003	16037.374	0.000				
21½	16038.647	0.001	16037.995	0.004				
22½	16039.295	0.002	16038.624	0.001				
23½	16039.954	0.000	16039.271	0.003	band			
24½	16040.630	0.001	16039.929	0.001	head			
25½	16041.317	-0.001	16040.603	0.000				
26½	16042.022	0.000	16041.290	-0.001				
27½	16042.741	0.001	16041.996	0.002				
28½	16043.474	0.002	16042.710	0.000				
29½	16044.217	-0.001	16043.442	0.001				
30½	16044.978	0.000	16044.187	0.001				
31½	16045.753	0.001	16044.946	0.001				
32½	16046.545	0.005	16045.719	0.000	16025.917	0.000		
33½	16047.344	0.002	16046.505	-0.001	16026.115	0.001	16025.879	-0.004

TABLE 1. (Continued.)

J	R_2		Q_{21}		Q_2		P_{21}	
34½	16048.158	0.000	16047.303	-0.004	16026.324	-0.002	16026.078	0.000
35½	16048.987	-0.001	16048.122	0.000	16026.555	0.003	16026.288	-0.001
36½	16049.830	-0.002	16048.948	-0.002	16026.797	0.004	16026.513	-0.002
37½	16050.689	0.000	16049.792	-0.001	16027.049	0.000	16026.756	0.001
38½	16051.560	-0.001	16050.649	-0.001	16027.321	0.001	16027.013	0.003
39½	16052.445	-0.001	16051.519	-0.001	16027.611	0.006	16027.281	0.002
40½	16053.346	0.002	16052.402	-0.002	16027.906	0.000	16027.566	0.002
41½	16054.258	0.001	16053.300	-0.002	16028.222	0.002	16027.863	0.000
42½	16055.182	-0.001	16054.215	0.002	16028.552	0.002	16028.181	0.004
43½	16056.120	-0.003	16055.137	-0.001	16028.893	-0.001	16028.507	0.002
44½	16057.086	0.010	16056.078	0.001	16029.253	0.000	16028.849	0.001
45½	16058.039	-0.004	16057.028	-0.001	16029.627	0.001	16029.206	0.000
46½	16059.022	-0.001	16057.990	-0.005	16030.016	0.002	16029.574	-0.004
47½	16060.011	-0.006	16058.972	-0.002	16030.416	0.000	16029.966	0.001
48½	16061.029	0.005	16059.968	0.001	16030.833	0.000	16030.361	-0.005
49½	16062.036	-0.009	16060.963	-0.010	16031.267	0.003	16030.779	-0.003
50½	16063.076	-0.002	16061.991	-0.002	16031.707	-0.003	16031.207	-0.005
51½	16064.126	0.000	16063.024	-0.001	16032.173	0.003	16031.654	-0.003
52½	16065.185	-0.001	16064.074	0.002			16032.116	0.000
53½	16066.257	-0.003	16065.128	-0.003				
54½	16067.348	0.001	16066.207	0.003				
55½	16068.448	0.001	16067.306	0.016				
56½	16069.559	-0.001	16068.376	-0.013				
57½	16070.687	0.000	16069.495	-0.006				
58½	16071.829	0.003	16070.631	0.005				
59½			16071.771	0.006				

J	R_{21}		P_2		P_1	
1½	16029.963	-0.002			15961.359	0.002
2½	16030.926	0.001			15961.083	-0.005
3½	16031.905	0.005			15960.822	-0.005
4½	16032.892	0.002	16023.649	-0.009	15960.572	-0.005
5½			16022.818	0.002	15960.333	-0.002
6½	16034.917	0.002	16021.990	0.001	15960.104	0.001
7½	16035.953	0.003	16021.180	0.003	15959.880	0.000
8½	16037.001	0.002	16020.382	0.002	15959.669	0.003
9½	16038.066	0.003	16019.603	0.005	15959.467	0.005
10½	16039.147	0.005	16018.836	0.006	15959.270	0.003
11½	16040.239	0.003	16018.074	-0.004	15959.086	0.005
12½			16017.336	-0.004	15958.910	0.005
13½	16042.468	0.000	16016.621	0.004	15958.740	0.002
14½	16043.609	0.003	16015.909	0.001	15958.584	0.004
15½	16044.763	0.004	16015.213	-0.002	15958.433	0.002
16½	16045.931	0.005	16014.538	0.002		
17½	16047.108	0.000	16013.872	0.000		
18½	16048.307	0.002	16013.223	0.000		

TABLE 1. (Continued.)

J	R_{21}		P_2	
19½	16049.520	0.003	16012.587	-0.001
20½	16050.744	0.001	16011.969	0.001
21½	16051.986	0.002	16011.362	-0.001
22½	16053.246	0.007	16010.764	-0.009
23½	16054.513	0.004	16010.195	-0.002
24½	16055.799	0.005	16009.632	-0.004
25½	16057.090	-0.003	16009.088	-0.001
26½	16058.407	0.001	16008.556	-0.001
27½	16059.736	0.002	16008.037	-0.003
28½	16061.077	0.000	16007.536	-0.001
29½	16062.436	0.002	16007.045	-0.004
30½	16063.810	0.005	16006.569	-0.006
31½	16065.191	0.000	16006.115	-0.001
32½	16066.589	-0.002	16005.674	0.003
33½	16068.002	-0.004	16005.243	0.002
34½	16069.435	0.001	16004.824	-0.002
35½	16070.873	-0.004	16004.427	0.003
36½	16072.330	-0.005	16004.032	-0.006
37½	16073.806	0.000	16003.667	0.002
38½	16075.301	0.009	16003.307	0.000
39½	16076.792	0.001	16002.965	0.001
40½	16078.303	-0.002	16002.629	-0.005
41½	16079.834	0.001	16002.333	0.014
42½	16081.382	0.007	16002.021	0.003
43½	16082.923	-0.008	16001.728	-0.004
44½	16084.516	0.015	16001.459	-0.001
45½	16086.085	0.000	16001.203	0.001
46½	16087.682	0.000	16000.965	0.007
47½	16089.294	0.000	16000.731	0.002
48½	16090.930	0.011	16000.514	0.001
49½	16092.560	0.002	16000.315	0.003
50½	16094.203	-0.008	16000.126	0.001
51½	16095.872	-0.006		
52½	16097.566	0.008		
53½	16099.250	-0.002		
54½	16100.957	-0.002		
55½	16102.683	0.003		
56½	16104.412	-0.003		

TABLE 2. Resolved LIF Line Positions in the $\tilde{A}^2\Pi$ - $\tilde{X}^2\Sigma^+$ System of CaOH

	$\tilde{A}(100)$ - $\tilde{X}(100)$							
J	Q_1		P_{12}		Q_2		R_{21}	
4½							16040.823	-0.007
5½	15979.099	-0.007			16033.472	-0.056	16041.872	-0.016
6½			15970.447	-0.030	16033.237	-0.022	16042.916	-0.040
7½	15979.939	0.072			16032.971	-0.029		
8½	15980.272	0.010	15968.639	0.055				
9½			15967.641	-0.011				
10½	15981.112	0.028					16047.344	0.022
11½	15981.517	0.007	15965.863	0.042	16032.039	-0.020		
12½			15964.910	-0.011				
13½	15982.425	0.031					16050.728	0.035
14½			15963.140	-0.012	16031.420	-0.032		
15½	15983.340	0.022					16053.074	0.088
16½	15983.829	0.033	15961.425	-0.001	16031.117	0.023	16054.240	0.093
17½			15960.601	0.022	16030.950	0.020		
18½							16056.575	0.081
19½	15985.273	-.020			16030.662	0.033	16057.623	-0.059
20½	15985.811	-.001	15958.067	-0.036	16030.439	-0.053		
21½			15957.299	-0.001			16060.129	0.046
22½					16030.267	0.019	16061.215	-0.082
23½					16030.111	-0.028	16062.421	-0.100
24½					16029.969	-0.072	16063.792	0.039
25½					16029.974	0.023		
26½								
27½							16067.423	-0.079
28½					16029.687	-0.053	16068.747	-0.023
29½					16029.628	-0.061		

	$\tilde{A}(100)$ - $\tilde{X}(100)$				$\tilde{A}(100)$ - $\tilde{X}(200)$			
J	R_2		P_2		Q_1		P_{12}	
4½					15377.680	0.029		
5½							15370.391	-0.008
6½								
7½					15378.849	-0.008		
8½					15379.303	0.014	15367.643	-0.007
9½							15366.733	-0.031
10½					15380.210	0.015	15365.875	-0.017
11½	16040.452	-0.053			15380.696	0.025	15365.037	0.002
12½	16040.920	-0.052			15381.179	0.018	15364.217	0.024
13½			16022.564	-0.011	15381.701	0.035	15363.339	-0.027
14½			16021.687	-0.029	15382.198	0.012	15362.568	0.013

TABLE 2. (Continued.)

	$\tilde{A}(100)$ - $\tilde{X}(100)$		$\tilde{A}(100)$ - $\tilde{X}(200)$	
J	R_2	P_2	Q_1	P_{12}
15½			15382.748 0.027	15361.703 -0.055
16½			15383.293 0.023	15360.999 0.023
17½			15383.802 -0.033	15360.236 0.026
18½			15384.346 -0.068	15359.437 -0.022
19½			15385.013 0.004	15358.662 -0.061
20½			15385.583 -0.035	15358.060 0.057
21½			15386.190 -0.052	15357.278 -0.020
22½			15386.872 -0.010	
23½			15387.562 0.026	
24½			15388.223 0.017	15355.291 0.016
25½			15388.929 0.039	15354.649 0.017
26½			15389.596 0.006	
27½			15390.316 0.011	
28½			15391.034 -0.001	15352.791 -0.007
29½			15391.820 0.039	15352.181 -0.037

	$\tilde{A}(100)$ - $\tilde{X}(300)$		$\tilde{A}(100)$ - $\tilde{X}(400)$
J	Q_1	P_{12}	Q_1
4½	14784.804 0.013		
5½		14777.656 0.068	
6½	14785.693 0.063		
7½	14786.005 -0.073	14775.809 0.001	
8½	14786.510 -0.035	14774.857 -0.089	
9½		14774.110 0.006	
10½	14787.508 -0.028		
11½	14787.978 -0.083	14772.435 -0.043	
12½	14788.662 0.058	14771.664 -0.031	
13½	14789.080 -0.087	14770.990 0.060	
14½		14770.158 -0.027	14205.866 -0.073
15½	14790.252 -0.099		14206.603 0.005
16½		14768.704 -0.050	14207.327 0.046
17½	14791.585 -0.028		14207.996 0.009
18½	14792.312 0.040	14767.303 -0.099	14208.640 -0.077
19½	14792.850 -0.101	14766.735 -0.020	14209.470 0.001
20½	14793.596 -0.054	14766.032 -0.096	14210.402 0.157
21½		14765.499 -0.022	14211.034 -0.011
22½			
23½	14795.887 0.025		
24½		14763.847 0.027	
25½			14214.422 -0.054
26½	14798.286 0.036		
27½		14762.307 0.008	

TABLE 2. (Continued.)

	$\tilde{A}(100)$ - $\tilde{X}(02^00)^2\Sigma^+$					
J	Q_2		R_{21}		R_2	
4½			15961.133	-0.024		
5½	15953.802	-0.034	15962.166	-0.041		
6½	15953.542	-0.014	15963.303	0.038		
7½	15953.271	-0.012				
8½						
9½						
10½			15967.570	-0.003		
11½	15952.224	-0.047			15960.714	-0.003
12½					15961.155	-0.008
13½			15970.864	-0.019		
14½	15951.522	-0.071				
15½			15973.232	0.104		
16½	15951.216	0.036	15974.342	0.081		
17½	15951.002	0.017				
18½			15976.645	0.095		
19½	15950.634	0.016				
20½						
21½			15980.120	0.083		
22½	15950.126	0.000				
23½						
24½						
25½	15949.702	-0.001				
26½						
27½			15987.158	-0.051		
28½	15949.261	-0.089	15988.374	-0.055		
29½	15949.170	-0.079				

	$\tilde{A}(100)$ - $\tilde{X}(02^20)^2\Delta$							
J	Q_2		R_{21}		R_2		P_2	
4½			15938.174	0.046	15934.762	-0.046		
5½	15930.809	-0.010	15939.219	0.036	15935.166	-0.034		
6½	15930.543	-0.003	15940.241	-0.006	15935.570	-0.030	15926.202	0.037
7½	15930.263	-0.018					15925.255	0.028
8½							15924.283	-0.015
9½								
10½			15944.594	0.004	15937.273	-0.016		
11½	15929.300	-0.012	15945.724	0.001	15937.833	0.074		
12½	15929.054	-0.063	15946.824	-0.021	15938.182	-0.036	15920.688	0.017
13½	15928.915	0.003	15947.910	-0.028	15938.610	-0.038	15919.832	0.021
14½	15928.649	-0.029					15918.949	0.007
15½			15950.247	0.034	15939.628	0.032	15918.076	0.032

TABLE 2. (Continued.)

	$\tilde{A}(100)$ - $\tilde{X}(02^20)^2\Delta$							
J	Q_2		R_{21}		R_2		P_2	
16½	15928.339	0.040	15951.402	0.040	15940.112	0.029		
17½	15928.166	0.043					15916.272	-0.066
18½			15953.693	0.006	15941.087	0.003	15915.555	0.057
19½	15927.832	0.036						
20½							15913.768	-0.078
21½			15957.142	-0.095	15942.634	-0.014		
22½	15927.371	-0.001						
23½							15911.448	0.014
24½			15960.881	0.020	15944.265	-0.023		
25½	15927.028	0.002						
26½							15909.125	0.022

TABLE 3. Resolved LIF Line Positions in the $\tilde{A}^2\Pi$ - $\tilde{X}^2\Sigma^+$ System of CaOD

	$\tilde{A}(100)$ - $\tilde{X}(100)$							
J	R_2		P_2		Q_2		R_{21}	
3½	16044.795	0.011						
4½	16045.165	-0.001						
5½	16045.527	-0.035	16038.145	-0.018				
6½	16045.971	-0.002	16037.340	-0.001				
7½	16046.382	-0.017						
8½	16046.823	-0.016	16035.754	0.013				
9½	16047.284	-0.009	16034.949	-0.014			16053.344	0.038
10½	16047.778	0.016	16034.168	-0.031	16040.629	-0.048		
11½	16048.226	-0.019						
12½	16048.680	-0.063	16032.722	0.005	16040.379	-0.050		
13½	16049.197	-0.059	16031.968	-0.029				
14½	16049.735	-0.047						
15½	16050.278	-0.045	16030.547	-0.055				
16½	16050.837	-0.042	16029.889	-0.037				
17½	16051.442	-0.006	16029.221	-0.044				
18½	16052.023	-0.009	16028.585	-0.034				
19½	16052.668	0.037	16027.960	-0.027				
20½	16053.269	0.026	16027.333	-0.037				
21½	16053.907	0.037	16026.740	-0.027				
22½	16054.550	0.039	16026.143	-0.036				
23½	16055.216	0.049	16025.589	-0.017				
24½	16055.890	0.054	16025.008	-0.039				
25½	16056.561	0.041	16024.476	-0.027				
26½	16057.238	0.020	16023.958	-0.015				
27½	16057.948	0.019	16023.422	-0.036				
28½	16058.689	0.034	16022.937	-0.021				
29½	16059.440	0.045						
30½	16060.185	0.036						
.								
.								
.								
40½							16093.235	-0.007
41½					16043.501	0.000		
42½							16096.282	-0.008
43½					16044.172	-0.001		
44½								
45½								
46½								
47½					16045.702	0.009		
48½					16046.097	-0.013		

TABLE 3. (Continued.)

	$\tilde{A}(100)$ - $\tilde{X}(100)$				$\tilde{A}(100)$ - $\tilde{X}(200)$			
J	P_1		R_1		R_2		P_2	
3½			15979.966	0.057	15445.617	0.050		
4½			15980.980	0.047	15445.949	-0.020		
5½	15974.541	0.051					15438.992	0.003
6½	15974.361	0.052			15446.812	-0.015	15438.189	-0.006
7½			15984.122	0.056	15447.286	0.002		
8½					15447.751	-0.009		
9½	15973.883	0.051			15448.252	-0.001	15435.961	0.038
10½					15448.764	-0.002		
11½					15449.320	0.024	15434.482	-0.019
12½	15973.477	0.030			15449.850	0.005		
13½			15990.648	0.041	15450.381	-0.031	15433.165	0.011
14½			15991.761	0.029				
15½	15973.188	0.034			15451.614	0.012		
16½	15973.096	0.020			15452.214	-0.010		
17½			15995.146	-0.016	15452.857	-0.007	15430.677	-0.004
18½			15996.332	0.008	15453.490	-0.033		
19½	15972.922	0.022			15454.161	-0.038		
20½	15972.890	0.029			15454.865	-0.029	15429.055	0.034
21½			15999.843	-0.020	15455.608	0.001		
22½			16001.058	-0.002	15456.330	-0.008		
23½	15972.830	0.033			15457.081	-0.007	15427.563	0.036
24½	15972.789	-0.005			15457.854	-0.001		
25½					15458.673	0.033		
26½					15459.436	-0.007		

	$\tilde{A}(100)$ - $\tilde{X}(300)$				$\tilde{A}(100)$ - $\tilde{X}(02^00)^2\Sigma^+$			
J	R_2		P_2		R_1		P_1	
3½	14852.179	0.022			16065.653	0.030		
4½	14852.601	0.025			16066.645	0.016		
5½			14845.547	-0.071			16060.181	0.017
6½			14844.851	0.003			16059.974	0.017
7½	14853.993	0.028			16069.648	-0.034		
8½								
9½			14842.639	-0.033			16059.387	0.016
10½	14855.581	0.028			16072.782	-0.005		
11½	14856.118	-0.008						
12½			14840.648	-0.046			16058.858	0.019
13½			14840.082	0.003	16075.898	-0.042		
14½	14857.973	-0.003			16076.948	-0.054		
15½	14858.671	0.035					16058.383	0.026
16½			14838.415	0.049			16058.205	-0.002

TABLE 3. (Continued.)

	$\tilde{A}(100)$ - $\tilde{X}(300)$				$\tilde{A}(100)$ - $\tilde{X}(02^00)^2\Sigma^+$			
J	R_2		P_2		R_1		P_1	
17½			14837.692	-0.147	16080.176	-0.041		
18½	14860.733	-0.015			16081.270	-0.028		
19½							16057.806	0.018
20½			14836.399	0.008			16057.709	0.050
21½	14863.032	-0.024			16084.552	-0.015		
22½					16085.617	-0.048		
23½			14835.140	-0.001			16057.332	0.034
24½	14865.569	0.011					16057.214	0.027
25½								
26½	14867.310	-0.023	14834.104	0.015				

	$\tilde{A}(100)$ - $\tilde{X}(02^20)^2\Delta$							
J	R_1		Q_1		P_1		P_{12}	
5½					16044.180	-0.027	16040.544	-0.032
6½					16043.987	-0.014	16039.768	0.002
7½								
8½			16048.941	0.062				
9½					16043.440	0.017	16037.379	0.006
10½								
11½			16050.240	0.067				
12½					16042.923	0.023	16035.017	-0.018
13½								
14½			16051.502	-0.018				
15½			16051.982	0.002	16042.456	0.026	16032.689	-0.063
16½					16042.298	0.014	16031.972	-0.030
17½	16064.241	-0.058						
18½	16065.333	-0.052	16053.418	0.026				
19½			16053.889	0.015	16041.857	-0.024	16029.787	0.000
20½					16041.814	0.057	16029.068	0.008
21½	16068.633	-0.038						
22½	16069.728	-0.047	16055.388	0.043				
23½			16055.880	0.035	16041.452	0.037	16026.902	-0.006
24½					16041.311	0.000	16026.189	-0.011

TABLE 4. Line Positions for the $\tilde{A}(010)^2\Delta_{5/2}$ - $\tilde{X}(010)^2\Pi$ Band of CaOH

J	${}^{S}R_{21}(e)$	${}^{S}R_{21}(f)$	$P_2(e)$	$P_2(f)$
2½	16040.967 -.003	16040.967 .001		
3½	16042.043 -.005	16042.043 .003		
4½	16043.138 -.007	16043.138 .008		
6½	16045.390 .000	16045.354 -.005		
7½	16046.534 -.004	16046.501 .003		
8½	16047.703 -.002	16047.648 -.005		
9½	16048.895 .006	16048.822 -.002		
10½	16050.096 .006	16050.014 .003		
11½		16051.222 .007	16026.815 .003	16026.930 .006
12½	16052.548 .002		16025.998 -.001	16026.128 -.002
13½	16053.796 -.004	16053.662 -.007	16025.203 .000	16025.365 .011
14½	16055.073 .002	16054.921 .001	16024.418 -.005	16024.598 .003
15½	16056.364 .004	16056.185 -.002	16023.658 -.001	16023.857 .002
16½	16057.665 -.001	16057.465 -.005	16022.915 .003	16023.137 .005
17½	16058.991 .002	16058.765 -.004	16022.179 -.002	16022.426 -.001
18½	16060.338 .009	16060.083 .000	16021.465 -.002	16021.743 .003
19½	16061.692 .005	16061.412 -.002	16020.770 .001	16021.070 .000
20½	16063.060 -.002	16062.765 .005	16020.087 .000	16020.419 .001
21½	16064.450 -.003	16064.119 -.002		16019.786 .001
22½	16065.868 .006	16065.488 -.010	16018.775 .003	16019.171 .003
23½	16067.290 .001	16066.896 .005	16018.139 -.001	16018.586 .016
24½	16068.733 .001	16068.300 .001	16017.521 -.002	16017.991 .002
25½	16070.186 -.006	16069.724 .001	16016.916 -.007	16017.419 -.007
26½	16071.669 .001	16071.162 .000	16016.324 -.015	16016.878 -.003
27½	16073.165 .003	16072.621 .004	16015.771 .000	
28½	16074.678 .005	16074.088 .001	16015.218 -.002	16015.843 .000
29½	16076.200 .000	16075.568 -.004	16014.683 -.002	16015.343 -.007
30½	16077.751 .007	16077.071 -.001	16014.164 -.001	16014.890 .015
31½	16079.308 .003	16078.587 .000	16013.663 .000	16014.415 -.002
32½	16080.885 .003	16080.114 -.003	16013.170 -.006	16013.984 .007
33½	16082.475 -.001	16081.663 .000	16012.702 -.003	16013.549 -.006
34½	16084.087 .001	16083.220 -.003	16012.255 .004	
35½	16085.715 .002	16084.798 .001	16011.813 .001	16012.761 .000
36½	16087.355 -.001	16086.389 .002	16011.387 -.003	16012.390 -.001
37½	16089.019 .003	16087.990 -.001	16010.985 .001	16012.037 .000
38½	16090.682 -.010	16089.609 .000	16010.589 -.004	16011.701 .000
39½	16092.396 .012	16091.242 .000	16010.215 -.004	16011.387 .006
40½	16094.093 .001	16092.887 -.002		16011.083 .004
41½	16095.816 -.001	16094.552 .003		16010.791 -.002
42½	16097.556 -.001	16096.224 .000		16010.518 -.007
43½	16099.317 .003	16097.907 -.004		16010.272 .000
44½		16099.613 .000		16010.032 -.004
45½	16102.877 .002	16101.328 .001		
46½	16104.678 -.002	16103.056 .003		
47½	16106.500 .000	16104.793 .001		
48½	16108.333 -.003	16106.543 .002		
49½	16110.185 -.002	16108.303 .001		
50½	16112.051 -.004	16110.075 .002		

TABLE 4. (Continued.)

J	${}^{S}R_{21}(e)$	${}^{S}R_{21}(f)$	$P_2(e)$	$P_2(f)$
51½	16113.932 -.006	16111.852 .000		
52½	16115.834 -.002	16113.645 .006		
53½		16115.433 .002		

J	$R_2(e)$	$Q_{21}(ef)$	$R_2(f)$	$Q_{21}(fe)$
1½	16038.575 .000		16038.575 -.004	
2½		16038.575 .003		16038.575 -.001
3½			16039.380 -.009	
4½				
5½				
6½	16040.677 -.018			
7½				
8½			16041.717 -.004	
9½	16042.155 -.006			
10½	16042.678 -.005		16042.767 -.010	
11½	16043.212 -.008		16043.328 -.004	
12½			16043.900 -.004	
14½			16045.091 -.010	
.				
.				
28½			16055.425 .002	
29½	16055.624 .000		16056.290 .002	16055.392 .004
30½	16056.457 -.006	16055.587 -.001	16057.169 -.002	16056.254 .002
31½	16057.313 -.004	16056.419 -.007	16058.069 -.002	16057.135 .001
32½	16058.187 .000	16057.276 -.003	16058.987 .000	16058.039 .007
33½	16059.072 -.001	16058.150 .002	16059.924 .004	16058.946 -.001
34½	16059.976 .003	16059.030 -.002		16059.880 .001
35½		16059.924 -.007		16060.833 .006
36½	16061.829 .008			
37½	16062.772 .005	16061.785 .009	16063.826 .010	
38½	16063.729 .000	16062.730 .008	16064.831 .000	16063.777 .006
39½	16064.708 .002	16063.679 -.003	16065.864 .002	16064.787 .003
40½	16065.696 -.002	16064.661 .003	16066.903 -.006	16065.816 .002
41½	16066.703 -.003	16065.651 .002	16067.971 -.001	16066.859 -.001
42½	16067.728 .000	16066.653 -.002	16069.051 .001	16067.921 .000
43½	16068.763 -.002	16067.679 .002	16070.144 .001	16068.999 .001
44½	16069.813 -.005	16068.719 .006	16071.251 -.001	16070.090 -.001
45½	16070.883 -.002	16069.761 -.003	16072.376 .001	16071.199 .001
46½	16071.968 .001	16070.827 -.003	16073.512 -.001	16072.323 .003
47½	16073.068 .004	16071.909 -.002	16074.662 -.003	16073.458 .001
48½	16074.173 -.003	16072.996 -.010	16075.824 -.006	16074.609 .002
49½	16075.308 .006	16074.113 -.004		16075.767 -.004
50½	16076.441 -.002	16075.252 .010	16078.200 .003	16076.945 -.002
51½		16076.384 .002	16079.400 .003	16078.134 -.002
52½	16078.767 -.002	16077.538 .001	16080.600 -.006	16079.341 .007
53½	16079.958 .004	16078.703 -.003	16081.823 .000	16080.533 -.010
54½		16079.891 .002	16083.050 .005	16081.763 .005

TABLE 4. (Continued.)

J	$R_2(e)$	$Q_{21}(ef)$	$R_2(f)$	$Q_{21}(fe)$
55½	16082.363 -.004		16084.276 .005	16082.978 -.002
56½	16083.599 .004	16082.297 -.003		16084.207 .003
57½	16084.840 .002	16083.532 .005	16086.714 -.007	
58½	16086.097 .003	16084.777 .009		
59½	16087.358 -.007	16086.019 -.005		
60½		16087.287 -.007		

TABLE 5. Line Positions for the $\tilde{A}(010)^2\Delta_{3/2}$ - $\tilde{X}(010)^2\Pi$ Band of CaOH

J	$R_1(e)$		$R_1(f)$		$^OP_{12}(e)$		$^OP_{12}(f)$	
10½	15984.385	-.001						
11½	15985.522	.001						
12½	15986.657	-.010					15960.439	.007
13½	15987.824	.001	15987.704	-.001			15959.583	.010
14½	15988.992	.002	15988.848	-.006			15958.720	-.006
15½	15990.165	-.003	15990.015	.001	15957.671	-.012	15957.889	-.001
16½	15991.351	-.006	15991.182	-.002	15956.823	-.009		
17½	15992.552	-.005	15992.354	-.009	15955.996	.006	15956.256	.002
18½	15993.764	-.004	15993.553	.000	15955.160	.001	15955.464	.011
19½	15994.990	.001	15994.746	-.006	15954.336	-.001	15954.670	.005
20½	15996.222	.001	15995.956	-.006	15953.521	-.004	15953.894	.006
21½	15997.469	.005	15997.183	.001	15952.727	.003	15953.127	.004
22½	15998.713	-.005	15998.400	-.012	15951.937	.005	15952.378	.007
23½	15999.983	.000	15999.653	.000	15951.156	.006	15951.625	-.006
24½	16001.267	.008	16000.907	.002	15950.378	-.001	15950.911	.008
25½	16002.545	.000	16002.166	-.001	15949.630	.013	15950.199	.011
26½	16003.843	.000	16003.441	.001	15948.860	-.006	15949.493	.007
27½	16005.148	-.003	16004.725	.001	15948.138	.013	15948.795	-.002
28½	16006.471	.001	16006.020	.000	15947.396	.002		
29½	16007.800	.000	16007.324	-.003	15946.661	-.012	15947.456	-.001
30½	16009.140	-.002	16008.646	.000	15945.962	-.001	15946.809	.001
31½	16010.495	.001	16009.980	.002	15945.261	-.002		
32½	16011.856	-.001	16011.321	-.001	15944.576	.003	15945.545	-.007
33½	16013.230	-.001	16012.680	.001	15943.893	-.001	15944.950	.005
34½	16014.620	.004	16014.050	.000	15943.228	.002	15944.352	-.002
35½	16016.011	-.002	16015.432	-.003	15942.566	-.002	15943.780	.002
36½	16017.420	.000	16016.835	-.001	15941.921	.001	15943.228	.010
37½	16018.832	-.006	16018.248	-.004	15941.279	-.004	15942.681	.006
38½	16020.269	.001	16019.683	-.002	15940.658	.001		
39½	16021.708	.000	16021.135	.000	15940.043	.002		
40½	16023.160	.000	16022.604	-.001	15939.436	-.001		
41½	16024.625	.002	16024.093	-.001	15938.851	.008		
42½	16026.095	-.002	16025.604	-.001	15938.255	-.005		
43½			16027.138	.000	15937.691	.003		
44½	16029.079	.000	16028.699	.005				
45½	16030.583	-.004	16030.269	-.005				
46½	16032.100	-.006	16031.878	-.001				
47½			16033.507	-.001				
48½			16035.162	.001				
49½			16036.834	-.004				
50½	16038.298	.003	16038.543	.006				
51½	16039.878	.008	16040.253	-.006				
52½	16041.449	-.008	16042.007	.007				
53½			16043.749	-.012				
54½			16045.533	-.007				
55½	16046.285	-.002	16047.342	.006				
56½	16047.917	-.003	16049.155	.006				
57½	16049.561	-.004	16050.987	.011				
58½	16051.218	-.002	16052.824	.007				

TABLE 5. (Continued.)

J	$^{Q}R_{12}(e)$	$Q_1(ef)$	$^{Q}R_{12}(f)$	$Q_1(fe)$
9½		15976.092 .002		15976.156 -.002
10½		15976.517 -.006		15976.602 -.004
11½		15976.965 .000		15977.072 .006
12½		15977.420 .003		15977.540 .003
13½		15977.878 .000		15978.020 .001
14½		15978.351 .002		15978.513 .001
15½				15979.017 .000
16½		15979.322 .002		15979.537 .004
⋮				
28½			15987.350 -.006	
29½	15987.222 -.003			15987.322 .001
30½	15987.854 -.007	15987.184 -.004		
31½	15988.506 .000	15987.819 -.004	15989.461 .000	15988.706 -.002
32½	15989.176 .014	15988.464 -.004	15990.192 .001	15989.427 .004
33½	15989.818 -.010	15989.123 .000	15990.936 .000	15990.160 .009
34½	15990.500 -.003	15989.785 -.002		15990.900 .005
35½	15991.184 -.005	15990.456 -.005	15992.483 .010	15991.657 .003
36½	15991.881 -.003	15991.139 -.007	15993.266 .000	15992.431 .001
37½	15992.587 -.003	15991.839 -.001	15994.086 .009	15993.226 .004
38½	15993.307 .002	15992.548 .004		15994.036 .005
39½	15994.036 .005	15993.266 .008	15995.760 .004	15994.864 .004
40½		15993.982 -.001	15996.627 .002	15995.703 -.005
41½	15995.520 .008	15994.715 -.002		15996.577 .001
42½	15996.268 .000	15995.458 -.003		15997.467 .001
43½		15996.220 .004		15998.376 -.004
44½	15997.809 -.001			
45½	15998.605 .009	15997.754 -.002		16000.284 .004
46½	15999.383 -.010	15998.544 .003		
47½	16000.209 .009	15999.331 -.006		16002.281 -.002
48½		16000.143 .001		
49½	16001.855 .010	16000.955 -.004		
50½		16001.788 .003		
51½		16002.626 .004		

TABLE 6. Line Positions for the $\tilde{A}(010)\kappa^2\Sigma^{(-)}$ - $\tilde{X}(000)^2\Sigma^+$ Band of CaOH

J	$^{Q}R_{12}$		$^{O}P_{12}$		$^{S}R_{21}$		$^{Q}P_{21}$	
1½			16406.913	.003			16408.717	-.008
2½			16405.689	.002			16408.646	-.002
3½			16404.478	.001	16414.513	-.001	16408.577	-.008
4½			16403.280	.001	16415.828	.003		
5½			16402.086	-.008	16417.152	.003		
6½	16409.978	-.003	16400.927	.005	16418.492	.007		
7½	16410.182	-.002	16399.762	-.001			band head	
8½	16410.398	-.002	16398.616	-.001	16421.206	.012		
9½	16410.631	.002	16397.484	.001	16422.573	.006		
10½	16410.870	.000	16396.365	.002	16423.952	.000		
11½	16411.122	-.003	16395.257	.001	16425.352	.002		
12½	16411.387	-.005	16394.162	.001	16426.763	.003	16408.577	.001
13½	16411.667	-.005	16393.077	-.003			16408.646	.008
14½	16411.960	-.005	16392.007	-.004	16429.604	-.012	16408.717	.005
15½	16412.270	-.001	16390.955	-.001	16431.061	-.001	16408.801	.003
16½	16412.588	-.002	16389.913	-.001	16432.509	-.011	16408.900	.003
17½	16412.920	-.001	16388.882	-.003	16433.986	-.004	16409.008	-.001
18½	16413.265	-.001	16387.856	-.014	16435.467	-.006	16409.138	.006
19½	16413.621	-.003	16386.875	.008	16436.973	.006	16409.279	.011
20½	16413.988	-.006	16385.878	.000	16438.490	.017	16409.427	.011
21½	16414.374	-.004	16384.890	-.013	16439.986	-.005		
22½	16414.772	-.002	16383.940	.000	16441.525	.004		
23½	16415.182	-.002	16383.000	.008	16443.060	-.003		
24½	16415.606	-.001	16382.055	-.001			16410.138	.005
25½	16416.042	.000	16381.129	-.005	16446.170	-.012	16410.341	-.002
26½	16416.490	-.001	16380.228	.002	16447.758	-.001	16410.568	.003
27½	16416.954	.001	16379.333	.002			16410.801	.002
28½	16417.428	-.001	16378.450	.000			16411.045	.000
29½	16417.923	.006	16377.584	.002	16452.564	.004	16411.305	.001
30½	16418.422	.003	16376.727	-.002	16454.193	.010	16411.571	-.004
31½	16418.933	-.001	16375.885	-.004	16455.817	-.001	16411.858	.000
32½	16419.465	.002	16375.059	-.004	16457.461	-.003	16412.154	.002
33½	16419.993	-.011	16374.250	-.001	16459.116	-.006	16412.458	-.002
34½	16420.560	.000	16373.458	.006	16460.783	-.008	16412.777	-.002
35½	16421.128	-.001	16372.669	.001			16413.110	.000
36½	16421.709	-.002	16371.905	.007			16413.450	-.003
37½	16422.307	.000	16371.143	.000			16413.808	.000
38½	16422.918	.001	16370.402	.001			16414.171	-.004
39½	16423.543	.002	16369.676	.002				
40½	16424.182	.003	16368.962	.001			16414.938	-.008
41½	16424.832	.002	16368.254	-.009			16415.342	-.006
42½	16425.505	.008						
43½	16426.182	.005						
44½	16426.878	.005						
45½	16427.585	.002						
46½	16428.313	.004						

TABLE 7. Line Positions for the $\tilde{A}(010)\mu^2\Sigma^{(+)}$ - $\tilde{X}(000)^2\Sigma^+$ Band of CaOH

J	R_1		P_1		R_2		P_2	
½	16311.007	.005			16311.310	.011		
1½	16311.792	.002	16309.556	.002	16311.904	.002	16308.701	-.001
2½	16312.592	.002	16309.003	.008	16312.516	.000		
3½	16313.401	.001	16308.444	-.002	16313.135	-.006	16307.224	.001
4½	16314.218	-.003					16306.503	.004
5½			16307.379	-.002	16314.419	-.003	16305.788	.001
6½	16315.879	-.018	16306.863	-.002	16315.073	-.005	16305.085	.000
7½	16316.753	.002	16306.360	-.001	16315.749	.004	16304.397	.003
8½	16317.620	.004	16305.863	-.004	16316.422	-.001	16303.717	.003
9½	16318.510	.018	16305.391	.007	16317.108	-.003	16303.045	.001
10½	16319.373	-.006	16304.907	-.006	16317.809	.000	16302.392	.007
11½	16320.268	-.009	16304.458	.006	16318.510	-.008	16301.751	.014
12½	16321.182	-.004	16304.000	-.003	16319.237	.001	16301.099	.000
13½	16322.104	-.002	16303.559	-.006	16319.968	.002	16300.467	-.005
14½	16323.027	-.010	16303.134	-.004	16320.705	.000	16299.858	.002
15½	16323.975	-.003	16302.723	.000	16321.453	-.001	16299.248	-.002
16½	16324.928	-.003	16302.316	-.002	16322.213	.000	16298.652	-.002
17½	16325.890	-.005	16301.924	-.001			16298.082	.014
18½	16326.869	-.001	16301.541	-.002	16323.762	.001	16297.496	.003
19½	16327.848	-.007	16301.167	-.006	16324.549	.000	16296.935	.007
20½	16328.850	-.002	16300.807	-.006	16325.352	.004	16296.373	.000
21½	16329.859	-.001	16300.470	.005	16326.156	.001	16295.828	-.001
22½	16330.877	-.001	16300.125	-.004	16326.974	.002	16295.294	.000
23½	16331.905	-.003	16299.803	-.001	16327.806	.008	16294.772	.003
24½	16332.941	-.007	16299.487	-.003	16328.636	.004	16294.255	.001
25½	16334.000	.000	16299.184	-.003	16329.478	.002	16293.746	-.002
26½	16335.056	-.006	16298.897	.001	16330.329	.001	16293.250	-.002
27½	16336.134	-.001	16298.623	.006	16331.191	.002	16292.765	.000
28½	16337.218	-.001	16298.345	-.003	16332.057	.000	16292.286	-.001
29½	16338.324	.010	16298.082	-.009	16332.941	.007	16291.816	-.002
30½	16339.422	.002	16297.843	-.003	16333.818	.000	16291.352	-.005
31½	16340.538	.001	16297.612	.000	16334.702	-.006	16290.901	-.004
32½	16341.665	.000	16297.390	.000	16335.603	-.003	16290.463	.002
33½	16342.804	.001	16297.180	.001	16336.511	.001	16290.023	-.002
34½	16343.954	.001	16296.981	.002	16337.418	-.001	16289.595	-.001
35½	16345.115	.002	16296.794	.003	16338.324	-.009	16289.172	-.001
36½	16346.292	.008	16296.618	.004	16339.253	.002	16288.758	.001
37½	16347.471	.005	16296.451	.002	16340.171	-.001		
38½	16348.664	.005	16296.299	.003	16341.094	-.002		
39½	16349.871	.009	16296.157	.003	16342.015	-.006		
40½	16351.090	.013	16296.018	-.005	16342.945	-.001		
41½	16352.303	.001	16295.912	.008	16343.867	-.004		
42½	16353.543	.005			16344.791	-.002		
43½	16354.785	.001			16345.708	-.003		
44½	16356.043	.001			16346.625	.000		
45½	16357.312	.002			16347.536	.002		
46½	16358.591	.002			16348.433	-.005		

TABLE 7. (Continued.)

J	R_1	P_1	R_2	P_2
47½	16359.880	.002	16349.336	.001
48½	16361.179	.001	16350.231	.004
49½	16362.489	.000		
50½	16363.810	-.001	16352.000	.003
51½	16365.138	-.005	16352.879	.002
52½	16366.483	-.003	16353.758	.003
53½	16367.835	-.004	16354.634	.002
54½	16369.196	-.007	16355.513	.004
55½	16370.571	-.007	16356.386	-.002
56½	16371.949	-.014	16357.256	-.013
57½			16358.155	.003
58½			16359.042	.002
59½			16359.934	.002
60½			16360.832	.002

TABLE 8. Line Positions for the $\tilde{A}(010)$ - $\tilde{X}(010)/(000)$ Bands of CaOH

$\tilde{A}(010)\kappa^2\Sigma$ - $\tilde{X}(010)^2\Pi$		$\tilde{A}(010)\mu^2\Sigma$ - $\tilde{X}(010)^2\Pi$		$\tilde{A}(010)^2\Delta_{3/2}$ - $\tilde{X}(000)^2\Sigma$	
J	$P_2(e)$	$P_2(f)$		J	R_{12}
3½		15954.660	.005	40½	16347.070 -.001
4½		15953.946	.002	41½	16347.861 .004
5½		15953.246	.000	42½	16348.664 .001
6½		15952.560	-.002	43½	16349.486 -.004
7½		15951.893	.002	44½	16350.336 -.004
8½		15951.223	-.010	45½	16351.216 .002
9½		15950.591	.003	46½	16352.103 -.008
10½	16048.628 .002	15949.955	-.001	47½	16353.029 -.002
11½	16048.013 .005	15949.338	.000	48½	16353.974 -.001
12½	16047.409 .005	15948.732	.000	49½	16354.939 -.003
13½	16046.814 .001	15948.144	.004	50½	16355.929 -.002
14½	16046.233 -.004	15947.561	.001	51½	16356.939 -.001
15½	16045.676 .003	15946.997	.003	52½	16357.970 .000
16½	16045.116 -.008	15946.438	-.002	53½	16359.017 .000
17½	16044.593 .006	15945.898	-.001	54½	16360.082 -.001
18½	16044.063 -.002	15945.368	-.003	55½	16361.173 .009
19½	16043.558 .002	15944.855	-.001	56½	16362.260 -.001
20½	16043.062 .001	15944.352	-.001	57½	16363.371 -.001
21½	16042.581 .002	15943.861	-.002	58½	16364.500 .004
22½	16042.110 -.001	15943.383	-.002	59½	16365.638 .004
23½	16041.654 -.003	15942.922	.002		
24½	16041.213 -.003	15942.470	.003		
25½	16040.780 -.008	15942.025	-.001		
26½	16040.373 -.001	15941.598	.001		
27½	16039.975 .001	15941.181	.002		
28½	16039.592 .004	15940.776	.002		
29½	16039.212 -.002	15940.380	.000		
30½	16038.852 -.003	15939.996	-.001		
31½	16038.507 -.002	15939.622	-.003		
32½	16038.174 -.002	15939.262	-.001		
33½	16037.856 -.001	15938.909	-.003		
34½	16037.555 .003	15938.570	.000		
35½	16037.259 -.001	15938.240	.002		
36½	16036.977 -.004	15937.917	.002		
37½	16036.705 -.011	15937.600	.001		
38½	16036.469 .004	15937.294	.002		
39½	16036.229 .003	15936.992	.002		
40½	16036.003 .001	15936.695	.000		
41½		15936.407	.003		
42½		15936.121	.005		
43½	16035.405 -.004	15935.832	.001		
44½	16035.238 .000	15935.538	-.010		
45½		15935.267	.003		

TABLE 9. Line Positions for the $\tilde{A}(010)^2\Delta_{5/2}$ - $\tilde{X}(010)^2\Pi$ Band of CaOD

J	${}^{S}R_{21}(e)$	${}^{S}R_{21}(f)$	$P_2(e)$	$P_2(f)$
3½	16036.863 -.002			
4½	16037.859 .000			
5½	16038.861 -.006			
6½				
7½	16040.931 .000			
8½	16041.993 .007			16025.367 -.006
9½	16043.052 -.004		16024.507 -.008	16024.601 .003
10½	16044.144 .002	16044.049 -.009	16023.738 -.001	16023.835 -.004
11½		16045.143 .000	16022.971 -.006	16023.087 -.009
12½	16046.355 -.005	16046.249 .008	16022.227 -.003	16022.369 .001
13½	16047.492 .000	16047.346 -.007	16021.495 -.001	16021.660 .004
14½	16048.642 .002	16048.481 .002	16020.777 .000	16020.960 .000
15½	16049.805 .003	16049.608 -.011	16020.071 -.001	16020.281 .002
16½	16050.990 .010	16050.772 -.001	16019.381 .000	16019.609 -.005
17½	16052.178 .004	16051.939 -.001	16018.705 .001	16018.971 .006
18½	16053.387 .005	16053.122 .002		16018.337 .006
19½	16054.605 -.001	16054.316 .001	16017.391 -.002	16017.714 .001
20½	16055.843 -.002		16016.758 -.001	16017.108 -.002
21½	16057.098 .000	16056.746 .002	16016.134 -.005	16016.524 .001
22½		16057.992 .013	16015.536 .004	16015.952 .001
23½	16059.655 .003	16059.226 -.001	16014.944 .004	16015.395 .000
24½	16060.956 .005	16060.486 -.003	16014.351 -.011	16014.859 .004
25½	16062.278 .013	16061.766 .002	16013.809 .011	
26½	16063.597 .003	16063.046 -.006	16013.244 -.004	
27½	16064.940 .002	16064.355 .002	16012.711 -.002	16013.326 .000
28½	16066.294 -.003	16065.662 -.006	16012.195 .004	16012.848 .001
29½	16067.674 .003	16066.994 -.001	16011.684 .001	16012.383 .000
30½	16069.062 .002	16068.336 .001	16011.192 .002	16011.942 .007
31½	16070.466 .002	16069.691 .003	16010.704 -.006	16011.506 .004
32½	16071.893 .011	16071.042 -.012	16010.247 .003	16011.087 .003
33½	16073.321 .006	16072.433 .001	16009.796 .003	
34½	16074.770 .007	16073.816 -.006	16009.351 -.004	16010.293 .001
35½	16076.226 .001	16075.227 .003	16008.931 .000	16009.916 -.002
36½	16077.707 .005	16076.639 .001		16009.561 .002
37½	16079.192 -.002	16078.061 -.002	16008.126 .000	16009.214 .000
38½	16080.697 -.003		16007.747 .003	16008.891 .008
39½	16082.221 .000		16007.380 .004	
40½	16083.754 -.002	16082.397 -.006		16008.265 .003
41½	16085.305 -.001			16007.973 .001

TABLE 9. (Continued.)

J	$R_2(e)$		$Q_{21}(ef)$		$R_2(f)$		$Q_{21}(fe)$	
36½					16055.363	.006		
37½	16055.166	-.004			16056.236	-.004	16055.313	-.002
38½	16056.024	.006	16055.131	.004	16057.127	-.008	16056.194	-.002
39½	16056.880	.001	16055.978	.005	16058.046	.003	16057.090	-.001
40½	16057.754	.000	16056.829	-.004	16058.972	.010		
41½			16057.705	-.002	16059.890	-.003	16058.917	.001
42½	16059.543	.001	16058.596	.003	16060.834	.000	16059.843	-.002
43½	16060.457	.001	16059.496	.003	16061.787	.003	16060.780	-.005
44½	16061.392	.009	16060.410	.004	16062.741	-.001	16061.733	-.001
45½	16062.324	.000	16061.332	.000			16062.689	-.002
46½	16063.280	.003	16062.279	.008	16064.669	-.007		
47½	16064.246	.003	16063.221	-.002	16065.657	.007	16064.616	-.007
48½			16064.191	.002	16066.611	-.014	16065.587	-.008
49½	16066.210	-.005	16065.151	-.016	16067.596	-.004	16066.579	.010
50½	16067.222	.002	16066.157	-.001			16067.546	.002
51½	16068.236	-.002	16067.154	-.008	16069.554	.003	16068.509	-.009
52½	16069.272	.003	16068.171	-.008	16070.535	.010	16069.496	.004
53½	16070.318	.005	16069.206	-.003			16070.461	-.004
54½	16071.358	-.011	16070.256	.005				
55½	16072.441	.003	16071.305	-.002				
56½	16073.512	-.008	16072.385	.010				
57½	16074.615	.000	16073.453	-.003				
58½			16074.544	-.005				

TABLE 10. Line Positions for the $\tilde{A}(010)^2\Delta_{3/2}$ - $\tilde{X}(010)^2\Pi$ Band of CaOD

J	$R_1(e)$	$R_1(f)$	$^OP_{12}(e)$	$^OP_{12}(f)$
7½			15960.756 .002	
8½	15976.488 -.001	15976.435 -.005		15959.982 .002
9½		15977.440 -.001	15959.082 .011	15959.150 -.009
10½	15978.524 .001	15978.449 -.001		
11½				
12½	15980.592 -.004	15980.488 -.007	15956.613 .003	15956.760 .000
13½	15981.648 .000	15981.539 .008	15955.802 -.005	15955.984 .003
14½	15982.715 .006	15982.571 -.005	15955.010 -.003	15955.215 .002
15½	15983.786 .006	15983.627 -.004	15954.223 -.004	15954.461 .004
16½	15984.864 .003	15984.693 -.002		15953.710 -.001
17½	15985.955 .003	15985.776 .008	15952.682 .000	15952.979 .003
18½	15987.062 .010	15986.849 -.002		
19½	15988.161 -.002	15987.943 -.002	15951.167 -.004	15951.536 -.005
20½	15989.279 -.004	15989.053 .005		15950.844 .003
21½	15990.417 .003	15990.160 -.002	15949.691 -.005	
22½	15991.555 .001	15991.288 .001		15949.473 -.004
23½	15992.699 -.005	15992.426 .003	15948.255 .000	
24½	15993.862 -.002	15993.571 .000	15947.535 -.013	15948.174 .011
25½	15995.036 .002	15994.732 .001	15946.848 -.003	15947.535 .010
26½	15996.213 -.001	15995.905 .001	15946.160 -.002	15946.891 -.011
27½	15997.403 .000	15997.093 .002	15945.483 .002	15946.297 .004
28½	15998.601 -.002	15998.294 .002	15944.810 .000	15945.699 .000
29½	15999.812 -.001	15999.507 -.001	15944.157 .009	15945.115 -.006
30½	16001.033 .001	16000.742 .001	15943.494 -.001	15944.562 .003
31½	16002.262 .000	16001.996 .005	15942.845 -.006	
32½	16003.501 -.001	16003.257 -.002	15942.211 -.006	
33½	16004.750 -.002	16004.548 .001	15941.591 .000	
34½	16006.012 .001	16005.853 -.001	15940.974 -.001	
35½	16007.285 .004	16007.184 .003	15940.371 .003	
36½	16008.555 -.006	16008.537 .009	15939.774 .004	
37½	16009.847 -.004	16009.894 -.001	15939.172 -.010	
38½	16011.152 .001	16011.284 .003	15938.594 -.008	
39½	16012.459 -.003	16012.685 -.001	15938.037 .004	
40½	16013.788 .006	16014.112 .003		
41½	16015.110 -.003	16015.549 .000		
42½	16016.450 -.003	16017.006 .001	15936.384 .003	
43½	16017.801 -.004	16018.477 .001	15935.845 -.004	
44½	16019.161 -.005	16019.961 .001	15935.330 .003	
45½	16020.531 -.006	16021.459 .001		
46½	16021.916 -.003	16022.969 .000	15934.307 -.005	
47½	16023.312 .000	16024.495 .003	15933.823 .004	
48½		16026.022 -.004	15933.349 .013	
49½		16027.569 -.002	15932.866 .003	
50½		16029.124 -.002		
51½		16030.685 -.007		
52½		16032.269 .001	15931.509 .006	
53½			15931.075 .005	

TABLE 10. (Continued.)

J	$^{Q}R_{12}(e)$	$Q_1(ef)$	$^{Q}R_{12}(f)$	$Q_1(fe)$
5½		15969.487 -.003		15969.515 .001
6½				15969.882 .000
7½		15970.209 -.006		15970.263 .003
8½				15970.646 -.003
9½		15970.973 .000		15971.048 .001
10½		15971.363 -.001		15971.463 .007
11½		15971.764 .000		15971.879 .004
12½		15972.178 .005		15972.312 .007
13½		15972.591 .001		15972.748 .002
14½		15973.024 .009		15973.203 .006
15½		15973.452 .003		15973.664 .005
16½		15973.896 .005		15974.137 .005
17½		15974.345 .004		15974.620 .004
18½		15974.801 .000		15975.115 .004
19½		15975.268 .000		15975.617 .000
20½		15975.748 .004		15976.143 .007
21½		15976.229 .000		15976.662 -.004
22½		15976.733 .011		
23½		15977.225 .001	15978.364 .006	15977.754 -.009
24½			15978.939 -.002	15978.330 -.001
25½	15978.808 -.001	15978.247 -.005	15979.547 .010	15978.908 -.004
26½		15978.776 -.004	15980.147 -.001	15979.508 .001
27½	15979.889 -.003	15979.319 .003	15980.772 -.002	15980.117 .000
28½	15980.453 .007	15979.860 .000		15980.742 .000
29½	15981.000 -.009	15980.416 .003	15982.079 .002	15981.386 .002
30½	15981.571 -.010	15980.971 -.004	15982.747 -.007	15982.046 .004
31½	15982.153 -.008	15981.534 -.011		15982.712 -.007
32½	15982.747 -.003	15982.118 -.007		15983.411 -.003
33½		15982.712 .000		15984.131 .001
34½	15983.952 -.002	15983.307 -.002		15984.861 -.005
35½	15984.576 .006	15983.915 .001		15985.620 -.004
36½	15985.186 -.008	15984.532 .003		15986.412 .009
37½	15985.819 -.008			15987.203 -.002
38½	15986.464 -.005			15988.026 -.002
39½	15987.115 -.004			15988.863 -.010
40½	15987.782 .003		15990.656 -.013	
41½		15987.736 .003	15991.567 -.006	15990.628 .006
42½	15989.122 -.004	15988.397 -.003		
43½	15989.815 .003	15989.073 -.004		
44½	15990.507 -.001	15989.759 -.003		
45½	15991.220 .007	15990.458 .001		
46½	15991.927 .000	15991.163 .003		
47½	15992.649 -.001	15991.871 -.002		
48½	15993.377 -.005	15992.592 -.003		
49½	15994.131 .008	15993.330 .004		
50½		15994.078 .011		
51½		15994.815 -.001		
52½		15995.580 .005		

TABLE 11. Line Positions for the $\tilde{A}(010)\kappa^2\Sigma^{(-)}$ - $\tilde{X}(000)^2\Sigma^+$ Band of CaOD

J	$^sR_{21}$	$^QR_{12}$	$^QP_{21}$	$^OP_{12}$
½		16311.507 -.003		
1½	16313.988 .003	16311.656 -.005	16311.140 .003	
2½		16311.815 -.010	16311.040 .001	
3½	16316.271 -.007	16311.995 -.008	16310.956 .002	16307.424 .003
4½	16317.446 .002	16312.186 -.007	16310.883 .001	16306.373 .000
5½	16318.628 .005	16312.386 -.011		16305.335 -.003
6½	16319.816 .001	16312.598 -.016		16304.318 .001
7½	16321.019 -.001	16312.841 -.004		16303.311 .001
8½	16322.243 .005	16313.088 -.001		16302.319 .004
9½	16323.473 .004	16313.346 .000	Band head	16301.329 -.005
10½	16324.714 .001	16313.615 -.001		16300.363 -.004
11½	16325.972 .003	16313.887 -.013		16299.403 -.010
12½	16327.240 .002	16314.198 .000		16298.472 -.001
13½	16328.522 .002	16314.504 -.004		16297.549 .003
14½	16329.817 .002	16314.830 -.003	16310.883 .001	16296.636 .003
15½	16331.124 .002	16315.166 -.004	16310.956 .003	16295.734 .001
16½	16332.446 .004	16315.521 -.001	16311.040 .003	16294.849 .002
17½	16333.779 .004	16315.882 -.005	16311.140 .005	16293.979 .004
18½	16335.119 -.001	16316.264 -.001	16311.244 -.001	16293.120 .003
19½	16336.483 .005	16316.657 .000	16311.372 .004	16292.276 .004
20½	16337.851 .003	16317.052 -.011	16311.507 .004	16291.441 .000
21½	16339.233 .002	16317.480 -.002	16311.656 .004	16290.630 .005
22½	16340.631 .005	16317.918 .003	16311.815 .001	16289.822 .000
23½	16342.032 -.002	16318.369 .007	16311.995 .007	16289.031 -.002
24½	16343.455 .001	16318.823 .000	16312.186 .011	16288.257 -.001
25½	16344.885 -.001	16319.296 -.001	16312.386 .011	16287.499 .001
26½	16346.330 -.001	16319.789 .003	16312.598 .011	16286.754 .003
27½	16347.786 -.002	16320.285 -.003		16286.021 .002
28½	16349.258 .000	16320.803 -.002		16285.302 .001
29½	16350.737 -.002	16321.336 .000	16313.311 .010	16284.604 .006
30½	16352.231 -.002	16321.880 -.001	16313.569 .004	16283.900 -.009
31½	16353.735 -.004	16322.442 .002	16313.845 .004	16283.244 .010
32½	16355.255 -.002	16323.018 .004	16314.129 .000	
33½	16356.781 -.006	16323.611 .008	16314.427 -.003	16281.928 -.002
34½	16358.326 -.003	16324.205 -.001	16314.742 -.002	16281.304 .004
35½	16359.881 -.002		16315.073 .003	16280.691 .006
36½	16361.446 -.003	16325.460 .001	16315.406 -.003	16280.087 .001
37½	16363.025 -.003	16326.111 .002	16315.753 -.008	16279.510 .008
38½	16364.615 -.003	16326.778 .004	16316.119 -.006	16278.942 .008
39½	16366.212 -.007	16327.457 .001	16316.496 -.005	
40½	16367.827 -.006	16328.161 .006	16316.888 -.002	
41½	16369.452 -.007	16328.875 .003	16317.286 -.005	
42½	16371.098 .002	16329.612 .004		
43½	16372.737 -.008	16330.367 .004		
44½	16374.399 -.006			
45½	16376.077 .000	16331.937 .000		

TABLE 11. (Continued).

J	$^{S}R_{21}$		$^{Q}R_{12}$		$^{Q}P_{21}$		$^{O}P_{12}$	
46½	16377.759	-.002	16332.760	.001				
47½	16379.456	-.001	16333.600	-.006				
48½	16381.165	.001	16334.473	-.007				
49½			16335.377	-.005				
50½	16384.612	.000	16336.305	-.009				
51½	16386.358	.005						
52½	16388.107	.001						
53½	16389.870	.001						

TABLE 12. Line Positions for the $\tilde{A}(010)\mu^2\Sigma^{(+)}$ - $\tilde{X}(000)^2\Sigma^+$ Band of CaOD

J	R_1	R_2	P_1	P_2
½		16226.419 .004		
1½				
2½	16227.781 .001	16227.460 -.001		
3½	16228.551 .000	16228.014 .014	16223.997 .007	
4½	16229.326 -.007	16228.551 .001	16223.539 .001	
5½	16230.126 .001	16229.122 .012	16223.106 .010	16221.348 .012
6½	16230.930 .001	16229.677 -.004	16222.666 .000	16220.680 .006
7½	16231.736 -.008	16230.278 .015	16222.249 .002	16220.022 -.001
8½	16232.569 -.001	16230.859 .005	16221.835 -.005	16219.381 -.001
9½	16233.403 -.004	16231.458 .002	16221.439 -.004	16218.754 .002
10½	16234.257 .002	16232.072 .003		
11½	16235.110 -.004	16232.689 -.002	16220.680 -.003	
12½		16233.320 -.003	16220.314 -.006	16216.919 -.006
13½	16236.853 -.012	16233.975 .009	16219.963 -.005	16216.347 .011
14½	16237.757 -.001	16234.622 .004	16219.618 -.010	16215.754 -.004
15½	16238.664 .003	16235.284 .005	16219.297 -.001	16215.197 .007
16½	16239.578 .002	16235.955 .005	16218.979 -.001	16214.631 -.001
17½	16240.498 -.004	16236.636 .006	16218.671 -.003	16214.085 .001
18½	16241.440 .001	16237.323 .003	16218.376 -.003	16213.553 .008
19½	16242.380 -.007	16238.021 .003		16213.018 .002
20½	16243.348 .002	16238.726 .002	16217.817 -.005	16212.496 .000
21½	16244.315 -.001	16239.446 .007	16217.560 -.001	
22½		16240.163 .001	16217.312 .001	16211.483 .000
23½	16246.288 -.002	16240.893 .002	16217.068 -.005	
24½	16247.295 .001	16241.631 .003	16216.845 -.001	16210.502 -.003
25½	16248.307 -.002	16242.380 .009	16216.623 -.008	16210.012 -.015
26½	16249.334 -.001	16243.122 .002	16216.425 -.002	16209.556 .000
27½	16250.362 -.010	16243.869 -.004	16216.229 -.006	16209.089 -.004
28½	16251.421 .001	16244.627 -.004		16208.644 .009
29½	16252.477 -.002	16245.386 -.005	16215.878 -.007	16208.175 -.007
30½	16253.547 -.003	16246.141 -.013		
31½	16254.637 .006	16246.916 -.001	16215.579 -.002	
32½	16255.719 -.005	16247.675 -.006	16215.439 -.007	
33½	16256.828 .000	16248.442 -.002	16215.321 -.002	
34½	16257.942 .000	16249.202 -.004	16215.197 -.014	
35½	16259.069 .001	16249.966 .000	16215.106 -.005	
36½	16260.197 -.008	16250.721 -.003	16215.023 .001	
37½	16261.355 .002	16251.473 -.007	16214.948 .002	
38½	16262.514 .002	16252.229 -.005	16214.875 -.005	
39½	16263.682 .000	16252.988 .000	16214.827 .001	
40½	16264.868 .005	16253.743 .000		
41½	16266.061 .005	16254.491 -.007		
42½	16267.265 .006	16255.256 .001		
43½	16268.478 .005	16256.019 .003		
44½	16269.704 .006	16256.787 .007		
45½	16270.940 .006	16257.546 -.002		

TABLE 12. (Continued.)

J	R_1		R_2		P_1	P_2
46½	16272.184	.002	16258.320	-.002		
47½	16273.442	.002	16259.106	.005		
48½	16274.711	.002	16259.893	.006		
49½	16275.994	.005	16260.683	.004		
50½	16277.284	.004	16261.487	.009		
51½			16262.295	.010		
52½	16279.898	.004				
53½	16281.221	.003				
54½	16282.557	.005				
55½	16283.900	.002				
56½	16285.250	-.004				
57½	16286.619	-.001				
58½	16287.992	-.006				
59½	16289.382	-.005				
60½	16290.779	-.007				
61½	16292.190	-.006				
62½	16293.612	-.004				

TABLE 13. Line Positions for the $\tilde{A}(010)$ - $\tilde{X}(010)/(000)$ Bands of CaOD

	$\tilde{A}(010)\kappa^2\Sigma$ - $\tilde{X}(010)^2\Pi$		$\mu^2\Sigma$ - $\tilde{X}(010)^2\Pi$	$^2\Delta_{3/2}$ - $\tilde{X}(000)^2\Sigma$
J	$R_2(e)$	$P_2(e)$	$P_2(f)$	R_{12}
4½	16047.865 -.004		15955.478 -.003	
5½	16048.430 -.008		15954.814 .002	
6½				
7½	16049.606 -.005		15953.498 -.010	
8½	16050.210 -.006	16038.700 -.004		
9½		16038.078 -.005		
10½		16037.478 .003	15951.632 -.004	
11½		16036.875 -.004	15951.028 -.006	
12½		16036.300 .005	15950.441 -.002	
13½		16035.721 -.003	15949.867 .004	
14½		16035.165 .001	15949.297 .003	
15½		16034.616 -.001	15948.740 .005	
16½		16034.076 -.005	15948.181 -.006	
17½		16033.559 .001	15947.657 .007	
18½		16033.053 .006	15947.130 .007	
19½		16032.547 -.001	15946.612 .006	
20½		16032.057 -.004	15946.102 .003	
21½		16031.584 -.003	15945.610 .008	
22½		16031.120 -.004	15945.114 .000	
23½		16030.672 -.002	15944.643 .008	
24½		16030.243 .008	15944.171 .006	
25½			15943.705 .001	
26½		16029.398 .003	15943.255 .005	
27½		16028.993 .000	15942.806 .002	
28½		16028.606 .003	15942.362 -.002	
29½		16028.223 -.002	15941.929 -.002	
30½		16027.859 .000	15941.499 -.003	
31½		16027.509 .004	15941.084 .006	
32½		16027.159 -.004	15940.655 -.002	
33½		16026.828 -.005	15940.239 .001	
34½		16026.520 .004	15939.818 -.003	
35½		16026.210 .000	15939.408 .004	16252.562 -.005
36½		16025.918 .002	15938.985 -.002	16253.341 -.004
37½		16025.635 .000		16254.145 .000
38½		16025.360 -.005	15938.147 -.004	16254.960 -.005
39½		16025.105 -.002	15937.733 .000	16255.800 -.004
40½			15937.310 -.004	16256.660 -.003
41½		16024.625 -.003	15936.902 .006	16257.540 .001
42½		16024.404 -.003	15936.473 -.007	16258.432 .000
43½		16024.187 -.010		16259.336 -.005
44½		16023.982 -.018		16260.258 -.007
45½		16023.818 .004		16261.203 -.001
46½		16023.640 .000		16262.153 -.003
47½				16263.118 -.003

TABLE 13. (Continued.)

	$\tilde{A}(010)\kappa^2\Sigma$ - $\tilde{X}(010)^2\Pi$		$\mu^2\Sigma$ - $\tilde{X}(010)^2\Pi$	$^2\Delta_{3/2}$- $\tilde{X}(000)^2\Sigma$
J	$R_2(e)$	$P_2(e)$	$P_2(f)$	R_{12}
48½		16023.339 .010		16264.103 .005
49½	16085.128 -.001	16023.187 .004		16265.095 .007
50½	16086.222 .001			16266.095 .006
51½	16087.333 .009	16022.958 .006		16267.108 .007
52½	16088.433 -.005	16022.842 -.008		16268.131 .008
53½	16089.564 .000	16022.758 -.002		16269.161 .004
54½	16090.700 -.001	16022.678 -.004		
55½	16091.841 -.008	16022.612 -.004		
56½	16093.004 -.004	16022.560 -.002		
57½	16094.182 .005			
58½	16095.355 -.003			
59½	16096.558 .008			
60½	16097.756 .003			

TABLE 14. Line Positions for the $\tilde{A}(100)^2\Pi_{3/2}$ - $\tilde{X}(000)^2\Sigma^+$ Band of CaOH

J	R_2		P_2		Q_2	
1½					16643.693	-.004
2½	16645.724	-.013			16643.390	.013
3½	16646.092	-.005			16643.065	.002
4½	16646.455	-.008			16642.750	-.004
5½	16646.829	-.005			16642.452	.002
6½	16647.207	-.004			16642.146	-.006
7½	16647.589	-.005			16641.857	-.003
8½	16647.982	.000			16641.568	-.004
9½	16648.376	.000			16641.287	-.003
10½	16648.773	-.003			16641.012	-.001
11½	16649.178	-.003			16640.741	.000
12½	16649.593	.001	16632.071	.005	16640.477	.003
13½	16650.014	.005	16631.137	.001	16640.211	-.001
14½	16650.431	.000	16630.210	-.001	16639.954	-.001
15½	16650.860	.000	16629.298	.005	16639.704	.002
16½	16651.290	-.004	16628.388	.008	16639.458	.003
17½	16651.732	-.003	16627.479	.005	16639.214	.002
18½	16652.183	.002	16626.567	-.007	16638.977	.003
19½	16652.641	.007	16625.685	.004	16638.747	.006
20½	16653.095	.002	16624.796	.002	16638.515	.003
21½	16653.565	.006	16623.918	.005	16638.284	-.004
22½	16654.028	-.003	16623.041	.001	16638.074	.005
23½	16654.504	-.006	16622.172	-.001	16637.854	-.001
24½	16655.000	.004	16621.321	.008	16637.650	.004
25½	16655.486	-.003	16620.472	.011	16637.445	.004
26½	16655.990	.001	16619.621	.005	16637.242	.001
27½	16656.496	.000	16618.804	.026	16637.046	.000
28½	16657.004	-.007	16617.956	.008	16636.854	-.003
29½	16657.523	-.010	16617.133	.008	16636.676	.004
30½	16658.056	-.007			16636.492	.000
31½	16658.586	-.015			16636.319	.001
32½					16636.148	-.001
33½					16635.989	.003
34½					16635.833	.005
35½					16635.677	.001
36½					16635.519	-.010
37½					16635.384	-.004
38½					16635.251	-.003

TABLE 15. Line Positions for the $\tilde{A}(100)^2\Pi_{1/2}$ - $\tilde{X}(000)^2\Sigma^+$ Band of CaOH

J	R_1		P_1		Q_{12}	
2½			16585.447	-.009		
3½			16585.159	.001		
4½			16584.866	.001		
5½			16584.582	.004		
6½			16584.303	.006		
7½			16584.025	.004		
8½			16583.756	.005		
9½			16583.492	.005		
10½			16583.233	.005		
11½	16599.201	.003	16582.981	.006		
12½	16600.294	-.003	16582.734	.006		
13½	16601.398	-.004	16582.493	.007		
14½	16602.508	-.004	16582.259	.009		
15½	16603.626	-.002	16582.027	.008		
16½	16604.744	-.005				
17½	16605.873	-.002				
18½	16607.000	-.006				
19½	16608.140	-.003				
20½	16609.289	.004				
21½	16610.431	-.001				
22½	16611.580	-.004				
23½	16612.742	.000				
24½	16613.910	.005				
25½	16615.076	.003				
26½	16616.253	.006				
27½	16617.427	.002				
28½	16618.610	.001				
29½	16619.800	.002			16579.272	.001
30½	16621.000	.007	16579.236	.000	16579.132	-.001
31½	16622.181	-.011	16579.094	-.002	16578.992	-.008
32½	16623.388	-.009	16578.962	.000	16578.872	.000
33½	16624.600	-.007	16578.833	-.001	16578.749	-.002
34½	16625.814	-.008	16578.709	-.002	16578.636	.000
35½	16627.036	-.006	16578.595	.001	16578.526	.000
36½	16628.265	-.003	16578.485	.001	16578.419	-.003
37½	16629.493	-.006	16578.375	-.004	16578.323	-.001
38½	16630.736	.001	16578.283	.003	16578.235	.002
39½	16631.980	.003	16578.189	.002		
40½	16633.232	.009				
41½	16634.482	.007				
42½	16635.739	.006				

TABLE 15. (Continued.)

J	Q_1		R_{12}		P_{12}	
1½	16586.697	-.008				
2½	16587.018	-.012				
3½	16587.359	-.003				
4½	16587.697	-.002				
5½	16588.042	.000				
6½	16588.396	.005				
7½	16588.749	.003				
8½	16589.107	.000			16577.387	-.004
9½	16589.478	.005			16576.410	-.006
10½	16589.847	.001			16575.444	-.003
11½	16590.228	.004			16574.482	-.003
12½	16590.613	.004			16573.525	-.003
13½	16591.003	.004			16572.574	-.004
14½	16591.399	.003			16571.632	-.002
15½	16591.802	.004			16570.694	-.002
16½					16569.756	-.009
17½					16568.840	.000
18½					16567.924	.002
19½					16567.013	.003
20½					16566.100	-.004
21½					16565.202	-.003
22½					16564.312	-.001
23½					16563.425	-.002
24½					16562.551	.003
25½					16561.673	-.003
26½					16560.810	-.001
27½					16559.949	-.004
28½					16559.101	.000
29½					16558.259	.003
30½					16557.419	.000
31½					16556.587	-.001
32½			16600.147	-.003	16555.762	-.003
33½	16600.108	-.003	16600.672	-.002	16554.948	-.001
34½	16600.633	-.001	16601.202	-.003	16554.135	-.005
35½	16601.165	.001	16601.746	.004	16553.334	-.004
36½	16601.701	.001	16602.289	.002	16552.541	-.003
37½	16602.245	.002	16602.839	.001	16551.758	.002
38½	16602.794	.001	16603.391	-.004	16550.974	-.003
39½	16603.350	.000	16603.973	.013	16550.204	.000
40½	16603.923	.010	16604.536	.005	16549.437	-.003
41½	16604.485	.002	16605.108	-.002		
42½	16605.057	-.003	16605.691	-.004		
43½	16605.648	.004	16606.289	.002		
44½	16606.236	.001	16606.887	.001		
45½	16606.834	.001	16607.494	.003		
46½	16607.438	.000				
47½	16608.052	.003	16608.729	.005		
48½	16608.667	-.001	16609.363	.012		
49½	16609.290	-.004	16609.987	.002		

TABLE 15. (Continued.)

J	Q_1		R_{12}		P_{12}
50½	16609.926	-.001	16610.626	.000	
51½	16610.566	-.001	16611.279	.004	
52½	16611.216	.002	16611.930	.000	
53½	16611.868	.000	16612.579	-.014	
54½	16612.527	-.002	16613.258	-.004	
55½	16613.198	.000	16613.933	-.006	
56½	16613.878	.004	16614.623	.000	
57½	16614.555	-.002	16615.315	.000	
58½	16615.242	-.005			

TABLE 16. Line Positions for the $\tilde{A}(020)\kappa^2\Pi_{1/2}$ - $\tilde{X}(020)(000)$ Bands of CaOH

	$\tilde{A}(020)\kappa^2\Pi_{1/2}$ - $\tilde{X}(020)^2\Delta$		$\tilde{A}(020)\kappa^2\Pi_{1/2}$ - $\tilde{X}(000)^2\Sigma^+$	
J	$R_2(f)$	$Q_{21}(fe)$	R_2	Q_2
1½				16783.739 .003
2½				16783.459 .004
3½				16783.205 .010
4½	16075.090 .012			16782.963 .010
5½	16075.569 .006			16782.738 .007
6½	16076.071 .001			16782.536 .008
7½	16076.600 -.001			16782.349 .006
8½	16077.155 .000			16782.189 .012
9½	16077.728 -.003		16789.217 -.006	16782.048 .020
10½	16078.328 -.002		16789.779 -.003	16781.915 .018
11½	16078.950 .000		16790.345 -.015	16781.805 .021
12½	16079.578 -.015		16790.947 -.009	16781.703 .016
13½	16080.245 -.012		16791.556 -.014	16781.623 .017
14½	16080.939 -.002		16792.197 -.004	16781.557 .015
15½	16081.643 -.004		16792.845 -.004	
16½			16793.503 -.011	
17½			16794.178 -.017	
18½			16794.868 -.024	
19½			16795.584 -.021	
20½			16796.316 -.017	
21½	16086.308 .009		16797.066 -.011	
22½	16087.137 -.004	16086.273 .001	16797.831 -.004	
23½	16087.979 -.022	16087.106 -.007	16798.614 .007	
24½	16088.876 -.004	16087.979 .006	16799.386 -.008	
25½	16089.770 -.007	16088.849 -.001	16800.186 -.009	
26½	16090.665 -.026	16089.739 -.007	16801.012 .003	
27½	16091.620 -.003	16090.665 .006	16801.835 -.002	
28½	16092.582 .011	16091.589 .000	16802.676 -.001	
29½		16092.538 .001	16803.540 .009	
30½	16094.525 .005		16804.405 .008	
31½		16094.476 -.007	16805.298 .022	
32½	16096.532 -.003		16806.197 .030	
33½	16097.566 -.001	16096.490 -.005	16807.103 .033	
34½	16098.616 .001	16097.529 .003		
35½	16099.706 .027	16098.573 .000		
36½	16100.761 .002	16099.655 .019		
37½	16101.857 .002	16100.710 -.005		
38½	16102.963 -.003	16101.810 .000		
39½	16104.093 .000	16102.928 .008		
40½	16105.237 .002	16104.047 .002		
41½	16106.392 -.001	16105.197 .011		
42½	16107.567 .001	16106.344 .001		
43½	16108.751 -.002	16107.515 .001		
44½		16108.691 -.010		

TABLE 17. Line Positions for the $\tilde{A}(020)\kappa^2\Pi_{3/2}$ - $\tilde{X}(020)(000)$ Bands of CaOH

	$\tilde{A}(020)\kappa^2\Pi_{3/2}$ - $\tilde{X}(020)^2\Sigma^+$				$\tilde{A}(020)\kappa^2\Pi_{3/2}$ - $\tilde{X}(000)^2\Sigma^+$			
J	R_1		P_{12}		Q_1		P_1	
3½					16770.956	-.006		
4½					16771.294	-.004	16768.270	-.019
5½			16075.327	-.006	16771.617	-.016	16767.956	-.002
6½	16088.384	-.003	16074.351	.000	16771.964	-.005	16767.632	.004
7½	16089.411	-.007	16073.367	-.006	16772.309	.003	16767.298	-.001
8½	16090.446	-.008	16072.394	-.003	16772.637	-.007	16766.976	.003
9½	16091.496	.000	16071.425	-.001	16772.977	-.006	16766.654	.005
10½	16092.543	.000			16773.323	-.001	16766.326	-.002
11½	16093.600	.003	16069.503	.008	16773.662	-.004	16766.013	.003
12½	16094.656	-.002	16068.534	-.002	16774.003	-.006	16765.703	.008
13½	16095.726	.001	16067.588	.006	16774.352	-.004	16765.390	.005
14½	16096.799	-.001	16066.634	.001	16774.703	-.001	16765.084	.006
15½	16097.881	-.001	16065.694	.005	16775.055	-.001	16764.782	.006
16½	16098.975	.003	16064.757	.005	16775.411	.001	16764.483	.004
17½	16100.083	.012	16063.825	.005	16775.773	.005	16764.190	.003
18½	16101.172	-.006	16062.896	.000	16776.147	.017	16763.907	.007
19½	16102.296	.002	16061.979	.001	16776.499	.003	16763.626	.006
20½	16103.421	.001	16061.070	.003	16776.864	-.002	16763.349	.004
21½	16104.565	.010	16060.170	.006	16777.244	.004	16763.082	.004
22½	16105.700	.001	16059.272	.004	16777.619	.000	16762.823	.006
23½	16106.855	.001	16058.385	.004	16778.001	-.003	16762.568	.005
24½	16108.020	.001	16057.505	.003	16778.391	-.002	16762.322	.006
25½	16109.194	.000	16056.632	.000	16778.787	-.002	16762.082	.005
26½	16110.375	-.006	16055.770	-.001	16779.185	-.005	16761.851	.005
27½	16111.579	.001	16054.925	.006	16779.592	-.005	16761.622	-.001
28½	16112.781	-.005	16054.081	.004	16779.999	-.011	16761.407	-.001
29½	16114.002	-.004	16053.253	.009	16780.425	-.004	16761.202	.000
30½	16115.240	.003	16052.416	-.006	16780.850	-.005	16761.006	.002
31½	16116.476	-.004	16051.612	.002	16781.280	-.007	16760.815	.001
32½	16117.733	-.001	16050.806	-.002	16781.728	.001	16760.635	.001
33½	16118.999	-.002					16760.462	-.001
34½	16120.281	.002	16049.237	.000	16782.624	-.002	16760.300	-.001
35½	16121.567	-.003	16048.464	-.004	16783.074	-.013	16760.146	-.003
36½	16122.871	-.003	16047.712	.001	16783.549	-.006	16760.003	-.003
37½	16124.187	-.003	16046.958	-.006	16784.023	-.007	16759.873	.001
38½	16125.516	-.002	16046.218	-.012	16784.511	-.002	16759.747	-.001
39½	16126.860	.001	16045.502	-.005	16784.999	-.004	16759.634	.000
40½	16128.217	.004	16044.790	-.006	16785.508	.007	16759.532	.002
41½	16129.580	.000	16044.094	-.003	16786.010	.003	16759.439	.003
42½			16043.414	.003	16786.534	.014		
43½			16042.738	.001	16787.061	.019		
44½			16042.077	.002	16787.595	.024		
45½			16041.433	.007				
46½			16040.807	.017				
47½			16040.195	.028				

TABLE 18. Line Positions for the $\tilde{A}(020)\mu^2\Pi_{3/2}$ - $\tilde{X}(000)^2\Sigma^+$ Band of CaOH

J	R_2		P_2		Q_2	
1½	16671.410	-.001				
2½	16671.802	.001				
3½	16672.211	.004	16666.739	.007	16669.133	.004
4½	16672.629	.002	16665.801	.016	16668.865	-.002
5½	16673.071	.008	16664.852	-.001	16668.628	.006
6½	16673.512	-.002	16663.934	-.003	16668.386	-.007
7½	16673.978	-.002	16663.046	.010	16668.167	-.013
8½	16674.460	-.001	16662.153	.003	16667.978	-.006
9½	16674.950	-.007	16661.274	-.006	16667.801	-.003
10½	16675.467	.001	16660.424	.000	16667.641	.001
11½	16675.989	-.002	16659.585	.002	16667.495	.003
12½	16676.525	-.004	16658.767	.010	16667.357	-.004
13½	16677.082	.001	16657.946	.001	16667.246	.001
14½	16677.644	-.003	16657.151	.003	16667.145	-.001
15½	16678.218	-.009	16656.365	.000		
16½	16678.818	-.002	16655.592	-.004		
17½	16679.427	.001	16654.848	.007		
18½	16680.040	-.006	16654.120	.020		
19½	16680.672	-.007	16653.379	.007		
20½	16681.314	-.010	16652.636	-.022		
21½	16681.973	-.009	16651.957	-.001		
22½	16682.652	-.001	16651.264	-.006		
23½	16683.333	-.003	16650.606	.010		
24½	16684.028	-.003	16649.941	.006		
25½	16684.736	-.002	16649.292	.006		
26½	16685.458	.001	16648.656	.006	16667.145	-.036
27½	16686.185	-.003	16648.032	.005	16667.246	-.037
28½	16686.935	.005	16647.415	-.001	16667.357	-.042
29½	16687.671	-.013	16646.823	.006	16667.495	-.035
30½	16688.448	-.002	16646.233	.003	16667.641	-.035
31½	16689.231	.005	16645.652	-.004	16667.801	-.035
32½	16690.017	.003	16645.076	-.017	16667.978	-.032
33½	16690.797	-.015	16644.549	.006	16668.167	-.031
34½	16691.612	-.009	16644.009	.006		
35½	16692.439	-.002	16643.479	.003		
36½	16693.261	-.011	16642.965	.005		
37½	16694.082	-.031	16642.457	.002		
38½			16641.969	.007		
39½			16641.476	-.004		
40½			16641.011	.002		

TABLE 19. Line Positions for the $\tilde{A}(020)\mu^2\Pi_{1/2}$ - $\tilde{X}(000)^2\Sigma^+$ Band of CaOH

J	R_1		P_1		Q_1	
1½					16649.741	.002
2½			16648.480	-.003	16650.073	-.008
3½	16653.671	-.003	16648.192	-.004	16650.431	-.003
4½	16654.751	-.007	16647.917	-.003	16650.789	-.009
5½	16655.841	-.012	16647.655	-.001	16651.174	.001
6½	16656.954	-.005	16647.415	.013	16651.558	-.003
7½	16658.057	-.018	16647.163	.003	16651.964	.004
8½	16659.211	.007	16646.926	-.003	16652.383	.013
9½	16660.341	-.002	16646.709	.000	16652.813	.020
10½	16661.494	.000	16646.497	-.003	16653.233	.005
11½	16662.658	.002	16646.307	.004	16653.672	-.002
12½	16663.823	-.007	16646.115	-.003	16654.135	.002
13½	16665.011	-.005	16645.953	.009	16654.601	-.003
14½	16666.206	-.007	16645.789	.007	16655.093	.005
15½			16645.652	.020	16655.598	.015
16½			16645.501	.007	16656.103	.012
17½	16669.867	-.009	16645.376	.007	16656.615	.003
18½	16671.138	.017	16645.261	.006	16657.157	.012
19½	16672.381	.002	16645.159	.005	16657.687	-.003
20½	16673.651	.003			16658.254	.006
21½	16674.949	.019			16658.821	.002
22½	16676.226	.002			16659.407	.006
23½	16677.533	.002			16659.999	.002
24½	16678.826	-.025			16660.605	.001
25½	16680.184	.002			16661.226	.002
26½	16681.527	.000			16661.856	.000
27½	16682.877	-.007			16662.503	.002
28½	16684.258	.005			16663.156	-.001
29½	16685.629	-.006			16663.823	-.003
30½	16687.024	-.006			16664.505	-.001
31½	16688.439	.002			16665.198	-.001
32½	16689.848	-.009			16665.898	-.005
33½	16691.293	.004			16666.614	-.006
34½	16692.733	-.001				

TABLE 20. Line Positions for the $\tilde{A}(100)^2\Pi_{3/2}$ - $\tilde{X}(000)^2\Sigma^+$ Band of CaOD

J	R_{21}		R_2		P_2		Q_2	
1½	16650.149	-.005	16648.946	.002			16647.403	.001
2½	16651.101	.000	16649.282	-.004			16647.135	.008
3½	16652.060	.001	16649.635	-.004			16646.869	.006
4½	16653.033	.005	16649.997	-.006			16646.619	.009
5½	16654.001	-.007	16650.375	-.003	16642.971	-.004	16646.369	.000
6½	16654.996	-.004	16650.762	-.002	16642.123	-.004	16646.144	.006
7½	16655.998	-.004	16651.156	-.004	16641.291	.001	16645.927	.008
8½	16657.017	.002	16651.561	-.006	16640.467	.003	16645.714	.004
9½	16658.041	.002	16651.977	-.009	16639.650	.000	16645.516	.003
10½	16659.075	.002	16652.405	-.010	16638.844	-.002	16645.331	.004
11½	16660.120	.001	16652.848	-.006	16638.050	-.003	16645.158	.006
12½	16661.174	-.002	16653.294	-.011	16637.270	-.001	16644.993	.006
13½	16662.243	-.001	16653.755	-.011	16636.499	-.001	16644.839	.004
14½	16663.321	-.002	16654.227	-.011	16635.740	.000	16644.695	.002
15½	16664.414	.002	16654.712	-.009	16634.992	.001	16644.570	.008
16½	16665.511	-.001			16634.252	-.001	16644.447	.004
17½	16666.620	-.004			16633.524	-.001	16644.346	.012
18½	16667.742	-.004			16632.809	.000	16644.243	.006
19½	16668.877	-.002			16632.104	.000		
20½	16670.017	-.005			16631.408	-.001		
21½	16671.175	-.002			16630.729	.004		
22½	16672.343	.001			16630.052	.000		
23½	16673.519	.001			16629.390	.000		
24½	16674.696	-.009			16628.738	-.001		
25½	16675.901	-.001			16628.094	-.005		
26½	16677.105	-.005			16627.470	.001		
27½	16678.326	-.003			16626.852	.002		
28½	16679.556	-.002			16626.244	.002		
29½	16680.798	.000			16625.647	.003		
30½	16682.049	.001			16625.055	-.003		
31½	16683.311	.002			16624.481	-.001		
32½	16684.578	-.003			16623.921	.004		
33½	16685.862	.000			16623.363	.001		
34½	16687.152	-.003			16622.818	.000		
35½	16688.458	.000			16622.288	.003		
36½	16689.772	.001			16621.762	.000		
37½	16691.095	.001			16621.252	.002		
38½	16692.429	.001			16620.750	.001		
39½	16693.775	.002			16620.261	.003		
40½	16695.125	-.002			16619.780	.002		
41½	16696.496	.004			16619.310	.001		
42½	16697.872	.005			16618.855	.005		
43½	16699.254	.001			16618.399	-.003		
44½	16700.649	.001			16617.963	-.001		
45½	16702.058	.004			16617.535	-.002		
46½	16703.471	.001			16617.122	.002		

TABLE 20. (Continued.)

J	R_{21}		R_2	P_2		Q_2
47½	16704.890	-.006		16616.710	-.004	
48½	16706.320	-.012		16616.317	-.002	
49½	16707.782	.004		16615.930	-.004	
50½	16709.239	.005		16615.554	-.006	
51½	16710.701	.000		16615.186	-.010	
52½	16712.180	.003				
53½	16713.659	-.004				
54½	16715.157	-.003				

TABLE 21. Line Positions for the $\tilde{A}(100)^2\Pi_{1/2}$ - $\tilde{X}(000)^2\Sigma^+$ Band of CaOD

J	R_1		P_1		P_{12}	
2½			16580.005	-.001		
3½			16579.770	.003		
4½			16579.544	.002		
5½			16579.328	.000		
6½			16579.127	.003		
7½			16578.931	.002		
8½			16578.744	.002		
9½			16578.566	.005		
10½			16578.392	.004	16571.460	-.002
11½			16578.226	.006	16570.661	-.007
12½	16594.109	-.002	16578.066	.007	16569.873	-.007
13½	16595.172	-.005	16577.910	.006	16569.095	-.003
14½	16596.247	-.002	16577.758	.004	16568.322	.001
15½	16597.322	-.005	16577.618	.008	16567.548	-.001
16½	16598.406	-.004			16566.782	-.001
17½	16599.497	-.001			16566.028	.006
18½	16600.587	-.005			16565.269	.003
19½	16601.693	.001			16564.509	-.006
20½	16602.795	-.002			16563.770	.001
21½	16603.914	.006			16563.030	.001
22½	16605.022	-.003			16562.296	.002
23½	16606.150	.002			16561.567	.003
24½	16607.274	-.003			16560.841	.000
25½	16608.412	.000			16560.123	.000
26½	16609.551	-.003			16559.416	.005
27½	16610.698	-.005			16558.710	.005
28½	16611.852	-.006			16558.004	-.001
29½	16613.015	-.005			16557.317	.005
30½	16614.182	-.008			16556.634	.009
31½	16615.363	-.005			16555.950	.004
32½	16616.548	-.005			16555.277	.004
33½	16617.743	-.003			16554.611	.004
34½	16618.942	-.005			16553.948	-.001
35½	16620.156	-.001			16553.299	.001
36½	16621.375	-.001				
37½	16622.603	-.001				
38½	16623.844	.002				

TABLE 21. (Continued.)

J	Q_1		R_{12}	
2½	16581.477	-.004		
3½	16581.829	-.004		
4½	16582.194	-.005		
5½	16582.575	-.002		
6½	16582.965	.000		
7½	16583.359	-.002		
8½	16583.766	.002		
9½	16584.177	.003		
10½	16584.588	-.002		
11½	16585.010	-.002		
12½	16585.440	.001		
13½	16585.873	.001		
14½	16586.320	.010		
15½	16586.753	.001		
.				
.				
.				
29½			16594.050	.003
30½	16594.019	.003	16594.576	-.003
31½	16594.545	-.002	16595.121	.003
32½	16595.088	.003	16595.663	-.001
33½	16595.627	-.002	16596.228	.012
34½	16596.185	.004	16596.773	-.003
35½	16596.738	-.002	16597.347	.003
36½	16597.308	.002	16597.920	.001
37½	16597.875	-.005	16598.507	.005
38½	16598.467	.005	16599.104	.011
39½	16599.061	.009	16599.707	.015
40½	16599.660	.010		

TABLE 22. Line Positions for the $\tilde{A}(020)\kappa^2\Pi_{1/2}$ - $\tilde{X}(020)$ Band of CaOD

	$(020)\kappa^2\Pi_{1/2}$ - $(020)^2\Sigma^+$		$(020)\kappa^2\Pi_{1/2}$ - $(020)^2\Delta$			
J	R_2		$R_{21}(e)$		$R_{21}(f)$	
1½	16075.505	-.007				
4½	16076.645	-.009				
5½	16077.074	.004				
9½	16078.912	-.005			16068.995	-.003
10½	16079.422	-.001	16070.167	.019	16070.110	-.005
11½	16079.946	-.002	16071.295	.017	16071.248	-.002
12½	16080.494	.004				
13½	16081.047	-.003	16073.591	.006		
14½	16081.632	.004	16074.769	.007	16074.767	.002
15½			16075.962	.007	16075.962	-.010
16½			16077.176	.012		
17½	16083.467	.000				
18½	16084.106	-.009	16079.634	.007	16079.697	-.002
19½	16084.777	-.003	16080.878	-.003	16080.975	.000
20½	16085.458	-.004	16082.152	.002	16082.264	-.005
21½	16086.163	.001	16083.437	.004	16083.584	.004
22½	16086.879	.002			16084.906	-.001
23½	16087.606	-.004	16086.054	.012		
24½	16088.344	-.015	16087.368	.001		
25½	16089.120	-.005	16088.705	-.001		
26½	16089.909	.002	16090.053	-.006		
27½	16090.704	-.001	16091.420	-.004		
28½	16091.519	.000	16092.794	-.009		
29½	16092.353	.003	16094.190	-.005		
30½	16093.204	.008	16095.595	-.005		
31½	16094.056	-.002	16097.008	-.009		
32½	16094.941	.006	16098.441	-.005		
33½	16095.828	.000	16099.878	-.009		
34½	16096.730	-.007	16101.332	-.008		
35½	16097.660	-.001	16102.792	-.013		
36½	16098.602	.002	16104.280	-.002		
37½	16099.555	.001				
38½	16100.520	-.004				
39½	16101.510	.002				

TABLE 22. (Continued.)

	$(020)\kappa^2\Pi_{1/2}$ - $(020)^2\Delta$							
J	$R_2(e)$		$R_2(f)$		$P_2(e)$		$P_2(f)$	
5½	16061.126	.005	16061.075	-.008				
6½	16061.569	.008	16061.518	-.004				
7½	16062.024	.005	16061.976	-.002				
8½	16062.500	.006	16062.454	.000				
9½	16063.004	.019	16062.944	-.003				
10½	16063.497	.004	16063.447	-.012				
11½	16064.022	.004	16063.982	-.008				
12½	16064.568	.009	16064.537	-.001	16048.350	.007	16048.309	.001
13½	16065.122	.005	16065.104	-.001	16047.683	.027	16047.622	-.005
14½	16065.689	-.001	16065.672	-.017	16046.996	.010	16046.962	-.002
15½	16066.282	.002	16066.282	-.009	16046.355	.022	16046.317	-.002
16½	16066.887	.002	16066.887	-.024			16045.693	.000
17½	16067.489	-.016	16067.529	-.020	16045.092	.018	16045.092	.008
18½	16068.135	-.006	16068.184	-.019				
19½	16068.788	-.004	16068.855	-.020	16043.885	.006	16043.914	-.006
20½	16069.444	-.014	16069.553	-.011	16043.317	.012	16043.362	-.003
21½	16070.139	.000	16070.261	-.008	16042.757	.011	16042.820	-.006
22½			16070.979	-.012	16042.212	.009	16042.308	.003
23½			16071.709	-.021	16041.682	.007	16041.802	.001
24½					16041.166	.004	16041.319	.005
25½			16073.247	-.007			16040.858	.015
26½					16040.186	.007	16040.406	.017
27½			16074.831	-.011	16039.718	.008	16039.966	.015
28½			16075.646	-.013	16039.271	.016	16039.547	.018
29½					16038.823	.009	16039.141	.018
30½					16038.396	.010	16038.759	.027
31½			16078.185	-.014	16037.982	.009		
32½					16037.580	.007		

TABLE 23. Line Positions for the $\tilde{A}(020)\kappa^2\Pi_{3/2}$ - $\tilde{X}(020)(000)$ Bands of CaOD

$\tilde{A}(020)\kappa^2\Pi_{3/2}$ - $\tilde{X}(020)^2\Sigma^+$			$\tilde{A}(020)\kappa^2\Pi_{3/2}$ - $\tilde{X}(000)^2\Sigma^+$					
J	Q_1		Q_1		R_1		P_{12}	
2½	16061.488	.006						
3½	16061.763	.007	16580.952	-.001				
4½	16062.032	.005	16581.228	.000				
5½	16062.303	.005	16581.500	-.003				
6½	16062.574	.003	16581.788	.008				
7½	16062.850	.004	16582.064	.003				
8½	16063.133	.008	16582.353	.006			16571.780	.010
9½	16063.421	.012					16570.847	.002
10½	16063.693	-.004			16590.080	.004	16569.920	-.006
11½					16591.016	-.002	16569.010	-.002
12½	16064.291	-.002	16583.547	-.001			16568.103	-.003
13½	16064.611	.011	16583.876	.011	16592.933	.007	16567.200	-.006
14½					16593.901	.008	16566.308	-.006
15½			16584.519	-.002	16594.876	.007	16565.423	-.006
16½	16065.578	.016	16584.852	-.009	16595.867	.013	16564.534	-.018
17½	16065.900	.002	16585.198	-.011	16596.856	.007	16563.675	-.008
18½			16585.559	-.006	16597.866	.013	16562.808	-.014
19½					16598.875	.009	16561.960	-.010
20½					16599.896	.006	16561.108	-.018
21½					16600.928	.006	16560.272	-.019
22½					16601.973	.008	16559.442	-.023
23½					16603.024	.006	16558.622	-.026
24½					16604.086	.005		
25½					16605.155	.002		
26½					16606.235	-.001		
27½					16607.330	.002		
28½					16608.431	.000		
29½					16609.546	.002		
30½					16610.671	.005		
31½					16611.798	-.001		
32½					16612.941	.000		
33½					16614.095	.001		

TABLE 24. Line Positions for the $\tilde{A}(020)\mu^2\Pi_{3/2}$ - $\tilde{X}(000)^2\Sigma^+$ Band of CaOD

J	R_2		Q_2	
1½	16490.546	.002		
2½	16490.919	.000	16488.729	.000
3½	16491.307	-.007	16488.504	.004
4½	16491.726	-.002	16488.299	.006
5½	16492.168	.007	16488.107	.000
6½	16492.614	.002	16487.950	.008
7½	16493.084	.002	16487.805	.006
8½	16493.567	-.002		
9½	16494.072	-.002		
10½	16494.594	-.002		
11½	16495.138	.004		
12½	16495.686	-.003		
13½	16496.260	.001		
14½	16496.839	-.006		
15½	16497.447	.002		
16½	16498.059	-.002		
17½	16498.691	.000	16487.492	.012
18½	16499.338	.003	16487.567	.013
19½	16499.990	-.003	16487.649	.004
20½	16500.663	-.002	16487.753	-.001
21½	16501.353	.003	16487.878	-.003
22½	16502.047	.000	16488.019	-.005
23½	16502.757	-.001	16488.183	-.001
24½	16503.483	.001	16488.357	-.003
25½	16504.219	.002	16488.555	.002
26½	16504.970	.005	16488.760	-.001
27½	16505.724	-.001	16488.984	-.001
28½	16506.496	-.001	16489.223	-.001
29½	16507.278	-.002		
30½	16508.076	.002		
31½	16508.877	-.003		
32½	16509.699	.002		
33½	16510.526	.001		
34½	16511.370	.006		
35½	16512.214	.000		
36½	16513.074	.000		
37½	16513.944	.000		
38½	16514.828	.003		
39½	16515.721	.006		
40½	16516.615	-.001		
41½	16517.521	-.006		
42½	16518.450	.002		
43½	16519.386	.008		
44½	16520.319	.002		
45½	16521.269	.002		
46½	16522.228	.003		
47½	16523.185	-.008		
48½	16524.166	-.004		
49½	16525.151	-.005		
50½	16526.153	.003		

TABLE 25. Line Positions for the $\tilde{A}(020)\mu^2\Pi_{1/2}$ - $\tilde{X}(020)(000)$ Bands of CaOD

	$\tilde{A}(020)\mu^2\Pi_{1/2}$ - $\tilde{X}(020)^2\Sigma^+$						$\tilde{A}(020)\kappa^2\Pi_{1/2}$ - $\tilde{X}(000)^2\Sigma^+$	
J	Q_1		R_1		P_1		P_1	
2½							16477.627	-.004
3½							16477.351	-.003
4½							16477.082	.003
5½							16476.783	-.024
6½	15961.047	-.007					16476.540	.003
7½	15961.365	.003			15957.058	.004	16476.265	-.005
8½	15961.669	-.006					16476.003	-.002
9½	15962.003	.011			15956.511	-.003	16475.733	-.010
10½	15962.315	-.001			15956.253	.006	16475.490	.006
11½	15962.645	.000			15955.984	.001	16475.223	-.005
12½	15962.983	.002	15971.585	.001	15955.726	.005	16474.990	.014
13½	15963.330	.007	15972.537	-.006	15955.461	-.001	16474.736	.009
14½	15963.680	.007	15973.503	-.004	15955.210	.004	16474.482	.000
15½			15974.475	.001	15954.950	-.004	16474.245	.004
16½	15964.404	.009	15975.444	-.001	15954.700	-.006	16474.011	.006
17½	15964.778	.010	15976.420	-.001	15954.463	.001	16473.771	-.003
18½	15965.146	-.004	15977.395	-.007	15954.224	.002	16473.560	.013
19½	15965.553	.013	15978.383	-.005			16473.324	-.002
20½	15965.947	.008	15979.376	-.003	15953.762	.004	16473.109	-.001
21½	15966.348	.000	15980.369	-.007	15953.533	-.001	16472.896	-.004
22½	15966.764	-.002	15981.371	-.008	15953.316	.001	16472.703	.006
23½	15967.193	-.001	15982.387	-.001	15953.106	.003	16472.494	-.006
24½	15967.632	.000	15983.398	-.005	15952.901	.005	16472.310	.001
25½	15968.083	.003	15984.425	.000	15952.695	-.002	16472.124	-.001
26½	15968.534	-.005	15985.452	-.002	15952.505	.001	16471.954	.005
27½	15969.002	-.006	15986.488	-.002			16471.779	-.001
28½	15969.487	-.002	15987.532	-.002	15952.147	.006	16471.620	.002
29½			15988.590	.005			16471.467	.003
30½			15989.643	-.001	15951.805	-.003	16471.320	.002
31½			15990.714	.004	15951.654	.001	16471.182	.002
32½			15991.784	-.001	15951.510	.003	16471.048	-.002
33½			15992.866	-.002	15951.371	.002	16470.922	-.007
34½			15993.964	.004	15951.243	.003	16470.810	-.006
35½			15995.060	.000	15951.124	.004	16470.708	-.003
36½			15996.171	.003	15951.013	.005	16470.612	-.004
37½			15997.286	.000	15950.913	.007	16470.531	.002
38½			15998.415	.002	15950.813	-.001	16470.457	.006
39½			15999.549	.001	15950.730	.000	16470.378	-.004
40½			16000.692	-.001	15950.654	-.003	16470.322	.000
41½			16001.846	-.002				
42½			16003.010	-.001				
43½			16004.186	.001				
44½			16005.360	-.008				

BIBLIOGRAPHY

1. J. F. W. Herschel, *Trans. Roy. Soc. Edinburgh*, **9**, No. II, 445 (1823).
2. C. G. James and T. M. Sugden, *Nature*, **175**, 333 (1955).
3. A. Lagerqvist and L. Huldt, *Naturwissensch.* **42**, 365 (1955).
4. L. Huldt and A. Lagerqvist, *Ark. Fys.* **11**, 347 (1956).
5. R. F. Wormsbecher, M. Trkula, C. Martner, R. E. Penn, and D. O. Harris, *J. Mol. Spectrosc.* **97**, 29 (1983)
6. J. B. West, R. S. Bradford, Jr., J. D. Eversole, and C. R. Jones, *Rev. Sci. Instrum.* **46**, 164 (1975).
7. R. C. Hilborn, Zhu Qingshi, and D. O. Harris, *J. Mol. Spectrosc.* **97**, 73 (1983).
8. J. Nakagawa, R. F. Wormsbecher, and D. O. Harris, *J. Mol. Spectrosc.* **97**, 37 (1983).
9. P. F. Bernath and S. Kinsey-Nielsen, *Chem. Phys. Lett.* **105**, 663 (1984).
10. M. Li, Y. Zhang, C. Wang, and Q. Zhu, *Appl. Laser*, **4**, 149 (1984).
11. Q. Zhu, M. Li, Y. Zhang, and C. Wang, *Acta Opt. Sin.* **5**, 765 (1985).
12. C. R. Brazier and P. F. Bernath, *J. Mol. Spectrosc.* **114**, 163 (1985).
13. W. T. M. L. Fernando, M. Douay, and P. F. Bernath, *J. Mol. Spectrosc.* **144**, 344 (1990).
14. R. A. Hailey, C. N. Jarman, W. T. M. L. Fernando, and P. F. Bernath, *J. Mol. Spectrosc.* **147**, 40 (1991).
15. W. L. Barclay Jr., M. A. Anderson, and L. M. Ziurys, *Chem. Phys. Lett.* **196**, 225 (1992).
16. L. M. Ziurys, W. L. Barclay, and M. M. Anderson, *Astrophys. J.* **384**, L63 (1992).
17. C. N. Jarman and P. F. Bernath, *J. Chem. Phys.* **97**, 1711 (1992).

18. T. C. Steimle, D. A. Fletcher, K. Y. Jung, and C. T. Scurlock, *J. Chem. Phys.* **96**, 2556 (1992).

19. M. F. Cai, T. A. Miller, and V. E. Bondybey, *Chem. Phys. Lett.* **158**, 475 (1989).

20. C. J. Whitham, B. Soep, J. P. Visticot, and A. Keller, *J. Chem. Phys.* **93**, 991 (1990).

21. C. T. Scurlock, D. A. Fletcher, and T. C. Steimle, *J. Mol. Spectrosc.* **159**, 350 (1993).

22. P. I. Presunka and J. A. Coxon, *Can. J. Chem.* **71**, 1689 (1993).

23. P. I. Presunka and J. A. Coxon, *J. Chem. Phys.* **101**, 201 (1994).

24. P. I. Presunka and J. A. Coxon, *Chem. Phys.* **190**, 97 (1995).

25. C. W. Bauschlicher, Jr., S. R. Langhoff, and H. Partridge, *J. Chem. Phys.* **84**, 901 (1986).

26. C. W. Bauschlicher, Jr. and H. Partridge, *Chem. Phys. Lett.* **106**, 65 (1984)

27. C. W. Bauschlicher, Jr., S. R. Langhoff, T. C. Steimle, and J. E. Shirley, *J. Chem. Phys.* **93**, 4179 (1990).

28. J. V. Ortiz, *J. Chem. Phys.* **92**, 6728 (1990).

29. J. M. Mestdagh and J. P. Visticot, *Chem. Phys.* **155**, 79 (1991).

30. A. R. Allouche and M. Aubert-Frecon, *J. Mol. Spectrosc.* **163**, 599 (1994).

31. Z. J. Jakubek and R. W. Field, *J. Chem. Phys.* **98**, 6574 (1993).

32. W. W. Duley and T. J. Millar, *Ap. J.* **220**, 124 (1978).

33. T. Tsuji, *Astron. Astrophys.* **23**, 411 (1973).

34. P. Pesch, *Astrophys. J.* **174**, L155 (1974).

35. B. E. Turner and T. C. Steimle (unpublished results).

36. M. D. Oberlander, R. P. Kampt, and J. M. Parson, *Chem. Phys. Lett.* **176**, 385 (1991).

37. B. S. Cheong and J. M. Parson, *J. Chem. Phys.* **100**, 2637 (1994).

38. R. Renner, *Z. Physik.* **92**, 172 (1934).

39. K. Dressler and D. A. Ramsay, *J. Chem. Phys.* **27**, 971 (1957).

40. A. H. Nielsen, *J. Chem. Phys.* **11**, 160 (1943).

41. J. A. Pople, *Mol. Phys.* **3**, 16 (1960).

42. J. T. Hougen, *J. Chem. Phys.* **36**, 519 (1962).

43. J. T. Hougen, *J. Chem. Phys.* **37**, 403 (1962).

44. J. T. Hougen and J. P. Jesson, *J. Chem. Phys.* **38**, 1524 (1963).

45. G. Herzberg, *Electronic Spectra and Structure of Polyatomic Molecules*, Van Nostrand, Princeton, 1966.

46. J. M. Brown and F. Jorgensen, *Mol. Phys.* **47**, 1065 (1982).

47. Ch. Jungen and A. J. Merer, in *Molecular Spectroscopy: Modern Research* (K. Narahari Rao, Ed.), Vol. II, Chap. 3, Academic Press, New York, 1976.

48. J. M. Brown and F. Jorgensen, *Adv. Chem. Phys.* **52**, 117 (1983).

49. J. W. C. Johns, *J. Mol. Spectrosc.* **15**, 473 (1965).

50. J. W. C. Johns and U. Ringstrom, *J. Mol. Spectrosc.* **42**, 274 (1972).

51. J. M. Brown, *J. Mol. Spectrosc.* **56**, 159 (1975).

52. J. W. C. Johns, *Can. J. Phys.* **39**, 1738 (1961).

53. A. G. Adam, A. J. Merer, and D. M. Steunenberg, *J. Chem. Phys.* **92**, 2848 (1990).

54. R. N. Dixon, *Phil. Trans. Roy. Soc. Lond. A*, **252**, 165 (1960).

55. P. S. H. Bolman, J. M. Brown, A. Carrington, I. Kopp, and D. A. Ramsay, *Proc. Roy. Soc. Lond. A*, **343**, 17 (1975).

56. D. R. Woodward, D. A. Fletcher, and J. M. Brown, *Mol. Phys.* **62**, 517 (1987).

57. R. N. Dixon and D. A. Ramsay, *Can. J. Phys.* **46**, 2619 (1968).

58. F. J. Northrup and T. J. Sears, *Mol. Phys.* **71**, 45 (1990).

59. C. Larcher, D. Gauyacq, and J. Rostas, *J. Chem. Phys.* **77**, 655 (1980).

60. J. M. Frye and T. J. Sears, *Mol. Phys.* **62**, 919 (1987).

61. M. Wu, F. J. Northrup, and T. J. Sears, *J. Chem. Phys.* **97**, 4583 (1992).

62. G. Herzberg, *Infrared and Raman Spectra of Polyatomic Molecules*, Van Nostrand, Princeton, 1945.

63. G. Herzberg and E. Teller, *Z. Phys. Chem.* **B21**, 410 (1933).

64. G. Herzberg, *Spectra of Diatomic Molecules*, Van Nostrand, Princeton, 1950.

65. J. A. Pople and H. C. Longuet-Higgins, *Mol. Phys.* **1**, 372 (1958).

66. J. M. Brown, *J. Mol. Spectrosc.* **68**, 412 (1977).

67. D. Gauyacq and Ch. Jungen, *Mol. Phys.* **41**, 383 (1980).

68. A. D. Walsh, *J. Chem. Soc.* 2266 (1953).

69. T. J. Odiorne and P. R. Brooks, *J. Chem. Phys.* **55**, 1981 (1971).

70. A. Gupta, D. S. Perry, and R. N. Zare, *J. Chem. Phys.* **72**, 6250 (1980).

71. S. Gerstenkorn and P. Luc, *Atlas du Spectre d'Absorption de la Molécule d'Iode*, Laboratoire Aime'-Cotton, CNRS II - 91405 Orsay, France.

72. L. Ramaley, S. C. Foster, and J. A. Coxon, *Chem. Biomed. Environ. Instrum.* **12**, 229 (1982).

73. B. A. Palmer, R. A. Keller, and R. S. Engleman, Jr., *An Atlas of Uranium Emission Intensities in a Hollow Cathode Discharge*, Los Alamos Scientific Report LA-8251-MS, 1980.

74. M. S. Sorem and A. L. Schawlow, *Opt. Commun.* **5**, 148 (1972).

75. P. F. Bernath and C. R. Brazier, *Astrophys. J.* **288**, 373 (1985).

76. L. Veseth, *J. Mol. Spectrosc.* **38**, 228 (1971).

77. J. M. Brown and J. K. G. Watson, *J. Mol. Spectrosc.* **65**, 65 (1977).

78. L. Veseth, *J. Phys.* B, **3**, 1677 (1970).

79. A. J. Merer, *Mol. Phys.* **23**, 309 (1972).

80. J. A. Coxon, M. Li, and P. I. Presunka, *J. Mol. Spectrosc.* **150**, 33 (1991).

81. K. Kawaguchi, E. Hirota, and C. Yamada, *Mol. Phys.* **44**, 509 (1981).

82. J. M. Brown, E. A. Colbourn, J. K. G. Watson, and F. D. Wayne, *J. Mol. Spectrosc.* **74**, 294 (1979).

83. A. J. Merer and J. M. Allegretti, *Can. J. Phys.* **49**, 2859 (1971).

84. H. H. Nielsen, *Rev. Mod. Phys.* **23**, 90 (1951).

85. E. Fermi, *Z. Phys.* **71**, 250 (1931).

86. R. N. Dixon, D. Field, and M. Noble, *Chem. Phys. Lett.* **50**, 1 (1977).

87. D. R. Lide, Jr. and C. Matsumura, *J. Chem. Phys.* **50**, 3080 (1969).

88. J. M. Brown, Private communication (1995)

89. N. H. Rosenbaum, J. C. Owrutsky, L. M. Tack, and R. J. Saykally, *J. Chem. Phys.* **84**, 5308 (1986).

90. P. F. Bartunek and E. F. Barker, *Phys. Rev.* **48**, 516 (1935).

91. W. G. Penney and G. B. B. M. Sutherland, *Proc. Roy. Soc. London*, **156**, 654 (1936).

92. F. Dorman and C. C. Lin, *J. Mol. Spectrosc.* **12**, 119 (1964).

93. J. Pliva, *Collection Czech. Chem. Commun.* **23**, 1846 (1958).

94. J. Pliva, in *Proceedings of the Conference on Critical Evaluation of Chemical and Physical Structural Data*, ed. D. R. Lide, National Academy of Sciences, Washington, D.C., 1974.

95. I. M. Mills, in *Vibration-rotation structure in Asymmetric and Symmetric Top Molecules*, ed. K. N. Rao and C. W. Mathews, *Molecular Spectroscopy: Modern Research* (Academic Press), 1972.